

VOL.107 NO.HY11. NOV. 1981

# **JOURNAL OF THE HYDRAULICS DIVISION**

PROCEEDINGS OF  
THE AMERICAN SOCIETY  
OF CIVIL ENGINEERS



**THIS ISSUE  
INCLUDES  
SIX PAPERS ON  
HYDRAULIC MODELS**

## AMERICAN SOCIETY OF CIVIL ENGINEERS

### BOARD OF DIRECTION

#### *President*

James R. Sims

#### *Past President*

Irvan F. Mendenhall

#### *President Elect*

John H. Wiedeman

#### *Vice Presidents*

Lyman R. Gillis

Albert A. Grant

Paul A. Kuhn

William H. Taylor

#### *Directors*

Martin G. Abegg

L. G. Byrd

Frederick W. DeWitt

Larry J. Feeser

John A. Focht, Jr.

Sergio Gonzalez-Karg

Kenneth D. Hansen

Ronald C. Hirschfield

Louis M. Laushey

Leon D. Luck

Arthur R. McDaniel

Robert L. Morris

Paul R. Munger

William R. Neuman

Leonard S. Oberman

John D. Parkhurst

Celestino R. Pennoni

Robert B. Rhode

Gerald E. Speitel

Lawrence E. Wilson, Jr.

Richard S. Woodruff

### EXECUTIVE OFFICERS

Eugene Zwayer, *Executive Director*

Julie E. Gibouleau, *Assistant to the Executive Director*

Louis L. Meier, *Washington Counsel/Assistant Secretary*

William H. Wisely, *Executive Director Emeritus*

Michael N. Salgo, *Treasurer*

Elmer B. Isaak, *Assistant Treasurer*

### STAFF DIRECTORS

Donald A. Buzzell, *Managing Director for Education and Professional Affairs*

Robert A. Crist, Jr., *Managing Director for Publications and Technical Affairs*

Alexandra Bellow, *Director, Human Resources*

Joe DeFiglia, *Director, Management Information Services*

David Dresia, *Director, Publications Production and Marketing*

Barker D. Herr, *Director, Membership*

Richard A. Jeffers, *Controller*

Carl E. Nelson, *Director, Field Services*

Don P. Reynolds, *Director, Policy, Planning and Public Affairs*

Bruce Rickerson, *Director, Legislative Services*

Albert W. Turchick, *Director, Technical Services*

George K. Wadlin, *Director, Education Services*

R. Lawrence Whipple, *Director, Engineering Management Services*

### COMMITTEE ON PUBLICATIONS

William R. Neuman, *Chairman*

Martin G. Abegg, Ronald C. Hirschfield

John A. Focht, Jr., Paul R. Munger

Lawrence E. Wilson, Jr.

### HYDRAULICS DIVISION

#### *Executive Committee*

Rudolph P. Savage, *Chairman*

George E. Hecker, *Vice Chairman*

Ronald E. Nece, Patrick J. Ryan

Charles S. Mifkovic, *Secretary*

John J. Cassidy, *Management Group D Contact Member*

#### *Publications Committee*

Melvin W. Anderson, *Chairman and Editor*

John A. Hoopes, *Vice Chairman*

Philip H. Burgi, *Hydraulic Structures*

Richard H. (Pete) Hawkins, *Surface Water Hydrology*

John A. Hoopes, *Hydromechanics, General*

Gerhard H. Jirka, *Hydraulic Transport and Dispersion*

Chintu Lai, *Hydromechanics, Open Channels*

Frederick A. Locher, *Hydromechanics, Open Channels*

Donn G. DeCoursey, *Sedimentation*

Bryan R. Pearce, *Tidal Hydraulics*

John A. Roberson, *Hydromechanics, Closed Conduits*

John L. Wilson, *Groundwater Hydrology*

George E. Hecker, *Exec. Comm. Contact Member*

### PUBLICATION SERVICES DEPARTMENT

David Dresia, *Director, Publications*

Production and Marketing

#### *Technical and Professional Publications*

Richard R. Torrens, *Manager*

Chuck Wahrhaftig, *Chief Copy Editor*

Corinne Bernstein, *Copy Editor*

Linda Ellington, *Copy Editor*

Walter Friedman, *Copy Editor*

Shiela Menaker, *Production Co-ordinator*

Richard C. Scheblein, *Draftsman*

#### *Information Services*

Melanie G. Edwards, *Editor*



## PERMISSION TO PHOTOCOPY JOURNAL PAPERS

Permission to photocopy for personal or internal reference beyond the limits in Sections 107 and 108 of the U.S. Copyright Law is granted by the American Society of Civil Engineers for libraries and other users registered with the Copyright Clearance Center, 21 Congress Street, Salem, Mass. 01970, provided the appropriate fee is paid to the CCC for all articles bearing the CCC code. Requests for special permission or bulk copying should be addressed to the Manager of Technical and Professional Publications, American Society of Civil Engineers.

## CONTENTS

<b>Introduction to Six Papers on Hydraulic Models</b> . . . . .	1281
<b>Development of the River Seine Estuary: Case Study</b> <i>by François Parthiot</i> . . . . .	1283
<b>Prevention of Shoaling at Port Orford, Oregon</b> <i>by C. E. Chatham</i> . . . . .	1303
<b>Umfolozi Road Bridge Hydraulic Model Investigation</b> <i>by J. A. Zwamborn</i> . . . . .	1317
<b>Modeling Cavitation for Closed Conduit Flow</b> <i>by J. Paul Tullis</i> . . . . .	1335
<b>Physical Modeling of Rotterdamse Waterweg Estuary</b> <i>by Herman N. C. Breusers and Ad G. van Os</i> . . . . .	1351
<b>Heated Discharge in an Estuary: Case Study</b> <i>by James B. Nystrom, George E. Hecker, and Han C. Moy</i> . . . . .	1379

The Journal of the Hydraulics Division (ISSN 0044-796X) is published monthly by the American Society of Civil Engineers. Publications office is at 345 East 47th Street, New York, N.Y. 10017. Address all ASCE correspondence to the Editorial and General Offices at 345 East 47th Street, New York, N.Y. 10017. Allow six weeks for change of address to become effective. Subscription price to members is \$16.50. Nonmember subscriptions available; prices obtainable on request. Second-class postage paid at New York, N.Y. and at additional mailing offices. HY.

POSTMASTER: Send address changes to American Society of Civil Engineers, 345 East 47th Street, New York, NY 10017.

The Society is not responsible for any statement made or opinion expressed in its publications.

<b>Instrumentation for Aerated Flow on Spillways</b> by Paul Cain and Ian R. Wood . . . . .	1407
<b>Measurements of Self-Aerated Flow on a Spillway</b> by Paul Cain and Ian R. Wood . . . . .	1425
<b>Bed Load Discharge Coefficient</b> by Peter Engel and Y. Lam Lau . . . . .	1445
<b>Particle Counter for Sediment Transport Studies</b> by John P. Downing, Jr. . . . .	1455
<b>Buoyant Surface Jets</b> by Gerhard H. Jirka, E. Eric Adams, and Keith D. Stolzenbach . . . .	1467
<b>Hydraulic Exponents</b> by Ven Te Chow . . . . .	1489
<b>Modeling Circulation in Depth-Averaged Flow</b> by Victor M. Ponce and Steven B. Yabusaki . . . . .	1501
<b>Approximate Error Bounds for Simulated Hydrographs</b> by David C. Garen and Stephen J. Burges . . . . .	1519
<b>SWMM Model and Level of Discretization</b> by Nabil A. Zaghoul . . . . .	1535
<b>Efficient Cooling Ponds: Design</b> by Gerhard H. Jirka, Carl F. Cerco, and Donald R. F. Harleman . . . .	1547

---

## DISCUSSION

Proc. Paper 16615

---

<b>Aggradation in Streams Due to Overloading</b> , by Jagdish P. Soni, Ramachandra J. Gardo, and Kittur G. Ranga Raju (Jan., 1980. Prior Discussions: Nov., 1980). closure . . . . .	1567
<b>Finite Element Method for Direct Runoff Flow</b> , by Mutsuto Kawahara and Teruyuki Yokohama (Apr., 1980. Prior Discussion: Mar., 1981). closure . . . . .	1568
<b>Calibration of Bed-Load Samplers</b> , by Peter Engel and Y. Lam Lau (Oct., 1980, Prior Discussion: May, 1981). closure . . . . .	1569

<b>Adaptation of ILLUDAS for Continuous Simulation</b> , by Harry G. Wenzel, Jr., and Michael L. Voorhees (Nov., 1980).	
<i>errata</i> . . . . .	1570
<b>Erosion by Circular Wall Jets in Cross Flow</b> , by Nallamuthu Rajaratnam (Nov., 1980).	
<i>errata</i> . . . . .	1571
<b>Sand Bed Instability Due to Bed Load Motion</b> ,* by Hiroji Nakagawa and Tetsuro Tsujimoto (Dec., 1980).	
<i>by A. J. Sutherland, B.C. Phillips, and R. G. Bell</i> . . . . .	1571
<b>Re-Examination of Nikuradse Roughness Data</b> ,* by William R. Brownlie (Jan., 1981).	
<i>by R. Fuentes and S. Carrasquel</i> . . . . .	1573
<b>Modeling Transverse Mixing in Natural Systems</b> ,* by Y. Lam Lau and B. G. Krishnappan (Feb., 1981).	
<i>by Forrest M. Holly, Jr.</i> . . . . .	1575
<i>by Nobuhiro Yotsukura</i> . . . . .	1577
<b>Uncertainties Resulting from Changes in River Form</b> ,* by Durl E. Burkham (May, 1981).	
<i>by Victor M. Ponce</i> . . . . .	1579

## INFORMATION RETRIEVAL

The key words, abstract, and reference "cards" for each article in this Journal represent part of the ASCE participation in the EJC information retrieval plan. The retrieval data are placed herein so that each can be cut out, placed on a 3 × 5 card and given an accession number for the user's file. The accession number is then entered on key word cards so that the user can subsequently match key words to choose the articles he wishes. Details of this program were given in an August, 1962 article in CIVIL ENGINEERING, reprints of which are available on request to ASCE headquarters.

---

\*Discussion period closed for this paper. Any other discussion received during this discussion period will be published in subsequent Journals.

# STATEMENT OF OWNERSHIP

The *Journal of the Hydraulics Division* is edited and published by the American Society of Civil Engineers, with general business offices at 345 East 47th Street, New York, N.Y. 10017. The Manager of Technical and Professional Publications is Richard R. Torrens.

This Journal is owned wholly by the American Society of Civil Engineers, a nonprofit educational and professional organization with about 78,000 members. There are no individual owners or stockholders.

	Average No. Copies Each Issue During Preceding 12 Months	Single Issue Nearest To Filing Date
Total no. copies printed (net press run)	7,613	7,738
Paid mail circulation	5,558	5,870
Sales through dealers and counter sales	None	None
Free distribution	None	None
Total distribution	5,558	5,870
Left Over (extra for new orders, office use, etc.)	2,055	1,868
Total	7,613	7,738

I certify that the above statements made by me are correct and complete.—Richard R. Torrens, Manager of Technical and Professional Publications.

## 16678 DEVELOPMENT OF THE RIVER SEINE ESTUARY

**KEY WORDS:** Channel stabilization; Environmental engineering; Estuaries; Hydraulics; Laboratories; Models; Navigation; Ocean engineering; Tides; Water current; Waves

**ABSTRACT:** A movable bed scale model of the Seine estuary in France was originally developed more than 30 years ago to study the means of stabilizing the main shipping channel. This is a detailed account of how the model was designed, built, calibrated and operated, to provide valuable information for design of the channel training works completed in 1963. After this first success, a new version of the model was built in 1967, with certain detailed changes, and has continued serving for studies of development works in the estuary to the present day. Hydraulic and sedimentological characteristics of the estuary are described, as well as the model design criteria which led to the choice of scales and bed material. Other modelled features are waves, tides, and offshore current. The calibration tests included the successful reproduction of the natural evolution of the estuary observed over a period of almost 100 years. The conclusion shows how optimum efficiency can be achieved by using a mathematical model of estuary tides and currents in combination with a movable bed scale model.

**REFERENCE:** Parthiot, Francois (Engr., SOGREAH, Grenoble, France), "Development of the River Seine Estuary: Case Study," *Journal of the Hydraulics Division, ASCE*, Vol. 107, No. HY11, **Proc. Paper 16678**, November, 1981, pp. 1283-1301

## 16655 PREVENTION OF SHOALING AT PORT ORFORD, OREGON

**KEY WORDS:** Breakwaters; Harbors; Harbor structures; Hydraulic models; Shoaling; Simulation models; Testing; Wave height

**ABSTRACT:** A 1:100-scale undistorted hydraulic model of Port Orford, Oregon, and sufficient offshore area to permit generation of the required test waves were used to develop and test several plans of improvement proposed to eliminate harbor shoaling without adversely affecting wave heights at the existing pier. Improvement plans consisted of removal of portions of the existing breakwater, realignment or lengthening of the existing breakwater, and construction of new breakwater structures in the vicinity of Fort Point and Battle Rock. A 54-ft-long wave machine, electrical wave height measuring and recording apparatus, and coal and nylon tracer materials were used in the model. Tests were conducted with prebreakwater and existing breakwater conditions, and the results were compared to determine the causes and sources of harbor shoaling. Improvement plans were then tested and compared with existing prototype conditions. Of the plans tested, the optimum configuration appeared to be an 1100-ft-long angled breakwater extending from Fort Point.

**REFERENCE:** Chatham, C. E. (Hydr. Research Engr. and Chief, Wave Processes Branch, Wave Dynamics Div., Hydr. Lab., U.S. Army Engr. Waterways Experiment Station, P.O. Box 631, Vicksburg, Miss. 39180), "Prevention of Shoaling at Port Orford, Oregon," *Journal of the Hydraulics Division, ASCE*, Vol. 107, No. HY11, **Proc. Paper 16655**, November, 1981, pp. 1303-1316

## 16669 UMFOLOZI ROAD BRIDGE HYDRAULIC MODEL

**KEY WORDS:** Bridge location; Bridges (piers); Hydraulic models; Movable bed models; Rivers; Scour; Sediments

**ABSTRACT:** A movable-bed hydraulic model study was carried out of a new road bridge across the Umfolozi River in Zululand, Natal. The model was designed in accordance with the shear/settling velocity criterion,  $V_{*r} = W_r$ , and crushed anthracite was used as bed material (170 $\phi$ ). The horizontal and vertical scales were 1 in 250 and 1 in 100 respectively. The velocity scale was based on Froude's law and, with the large tractive force in this steep river, it was found necessary to deviate from the criterion  $Re_r = 1$ . Tests were run to determine the best river crossing, the required bridge length and the optimum orientation of the bridge piers, particularly with regard to minimum river bed scour. When a major flood occurred during the early stages of bridge construction, an opportunity arose to check on the predicted scour depths. Scour depths recorded in nature were reproduced to an accuracy of about 10 percent in the model and, because of the greater confidence which could be placed on the model results, considerable savings were effected in the bridge foundations.

**REFERENCE:** Zwamborn, J. A. (Sr. Research Officer, National Research Inst. for Oceanology, South African Council for Scientific and Industrial Research, South Africa), "Umfolozi Road Bridge Hydraulic Model Investigation," *Journal of the Hydraulics Division, ASCE*, Vol. 107, No. HY11, **Proc. Paper 16669**, November, 1981, pp. 1317-1333

## 16650 MODELING CAVITATION FOR CLOSED CONDUIT FLOW

**KEY WORDS:** Cavitation; Closed conduit flow; Hydraulics; Limits; Model studies; Pipe bends; Pipe flow; Scale effect

**ABSTRACT:** A portion of a model study is discussed which describes an experimental procedure for determining four cavitation limits and how to evaluate and adjust for scale effects. The item tested was a long radius elbow but the procedure applies to any pipe component or valve used in closed conduit flow. Cavitation limits evaluated are incipient, critical, incipient damage, and choking cavitation. Scale effects associated with change in size and velocity of pressure are evaluated and used to adjust the model data to the prototype conditions. No scale effects related to changes in velocity or pressure are found for any of the four cavitation limits. Incipient and critical cavitation are found to change significantly with size of elbow.

**REFERENCE:** Tullis, J. Paul (Prof. of Civ. Engrg., Utah Water Research Lab. Utah State Univ., Logan, Utah 84322), "Modeling Cavitation for Closed Conduit Flow," *Journal of the Hydraulics Division*, ASCE, Vol. 107, No. HY11, **Proc. Paper 16650**, November, 1981, pp. 1335-1349

## 16622 MODELLING THE ROTTERDAMSE WATERWEG ESTUARY

**KEY WORDS:** Density-flow; Dispersion; Estuaries; Hydraulics; Models; Navigation; Salinity; Sedimentation; Tides; Water quality

**ABSTRACT:** Hydraulic scale models are still the most powerful tools in studying estuarine problems (density flows and salinity intrusion). Weak points are, however, uncertainties in the scaling laws for vertical mixing of salt and momentum and in the boundary conditions. Experience with the Rotterdamse Waterweg model shows the importance of an automated model operation and control and the availability of adequate boundary conditions from nature. A very good reproduction of tidal propagation, flow field and density distribution was possible. The model has been useful in providing support for management decisions related to the development of the estuary.

**REFERENCE:** Breusers, Herman N. C. (Coordinator of Basic Research, Delft Hydraulics Lab., Delft, The Netherlands), and van Os, Ad G., "Physical Modelling of Rotterdamse Waterweg Estuary," *Journal of the Hydraulics Division*, ASCE, Vol. 107, No. HY11, **Proc. Paper 16622**, November, 1981, pp. 1351-1370

## 16654 HEATED DISCHARGE IN AN ESTUARY: CASE STUDY

**KEY WORDS:** Environmental engineering; Hydraulics; Hydrothermal alteration; Models; Nuclear electric power generation; Powerplants; Rivers; Thermal pollution; Water resources; Water temperature

**ABSTRACT:** Two physical model studies were conducted to evaluate the thermal patterns produced in the Hudson River by the condenser cooling water discharge from the Indian Point Nuclear Generating Station. Model similitude criteria are developed and applied to the Indian Point site to determine model scale ratios. Model construction, verification, and operation techniques are described. Typical results show surface temperature rise patterns near the plant discharge and within a 15 mile reach of the river. Sensitivity of thermal patterns to variations in freshwater runoff, plant load, and discharge structure geometry are illustrated. Model results are evaluated with respect to scale effects, and limitations due to inability to simulate certain phenomena occurring in the field. Model results are compared to an extensive field survey program and one-dimensional time averaged mathematical model.

**REFERENCE:** Nystrom, James B. (Lead Research Engr., Alden Research Lab., and Instr. Mech. Engrg., Worcester Polytechnic Inst., Holden, Mass.), Hecker, George E., and Moy, Han C., "Heated Discharge in an Estuary: Case Study," *Journal of the Hydraulics Division*, ASCE, Vol. 107, No. HY11, **Proc. Paper 16654**, November, 1981, pp. 1371-1406

## 16637 INSTRUMENTATION FOR AERATED FLOW ON SPILLWAYS

**KEY WORDS:** Aeration; Field tests; Hydraulics; Instrumentation; Laboratory tests; Open channels; Spillways; Velocity measurement

**ABSTRACT:** Instruments that have been used for measuring air concentration and velocities in self-aerated flow are examined. For air concentration measurements it is shown that the conductivity probe is satisfactory. For the velocity measurement the concentration measurements together with a pressure cell measuring the total head was attempted but the measurements were difficult to interpret. A correlation probe which detected the air water interface as it passed between two needles proved satisfactory for mean velocity measurements and the signal from a single resistance probe was used to estimate the bubble size. All of the probes were tested in the laboratory and on Aviemore spillway and based on this experience suggestions are made for future instruments.

**REFERENCE:** Cain, Paul (Engr., New Zealand Electricity Div., Ministry of Energy, Wellington, New Zealand), and Wood, Ian R., "Instrumentation for Aerated Flow on Spillways," *Journal of the Hydraulics Division*, ASCE, Vol. 107, No. HY11, **Proc. Paper 16637**, November, 1981, pp. 1407-1424

## 16638 SELF-AERATED FLOW ON A SPILLWAY

**KEY WORDS:** Aeration; Cavitation; Dams (concrete); Dams (gravity); Hydraulics; Open channels; Spillways; Velocity distribution

**ABSTRACT:** Measurements are made on the spillway on a 36-m high concrete gravity dam. The measurements include the point of inception, and the velocity distribution and air concentration distribution and bubble size in the developing region of the flow. The measurements show that there appears to be a universal velocity distribution which is independent of the mean air concentration for average air concentrations of between 0 and 0.5, and the air concentration becomes progressively more uniform with the distance downstream. However at 200 times the depth at the point on inception downstream of this point it is still growing. At 100 times the depth at the point of inception a significant air concentration has reached the spillway floor. A simplified formulae for computing the position and properties at the point of inception is also presented.

**REFERENCE:** Cain, Paul (Engr., Pearson Bridge Ltd., P.O. Box 137, St. Leonards, N.S.W. 2065, Australia), and Wood, Ian R., "Measurements of Self-Aerated Flow on a Spillway," *Journal of the Hydraulics Division*, ASCE, Vol. 107, No. HY11, **Proc. Paper 16638**, November, 1981, pp. 1425-1444

## 16657 BED LOAD DISCHARGE COEFFICIENT

**KEY WORDS:** Bed forms; Bed load; Dimensional analysis; Discharge coefficients; Dunes; Flow separation; Flow visualization; Grain size; Sand; Two dimensional flow

**ABSTRACT:** Using dimensional analysis, the bed-load discharge coefficient for the case of two-dimensional flow over dunes is expressed in terms of bed-form geometry and the sand size of the bed material. Experiments are conducted in a rectangular flume using artificial dunes and a flow visualization method to measure the flow separation length from which the bed-load coefficients were determined. The results show that the bed-load coefficient is affected significantly by sand-grain size only when the dunes are flat. When dunes are steep, the value of the bed-load coefficient is affected mainly by the dune steepness. Application of the bed-load coefficient results in some improvement of estimating bed load.

**REFERENCE:** Engel, Peter (Research Engr., Environmental Hydr. Sect., Hydr. Div., National Water Research Inst., Burlington, Ontario Canada), and Lau, Y. Lam, "Bed Load Discharge Coefficient," *Journal of the Hydraulics Division*, ASCE, Vol. 107, No. HY11, **Proc. Paper 16657**, November, 1981, pp. 1445-1454

## 16633 PARTICLE COUNTER FOR SEDIMENT TRANSPORT STUDIES

**KEY WORDS:** Acoustic detection; **Bedload movement;** **Electromechanical transducers;** Electronic monitoring systems; Field investigations; Laboratory water content determinati; **Particle distribution;** **Sediment transport**

**ABSTRACT:** An acoustic instrument for the measurement of the mass transport of sand-sized sediment particles in laboratory and natural transport systems has been developed. The instrument consists of an electromechanical transducer for the detection of sediment particles entrained in a moving fluid (air or water) and an electronic circuit which counts the transient signals produced when particles impact the transducer. By virtue of the principle of detection, instrument response to fine-grained sediment (silt and clay) and low-density material is negligible. Laboratory tests and field experiment conducted in a sand-bedded stream demonstrate that the instrument responds systematically to the mass flux of particles and therefore is potentially useful for investigations of bedload transport. The instrument is best suited for studies of transport systems characterized by high transport rates and flow velocities and having well-sorted bed material.

**REFERENCE:** Downing, John P., Jr. (Doctoral Candidate, Dept. of Oceanography, Univ. of Washington, Seattle, Wash. 98198), "Particle Counter for Sediment Transport Studies," *Journal of the Hydraulics Division, ASCE*, Vol. 107, No. HY11, **Proc. Paper 16633**, November, 1981, pp. 1455-1465

## 16660 BUOYANT SURFACE JETS

**KEY WORDS:** **Buoyancy;** **Coastal engineering;** **Dimensional analysis;** Discharge (water); **Jets;** **Mixing;** Models; Plumes; Thermal pollution; Water pollution

**ABSTRACT:** A combination of dimensional analysis, simple physical reasoning and data inspection is used to define distinct geometrical properties and mixing characteristics within the near field of buoyant surface jets. For deep stagnant receiving water, the jet has a transition length, a maximum penetration depth and a limited dilution capacity which is primarily met through bottom entrainment. These characteristics are found to scale with a densimetric Froude number based on kinematic momentum and buoyancy fluxes and a characteristic source length. A criterion for shallow water is developed based on observations of reduced entrainment; relationships for shallow water dilution and bottom attachment lengths are given. A criterion is presented to distinguish free and shoreline-attached jets in crossflowing receiving water, and a simple trajectory relationship appears to describe jet trajectories in crossflowing deep receiving water.

**REFERENCE:** Jirka, Gerhard H. (Asst. Prof., School of Civ. and Environmental Engrg., Cornell Univ., Ithaca, N.Y.), Adams, E. Eric, and Stolzenbach, Keith D., "Buoyant Surface Jets," *Journal of the Hydraulics Division, ASCE*, Vol. 107, No. HY11, **Proc. Paper 16660**, November, 1981, pp. 1467-1487

## 16639 HYDRAULIC EXPONENTS

**KEY WORDS:** Channel flow; Channels; Flow; **Flow profiles;** **Hydraulics;** **Mathematical representations;** **Open channel flow;** **Open channels;** Water flow

**ABSTRACT:** Hydraulic exponents are the parameters  $M$  and  $N$  in the mathematical relations for open-channel flows as expressed in  $Z^2 = Cy^M$  and  $K^2 = Cy^N$ , in which  $Z$  = the section factor for critical-flow computation;  $K$  = the conveyance of the channel flow cross section;  $y$  = the flow depth; and  $C$  = a coefficient. This paper clarifies the mathematical derivation of the hydraulic exponents and their implication in application to the computation of flow profiles of gradually varied flow in a prismatic channel. The relationships between these hydraulic exponents, which are assumed to depend only on the average flow depth, and those, which are assumed to vary with the flow depth of a given range, are also explained.

**REFERENCE:** Chow, Ven Te (Prof. of Civ. and Hydrosystems Engrg., Univ. of Illinois at Urbana-Champaign, Urbana, Ill. 61801), "Hydraulic Exponents," *Journal of the Hydraulics Division, ASCE*, Vol. 107, No. HY11, **Proc. Paper 16639**, November, 1981, pp. 1489-1499



## 16640 MODELING CIRCULATION IN DEPTH-AVERAGED FLOW

**KEY WORDS:** Channels; Hydrodynamics; Mathematical models; Open channel flow; Turbulence; Two dimensional flow; Water circulation; Water flow

**ABSTRACT:** The clarification of the physical mechanisms leading to the generation of circulation in free surface flow is sought by using a depth-averaged two-dimensional mathematical model. The depth-averaged two-dimensional governing equation set is used as a basis for the development of a finite difference model employing a multioperational procedure to advance the values of the dependent variables in time. Two geometric configurations are extensively tested regarding the mathematical model itself and the boundary conditions. It is found that proper modeling of the effective stresses is a necessary condition for the resolution of steady, closed-streamline circulation in depth-averaged mathematical models. In addition, a competition exists between convective inertia and bed resistance. Circulating flow is inhibited when bed resistance predominates. The type of boundary condition specification is found to have a significant effect in the resulting flow pattern.

**REFERENCE:** Ponce, Victor M. (Assoc. Prof. of Civ. Engrg., San Diego State Univ., San Diego, Calif. 92182), and Yabusaki, Steven B., "Modeling Circulation in Depth-Averaged Flow," *Journal of the Hydraulics Division*, ASCE, Vol. 107, No. HY11, **Proc. Paper 16640**, November, 1981, pp. 1501-1518

## 16662 ERROR BOUNDS FOR SIMULATED HYDROGRAPHS

**KEY WORDS:** Error analysis; Hydrographs; Hydrology; Models; Monte Carlo method; Parameters; Simulation models; Uncertainty principle; Watersheds

**ABSTRACT:** The problem of quantifying uncertainty in hydrologic model output is examined, and a review of previous work on the topic is given. The study focuses on the estimation of error bounds for simulated hydrographs, assuming the model to be perfect and accounting only for output uncertainty caused by uncertainty in parameter values. First-order uncertainty analysis is applied to the Stanford Watershed Model to calculate the effects of parameter uncertainty as it propagates through the model. The first-order approximations to the mean and standard deviation of model output are compared to estimates of the same quantities, using Monte Carlo analysis. This was done to identify the degree of parameter error for which the first-order approximations are valid. First-order analysis was found to give good approximations if the coefficients of variation (standard deviation/mean) on sensitive parameters were less than about 0.25. First-order analysis allows a large reduction in computation over Monte Carlo methods for estimating error bounds on simulated hydrographs.

**REFERENCE:** Garen, David C. (Former Research Asst., Dept. of Civ. Engrg., Univ. of Washington, Seattle, Wash.), and Burges, Stephen J., "Approximate Error Bounds for Simulated Hydrographs," *Journal of the Hydraulics Division*, ASCE, Vol. 107, No. HY11, **Proc. Paper 16662**, November, 1981, pp. 1519-1534

## 16641 SWMM MODEL AND LEVEL OF DISCRETIZATION

**KEY WORDS:** Catchments; Computer models; Flow distribution; Hydrographs; Models; Overland flow; Rainfall; Runoff; Sewers; Storm water; Urban areas

**ABSTRACT:** The costs of setting up and running a storm water management model are largely determined by the level of discretization used for a particular catchment. This study investigates the level of discretization needed to adequately represent an urban watershed and to illustrate the effects of reducing the number of subcatchments on the accuracy of runoff simulation. A methodology is defined to achieve a representative equivalent catchment from theoretical considerations. Verification of the procedures involved a series of applications on both hypothetical and real areas. The simulation results of the simplified (coarse) discretization are compared with those of the detailed (fine) discretization of the same rainfall storms. The accuracy of the simulation is maintained by careful aggregation of the subcatchment parameters and the proper selection of the aggregated hydraulic width.

**REFERENCE:** Zaghoul, Nabil A. (Asst. Prof., Civ. Engrg. Dept., Univ. of Petroleum and Minerals, Box 396, Dhahran, Saudi Arabia.), "SWMM Model and Level of Discretization," *Journal of the Hydraulics Division*, ASCE, Vol. 107, No. HY11, **Proc. Paper 16641**, November, 1981, pp. 1535-1545

## 16671 EFFICIENT COOLING PONDS: DESIGN

**KEY WORDS:** Circulation; **Cooling;** Density currents; Dispersion; Hydrodynamics; **Ponds;** Powerplants; **Steam electric power generation;** **Thermal pollution;** Waste heat

**ABSTRACT:** The design of cooling ponds for the dissipation of waste heat from steam-electric power plants is considered from the point of view of steady-state performance, and of transient performance. Particular emphasis is put on the design of shallow ponds, as defined by classification criteria proposed earlier, which lack a predominant vertical stratification and are dominated by the throughflow hydrodynamics. Such pond types are frequently constructed by diking or excavating an offstream land area. A schematic laboratory study was performed to test the effect on pond performance of various design measures, notably internal baffle arrangements, discharge structures and a deep intake reservoir. An optimal pond design is suggested with moderate beffling (length/width ratio of 5 to 10) to prevent recirculation zones, a radial discharge structure to minimize entrance mixing and deep intake reservoir with a residence time of at least one half day to insure damping of diurnal intake temperature fluctuations.

**REFERENCE:** Jirka, Gerhard H. (Assoc. Prof., School of Civ. and Environmental Engrg., Cornell Univ., Ithaca, N.Y. 14853), Cerco, Carl F., and Harleman, Donald R. F., "Efficient Cooling Ponds: Design," *Journal of the Hydraulics Division, ASCE*, Vol. 107, No. HY11, **Proc. Paper 16671**, November, 1981, pp. 1547-1563

## **INTRODUCTION TO SIX PAPERS ON HYDRAULIC MODELS**

The first six papers in this issue were originally submitted to the Task Committee for Revision of Manual 25 on Hydraulic Models, a publication that will not be produced, and were selected by that committee and by the Committee on Research of the Hydraulics Division.

The hydraulic model case studies described in the papers provide a basic discussion and examples of physical hydraulic modeling techniques. It is hoped that these papers will stimulate further case study publications which, with these, can form the basis of a later overview of modeling techniques as a whole.

100

101

102

103

104

105

106

107

108

109

110

111

112

113

114

115

116

117

118

119

120

121

122

123

124

125

126

127

128

129

130

131

132

133

134

135

136

137

138

139

140

141

142

143

144

145

146

147

148

149

150

151

152

153

154

155

156

157

158

159

160

161

162

163

164

165

166

167

168

169

170

171

172

173

174

175

176

177

178

179

180

181

182

183

184

185

186

187

188

189

190

191

192

193

194

195

196

197

198

199

200

## DEVELOPMENT OF THE RIVER SEINE ESTUARY: CASE STUDY

By François Parthiot<sup>1</sup>

### INTRODUCTION

This article describes the study of an estuary on a movable bed scale model, a study which began as long ago as 1950, and which continues today with essentially the same model.

The preliminary tests and calibration tests were numerous and complex, and were complemented by a long historical test. The reliability of the model has been confirmed by this test, and by the successful performance of the structures built 20 yr ago following the first studies on the model.

The fact that the model was built so long ago means that many of its mechanical features and control systems are somewhat out of date, even on the new version built in 1967. Nevertheless, the basic design of the model, in other words the choice of scale and of bed material, the schematic representation of the phenomena, and the adjustment methods are still of considerable interest and are the main subject of this article.

Their value is confirmed by the fact that the development works undertaken in 1956 and in 1970, on the basis of the indications given by the model, have had the desired effect. The model is still in use, in conjunction with a mathematical model, for the study of solutions to new problems that are in some cases very different from those for which the model was originally built.

### PROBLEM OF NAVIGATION IN THE SEINE ESTUARY

The Seine estuary (Fig. 1), which is used by ships bound for the port of Rouen, 120 km upstream, is subject to intensive siltation, which constitutes a serious obstacle to navigation and seriously limits ship draft.

The deposits of sand and alluvium build up year by year, forming large and constantly shifting banks that are exposed at low tide (Fig. 2). Accordingly, the channels too used to be totally unstable. They were constantly shifting,

<sup>1</sup>Engr., SOGREAH, Grenoble, France.

Note.—Discussion open until April 1, 1982. Separate discussions should be submitted for the individual papers in this symposium. To extend the closing date one month, a written request must be filed with the Manager of Technical and Professional Publications, ASCE. Manuscript was submitted for review for possible publication on March 9, 1981. This paper is part of the Journal of the Hydraulics Division, Proceedings of the American Society of Civil Engineers, ©ASCE, Vol. 107, No. HY11, November, 1981. ISSN 0044-796X/81/0011-1283/\$01.00.



FIG. 1.—Map of the Tidal Seine

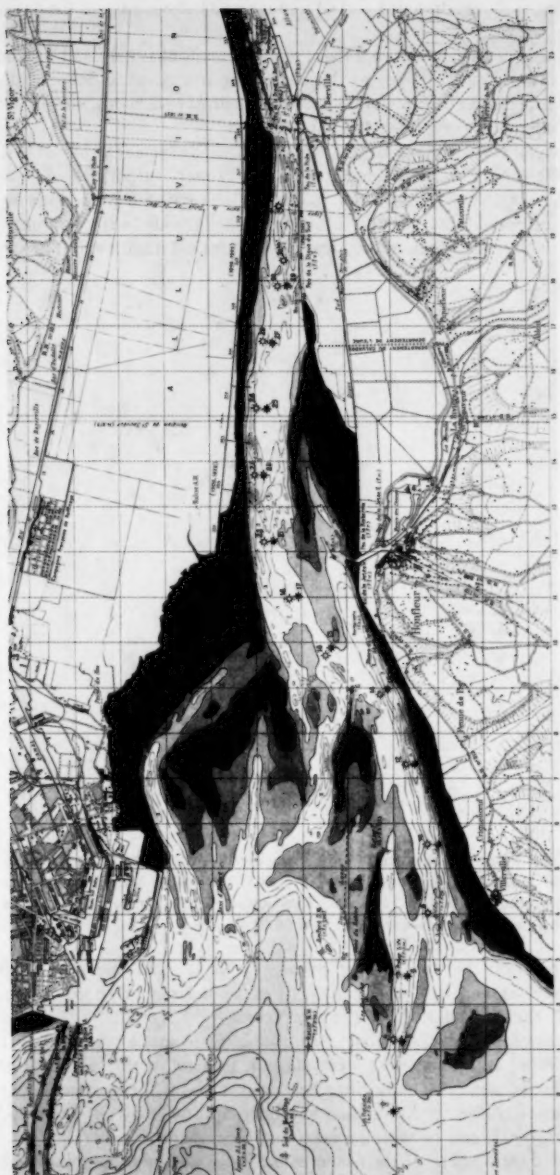


FIG. 2.—1947 Hydrographic Survey

thus, requiring frequent dredging and adjustments to the buoyage of the navigation channel.

Since the works carried out in 1956–1963, the main channel used by shipping has been made perfectly stable. At the same time it was made deeper, allowing a significant increase in the maximum permissible draft (+2.50 m), and an increase in traffic of about 50% between 1962 and 1964.

These results were obtained following studies undertaken by SOGREAH between 1950 and 1956, at the request of the French authorities. The aim of these studies was to determine the works to be carried out to open up and maintain as effectively as possible a channel 300 m wide, with a depth corresponding to  $-2$  or  $-3$  m below the local marine chart datum level. These works

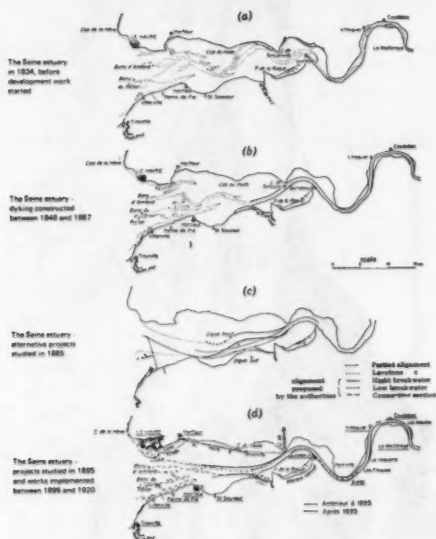


FIG. 3.—(a) The Seine Estuary in 1834, before Development Work Started; (b) The Seine Estuary-Dyking Constructed between 1848 and 1867; (c) The Seine Estuary Alternative Projects Studied in 1885; (d) The Seine Estuary Project Studied in 1885 and Works Implemented between 1895 and 1920

were to be performed in an area of extremely loose sand and mud, exposed to westerly storms and to a continual drift of sand from offshore, amounting to between 2,000,000 and 3,000,000  $m^3$  per year.

The authorities had decided that a thorough scale model study was to be carried out before any new works were started. In view of the failure of earlier projects in the estuary, the authorities had doubts about the consequences and the effectiveness of the scheme which had been approved by act of Parliament on January 11, 1932, and on which a start had been made.

Indeed, the development of the Seine estuary is a vast and complex problem,



the national importance of which had already been understood in the first half of the nineteenth century. The first complete hydrographic survey was carried out in 1834 by Beautemps-Beaupré (Fig. 3a), and at that time the river had the characteristics of an estuary over a distance of 60 km. Between 1848 and 1867, numerous longitudinal dykes were built in the upstream part of this estuary, alongside the low water bed as it was then (Fig. 3b). Following the elimination of certain sills, it was then possible for ships with a draft of 4.50 m to reach the port of Rouen in 12 hr instead of the 4-5 days which were previously necessary.

Since these works did nothing to solve the problem of sills in the navigation channel and shifting channels around the bar of the estuary, further projects were drawn up and debated at length between 1885 and 1895.

To assess their merits, it was even decided to build a scale model in Rouen between 1891 and 1894 (3). Its characteristics were as follows: horizontal scale, 1:50,000; vertical scale, 1:50; constant tides with a range of 8 m reproduced by the oscillating motion of a rectangular plunger, inclined so as to simulate effectively the north-westerly flood flow. The material used was initially natural sand from the actual estuary, later replaced by beach sand. Three series of tests corresponding to three different designs resulted in the selection of the design proposed by the authorities (Fig. 3c). This design was immediately implemented in 1895, involving the construction of an extension to the insubmersible northern breakwater and of a new southern breakwater between the Risle River and the town of Honfleur. These works gave poor results, the channel continuing to shift in the estuary, with depths as restricted as ever. This early example of the use of a movable bed scale model to study a problem of seabed evolution was, thus, a failure. Although the procedure adopted by the engineers at that time was correct (only a scale model could provide them with real assistance in defining and comparing different designs), they had inadequate knowledge of the laws of sediment transport and of model similitude.

The bed material used and the scales adopted were not suitable, and the indications given by the model were, thus, erroneous. As a result, the works carried out between 1895 and 1920 were largely ineffective (Fig. 3d). This clearly shows the requirement for a reliable sedimentological model, in other words a model that is accurate and sensitive, and faithfully reproduces natural phenomena.

The construction of such a model involves a considerable amount of research. It took more than a year to build the Seine estuary model and perform the preliminary tests. Then there were 10 months of calibration tests, followed by four months of historical tests. This duration of tests is a measure of the size and complexity of the problem. A wealth of fundamental practical data has been accumulated in the course of this study, and is used extensively today in all kinds of movable bed scale model studies.

#### HYDRAULIC AND SEDIMENTOLOGICAL PHENOMENA IN THE SEINE ESTUARY

**Origin of Alluvium.**—The materials transported downstream by the Seine are negligible; it has been shown that the deposits in the estuary itself originate mainly from the stock of fine sand in the Seine Bay.

This material drifts inshore on the flood tide, a phenomenon which is reinforced

by northwesterly storms, which help to lift the sand into suspension. A proportion of this material is transported offshore again on the ebb tide, but the difference nevertheless results in considerable deposition in the estuary, which at present amounts to about 2,000,000–3,000,000 m<sup>3</sup> per yr.

**Role of the Flood and Ebb Tides.**—The height of the high tide at Le Havre exceeds 6.2 m for 95% of the total number of tides occurring a year. At the entrance to the estuary, spring tides are such that the flood lasts only 3 hr, with the high water slack also lasting 3 hr and the ebb 6 hr.

Consequently, the flood tide runs particularly fast and lifts into suspension the bed material in the Seine estuary, which is then deposited further upstream in the estuary. The opposite effect of the ebb tide is less strong, except in the main channel, where it extends over a great distance. In the downstream part of the estuary, the ebb flow is dispersed, its speed reduced, and the material lifted upstream is deposited, to form a bar at the mouth of the estuary.

**Role of Waves.**—The northwesterly storm waves can have a marked effect on the bed of the Seine Bay out to depths of –5 to –10 m below the datum of the marine charts of Le Havre (lowest low water).

**Seine Discharge.**—The discharge of the Seine itself is low compared to the recorded discharges on the flood or the ebb tides.

#### **MODEL DESIGN—THEORETICAL AND PRACTICAL REASONS FOR CHOICE OF MODEL SCALE AND BED MATERIAL**

A large number of phenomena occur in an estuary. Some are less important than others in terms of their effects on the model of the seabed. In the first place, then, it is necessary to separate the phenomena to be represented from those to be ignored, the aim being to obtain the correct reproduction of the configuration of the bed, and an evolution of the banks and channels that corresponds to the natural evolution. This makes it essential to distinguish between the following:

1. The criteria on which it is judged whether similitude is respected, which depend on the requirements of the researcher with regard to his model and which must provide him with a rapid and sure means of comparison between the model and reality.
2. The conditions or relationships of similitude, which are not chosen but are imposed on the researcher whenever he needs to reproduce a variety of natural phenomena while retaining the relative importance of each. (The relationship of similitude have an absolute character insofar as one accepts the coherence of the physical laws used to establish them.)

As the knowledge of natural phenomena improves, the laws used to interpret them become more complete, but they involve mathematical equations, which contain an ever-increasing number of parameters (in this case turbulence, boundary layer, fluid mixture, transport by saltation, suspension, etc.). The conditions of similitude deduced from these equations become increasingly complex and difficult to reconcile with each other.

**Conditions of Similitude Applicable to the Seine Estuary Models.**—Two variable domains can be distinguished in the Seine estuary, a variable domain distinctly

fluvial in character, extending to downstream of Honfleur River at the low water slack, and a variable domain which is maritime in character, covering the entire estuary proper as soon as half tide is reached. It is, thus, necessary to study simultaneously: (1) Local similitude conditions for the river flow; (2) local similitude conditions for the maritime phenomena (waves, tidal currents, and zone of breaking waves); and (3) general similitude conditions for the phenomena of erosion and deposition in the general fluvio-marine area and the phenomena of alternative solid transport on the flood and ebb tides.

To satisfy these various requirements, a wide variety of relationships or conditions have to be taken into account, as follows: (1) Froude similitude; (2) a condition of the Chézy type; (3) the similitude of action on the bed material; (4) the Shields similitude; (5) the condition of similitude of the wave patterns; (6) Lacey's equation; and (7) the condition whereby the transport curves of the real and modelled bed materials are in vertical similarity.

This last condition is of fundamental importance. If  $q$  is the solid transport per unit width in a section of depth,  $h$ , and width,  $b$ , the equation of continuity for the material is

$$h \frac{\partial b}{\partial t} + b \frac{\partial h}{\partial t} + q \frac{\partial b}{\partial x} + b \frac{\partial q}{\partial x} = 0 \quad (1)$$

The similitude between bed deformation on the model and in the real situation requires that, on the basis of the above equation, the following relationship be taken into account, expressing the time scale,  $t$ , of bed evolution (different from the hydraulic time scale)

$$q = \frac{xy}{t} \quad (2)$$

The best similitude of bed evolution will, thus, be obtained if the solid transport in all the sections of the estuary varies in proportion to its variations in reality, and for an adequate range of velocities and depths. The curve of sediment transport in the field is drawn in terms of  $q$  and  $U$ , taking the appropriate scale factors into account and giving the approximate scale,  $t$ , of bed evolution by comparison with the transport curve of the material on the model. In fact, where estuary or tidal problems are concerned, this is not a good way of determining the time scale for bed evolution: first, because tide flows are alternate and are, therefore, almost nil at certain times; and, second, because tides are represented by only one tide of fixed coefficient. A more complex calculation was made using the Einstein bed load concept and has given very good results. To make this comparison of transport curves, the natural transport curve must of course be known. Since the volume of solid transport per unit width,  $p$ , close to the bed is practically impossible to measure, it was determined in the laboratory for a steady uniform sediment load. It is expressed as a function of the bed shear stress  $\tau$  on the bed:

$$p = f\tau \quad (3)$$

Once this transport had been determined, it was possible to calculate the concentration close to the bed and then, following the Schmidt and Rouse theory, the concentration,  $C(h)$  over the entire depth of water. The integration of local

transport,  $U(h) \cdot C(h)$ , at level  $h$  gives the required total transport  $q$ :

$$q = p \tau + \int_a^h UC \, dh \dots \dots \dots (4)$$

in which  $U(h)$  = fluid velocity at level  $h$ ; and  $C(h)$  = concentration of material in suspension at level  $h$ . This method is certainly open to criticism, but it was considered to be only means of establishing the transport curve.

**Adopted Similitude Criteria.**—For each of the natural factors represented on the model, a similitude criteria has to be adopted. These criteria are a function of the stated purpose of the model and of the degree of knowledge of each natural phenomenon.

**Tide.**—The model reproduces the tide law at the downstream limit. The criterion thus chosen was the correct reproduction of the tide curve at the port of Le Havre. The curves are adjusted to about  $\pm 30$  cm, which is also the tide level recording error at Le Havre.

At the same time, the model must correctly reproduce the tidal currents throughout the estuary. By chronophotography, the model's current field can be analysed and compared to that observed in the field, with a similar configuration of bed and development works.

**Bed Configuration.**—This is checked both in terms of the invariants, e.g., the hollows or sandbanks which are almost fixed in position and extent, and in terms of the characteristic shapes, such as the shape and position in plan of the channel meanders, the shape of the channel cross sections, and the position and elevation of the sills or changes of curvature. By comparing these invariants and characteristic shapes, it is possible to judge in an initial stage whether the overall modelling is correct. Subsequently, ultrasonic soundings are carried out to obtain quantitative data, such as the depths of the channels and natural hollows.

**Bed Transport.**—The areas of deposition and accumulation are identified by checking, over several successive tides, the movement of grains of red polystyrene of similar density and particle size characteristics.

**Wave Effects.**—The waves must play on the model the role which they effectively play in reality. By their action on the bed, they facilitate the lifting into suspension of the loose bed material by the currents. Correct reproduction of this action is vital if the tidal currents are to transport bed material over the entire extent of the estuary. It should be noted that the lightness of the material makes this wave adjustment a particularly delicate operation.

**Choice of Scales and Bed Material.**—It is important to bear in mind, in considering the choice of scales and bed material, that one of the main objectives of the model was to represent the transient conditions resulting from development works in the estuary, as well as the long-term evolution which determines the value of a given design. Indeed, with a view to obtaining better definition of the evolution scale, the original model test program provided for a test simulation of the evolution over the previous 60 yr.

These requirements, coupled with financial considerations, placed extra restrictions on the model builders in addition to those listed in the previous paragraphs.

The procedure adopted in making the fundamental choices concerning the scales and bed material was as follows:

1. Provisional application of a relationship between the vertical and horizontal scales and determination of a critical Reynolds number corresponding to the minimum value for the channels studied under maximum ebb flow conditions. From this can be deduced the minimum horizontal scale,  $x$ , of the model.

2. Choice of bed material according to the three criteria: roughness similitude, transport similitude, and the probable time scale for evolution.

3. Final determination of the vertical scale by means of tests on the overall model, involving the testing of several successive distortions.

The order of these operations is of vital importance for two reasons. First, it is impossible to make the characteristics of the material, particularly its density, vary continuously. Second, for a given distortion, there must be an optimum material, but there is no means of confirming that this distortion, fixed a priori, is precisely the optimum distortion for this material.

**Preliminary and Calibration Tests.**—Preliminary and calibration tests were undertaken to determine the scales and bed material to be adopted. Among the phenomena to be represented, the offshore currents in the downstream part of the estuary are also complex. The shape of the current spectra in this 20-km wide area requires division of the tide generator into a large number of independent cells (17 on the 1950 model and 20 on the 1967 model). It was, thus, necessary to build a prototype cell in order to check its operation. In a second stage, this cell was complemented by a rectangular flume, so that the first two series of tests necessary to determine the scales and bed material could be carried out: (1) Tests with steady flow to measure surface gradients and sediment loads; and (2) tests with reproduction of the upstream part of the estuary at the same horizontal scale as that of the overall model. The materials were tested in the same conditions as on the overall model, and could easily be changed for comparative tests. Discharges and levels could also be easily adjusted by modification of the boundary conditions, allowing different distortions of the tidal flows, in view of the fact that these flows depend on the vertical scale.

**Choice of Horizontal Scale.**—Earlier experiments at SOGREAH had shown that the proper scouring of the main and secondary channels could be reproduced if the local maximum Reynolds number (corresponding to the maximum ebb flow) were more than about 3,000. Therefore, if 20–30 m-wide channels are to be reproduced, a horizontal scale of the order of 1:1,000 seems appropriate in view of the maximum ebb flow speed of approx 1 m/s and assuming a distortion factor of the order of 10 (according to Lacey's law, for  $x = 1:100$ , which gives  $x/y = 10$ ).

**Testing and Selection of Loose Material.**—After a large number of materials of diverse origin had been envisaged (anthracite, permalin sawdust, pozzolan, plastic materials, ground perspex, etc.) two materials were selected because they could be obtained in large quantities and because considerable experience had already been obtained with them on earlier models: ground pumice stone and lime-treated sawdust.

Many experiments were conducted with both materials, covering sediment transport rates, Manning's coefficient, lifting into suspension, and wave effects. In conclusion, sawdust was found to be the most suitable material, for several reasons:

1. The intensity of transport is 25 times greater than with pumice stone for the same distortion, so that the duration of the tests is reduced, and there is a considerable saving in the overall study time.

2. It is lifted into suspension much more easily, which is important for the similitude of transport induced by the flood tide flow as a function of depth.

3. It is not nearly as rough as the pumice stone, a characteristic which is in accordance with the distortion imposed by the model's general similitude conditions, but which keeps the distortion of the surface gradients within acceptable limits.

**Tests to Determine Optimum Distortion Factor.**—These tests, as already explained, were first of all carried out on a partial model of the estuary at the horizontal scale of 1:800. This represented an 8.5 km section of the estuary where the north and south bank dyking considerably reduces its width, and where, consequently, there is relatively little potential for the main channel to shift. Tests on this partial model led to the conclusion that a distortion factor of approx 8–10 was adequate. Then, once the overall model had been built and adjusted for the hydraulic conditions corresponding to the tide coefficient of 100 (or 115) and to the chosen distortion factor (8, 10, or 12), the following points were examined:

1. Where and when the bed material was displaced (in what areas and at what times of the tide).

2. By what means of transport (bed load, saltation or suspension).

3. The evolution of a given profile on the occasion of shifting of banks, the filling in of a channel of the scouring of the bed close to the dykes.

In the final analysis, the distortion factor 8 appeared to be the most satisfactory. It was not considered worthwhile to undertake tests with a smaller distortion factor (6 or 7) since the distortion factor 8 already led to small values of flow speed and transport in suspension.

**Hydraulic Adjustments.**—The parameters subject to hydraulic adjustments are essentially: (1) The tide curves; (2) the high tide, HT, and low tide, LT, limit curves; and (3) the current spectra or fields. At the stage of the first calibration tests on the overall model, the main aim was to achieve better definition of the action of tide and waves on solid transport and on the bed topography.

**Changes Made on Reconstruction of Model in 1967.**—The new sedimentological model built in 1967 used in part the main structures of the model made for the earlier studies. Nevertheless, the limits and dimensions of the model and the measurement and data processing techniques were completely revised. In particular, it is worth noting that:

1. The downstream limits of the model were extended from 6–10 km further offshore to take account of the possible extension of the dyking to the level of the cape of La Hève and to avoid setting up an interaction between the new development works and the current regime at the downstream limit of the model.

2. The offshore boundary conditions were calculated by means of a mathematical model. The increased length at the limit of the model required the splitting

up of the tide generator into 20 independent cells. The cams corresponding to the generation of the 20 discharges were directly defined by calculation and required little subsequent adjustment.

3. The tide generator was equipped with 20 siphons in order to isolate the model from the cells in case of breakdown and, thus, to protect the model from the risk of gulleying, which would be caused if the water were drained off entirely.

4. The wave generator consists of swivelling units, so that three wave directions can be reproduced in a 20° wide sector ranging from 270–290° N. This was to take account of the direction of wave attack and its influence on the ends of the banks furthest downstream on either side of the shipping channel.

5. The horizontal scale was reduced to 1:1,000 in order to allow the extension of the model offshore.

6. The distortion factor was increased from 8–10 and the tide coefficient reduced from 100–95.

7. The mean diameter of the sawdust used was reduced from 600–400  $\mu$  in order to facilitate solid transport in the offshore part of the model, and the wave characteristics were adjusted in consequence.

8. Ultrasonic soundings were carried out systematically on the model at intervals corresponding to two years, whereas on the earlier model soundings were only effected at critical dates, complemented simply by photographs taken at low water.

#### HOW SCALE MODEL REPRODUCED PAST BED EVOLUTIONS

The aims of the historical tests were twofold: (1) To ascertain that the model was properly adjusted and could not only reproduce the estuary in a given condition but could also reproduce a succession of past evolutions over an extended period; and (2) to determine precisely the time scale applicable to all movements of the bed.

The historical tests conducted with the first model were divided into two main phases: evolution of sand banks and channels in the open estuary (1869–1898) and evolution taking account of artificial structures (1898–1953).

**Overall and Localized Evolution.**—A remarkable feature of the historical tests is that they reproduced not only the evolution at the ebb tide channel (a continuous north-south channel with transition states near the center) but also what are termed micro-evolutions (certain banks cut through, progressive variations of blocked channels, deepening of various depressions in the bed, and evolution of the characteristic shapes of certain banks). These micro-evolutions were often not noticed during the actual tests and were only discovered afterwards when comparing photographs of the model with the corresponding surveys of the estuary.

The most remarkable demonstration of the accurate performance of the model was the correct reproduction of the transient state of 1939. Until 1939, the main ebb tide channel ran along the south side of the estuary, but, in this year, the channel changed its course to run across the middle of the estuary (Fig. 4). Remarkably, this change was reproduced by the model at precisely the moment forecast on the basis of actual observations.

**Results Obtained from Historical Tests.**—Clearly, the historical tests are of



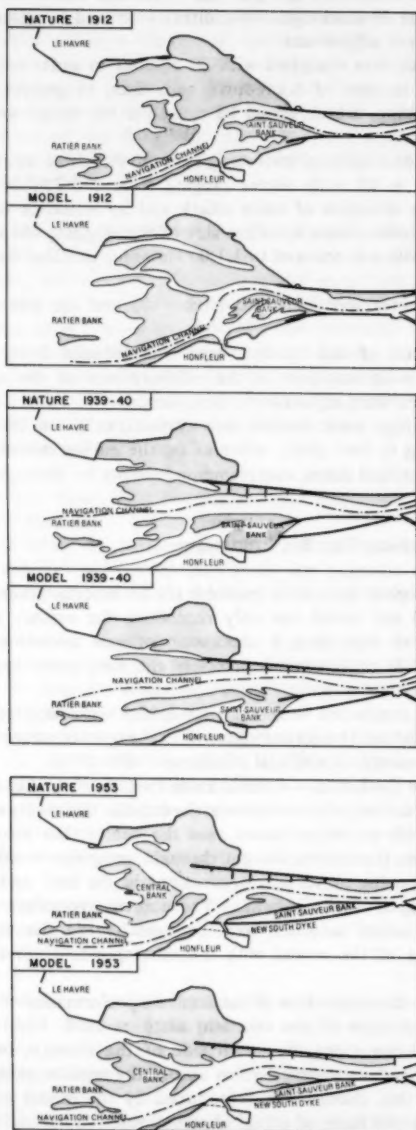


FIG. 4.—Historical Tests Compared with Nature



great value (4). The frequent occasions upon which agreement was observed between the state of the model and the natural state of the estuary made it possible, in the end, to adopt a scale of 9 model hr to 1 natural yr. The constancy of this time scale, which is about 1:1,000, was proved to be accurate to within 1%.

A precise time scale is an important factor in determining both the period during which a solution is stable and the duration of transition periods. Certain schemes, which were tested before the time scale had been determined, were considered to be satisfactory because they appeared to stabilize the channel for a "long" period. But these schemes were subsequently found to be unsatisfactory since stable conditions were not obtained until 5, 7, or 10 yr after the structures were built. Navigation would likely be disturbed during the transition period. In this way the determination of a time scale altered the validity of certain schemes. In other tests, the knowledge of this scale made it possible to reproduce the transition phases during the building of new structures. It also made possible the reproduction of annual or tri-monthly maintenance dredging operations.

**Remarks Concerning Evolution of Estuary.**—The fluctuation movements of bed material in the Seine estuary can be divided into two categories:

1. The specific evolution of the estuary itself, as if it were subjected to the permanent effects of tides of constant coefficient, river discharges following a constant cycle, and regular waves during a constant period of the tide cycle. Although subjected to constant effects, the channels and banks in the estuary are subject to changes; first, because the meanders evolve much as they do in a river, with the additional effect of the tides and particularly the flood tide flow, and, second, because the channel mouths silt up, resulting in the cutting through of banks to form new channels. If there are no changes in these external effects, it should, therefore, be possible to define the specific periods of evolution of the estuary on condition that the permanent phenomena reproduced correspond to the effective mean action of nature over a long period (20–30 yr).

2. The evolutions produced by periodic or random modifications to the natural phenomena. The phenomena acting on the estuary change according to laws which may or may not be periodic. Thus, the tide coefficients vary with return periods ranging from 15 days–18 yr. River discharges, and, thus, floods, can be observed at irregular intervals, as can storm wave conditions. The evolution of an estuary can be roughly assimilated to the movements of a system whose specific period is subjected to disturbing forces which combine with an almost constant mean action. At one stage, there were fears that the elimination of these disturbing effects (the model was to be operated with constant discharge and tide coefficient) would prevent certain evolutions from being simulated.

However, the operation of the model and, particularly, the historical test have shown that the essential evolutions are effectively reproduced since they are independent of the disturbing effects. One reason is that the chance disturbing factors are of relatively short duration and do not give rise to irreversible changes in the bed topography. This conclusion would not be valid if the regime of

the estuary were thrown completely out of balance, and for a long period, by occasional and unforeseeable phenomena.

#### PERFORMANCE OF TESTS

The tests were carried out day and night, except on weekends, to keep their duration within reasonable limits (one year in nature corresponding to about 9 hr of model operating time) and to avoid the rotting of the sawdust which would eventually occur, in spite of the chemical treatment, if the tests were extended over a long period.

**Reproduction of Fixed Initial Situation.**—This reproduction is essential in that it allows different tests, and, thus, different development schemes, to be compared with each other.

Thus, before each test there was a "bed preparation" phase. In spite of all precautions, it was impossible to avoid the unequal settling of the bed after a few tides, so some remodelling was necessary.

This phenomenon, already mentioned, produced a succession of rapid and confused changes. It is in agreement with the fact that the artificial levelling undertaken to reproduce the initial situation is of minimum stability, as suggested by P. A. Mantz (9). Accordingly the first hours of operation were characterized by the accumulation of washed material at the level of the bar.

However, once the model was well adjusted, it was found to be capable, on its own, of reproducing a given initial situation in the presence of the corresponding structures, at a speed which depended on the extent of the difference between the bed topography as initially modelled and the target situation.

With the bed topography being formed by the model itself, the phenomena of parasite settling or disorderly evolution at the beginning of the tests were actually eliminated. This is the method adopted successfully during the final tests of schemes in 1955 and 1956.

**Input of Loose Bed Material into the Model.**—A bed material supply facility located at the downstream limit of the model had been envisaged, in accordance with the fact that the fine sand originates from the Seine Bay. This position was found to be unsuitable, because the flow speeds offshore were low and a proportion of the sawdust settled to form a bank which is not present in nature, this is explained by the inadequate dispersion of the added sawdust.

The supply facility was then located upstream at the narrowing of the estuary and in the channel, where flow speeds were sufficiently high for the material to be carried downstream in a few tides. This solution works, provided that the dykes near the bar do not alter the distribution between the north and south banks.

This was the arrangement adopted for all the final tests carried out in 1955–1956. However, with the increase in distortion factor on the second model, from 8–10, and the use of a finer bed material (sawdust particle diameter 400  $\mu$  instead of 600  $\mu$ ), it was possible to locate the supply facility downstream, after the complementary adjustment of the waves and the identification of the appropriate area for this operation.

In any case, the quantity of sawdust introduced each time is small and the location of the supply point is of little importance as long as it is chosen in

such a way that the material does not settle on the spot, but is effectively carried over the whole model.

**Reproduction of Tide Cycles.**—It was initially planned to reproduce a cycle of tides ranging from spring to neap tides. Indeed, for a number of tests, the model functioned satisfactorily under these conditions.

However, experience gained in the operation of the model showed that there was no gain in terms of the precision of the topography, while the duration of the tests was about five times greater.

The choice of tide coefficient is not arbitrary, however. The transport of sawdust having been proved during preliminary studies to be approximately proportional to the fourth power of the tide coefficient, the tide coefficient chosen during the calibration of the model is close to the effective mean tide coefficient. For all the final tests, as well as for the historical tests, a constant tide coefficient of 100 was reproduced.

**Reference Test.**—Since the construction of the second model, all studies have begun with a reference test to determine the evolution that would occur if none of the works studied were implemented. This allows a full appraisal to be made of the advantages or disadvantages of any scheme tested subsequently.

**Test Duration.**—The overall duration of any long-term test had to be limited to 40 yr, because of the considerable deviations which could occur over longer periods. The continual input of material tends to reduce the overall volume of the flood and ebb, this effect becoming particularly marked after 40 yr. Moreover, it would be necessary to take into account the resulting reduction, in the long term, of the material input.

## MAIN RESULTS

**Period from 1950 to 1956.**—As soon as the model appeared capable of satisfactorily reproducing the present situation (in practice the situation of 1947), the actual tests began.

The series of tests preceding the historical tests showed that the structures to the north provided for in the 1932 project were totally ineffective. After the final adjustment and the historical tests, further runs of tests with various alternative designs for the northern dyking made it possible to determine the distance that should separate this dyking from the existing south bank dyking and its extension in the form of the Ratier bank dyke (under construction). The efficiency of the various schemes tested on the model was compared on the basis of the following criteria:

1. Stability and regularity of the navigation channel.
2. Duration of the transitory stage of stabilization and deepening of the channel.
3. Volume to be dredged annually to maintain the channel, as a function of the crest level and length of the submerged dykes.

It was on this last point that depended the economic comparison of the schemes, taking account of the relative costs of building more or less extensive dykes and the relative quantities of material to be dredged to complement the flushing effect of the ebb tide. Indeed, it was, to a certain extent, possible with the model to determine the volume to be dredged annually to maintain the depth

of the channel at a given level. The experience acquired in 20 yrs of operation of the model has in fact resulted in determination of the multiplying coefficient to be adopted to transpose the volumes on the model into absolute values, allowing more than just a comparison of the schemes with each other.

**Period From 1966 to 1970.**—The new model built in 1967 is used in conjunction with the mathematical model, which allows a preliminary classification of the alternative schemes and avoids the need to carry out an excessively large number of tests on the scale model.

The aim of this new series of studies was initially an increase in the depth of the navigation channel to elevation  $-4$  m (in relation to the zero of the marine charts, i.e., lowest low water).

The conclusion of a series of nine tests was that the desired increase in draft could be obtained by combining the construction of a regulating structure on the northern edge of the channel over a distance of 7–8 km (complementing the previously-built north-bank dyking) with the setting of the scour-resistant sill at the downstream end of the channel at a sufficiently low elevation, i.e., between  $-5$  and  $-6$  m. An additional conclusion was that this sill, located at the level of the bar at the estuary mouth, was to be maintained by concentrating dredging operations in this area.

**Periods 1971–72 and 1975–77.**—These more recent tests are different in that they are not exclusively aimed at studying structures concerning the navigation channel. Indeed, with the growth of the port of Le Havre, studies have to be made of the extension of this port by a new outer harbor and vast areas of port development land which necessarily involve encroaching on the northern part of the estuary. It is, thus, necessary to study the influence of these new development works on the estuary as a whole and more particularly their influence on the channel and on the volumes to be dredged to maintain it, both in the area of the downstream sill and in the upstream reaches.

Other specific development works recently studied (1975–77) are (1) A breach in the northern dyking designed to maintain in its present condition the extension of the northern trench scoured by flood tide flows (Fig. 5) to allow fishing to continue in this area; and (2) the transverse groin formed by the inclined embankment for the approach to a new bridge, blocking part of the northern foreshore.

Other tests have concerned the disposal of waste products into the Seine estuary, the aim was to study their dilution in the course of several tide cycles and to identify suitable sites for the disposal of dredging spoil to avoid the recycling of this material.

#### COMBINED USE OF MATHEMATICAL AND NEW SCALE MODELS

The use of a mathematical model in order to reproduce the morphological evolution of tidal estuaries cannot be recommended at the present (1977) state of our knowledge concerning simulation techniques. Indeed, there is no recognized theory permitting the formulation of sediment transport in the two-dimensional domain subject to the effect of tides. Thus, where a movable bed is concerned, a scale model seems to be the only acceptable way to predict the future evolution of the estuary. Nevertheless, the combined use of a mathematical (fixed bed) model and a scale (movable bed) model can considerably improve the quality

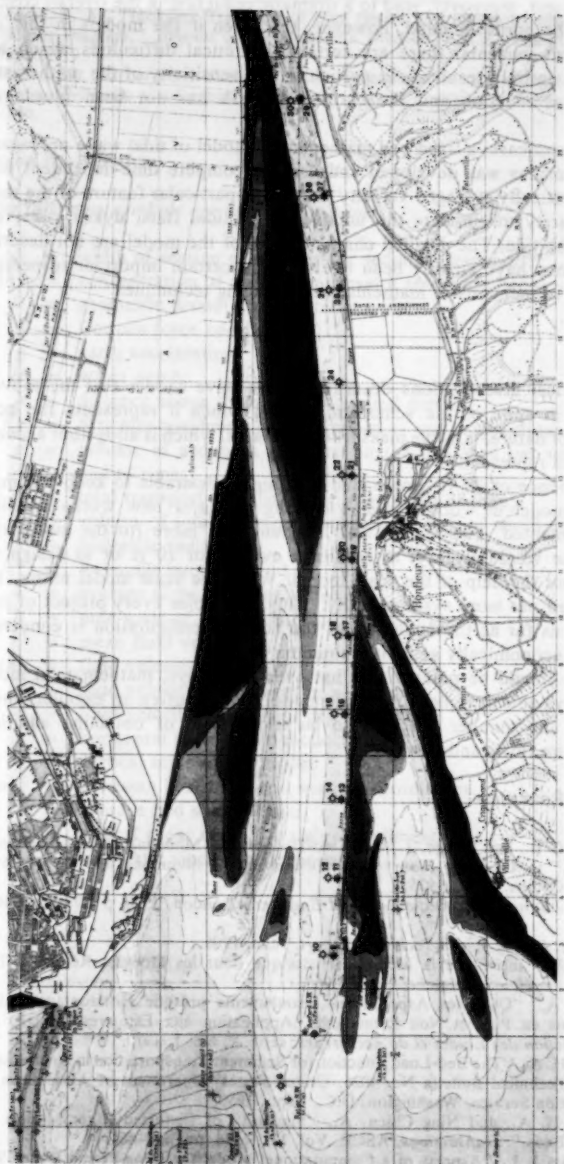


FIG. 5.—1967 Hydrographic Survey

of the latter and, moreover, lead to a dramatic reduction in the overall cost.

It should be borne in mind, however, that even if the models in this case only represent currents, there are certain theoretical difficulties which have not yet been entirely resolved. In particular, the sensitivity of the mathematical model to discretization and the choice of mesh has not been investigated sufficiently.

In the present case, a fixed bed mathematical model of tidal wave propagation in two dimensions was developed and used to compute time-dependent water levels and vertically averaged velocity vectors. A particular feature of the model was its capacity to simulate the uncovering of tidal flats, dykes, sills, etc., during the ebb tide. The detailed characteristics of the model are not described here since they have already been overtaken in certain important respects by more recent refinements of mathematical modelling techniques.

### CONCLUSIONS

The historical investigations described above have shown that the movable bed model, in spite of the schematic way in which it represents the actual phenomena of nature, is a true measuring apparatus, which is altogether accurate, sensitive, and representative.

The experience of 20 yr proves that it is highly desirable to keep a complex and costly model in working order, as long as major new works are likely to be implemented. The fact is that it would cost more (to the authority in charge of the whole estuary) to rebuild it every 5 or 10 yr or to design new works without the help of the scale model. When the scale model exists, tests can be carried out more systematically. Thus, it enables every project of some importance, as far as the evolution of the bottom configuration is concerned, to be tested economically and with minimum delay.

Finally, it should be pointed out that even nowadays, mathematical models are not always able to replace the scale model, but are often an excellent means of reducing the number of cases to be tested, and of obtaining additional information on flows and currents.

### APPENDIX I.—REFERENCES

1. Abbott, M. B., and Cunge, J. A., "Two Dimensional Modeling of Tidal Deltas and Estuaries," in *Unsteady Flow in Open Channels*, K. Mahmood and V. Yevjevich, ed., Fort Collins, Colo., 1975.
2. Bagnold, *Journal of Institution of Civil Engineers*, London, 1940, p. 27 and 1946-47, p. 447.
3. Banal, M., *Port of Rouen Technical Report*, June, 1956.
4. Chapon, J., "Intérêt de la Méthode Historique Pour les Modèles Réduits à Fond Mobile," *La Houille Blanche*, No. 8, 1960.
5. Daubert, A., "Quelques Aspects des Écoulements presque Horizontaux à Deux Dimensions en Plan et Non Permanents. Application aux Estuaires," EDF, *Bull. de la Direction des Etudes et de Recherches*, série A, No. 1, 1970.
6. Einstein, H. A., "The Bed-Load Function for Sediment Transportation in Open Channel Flows," Technical Bulletin No. 1026, United States Department of Agriculture Soil Conservation Service, Washington, D.C., Sept., 1950.
7. Einstein, H. A., and Ning Chien, A., "Similarity of Distorted River Models with Movable Beds," *Transactions, ASCE*, Vol. 121, 1956, pp. 440-461.
8. Leendertse, J. J., "Aspects of a Computational Model for Long-Period Water Wave

- Propagation," The Rand Corp., RM-5294-PR, May, 1967.
9. Mantz, P. A., "Incipient Transport of Fine Grains and Flakes by Fluids. Extended Shields Diagram," *Journal of the Hydraulic Division, ASCE*, Vol. 103, No. HY6, June, 1977.
  10. Rouse, H., "Criteria for Similarity in the Transportation of Sediment," *Proceeding of 1st Hydraulic Conference, Bulletin 20, State University of Iowa, Ames, Iowa, 1940.*

## APPENDIX II.—NOTATION

*The following symbols are used in this paper:*

- $b$  = width of section considered for sediment transport;
- $C(h)$  = concentration of sediment at level  $h$  above the bed;
- $D$  = geometric diameter of sediment grain;
- $f$  = Coriolis force coefficient;
- $g$  = earth acceleration;
- $H$  = water depth;
- $h$  = distance above the bed or computed depth;
- $K_x, K_y$  = Strickler roughness coefficients in  $x$ - and  $y$ - directions;
- $p$  = volume of sediment transport in the bed load per unit of width and of time;
- $Q$  = total transport through a section per unit of time;
- $q$  = volume of total sediment transport per unit of width and of time;
- $R$  = hydraulic radius;
- $R^*$  = Reynolds number;
- $S$  = average slope of water surface;
- $t$  = time scale of bed evolution;
- $U$  = mean fluid velocity;
- $U(h)$  = fluid velocity at level  $h$ ;
- $u$  = fluid velocity component in  $x$ - direction;
- $v$  = fluid velocity component in  $y$ - direction;
- $x$  = horizontal scale of the model;
- $y$  = vertical scale of the model;
- $x, y, z$  = cartesian horizontal and vertical coordinates;
- $\tau$  = average bed shear stress;
- $\tau_c$  = critical shear stress for a given sediment; and
- $\nu$  = kinematic viscosity coefficient.

The first of these is the fact that the...  
 The second is the fact that the...  
 The third is the fact that the...

The fourth is the fact that the...  
 The fifth is the fact that the...

The sixth is the fact that the...  
 The seventh is the fact that the...

The eighth is the fact that the...  
 The ninth is the fact that the...

The tenth is the fact that the...  
 The eleventh is the fact that the...

The twelfth is the fact that the...  
 The thirteenth is the fact that the...

The fourteenth is the fact that the...  
 The fifteenth is the fact that the...

The sixteenth is the fact that the...  
 The seventeenth is the fact that the...

The eighteenth is the fact that the...  
 The nineteenth is the fact that the...

The twentieth is the fact that the...  
 The twenty-first is the fact that the...

The twenty-second is the fact that the...  
 The twenty-third is the fact that the...



## PREVENTION OF SHOALING AT PORT ORFORD, OREGON

By C. E. Chatham<sup>1</sup>

### INTRODUCTION

#### Description of Prototype

Port Orford, Oregon, is on the Pacific Ocean, about 250 miles (400 km) south of the Columbia River entrance and about 50 miles (80.5 km) north of the Oregon-California border. The harbor is formed by a natural cove protected from the north and west by rock headland, which extends seaward in a southwesterly direction for approximately 1 mile (1.6 km). Prior to extension of the breakwater, the harbor was exposed to frequent southwesterly winter storms, which caused extensive damage to harbor facilities and severely curtailed use of the harbor.

In 1935, local interests constructed a combined breakwater-pier of piling, concrete, and stone to afford some protection for the harbor from southwesterly storm waves. The breakwater did not prove to be wholly effective, and harbor facilities were heavily damaged on several occasions. In 1961, a public hearing was held, and the Port Orford port commission requested a Federal project to extend the locally constructed breakwater approx 600 ft (183 m). A project providing for a 550-ft (168-m) extension of the breakwater was approved under the Rivers and Harbors Act of October 27, 1965, and completed on October 28, 1968.

### PROBLEM

Shortly after completion of the breakwater extension at Port Orford, the harbor area adjacent to the pier began to shoal, and, by late 1970, emergency dredging was required. Depths in the area at the time of dredging ranged from 3–14 ft (0.9–4.3 m) below mean lower low water, mllw, compared with former depths of 8–25 ft (2.4–7.6 m).

<sup>1</sup>Hydr. Research Engr.; Chief, Wave Process Branch, Wave Dynamics Div., Hydr. Lab., U.S. Army Engr. Waterways Experiment Station, P.O. Box 631, Vicksburg, Miss. 39180.

Note.—Discussion open until April 1, 1982. Separate discussions should be submitted for the individual papers in this symposium. To extend the closing date one month, a written request must be filed with the Manager of Technical and Professional Publications, ASCE. Manuscript was submitted for review for possible publication on March 9, 1981. This paper is part of the Journal of the Hydraulics Division, Proceedings of the American Society of Civil Engineers, ©ASCE, Vol. 107, No. HY11, November, 1981.

The Oregon coast in the vicinity of Port Orford consists of a series of headlands and long stretches of beach. Each beach segment, separated by headlands from an adjacent beach segment, can be considered an individual cell. Sediments originally derived from the headlands and from tributary coastal streams may move from one cell to adjacent cells or may remain largely isolated. Movement depends upon local conditions that may be unknown. Factors that must be considered include local currents and prevailing winds, storm activity, sediment availability, and nearshore and offshore subsurface configurations.

Sands located in the cell terminated at its northern end by the Port Orford headland tend to move from south to north during winter storms. Summer storms reverse the direction of the sediment movement toward the south. Construction of the breakwater at Port Orford sufficiently altered conditions so that prevailing summer winds and currents are no longer able to move the accumulation of sediments at the northern end of the cell back toward the south, and the harbor area, thus, will continue to shoal unless permanent remedial action is taken.

#### PURPOSES OF MODEL STUDY

The purposes of the model study were to: (1) Compare prebreakwater and existing breakwater conditions to determine the cause and source of harbor shoaling; (2) develop remedial plans in an attempt to eliminate shoaling at the pier without significantly increasing wave action at the pier; and (3) determine whether suitable design modifications of the proposed plans could be made that would reduce construction costs significantly and still have reasonable certainty of preventing shoaling at the pier.

#### MODEL DESIGN AND CONSTRUCTION

##### Design of Model

The Port Orford model (Fig. 1) was constructed to a linear scale of 1:100, model to prototype. Scale selection was based on the following factors: (1) Depth of water required in the model to prevent excessive bottom friction effects; (2) absolute size of model waves; (3) available shelter dimensions and the area required for constructing the model; (4) efficiency of model operation; (5) capabilities of available wave-generating and wave-measuring equipment; and (6) cost of model construction. A geometrically undistorted model was necessary to ensure accurate reproduction of wave patterns, i.e., both refraction and diffraction. Following selection of the linear scale, the model was designed and operated in accordance with Froude's model law (8). Scale relations used for design and operation of the model appear in Table 1.

The proposed plans of improvement for Port Orford included the use of rubble-mound breakwaters. Past experience and experimental research have shown that considerable wave energy passes through the interstices of this type of structure; thus, the transmission of wave energy was a matter of concern in the design of the 1:100-scale model. In small-scale models, rubble-mound structures reflect relatively more and absorb or dissipate relatively less wave energy than geometrically similar prototype structures (5). Also, the transmission of wave energy through the breakwater is relatively less for the small-scale

model than for the prototype. Consequently, some adjustment in small-scale-model rubble-mound structures is needed to ensure satisfactory reproduction of wave transmission characteristics. In past investigations (3,1) at the U.S. Army Engineer Waterways Experiment Station (WES), this adjustment was made by determining the wave energy transmission characteristics of the proposed structure in a two-dimensional model using a scale large enough to ensure negligible scale effects. A breakwater section then was developed for the small-scale, three-dimensional model that would provide essentially the same relative transmission of wave energy. Therefore, from previous findings for breakwaters and wave conditions similar to those at Port Orford, it was determined that a close approximation of the correct wave energy transmission characteristics could be obtained by increasing the size of the rock used in the 1:100-scale

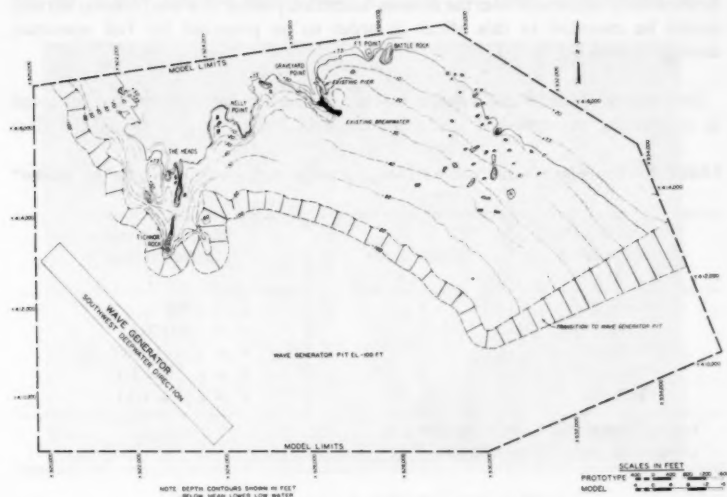


FIG. 1.—Model Layout

model to approximately two times that required for geometric similarity. Accordingly, in constructing the breakwater structures in the Port Orford model, the rock sizes were computed linearly by scale, then multiplied by 2.0 to arrive at the actual sizes used in the model.

Ideally, a quantitative, three-dimensional, movable-bed model investigation would best determine the effectiveness of various project plans at Port Orford. However, it is well-known that this type of model investigation is difficult and expensive to conduct, and each area in which such an investigation is contemplated must be carefully analyzed. The following computations and prototype data are considered essential for such investigations (2):

1. A computation of the littoral transport, based on the best available wave statistics.

2. An analysis of the sand size distribution over the entire project area (offshore to a point well beyond the breaker zone).

3. Simultaneous measurements of the following items over a period of erosion and accretion of the shoreline (to obtain the maximum probability of both erosion and accretion in a minimum amount of time, this measurement period should be chosen judiciously): (1) Continuous measurements of the incident wave characteristics. Such measurements would mean placing enough redundant sensors to obtain accurate estimates of the directional spectrum over the entire project area, and in addition, would mean conducting a rather sophisticated analysis of all these data; (2) bottom profiling of the entire project area using the shortest time intervals possible; (3) nearly continuous measurements of both longshore and onshore-offshore transport of sand. These measurements would be especially important over the erosion-accretion period. A wave forecast service would be essential to this effort in order to be prepared for full operation during the erosion period.

**Description of Model and Appurtenances.**—In view of the complexities involved in conducting movable-bed model studies and due to limited funds and time

TABLE 1.—Scale Relations Used for Design and Operation of the Port Orford Model<sup>a</sup>

Characteristics (1)	Dimensions <sup>b</sup> (2)	Model:Prototype scale relation (3)
Length	$L$	$L_r = 1:100$
Area	$L^2$	$A_r = 1:10,000$
Volume	$L^3$	$V_r = L_r^3 = 1:1,000,000$
Time	$T$	$T_r = L_r^{1/2} = 1:10$
Velocity	$L/T$	$V_r = L_r^{1/2} = 1:10$

<sup>a</sup>In accordance with Froude's model law.

<sup>b</sup>Dimensions are in terms of length,  $L$ , and time,  $T$ .

for the Port Orford project, the model was molded in cement mortar (fixed bed); and a tracer material was developed to determine qualitatively the degree of shoaling in the harbor for various improvement plans. The model reproduced approx 3 miles (4.8 km) of shoreline beginning at The Heads and extending eastward. It included the entire harbor area and underwater contours to an offshore depth of -60 ft (18.3 m) with a sloping transition to a wave generator pit elevation of -100 ft (30.5 m). The total area reproduced in the model was approximately 10,300 sq ft (957.9 m<sup>2</sup>), representing about 3.7 sq miles (9.6 km<sup>2</sup>) in nature. Fig. 2 shows a general view of the model with prebreakwater conditions installed. Model construction was based on the mllw datum. A local prototype grid system was used for horizontal control in the model.

Model waves were generated by a 54-ft-long (16.5-m), piston-type wave generator. The horizontal movement of the plunger caused a periodic displacement of water incident to this motion. The length of stroke and the period of horizontal motion were variable over the range necessary to generate waves with the required characteristics. In addition, the wave machine was mounted on retractable casters,

which enabled it to be positioned to generate waves from the required directions. Changes in water-surface elevation versus time were measured by electrical wave-height gages at selected locations in the model and recorded on chart paper by an electrically-operated oscillograph. The electrical output of each wave height gage was directly proportional to the submergence depth of the gage in the water.

**Selection of Tracer Material.**—As previously discussed, a fixed-bed model was constructed and a tracer material selected to determine qualitatively the degree of shoaling in the harbor for various improvement plans. The tracer material was chosen in accordance with the scaling relationships of Noda (7), which indicate a relationship or model law among the four basic scale ratios, i.e., the horizontal scale,  $\lambda$ ; the vertical scale,  $\mu$ ; the sediment size ratio,  $n_D$ ; and the relative specific weight ratio,  $n_\gamma$ , (Fig. 3). These relationships were



FIG. 2.—General View of Model Looking West

determined experimentally using a wide range of wave conditions and beach materials, and are valid mainly for the breaker zone.

Noda's scaling relationships indicate that movable-bed models with scales in the vicinity of 1:100 (model to prototype) should be distorted, i.e., use different horizontal and vertical scales. Since the fixed-bed model of Port Orford was undistorted to allow accurate reproduction of short-period wave and current patterns, the following procedure was used to select a tracer material. Using the prototype sand characteristics (median diameter,  $D_{50} = 0.21$  mm; and specific gravity = 2.65) and assuming the horizontal scale to be correct (i.e., 1:100), the median diameter for a given specific gravity of the tracer material and the vertical scale were computed. The vertical scale then was assumed to be correct, and the tracer median diameter and horizontal scale were computed. This resulted in a range of tracer material sizes for given specific gravities that could be used. A search was made of all available movable-bed materials



**MODEL TEST CONDITIONS AND PROCEDURES**

**Selection of Still-Water Level.**—Still-water levels, swl, for harbor wave-action models are selected so that the various wave-induced phenomena dependent upon water depths are accurately reproduced in the model. These phenomena include refraction of waves in the harbor area, overtopping of harbor structures by waves, reflection of wave energy from harbor structures, and transmission of wave energy through porous structures. Some of the more important factors contributing to selection of the optimum swl are as follows:

1. The maximum amount of wave energy that can reach a coastal area will ordinarily do so during a severe storm that coincides with the high-water phase of the astronomical tide cycle.
2. Severe storms are usually accompanied by some additional increase in the normal water level due to wind tide and mass transport.
3. A relatively high swl in the model is beneficial in minimizing the effects of bottom friction, which can be excessive in shallow areas of small-scale models.

Therefore, with consideration for the various factors contributing to and affected by the static water level in the prototype, and in view of the tendency toward more conservative results from the model investigation, it was desirable that a model swl be selected that closely approximated the higher water stages that normally prevail during severe storms in the prototype.

From the U.S. Coast and Geodetic Survey records (10), the mean tide level at Port Orford was 3.9 ft (1.2 m), and the mean higher high water level was +7.3 ft (2.2 m). The mean higher high water stage was considered to be representative of water levels to be expected during a severe storm, and an swl of +7.3 ft (2.2 m) was selected for use in the model. Toward the latter part of the model study, the U.S. Army Engineer District, Portland, NPP, also requested that some of the more promising plans of improvement be tested at an swl of 0.0 ft (0.0 m). The purpose of these tests was to insure that the relative effectiveness of the various plans was not sensitive to the swl.

**Wave Dimensions and Directions.**—In planning the test program for a model investigation of harbor wave-action problems, it is necessary to select dimensions and directions for the test waves that will afford a realistic test for the proposed improvement plans and allow an accurate evaluation of the elements of the various proposals. Surface wind waves are generated by the interactions between tangential stresses of wind flowing over water, resonance between the water surface and atmospheric turbulence, and interactions between individual wave components. The magnitude of the maximum wave that can be generated by a given storm depends upon the wind speed, the length of time that wind of a given speed continues to blow, and the water distance (fetch) over which the wind blows. Selection of test-wave conditions entails evaluation of such factors as:

1. The fetch and decay distances (the latter being the distance over which waves travel after leaving the generating area) for the various directions from which waves can attack the problem area.

2. The frequency of occurrence and duration of storm winds from the different directions.

3. The alignment, width, and relative geographic position of the harbor.

4. The alignments, lengths, and locations of the various structures in the harbor.

TABLE 2.—Characteristics of Test Waves Used in the Model

Deepwater wave direction (1)	Selected shallow-water wave test direction (2)	Selected Test Wave	
		Period seconds (3)	Height, in feet (meters) (4)
west	S 82°06' W	9	12, 17 (3.7), (5.2)
west	S 82°06' W	13	7, 13, 21 (2.1), (4.0), (6.4)
west	S 82°06' W	17	7, 15 (2.1), (4.6)
west-southwest	S 64°46' W	9	9, 15 (2.7), (4.6)
west-southwest	S 64°46' W	13	9, 17, 27 (2.7), (5.2), (8.2)
west-southwest	S 64°46' W	17	7, 17 (2.1), (5.2)
southwest	S 47°19' W	9	3, 9, 17 (0.9), (2.7), (5.2)
southwest	S 47°19' W	13	3, 11, 21 (0.9), (3.4), (6.4)
southwest	S 47°19' W	17	9, 15 (2.7), (4.6)
south-southwest	S 27°04' W	9	9, 17 (2.7), (5.2)
south-southwest	S 27°04' W	13	9, 23 (2.7), (7.0)
south	S 10°37' W	9	9, 15, 21 (2.7), (4.6), (6.4)
south	S 10°37' W	13	5, 11, 17 (1.5), (3.4), (5.2)
south-southeast	S 11°05' E	7	3, 7 (0.9), (2.1)
south-southeast	S 11°05' E	11	9, 15 (2.7), (4.6)

5. The refraction of waves caused by differentials in depth in the area seaward of the harbor, which may cause either a convergence or a divergence of wave energy at the harbor site.

When wind waves move into water of gradually decreasing depth, transformations take place in all wave characteristics, except wave period. The most important transformations with respect to the selection of test-wave characteristics



are the changes in wave height and direction of travel due to the phenomenon referred to as wave refraction. The changes in wave height and direction can be determined by plotting refraction diagrams and calculating refraction coefficients. These diagrams are constructed by plotting the position of wave orthogonals (lines drawn perpendicular to wave crests) from deep water into shallow water. If it is assumed that the waves do not break and that there is no lateral flow of energy, the ratio between the wave height in deep water,  $H_o$ , and the wave height in shallow water,  $H$ , will be inversely proportional to the square root of the ratio of the corresponding orthogonal spacings ( $b_o$  and  $b$ ) or  $H/H_o = K(b_o/b)^{1/2}$ . The quantity  $(b_o/b)^{1/2}$  is the refraction coefficient;  $K$  is the shoaling coefficient. Thus, the refraction coefficient multiplied by the shoaling coefficient gives a conversion factor for transfer of deepwater wave heights to shallow-water values. The shoaling coefficient, which is a function of wavelength and water depths, can be obtained from Ref. 9.

Wave refraction diagrams were prepared for representative wave periods from the critical directions of approach. The first set of diagrams represented the propagation of the wave fronts from deep water to shallow water, -60-ft (-18.3-m) contour. Two additional sets of diagrams were then prepared from the wave generator position to the harbor using: (1) Natural contours; and (2) model contours with the sloping transition. A comparison of these latter diagrams for representative-wave periods and critical directions revealed that the model accurately reproduced wave fronts in the harbor area.

Deepwater wave hindcast data by National Marine Consultants (6) for Station 1 (located approximately on the Oregon-California border) were obtained for use in selecting model test waves. These data represent the estimated durations and magnitudes of deepwater waves (sea and swell) approaching Port Orford from the various directions. The refraction-shoaling analysis described previously was used to transfer the deepwater waves into shallow water for use in the model. The shallow-water wave directions used in the model were the average directions of the refracted waves for the significant wave periods noted from each deepwater wave direction. The characteristics of test waves used in the model were selected as shown in Table 2. Wave heights were obtained in the model by parallel-wire, resistance-type wave gages that measured the change in water surface elevation with respect to time. The electrical output of each gage was recorded on chart paper by an oscillograph.

#### ANALYSIS OF MODEL DATA

The relative merits of the various plans tested were evaluated using: (1) A comparison of wave heights at selected locations in the harbor; (2) a comparison of current measurements and movement of tracer material; and (3) visual observations and photographs. In the wave height data analysis, the average height of the highest one-third of the waves recorded at each gage location was selected. All wave heights thus selected were then adjusted to compensate for the greater rate of wave height attenuation in the model as compared with the prototype, by the application of Keulegan's equation (4). From this equation, the reduction of wave heights in the model due to viscous bottom friction can be calculated as a function of water depth, width of wave front, wave period, water viscosity, and distance of wave travel.

**TEST RESULTS**

Test results of prebreakwater conditions indicated that no significant shoaling would occur at the pier or in the mooring area (Fig. 4) because waves breaking over Graveyard Point resulted in currents which swept this area clean. The current magnitudes were not reduced significantly by the existing breakwater,



**FIG. 4.—Typical Shoaling Pattern for Prebreakwater Conditions**

but a large eddy formed, bringing material toward the pier for most wave conditions. Therefore, with the existing breakwater, either direct or eddy currents (depending on wave direction) caused material from the area seaward and east of Battle Rock to enter the harbor between Fort Point and Huge Rock. In general, the smaller storm waves carried material along the beach while the larger waves deposited material adjacent to the pier and in the mooring area.

It was found that an 11-sec, 15-ft (4.6-m) test wave from the south-southeast produced the maximum wave heights and most unfavorable shoaling conditions in the harbor (Fig. 5).

Various modifications to the existing breakwater were generally unsuccessful. Plans involving removal of portions of this breakwater affected an increase in wave heights at the pier with only a slight reduction of shoaling. Plans involving



FIG. 5.—Typical Shoaling Pattern for Existing Conditions

slight reorientation or lengthening of this breakwater, or both, provided basically the same wave protection at the pier as existing conditions but did not improve shoaling.

Numerous breakwater and groin structures were proposed as a means of intercepting the sand moving past Battle Rock into the harbor, but these plans did not prove to be totally effective in preventing shoaling at the pier unless

they were extended a significant distance seaward.

After conducting extensive tests with structures of different lengths, orientations, and crown elevations, it was found that a breakwater with a +10-ft (3.05-m) crown elevation extending 500 ft (152.5 m) south and then 600 ft (183.0 m) southwesterly (Fig. 6) prevented tracer material from entering the harbor for all test waves, and tracer material already in the harbor was stable for all



FIG. 6.—Typical Shoaling Pattern for Best Breakwater Improvement Plan

test waves. Wave heights at the pier were generally the same or slightly reduced when compared with those for existing conditions.

#### CONCLUSIONS

Based on the results of the hydraulic model study it was concluded that:

1. Construction of the existing breakwater altered current patterns in the harbor, i.e., caused an eddy to form, in such a manner as to allow shoaling at the pier.

2. The source of sediment appeared to be the area seaward of Battle Rock and the beaches east of Battle Rock.

3. Removal of portions of the existing breakwater improved shoaling conditions slightly; however, wave conditions at the pier were worsened.

4. Realignment or lengthening of the existing breakwater did not improve shoaling conditions.

5. A 500-ft (152.5-m) breakwater extending due south from Fort Point prevented shoaling of the harbor by waves approaching from the southwest deepwater wave direction but allowed some shoaling by waves from the south and south-southeast.

6. Extension of the Fort Point Breakwater for 600 ft (183.0 m) at an angle of S 45° W prevented shoaling by waves from any direction, and material already in the harbor was stable, i.e., it did not move toward the pier.

7. Shoaling conditions were approximately the same for swl's of 0.0 and +7.3 ft (2.2 m) mllw, the only difference being a slight seaward shift of deposits for the lower water level.

As demonstrated in the Port Orford Study, fixed-bed models utilizing tracer material can be of considerable value in determining qualitatively the effects of various coastal structures on sediment transport. Since they are relatively inexpensive, such studies should be considered prior to coastal construction projects.

#### APPENDIX.—REFERENCES

1. Brasfield, C. W., and Ball, J. W., "Expansion of Santa Barbara Harbor, California; Hydraulic Model Investigation," Technical Report No. 2-805, U.S. Army Engineer Waterways Experiment Station, Dec., 1967, Vicksburg, Miss.
2. Chatham, C. E., Davidson, D. D., and Whalin, R. W., "Study of Beach Widening by the Perched Beach Concept, Santa Monica Bay, California; Hydraulic Model Investigation," Technical Report H-73-8, U.S. Army Engineer Waterways Experiment Station, June, 1973, Vicksburg, Miss.
3. Dai, Y. B., and Jackson, R. A., "Designs for Rubble-Mound Breakwaters, Dana Point Harbor, California; Hydraulic Model Investigation," Technical Report No. 2-725, U.S. Army Engineer Waterways Experiment Station, June, 1966, Vicksburg, Miss.
4. Keulegan, G. H., "The Gradual Damping of a Progressive Oscillatory Wave with Distance in a Prismatic Rectangular Channel," (Unpublished data), U.S. Bureau of Standards, May, 1950, Washington, D.C.
5. LeMéhauté, B., "Wave Absorbers in Harbors," Contract Report No. 2-122, U.S. Army Engineer Waterways Experiment Station, Vicksburg, Miss.; prepared under Contract No. DA-22-079-CIVENG-64-81 by National Engineering Science Co., June, 1965, Pasadena, Calif.
6. National Marine Consultants, "Wave Statistics for Seven Deep Water Stations Along the California Coast," Dec., 1960, Santa Barbara, Calif.
7. Noda, E. K., "Final Report; Coastal Movable-Bed Scale-Model Relationship," Report TC-191, Tetra Tech, Inc., Mar., 1971, Pasadena, Calif.
8. Stevens, J. C., et al., *Hydraulic Models, Manuals of Engineer Practice No. 25*, ASCE, 1942.

9. U.S. Army Coastal Engineering Research Center, "Shore Protection, Planning and Design," Technical Report No. 4, 3rd ed., 1966, Washington, D.C.
10. U.S. Coast and Geodetic Survey, "Tide Tables, West Coast, North and South America (Including the Hawaiian Islands), 1950-1961," Department of Commerce, Washington, D.C.

## UMFOLOZI ROAD BRIDGE HYDRAULIC MODEL INVESTIGATION

By J. A. Zwamborn<sup>1</sup>

### INTRODUCTION

This paper describes a movable-bed hydraulic model study which was made to determine the optimum position, length, and pier alignment of a new road bridge across the Umfolozi River in Zululand, Republic of South Africa. The model scaling techniques, which were based on theoretical considerations, were proved to be effectively correct by reproducing, in the model, recorded scour depths and general river bed changes caused by a major flood. The model study clearly showed that the originally proposed bridge site had serious disadvantages and a much better site was established in the hydraulic model. As a result, the required bridge length could be reduced from 1,200 ft (366 m) to 700 ft (213 m). In addition to the saving in bridge length, the study also resulted in a considerable saving on the foundation depth, due to the reliable scour depth predictions obtained from the movable-bed model.

### BACKGROUND

A movable-bed model study of a new road bridge across the Umfolozi River in Zululand, Natal was undertaken by the CSIR's Hydraulics Division from 1961-1962. The model was designed according to the shear/settling velocity criterion (9) and, after calibrating the model, tests were run to determine the best river crossing. A site, about 0.5 mile (0.8 km) downstream of the originally proposed sites, was recommended because flow lines were found to be more uniform in this area and the required bridge length could be reduced to about half its original size.

During the early stages of bridge construction, in July 1963, an extremely large flood occurred causing considerable damage to temporary structures. Major topographical changes took place in the affected river reach which were recorded by aerial photography. Moreover, maximum scour depths reached at the peak

<sup>1</sup>Sr. Chf. Research Officer, National Research Inst. for Oceanology, South African Council for Scientific and Industrial Research, Stellenbosch, South Africa.

Note.—Discussion open until April 1, 1982. Separate discussions should be submitted for the individual papers in this symposium. To extend the closing date one month, a written request must be filed with the Manager of Technical and Professional Publications, ASCE. Manuscript was submitted for review for possible publication on March 9, 1981. This paper is part of the Journal of the Hydraulics Division, Proceedings of the American Society of Civil Engineers, ©ASCE, Vol. 107, No. HY11, November, 1981. ISSN 0044-796X/81/0011-1317/\$01.00.

of the flood were derived from wash borings made along the bridge center line before and just after the flood.

Since the model was still available, it was decided to reproduce the July 1963 flood and to correlate its effect with the recorded changes in the Umfolozi River. A fairly good reproduction of the general river morphology and a very good reproduction of the scour depths at the bridge site were obtained, confirming the reliability of the scaling technique for this type of model. The same scaling laws were used for the design of a more recent model of the Illovo River in Natal which provided further proof of their general reliability (7).

**Problem Statement.**—A new road bridge had to be built in the national road from Durban to Mtubatuba in the north of Zululand. The Umfolozi River makes

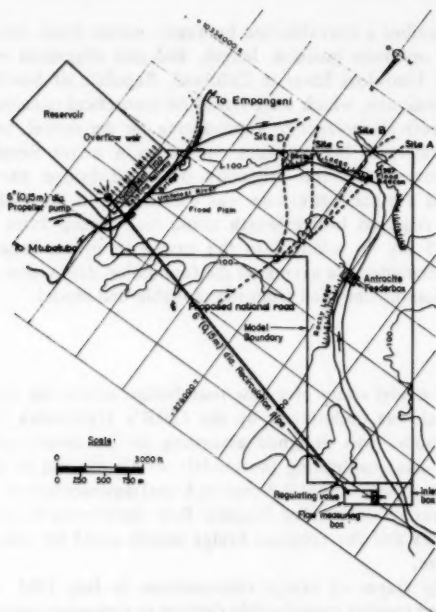


FIG. 1.—General Lay-out Plan and Model Boundaries

a sharp bend just upstream of the proposed crossing, consists of a 250 ft (76 m) wide sandy river bed with a very steep rocky south (right-hand) bank, and a partly overgrown sandy flood plain of some 2,000 ft (610 m) wide north of the actual river channel (Fig. 1). The 100 yr flood was estimated to be 200,000 cfs (5,600 cms), based on 1947–1955 flood data with an average water level slope of 1:2,000 (the average bottom slope over the area modelled was 1:2,700).

The existing railway bridge, situated about 1.5 mi (2.4 km) downstream of the proposed bridge sites, was constructed in 1928 and consists of eleven 150



ft (45.7 m) clear spans, thus providing a total flow width of 1,650 ft (503 m). The railway bridge crosses the river at an acute angle. Hydraulic calculations by the provincial road engineers indicated that, for a right-angle crossing, a road bridge consisting of twelve 100 ft (30.5 m) clear spans, i.e. a clear bridge opening of 1,200 ft (366 m), would be sufficient for the new bridge.

Three different road alignments, A, B, and C shown in Fig. 1, were considered by the roads department, and 120 ft (37 m) deep boreholes were sunk at these locations. Because no rock for pier foundations was found at any of the three sites, it was decided that the choice of the best site for the new bridge would be based on hydraulic considerations. However, due to the complicated flow conditions in the river bend, it was not considered possible to determine the optimum site on the basis of hydraulic computations alone, and the Natal Roads Department therefore asked the South African CSIR to study the problem in a hydraulic model with the following terms of reference:

1. Determination of the best site for a bridge crossing with respect to river-bed scour.
2. Determination of the minimum required bridge length.
3. Determination of the optimum bridge pier spacing and orientation.

In view of the above requirements, it was decided to design and construct a movable-bed model.

**Model Design.**—Approximately 4 mile (6.4 km) of river was reproduced in the model. As may be seen in Fig. 1, the downstream boundary of the model was just below the railway bridge, whereas the upstream boundary was situated in a fairly straight section of the river. These boundaries were chosen to ensure correct reproduction of flow conditions in the river bend area.

At the time, no indoor laboratory space was available and the model had to be built in the open air. Although sufficient space was available, apart from hydraulic requirements, the size of the model was, therefore, largely determined by practical considerations, namely construction time and cost. A horizontal scale of 1:250 was accepted as a reasonable compromise.

The vertical scale, model sediment size, and density were then determined on the basis of the following sediment movement similarity criteria (8,9,10):

$$\text{equal Froude numbers } \left( \frac{V}{\sqrt{gh}} \right)_r = 1 \dots \dots \dots (1)$$

$$\text{shear/settling velocity ratio } \left( \frac{V_*}{W} \right)_r = 1 \dots \dots \dots (2)$$

$$\text{roughness criterion } \left( C^1 \sqrt{\frac{S}{g}} \right)_r = 1 \dots \dots \dots (3)$$

$$\text{grain-Reynolds number } Re_{*r} < \sim 10 \dots \dots \dots (4)$$

These criteria were found to have a sound theoretical basis (9) and they result in much more practical model scales than the more common criteria  $[hS/(\rho_s/\rho - 1)d]_r = 1$  and  $Re_{*r} = 1$  which are based on equality of initiation of motion (2,4). For correct reproduction of local scour, e.g. around bridge piers, the velocity/settling velocity ratio,  $(V/W)_r$ , should be equal to unity (6) which

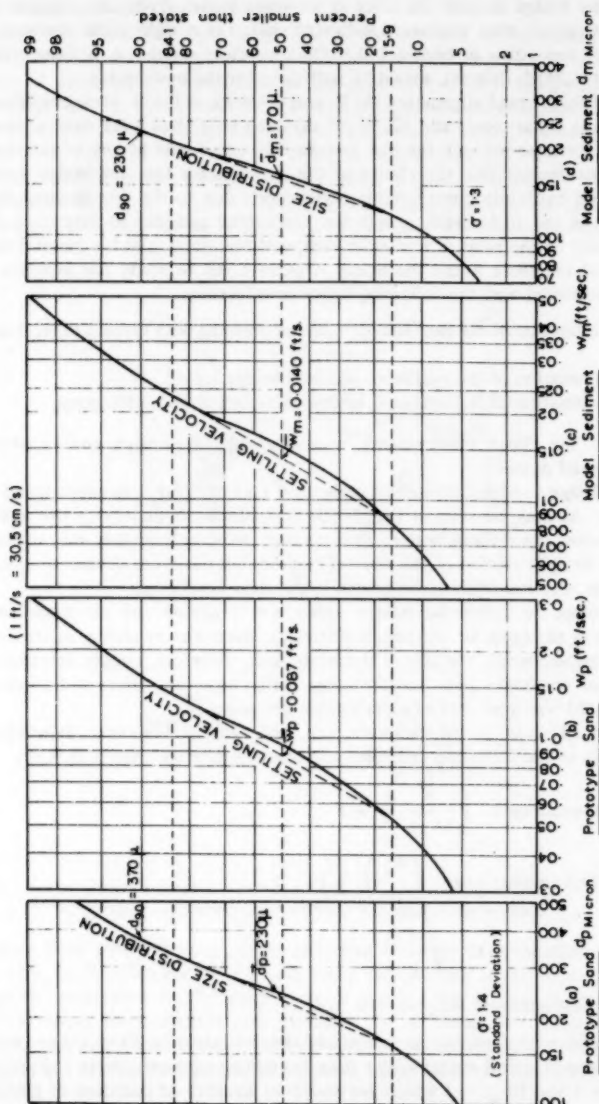


FIG. 2.—Determination of Size Distribution for Model Coal

would require an undistorted model. An additional requirement is, therefore, that the distortion should be kept as small as possible, e.g.  $S^{-1} \leq 3$  to 4 (10).

The following model scales were found to best satisfy the various requirements (1,3,11):

horizontal scale  $L_r = 250$  . . . . . (5)

vertical scale  $h_r = 100$  . . . . . (6)

Thus, the geometric distortion was  $S_r = 1/2.5$

velocity scale  $V_r = (g_r h_r)^{1/2} = 10$  . . . . . (7)

and flow rate scale  $Q_r = L_r h_r^{3/2} = 250,000$  . . . . . (8)

The 200,000 cfs (5,600 cms) 100 yr flood will thus be reproduced by 0.8 cfs (22.7 L/s) in the model.

sediment size and density scales  $W_r = V_{*r} = (g_r h_r S_r)^{1/2} = 6.33$  . . . . . (9)

Crushed anthracite, with a specific gravity of 1.35, was most readily available

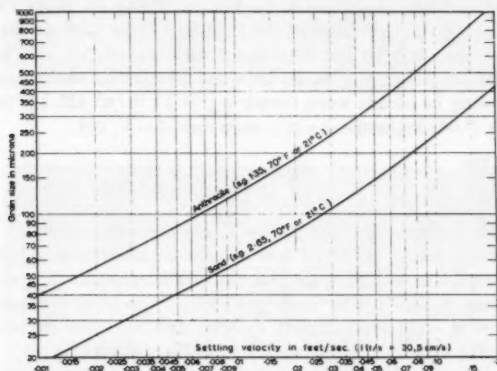


FIG. 3.—Settling-Velocity Curves

as model sediment to reproduce the fine sand,  $\bar{d}_p = 230 \mu$  (micron), of the Umfolozi river.

The average size distribution of three representative samples taken from the river bed is shown in Fig. 2(a). This was converted into the settling velocity distribution of Fig. 2(b), using Fig. 3. After applying the scale factor  $W_r = 6.33$  to this curve, the model grain size distribution in Figure 2(d) was calculated, using Fig. 3 again. The mean grain size was found to be  $\bar{d}_m = 170 \mu$ , which was considered acceptable, i.e. not too fine.

roughness criterion  $C_r^1 = g_r^{1/2} S_r^{-1/2} = 1.58$  . . . . . (10)

in which  $C^1$  = the grain roughness coefficient defined by  $C^1 = 5.75 g^{1/2} \log 12 h/d_{90}$  (9). The average water depth for 200,000 cfs (5,600 cms) was taken

at 20 ft (6.1 m) which yielded  $C_r^1 = 1.52$  (for smaller floods  $C_r^1$  approaches 1.58). Thus the roughness criterion, which is related to the movable-bed in the model, was very nearly satisfied.

$$\text{bed-shape criterion } Re_{*r} = \frac{V_{*r} d_r}{\nu_r} = 8.5 \dots \dots \dots (11)$$

It has been shown elsewhere that, in this type of model, a difference between the model and prototype value of the grain Reynolds number,  $Re_{*r}$ , is necessary to ensure similar bedform (ripples, dunes or anti-dunes) (9). Values of  $Re_{*r}$  up to about 10 were found to be acceptable.

$$\text{hydraulic time scale } t_r = \frac{L_r}{V_r} = 25 \dots \dots \dots (12)$$

$$\text{sediment time scale } Ts_r = \frac{L_r h_r \rho_{sr}}{q_{sr}} = \frac{49,000}{q_{sr}} \dots \dots \dots (13)$$

(with  $\rho_{sr} = 2.65$ ). To determine the bed-load ratio  $q_{sr}$ , the bed-load for both the prototype and the model had to be known. Using Du Boys's formula for the prototype, the tractive force in the Umfolozi river exceeds that for which other formulas available at the time had been checked, i.e.  $hS/[(\rho_s/\rho) - 1]$   $d = 5.77$ , and the average of Kalinske's and Shields' formulas for the model (6), the following bed-loads were found:  $q_{sp} = 17$  lb/sft (25 kg/ms); and  $q_{sm} = 0.03$  lb/sft (0.045 kg/ms).

$$\text{Thus } q_{sr} = 566 \dots \dots \dots (14)$$

$$\text{and } Ts_r = 90 \dots \dots \dots (15)$$

Of course, this sediment time scale is only very approximate (9).

**Model Construction.**—An aerial survey plan to a scale of 1:2500 with 2 ft (0.6 m) contours was available for the model construction. The extent of the model is shown in Fig. 1. The model was molded in concrete using masonite templates at 6 in. (152 mm) centers to form the river bed proper, and steel strips bent in the form of the contours, on the flood plain (Fig. 4).

Sand samples were collected from the river bed and from the size analyses it was found that the sand was very uniform, with a mean diameter of 230  $\mu$ . The sand was reproduced in the model using crushed and carefully sieved anthracite (sp gr 1.35) which was placed in a 2–6 in. (51 mm–152 mm) deep recess built into the study area of the model, i.e. from the railway bridge to just upstream of the river bend. After initial indicative test runs, the greater depth was introduced at the bridge sites to allow for unlimited scour.

Geological sections obtained during construction of the railway bridge and from information from washborings at the proposed bridge sites showed that the only rock in the area was at the right-hand river bank, carrying down at a slope of 1:2.5 below the river bed. The rest of the river bed consisted of fine sand with thin clay bands up to a depth 120 ft (36.5 m) below river bed level.

**Model Operation.**—Water was circulated with a 6 in. (152 mm) diameter low head propeller pump and the flow rate was controlled with a gate valve (Fig. 5). Flow measurements were done with a broad-crested weir and the hydraulic

gradients were controlled by an adjustable tailgate. Flow rates of up to twice the 100 yr design flood of 200,000 cfs (5,600 cms) could be reproduced.

For various practical reasons, the movable bed part of the model was kept as small as possible and the model section upstream of the bend, therefore, had a fixed bed for all the tests. Sediment (anthracite) was added by a dry/wet feeder placed just upstream of the movable bed part of the model (Fig. 1).

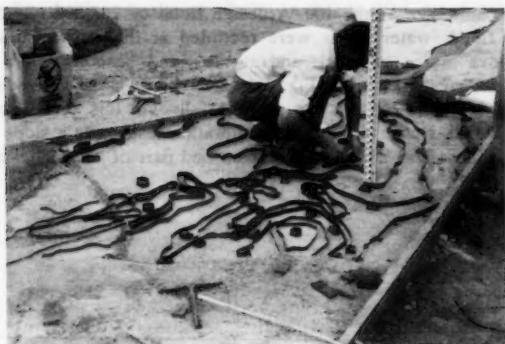


FIG. 4.—Construction of Umfolozi Model



FIG. 5.—General View of Umfolozi Model in Operation

The feeder system consisted of a conical feeder silo with a opening slot at the bottom and a saw-tooth control slide across the opening. The dry anthracite was mixed with water in a vortex chamber, and fed partly directly into the river bed and partly through a distribution pipe onto the flood plain. The feed rate could be accurately adjusted between 0.02 lb/s and 0.5 lb/s (0.01 kg/s and 0.23 kg/s).

Point gauges were used for water level measurement and water velocities

were measured by propeller current meters and by using photographic techniques. Scour recording during a flood could not be done by direct measurement because of the suspended anthracite. A simple electric probe was developed which was lowered into the water, showing a sudden increase in electric resistance when the probe touched the anthracite bed. Furthermore, scour-patterns after the flood were recorded by the well-known photography/string method.

**Model Verification.**—In 1957, a flood occurred which is estimated to have been of the same size as the 100 yr design flood of 200,000 cfs (5,600 cms). During this flood, water levels were recorded at the railway bridge 91.0 ft (27.7 m) above mean sea level, and at the flood beacon at site A, 95.1 ft (29.0 m) above mean sea level (Fig. 1). Since the distance between these two points was 8,250 ft (2,516 m), the average fall over this section of the river was about 1:2,000. Because the initial calibration tests gave a slope of 1:2,750, artificial roughness was added to the fixed bed part of the model in the form

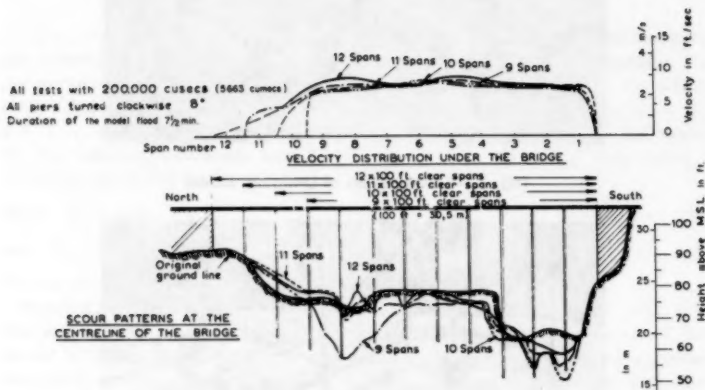


FIG. 6.—Various Bridge Lengths, Umfolozi Bridge, Site B

of stones fixed to the model surface with cement mortar, until the recorded 1957 flood levels were correctly reproduced.

No further prototype data were available for calibration purposes other than 16 wash-borings at the proposed bridge sites which provided information on the depth of easily erodable material.

The model sediment transport rate was calibrated against the calculated value of 0.03 lb/sft (0.045 kg/ms). A feed rate of 0.027 lb/sft (0.04 kg/ms) was found to give a stable bed in the feeding area for the design flood and this rate was therefore accepted. Finally, most tests were run for 7 1/2 min, or approximately 12 hr prototype time.

**Model Tests.**—The first tests were run without a road bridge and reproducing floods varying from 50,000 cfs–200,000 cfs (1,416 cms–5,663 cms). These initial tests showed that about 1,000 ft (305 m) downstream of the suggested site C, almost all the flow was concentrated in a narrow channel of about 500

ft (152 m) wide adjacent to the south bank, although the full width of the river in flood was over 2,000 ft (610 m). It was subsequently decided to include a fourth bridge crossing, namely site D (Fig. 1), in the investigation and comparative tests soon revealed that Sites B and D were much superior to Sites A and C. Detailed tests were therefore only carried out with a road bridge at Sites B and D.

With a 200,000 cfs (5,600 cms) flood reproduced in the model it was found that at Site B a bridge consisting of eleven 100 ft (30.5 m) clear spans (total

All tests with 200,000 cusecs (5663 cumecs)  
 Piers are perpendicular to the bridge axis  
 Duration of the model flood 7 1/2 min.

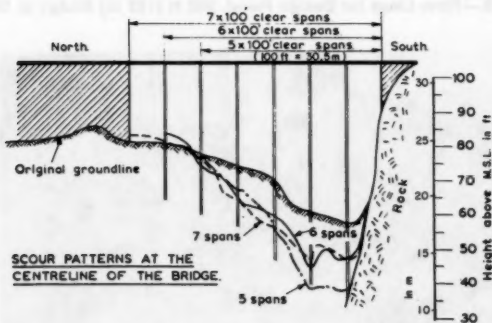
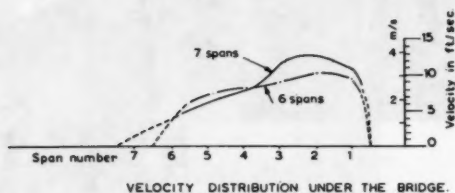


FIG. 7.—Various Bridge Lengths, Umfolozi Bridge, Site D

length 1,100 ft (335 m)) would be acceptable (Fig. 6). However, for floods exceeding the 100 yr design flood by up to 100%, the direction of approach of the flow relative to the orientation of the bridge piers was so bad, and the resulting local scour so severe, that Site B was not recommended. An additional drawback of Site B was the lack of an adequate safety factor in the case of a flood exceeding the accepted 100 yr flood of 200,000 cfs (5,600 cms).

Due to the natural contraction of the flow near Site D, it was found from the tests that six 100 ft (30.5 m) clear spans (total length 600 ft (183 m)) would

be sufficient for floods up to the design flood (Figs. 7, 8 and 9). Scour up to 20 ft (6 m) deep was found near the south bank and it was therefore considered advisable to replace the three 100 ft (30.5 m) spans with one long span of 300 ft (91 m) at the south end of the bridge. This situation was also tested with 300,000 and 400,000 cfs (8,495 and 11,330 cms) floods and, provided a groyne was built near Site B to guide the flow towards the bridge (Fig. 8), it was found acceptable from all points of view. On the basis of the movable-bed

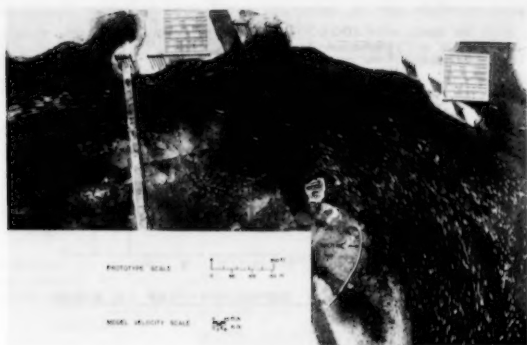


FIG. 8.—Flow Lines for Design Flood, 600 ft (183 m) Bridge at Site D

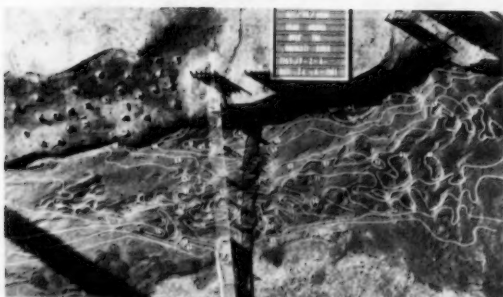


FIG. 9.—Contours After Design Flood, 600 ft (183 m) Bridge at Site D

model study it was therefore recommended to the authorities that a bridge consisting of one 300 ft (91 m) span and three 100 ft (30.5 m) spans be constructed at site D together with a groyne near Site B. The best orientation of the piers was found to be perpendicular to the bridge axis, and the maximum scour depth near the south bank was established at 20–30 ft (6–9 m) for floods up to 400,000 cfs (11,200 cms).

This recommendation was accepted and the bridge was constructed accordingly.



(An extra 100 ft (30.5 m) span was added to the north end in the final design after the occurrence of a 300,000 cfs (8,400 cms) flood during construction in July, 1963.) The considerable reduction in bridge length from the anticipated 1,200 ft (366 m), as well as the knowledge of probable scour depths required for safe foundation design, resulted in significant savings in the cost of the Umfolozi bridge.

**Confirmation of Model Predictions.**—Just after the construction of the Umfolozi bridge had begun, a severe flood occurred which reached an estimated peak flow rate of 300,000 cfs (8,400 cms), compared with the accepted 100 yr design flood of 200,000 cfs (5,000 cms) on July 4, 1963 (8). This flood caused major changes in the topography, as is clearly visible from a comparison of Figs. 10 and 11.



FIG. 10.—Downstream View, from Bridge Site B, Before July Flood



FIG. 11.—Downstream View, from Bridge Site B, After July Flood

The provincial administration immediately authorized another aerial survey covering the same area as the original one, and a comparison of the two yielded invaluable data on the changes in the river-bed and on the flood plain (Fig. 12). The most significant changes included a complete shift of the main river channel between the road bridge site and the railway bridge, a widening of the channel at the road bridge site from 250 ft to 600 ft (76 m to 183 m), (Fig. 14), scour up to 5 ft (1.5 m) deep on the flood plain some 3,000 ft (914 m) upstream of the bridge site, and deposition of up to 12 ft (3.7 m) in height on the flood plain just north of the bridge site.

From the cross-section at the bridge site taken just after the flood (Fig. 14), it can be seen that the depth of the river channel remained virtually unchanged.



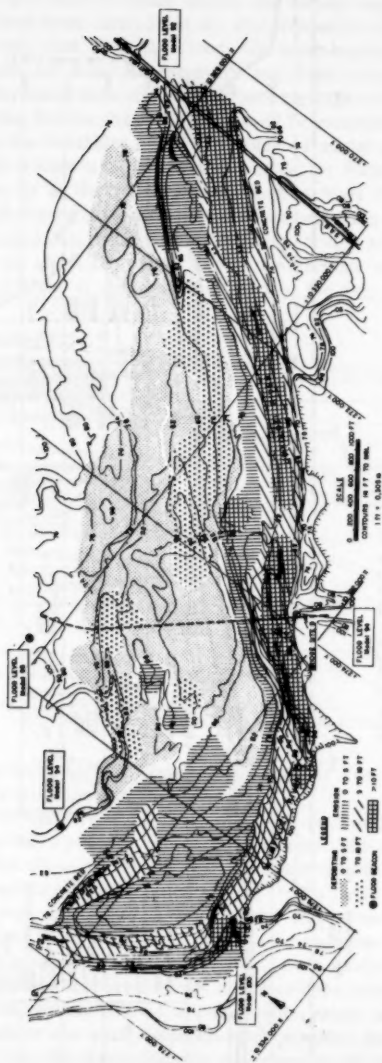


FIG. 13.—Model Topography After Correlation Test



However, from bridge foundations failures which had occurred in Natal, it was known that considerable scour holes develop during the rising stage of a flood which are filled in again during the falling stage. Extensive subsoil investigations had been carried out by the provincial roads department prior to the July flood. Just after the flood, six wash-borings were made by the National Institute for Road Research (5), and from a comparison of this data on the subsoil structure with information from loggings with a gamma ray probe, a maximum scour line for the July flood could be established (Fig. 14).

To check on the reliability of the movable-bed model results, the July flood was reproduced to scale in the still available model (8). Flood levels were obtained from debris marks at the railway bridge and at Sites D and A on both the north and south banks (Fig. 12). These levels were reproduced in the model to within 1 ft (0.3 m), except at the railway bridge where the model level was 1.7 ft (0.5 m) above the debris level (8). Anthracite was fed into the model by the feeder system at approximately double the rate used for the 200,000

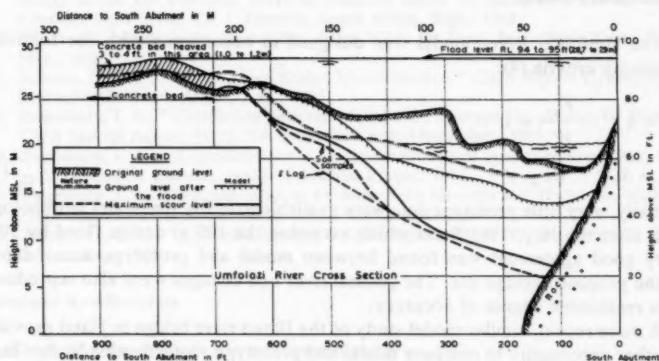


FIG. 15.—Scour Depths at Bridge Site D

cfs (5,600 cms) flood, i.e. 0.05 lb/sft (0.075 kg/ms). The duration of the model flood was 7 1/2 min at maximum flow rate.

The model topography after the flood was recorded by photograph and compared with the topography prior to the flood. The result, shown in Fig. 13, shows an excellent agreement with the prototype bed changes, shown in Fig. 12, both qualitatively and quantitatively.

Maximum scour depths in the model were determined from the depths to which quarter-inch (6 mm) diameter fluorescent sediment tracer piles, inserted at close centers into the anthracite river-bed, were washed away by the model flood. The agreement between model and prototype scour depths was found to be very good, within 10% of the maximum value, as may be seen from Fig. 15. This result was easily reproducible, provided the bed material in the model was put in to the correct density requirements (20–30% moisture together with gentle tamping).

It is interesting to mention that, prior to the July flood, considerable doubt

was expressed by some of the engineers responsible for the design of the bridge about the reliability of the scour depths as predicted from the model results which were 20–30 ft (6–9 m). Organic traces, obtained from bore-holes from a depth of over 100 ft (30.5 m), were originally claimed to be of very recent origin, indicating scour during recent years, at least to this depth. If allowance were to be made for such scour depths, the bridge pier foundations would have had to go extremely deep, up to about 150 ft (46 m). However, after the flood, which came at a very opportune time from the viewpoint of foundation design, much more confidence was placed on the model predictions and foundation levels were adjusted accordingly (Fig. 14). Moreover, a piece of wood which had a very fresh appearance (originally estimated to be 5 yr old), and which was found during pile-driving operations at a depth of 70 ft (21 m) at a position where the model predicted a scour depth of less than 15 ft (4.6 m), was established by carbon dating to be about 5,000 years old.

#### CONCLUDING REMARKS

The Umfolozi River model was designed in accordance with the following similarity criteria (9):

$$V_r = h_r^{1/2} \frac{V_{*r}}{W_r} = 1$$

$$C_r^1 = S_r^{-1/2} \quad Re_{*r} \neq 1 \quad \dots \dots \dots (16)$$

Initially, very little prototype data were available to verify the model morphology, but, after the July, 1963 flood which exceeded the 100 yr design flood by 50%, very good agreement was found between model and prototype scour depths at the proposed bridge site. The general river bed changes were also reproduced to a reasonable degree of accuracy.

A more recent, similar model study of the Illovo river bridge in Natal provided another opportunity to compare model and prototype scour depths. In this case, the recorded prototype scour of 40 ft (12 m) was reproduced in the model to within about 2 ft (0.6 m) (7). Thus, for similar type of rivers (steep gradients with large tractive force), movable bed models, designed in accordance with the above criteria, may be expected to yield reliable predictions of scour depths and probably also general river bed changes. It should be stressed, however, that repeatable results were only obtained when the anthracite was compacted according to fairly rigid standards using 20–30% moisture and gentle tamping.

Little confidence can be placed on bed-load formulas, particularly with the high tractive force which occurs in the Umfolozi River. As a result, the accuracy of the sediment time scale,  $T_s \approx 90$ , is very low indeed. However, it was found that maximum scour occurred invariably within 6 min after the start of the tests and, since a standard test duration of 7 1/2 min (about 12 hours prototype time) was adopted, also for the July, 1963 flood, the exact value of the sediment time scale was of little importance. Moreover, for smaller floods, the sediment time scale may well be different. In fact, it was found that the lower model flows at the tail of a flood had to be run much longer than the scaled-down prototype time to fill in the scour holes formed at the peak of the flood in a way similar to that observed in the actual river.

In summary, the model study resulted in the optimum placement of the Umfolozi River bridge, a reduction in length from the anticipated 1,200 ft (366 m) to 700 ft (213 m), and a considerable saving on the foundation depth, due to the reliability of the scour depth predictions.

#### APPENDIX I.—REFERENCES

1. American Society of Civil Engineers, Hydraulic models, *ASCE Manuals of Engineering Practice* No. 25, New York, July, 1942.
2. Bogardi, J., "Hydraulic Similarity of River Models with Movable Bed," *Acta Technica Oecademiae Scientiarum Hungaricae, Tomus XXIV, Fasciculi 3-4*, Budapest, 1959, pp. 417-445.
3. Chow, Ven Te, *Open Channel Hydraulics*, McGraw-Hill Book Co., Inc., London, England, 1959.
4. Einstein, H. A., and Chien, N., "Similarity of Distorted River Models with Movable Beds," *ASCE Transactions*, Vol. 121, 1956, pp. 440-462.
5. National Institute for Road Research, "Foundation Investigation for a Proposed New Bridge across the Umfolozi River on National Route 14, Sections 5 and 6," *CSIR Contract Report*, No. CR 1, Pretoria, South Africa, Sept., 1963.
6. Rouse, H., *Engineering Hydraulics*, John Wiley & Sons, Inc., New York, N.Y., Mar., 1958.
7. Scholtz, D. J. P., "Illovo River Bridge Model Studies," *CSIR Report C/Sea 75/15*, Stellenbosch, South Africa, Aug., 1975.
8. Zwamborn, J. A., "Correlation Between Model and Prototype Morphology of Rivers," *CSIR Special Report*, MEG 334, Pretoria, South Africa, Jan., 1965.
9. Zwamborn, J. A., "Reproducibility in Hydraulic Models of Prototype River Morphology," *La Houille Blanche*, No. 3, Grenoble, France, 1966.
10. Zwamborn, J. A., "Solution of River Problems with Movable Bed Hydraulic Models," *CSIR Report*, MEG 597, Pretoria, South Africa, Oct., 1967.
11. Zwamborn, J. A., "Hydraulic Models," *CSIR Report*, MEG 795, Stellenbosch, South Africa, July, 1969.

#### APPENDIX II.—NOTATION

*The following symbols are used in this paper:*

- $C^1$  = grain roughness coefficient;  
 $d$  = grain diameter;  
 $g$  = acceleration due to gravity;  
 $h$  = water depth;  
 $L$  = horizontal length;  
 $Q$  = flow rate;  
 $q_s$  = bed-load rate per unit width;  
 $Re_*$  = grain Reynolds number;  
 $S$  = slope;  
 $T_s$  = sediment time (scale);  
 $t$  = time;  
 $V$  = flow velocity;  
 $V_*$  = shear velocity;  
 $W$  = settling velocity;  
 $\nu$  = kinematic viscosity;  
 $\rho$  = density of water; and  
 $\rho_s$  = sediment density.





## MODELING CAVITATION FOR CLOSED CONDUIT FLOW

By J. Paul Tullis,<sup>1</sup> M. ASCE

### INTRODUCTION

A portion of a model study that describes an experimental procedure for determining four cavitation limits and how to evaluate and adjust for scale effects is discussed. The item tested was a long-radius elbow but the procedure applies to any pipe component or valve used in closed conduit flow. Cavitation limits evaluated are incipient, critical, incipient damage, and choking cavitation. Scale effects associated with changes in size and velocity or pressure are evaluated and used to adjust the model data to the prototype conditions. The objective of the paper is to demonstrate a procedure for modeling cavitation for closed-conduit flow, and not to present complete results of a model study. For more details about the prototype system and solutions to problems uncovered by the model study, one should refer to project reports on model tests (16,17).

### STATEMENT OF PROBLEM

The Kensico south effluent chamber is one of the key control structures in the municipal water supply system for the City of New York. The structure serves mainly as a control between Kensico and Hill View reservoirs. It contains three 64- × 60-in. (1,626 × 1,524 mm) reducing cone valves and two 5 × 15-ft (1.525 by 4.565 m) roller gates. The gates and valves control the flow in the 14-mile (22.54-km) 19.5-ft (5.948-m) diameter tunnel connecting the two reservoirs. The original operating schedule for the installation was, first, to open the cone valves until the flow was sufficient to provide adequate submergence on the gates. The gates would, then, be opened, and fine regulation would be achieved with one or more of the cone valves at partial openings.

The structure consists of a forebay, a bellmouth entrance close-coupled to a mitered 90° vaned elbow with the valve bolted to the outlet flange of the elbow and a short pipe discharging into the downtake shaft. The water surface

<sup>1</sup>Prof. of Civ. Engrg., Utah Water Research Lab., Utah State Univ., Logan, Utah 84322.

Note.—Discussion open until April 1, 1982. Separate discussions should be submitted for the individual papers in this symposium. To extend the closing date one month, a written request must be filed with the Manager of Technical and Professional Publications, ASCE. Manuscript was submitted for review for possible publication on March 9, 1981. This paper is part of the Journal of the Hydraulics Division, Proceedings of the American Society of Civil Engineers, ©ASCE, Vol. 107, No. HY11, November, 1981. ISSN 0044-796X/81/0011-1335/\$01.00.

elevation in the dwtake shaft depends upon the flow rate. At small flow rates, the water surface is below the outlet elevation of the valve, such that the mean pressure below the valve is negative. To suppress cavitation at the valve, an air inlet system was installed at the discharge side of the valve.

When the system was placed into operation, difficulties were uncovered. When the valves were opened beyond 55°, intense vibration occurred at the vaned elbows. It was determined that the vibrations were generated by cavitation. To suppress the cavitation and vibrations, concrete weir blocks were installed in the waterway to increase backpressure. This improved conditions for the cone valve operation, but, for safety considerations, the opening of the valves was still limited to 50°.

The combination of the weir blocks and restricted valve operation has limited the capacity of the Kensico-Hill View tunnel. As a result, consideration was given to replacing the vaned elbows with 64-in. (1,626-mm) diameter circular long radius elbows and removing of the weir blocks. To determine the adequacy of the proposed modifications an experimental research program was conducted at Colorado State University (16,17). The objectives of the experimental study were: (1) Evaluate discharge and loss coefficients for the entrance, elbow, and valve; (2) measure the pressure distribution on the inner and outer curves of the elbow; (3) determine cavitation limits for the model, elbow, and valve and scale the information to the prototype; (4) study air requirements of the valve to suppress cavitation and scale the data to the prototype; and (5) develop modifications or operating procedures to avoid any problems uncovered by the study. Only the cavitation study on the elbow is included in this paper. The other information is included in the model study reports (16,17).

**Conditions for Similarity.**—To study cavitation experimentally, it is necessary to determine the governing parameters that control the cavitation process and dictate the design and operation of models to insure dynamic similarity. The main variables affecting inception and subsequent levels of cavitation are the boundary geometry, flow variables of absolute pressure and velocity, and the critical pressure at which the vapor cavity can be formed. In addition to these, there are other variables which, under certain conditions, can have significant influence on the cavitation process. These include fluid properties of viscosity, surface tension, air content and contamination in the liquids, cleanliness of the boundary surfaces, and the size of the flow passage (7).

Since it is not possible to incorporate all of the influencing elements in a cavitation study, the general procedure has been to use a cavitation parameter, related to the velocity, absolute pressure, and critical pressure, and to evaluate the influence of the other factors in terms of scale effects.

The form of the cavitation index  $\sigma$  convenient for this study was:

$$\sigma = \frac{P_u - P_v}{\frac{\rho V^2}{2}} \dots \dots \dots (1)$$

in which  $P_u$  = the total pressure (pressure head plus velocity head) at the inlet to the elbow;  $P_v$  = the liquid vapor pressure (both pressures in absolute units);  $\rho$  = the liquid density; and  $V$  = the mean pipe velocity. If there were no scale effects, the experimental procedure would be simple and similarity would

be insured if  $\sigma_{\text{model}} = \sigma_{\text{proto}}$ . One would, therefore, be free to select any convenient and economical model scale and operate at any arbitrary set of flow conditions that would produce the proper  $\sigma$ . Unfortunately, scale effects do exist, and this simple procedure will not insure dynamic similarity. To make the study complete, the scale effects caused by ignoring important variables must be evaluated. This is the real heart of a successful cavitation study. It is easy to test a model and observe when it cavitates, but scaling the information to different conditions requires additional information. The three most important scale effects are those associated with: (1) Air content and water quality; (2) size of the system; and (3) Reynolds number, velocity or pressure.

The current state of knowledge of the influence of air content on cavitation is summarized in Ref. 4. It is, however, the experience of this researcher that for natural reservoir water, i.e., water which has been neither intentionally deaerated nor aerated, the air content scale effects are minor in comparison with those associated with velocity and size. Although this comment is based on numerous observations, it is presented as an observation and not as a fully documented conclusion. The water used in this study was not recirculated, so there was no alteration of the air content as is often a problem with recirculating water-tunnel experiments. Consequently, the influence of air content was not studied since both the model and the prototype water supplies are from large reservoirs with presumably similar air content and water quality.

The most crucial scale effects influencing closed conduit cavitation studies are those associated with size and velocity (5,8,10,12,13). Scale effects associated with size and velocity (or pressure) are shown to be independent, and are not properly accounted for by the Reynolds number. Investigating these scale effects for the elbow was considered of prime importance.

## MODEL

The capabilities of the Hydro Machinery Laboratory at Colorado State University dictated that the largest model size that could be tested at prototype pressure and velocities was a valve with a 12-in. (305-mm) diameter inlet. This resulted in a model scale of 1.0:5.33. For determining size scale effects considerable information was currently available for orifices (1,10,12) and valves (13), but no similar information was available for the elbow. Consequently, the decision was made to conduct size scale effects tests on 3-in. (76-mm), 6-in. (15-mm), and 12-in. (30-mm) geometrically similar elbows. The size scale effects data available from current literature and from the tests on the three elbow sizes would provide enough information to confidently scale the model data.

The model was designed and built to insure geometric similarity of the flow passages from the bellmouth entrance at the forebay to the discharge into shaft 18. The forebay and downshaft were not modeled geometrically similar to the prototype but were built so that the proper flow and velocity conditions could be provided at the elbow and valve. The model is shown in Fig. 1.

The bellmouth was fabricated of plexiglass. A standard 12-in. (305-mm) inside diameter long radius elbow was used to simulate the 64-in. (1,626-mm) diameter prototype elbow which produced the model scale of 1.0:5.33. Piezometers were installed on the inner and outer curves of the elbow at each ten degrees between 5° and 85°.

The conical plug of the model valve was fabricated from steel plate of various thicknesses rolled into conical sections and welded together. The body of the valve was also fabricated of steel and machined to proper tolerances. The air injection port on the outlet side of the valve was properly reproduced. A manual gear operator was utilized for positioning the valve, and a position indicator was mounted on top of the valve stem. Sealing surfaces were built up with epoxy and machined to proper contours and clearances. All wetted surfaces were covered with epoxy paint to prevent corrosion.

For the size scale effects studies on the long radius elbow, piping arrangements similar to that shown in Fig. 1 were also fabricated for the 3- and 6-in. (76- and 152-cm) elbows. For these smaller models, geometric similarity was main-

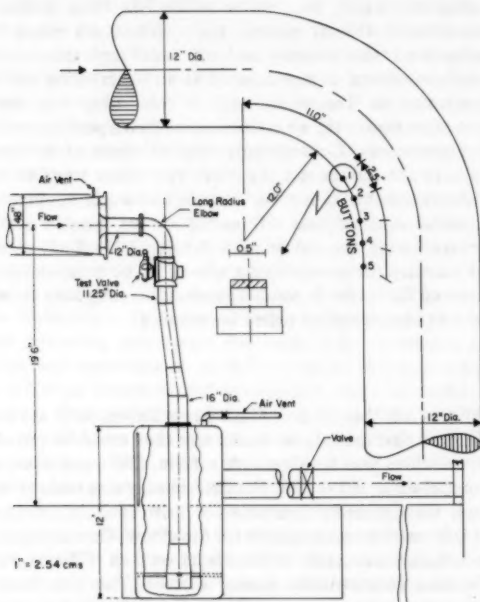


FIG. 1.—Experimental Facility

tained from the bellmouth entrance to the exit of the vertical pipe discharging from the elbow.

Water was supplied to the model from a large reservoir with a shut-off head in excess of 200 ft (61 m). Flow was controlled by 24-in. (610-mm) valves located upstream and downstream from the model, and was measured with calibrated orifice meters. The forebay was simulated with a settling chamber which expanded from 18-in. (457-mm) at the inlet to 48-in. (1,219-mm) at the bellmouth. The pressure in the settling chamber was varied to simulate elevation of the reservoir. At low water surface elevations, the water level in the downshaft

was simulated by an open water surface in the discharge tank. For higher water levels, the tank was pressurized.

#### DEFINITIONS AND PROCEDURES

Cavitation is a stochastic process, and its occurrence is associated with both the mean and the fluctuating properties of the flow. Consequently, no deterministic method can be utilized to evaluate various cavitation limits, such as incipient or incipient damage. One must, therefore, develop a method of averaging or statistical analysis. Directly related to this problem is selection of a test procedure, instrumentation for properly detecting cavitation, and analysis method for minimizing the problem of scale effects.

In approaching this research project three tasks were defined: (1) Determine what cavitation levels were of interest, and determine how these levels would be defined; (2) develop a test procedure and instrumentation for evaluating the cavitation limits; and (3) establish a method of analysis with particular emphasis on determination of the scale effects so that the model data could be scaled to the prototype.

Four cavitation limits were considered as a part of this study: incipient, critical, incipient damage, and choking. Incipient cavitation identifies early stages of cavitation, where the noise is light and intermittent. To determine this condition by ear, one must listen carefully for the light crackling sounds caused by individual cavitation events. At incipient cavitation the magnitude of the noise and vibrations would be negligible and the possibility of damage would be remote. It is considered to be a conservative design limit, and would not be recommended for most installations.

Critical cavitation represents a condition just beyond incipient, where the cavitation events are steady, but the noise level is still light. At critical, the cavitation does not cause any objectionable vibration or noise, and the possibility of cavitation damage is remote. This limit is recommended by the author as a reasonable design limit for essentially cavitation-free operation. Incipient damage is that condition at which pitting of the solid boundaries first begins. By definition, it is the condition in which the maximum local pitting rate is 1 pit/sq in./min on soft aluminum. Choking cavitation occurs when the mean pressure downstream from the control drops to vapor pressure and the maximum flow is reached for a given upstream pressure condition.

**Incipient and Critical Cavitation.**—The definitions of incipient and critical cavitation are associated with the number and intensity of individual cavitation events. Therefore, an evaluation of these limits can be based on a device that detects the number of events per unit time or displays an integrated output from some sensor, which detects the number and intensity of events. Many different types of instrumentation systems can be utilized to detect cavitation. These techniques can vary from sophisticated systems, such as a focused hydrophone (3), to a simple system, such as the human ear. The instrumentation system desired depends upon the type of information required. For example, the focused hydrophone (3) is useful in giving not only the flow conditions at which cavitation begins, but specifically identifying the zone where the cavitation occurs. If the exact location of cavitation is not of concern, considerably simpler systems can be employed. On the basis of previous investigations (14),

it was decided to utilize an accelerometer to detect cavitation for this model study. The sensor consists of a piezoelectric crystal, which is sensitive to vibrations of the system caused by flow disturbances or cavitation events. The accelerometer output can be handled in a number of ways including filtering out the background disturbances. However, for studies in systems where the background noise level is considerably less than the cavitation intensity, a simple averaging of the accelerometer output has been found to be adequate. The general procedure is to measure an average accelerometer output at closely spaced cavitation levels and display this information graphically to determine incipient and critical cavitation.

Several methods can be used to average the output of the accelerometer. The simplest is to merely average the fluctuating meter reading by eye. More sophisticated methods include using an averaging rms volt meter or numerically averaging with an A-D system and a computer. Several methods have been used by the author and the results found to be comparable.

The average accelerometer output is plotted against either  $\sigma$  on semilog paper or against velocity on log-log paper (14). Breaks between straight line segments of the data define inception and critical cavitation.

**Incipient Damage.**—A method for evaluating incipient damage was first developed by Knapp (6). It consists of installing soft aluminum strips in the cavitation damage zone, operating the system at a known cavitation level for a specified length of time, removing the aluminum specimen, and determining the maximum pitting intensity. This technique has been applied to determining incipient cavitation damage for valves (8) and sudden enlargements formed by placing nozzles and orifices (1,10,11) in a pipeline. The procedure consists of first determining the location of the damage and then measuring the maximum local pitting for several levels of cavitation from no damage to heavy damage. The maximum local pitting rate is then plotted on semilogarithmic paper as a function of the velocity for a constant upstream pressure. The result usually produces a linear relationship between the log of the pitting rate and the velocity. Incipient damage  $\sigma_{id}$  is then evaluated from the magnitude of the velocity and pressure at 1 pit/sq in./min (64 pits/mm<sup>2</sup>/min).

This procedure was applied to the elbow to evaluate incipient damage (2). The zone of cavitation damage was identified by inspecting the elbow after it has been operated for several weeks. Because of the complex contours of the elbow round aluminum buttons were used rather than the strips.

**Choking Cavitation.**—The procedure normally used for evaluating choking cavitation is to test at a constant upstream pressure and increase the discharge through the test component by lowering the downstream pressure in increments until the pressure immediately downstream from the test device dropped to vapor pressure. When this occurs further changes in the pressure conditions downstream do not increase the flow. This condition can also be observed if there is a viewport downstream from the test device. At choking, the separation region around the jet is filled with mostly water vapor and gives the appearance of a valve discharging into the atmosphere.

## EXPERIMENTAL RESULTS

**Incipient and Critical Cavitation.**—The method used to evaluate incipient and critical cavitation for the elbow is demonstrated in Fig. 2. This figure is a

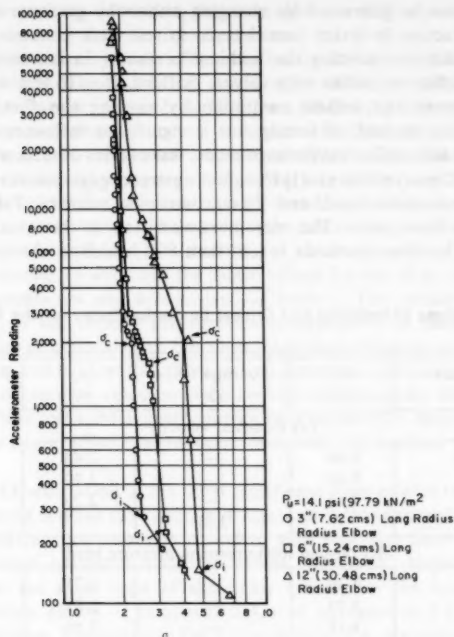


FIG. 2.—Determination of Incipient and Critical Cavitation Conditions

graphical display of the average accelerometer output at different values of  $\sigma$  for the 3-, 6-, and 12-in. (76-, 150-, and 305-mm) elbows all tested with a constant total upstream pressure head of 14.1 psi (97.29 kN/m<sup>2</sup>). These tests represent a constant upstream reservoir level. Displaying the data on a log-log plot (Fig. 2) has proven to be convenient for identifying these two limits. For most valves, elbows, and pipeline components, sharp breaks have been found in the slope of the curves which identify incipient ( $\sigma_i$ ) and critical ( $\sigma_c$ ). At velocities less than incipient (large  $\sigma$ ), the increase in accelerometer output as  $\sigma$  reduces is due to increased turbulence of the flow due to increased velocity or noise generated by the control valves. Once cavitation events begin, a large increase in the output of the accelerometer is observed for only slight decreases in  $\sigma$ . The intersection of these two straight lines (Fig. 2) defined  $\sigma_i$ . At critical cavitation, the rate of increase of noise suddenly decreases and produces a second break in the curve. The aural cavitation level at these two break points corresponds to those conditions previously described. It is also possible to evaluate choking conditions from these curves. It corresponds to the condition where the peak accelerometer reading occurs. This however is not the preferred method of evaluating choking, but it does produce values close to those evaluated from other methods.



Cavitation can be generated by changing either the pressure or velocity. It is common practice in water tunnel tests to test at a constant velocity and initiate cavitation by reducing the ambient pressure. In contrast, it has been a common practice in studies with valves, orifices, etc., to test with a constant upstream pressure and initiate cavitation by varying the flow velocity. To determine if the method of testing has a significant influence on the value of the incipient and critical cavitation indices, three series of tests were conducted on the 6-in. (152-mm) elbow at: (1) Constant upstream gage pressure; (2) constant total upstream pressure head; and (3) constant pipe velocity. Table 1 contains the data from these tests. The maximum variation in the average values of  $\sigma_i$  and  $\sigma_c$  for the three methods is less than 8%, which is about the accuracy

TABLE 1.—Values of Incipient and Critical Cavitation Index for the 6-Inch Elbow

Test condition (1)	$\sigma_i$ (2)	Average for $\sigma_i$ (3)	$\sigma_c$ (4)	Average for $\sigma_c$ (5)
(a) Constant velocity				
60 ft/sec	3.40	—	2.40	—
50	3.60	—	2.70	—
40	3.60	—	2.70	—
		3.53		2.60
(b) Constant total upstream pressure head				
14.1 psi <sup>2</sup>	3.30	—	2.75	—
25.0	3.20	—	2.85	—
40.0	3.15	—	2.50	—
60.0	3.40	—	2.50	—
		3.26		2.65
(c) Constant upstream gage pressure				
5 psi	3.35	—	2.75	—
15	3.20	—	2.80	—
25	3.35	—	2.70	—
		3.30		2.77

<sup>1</sup> 1 ft/sec = 305 mm/s.

<sup>2</sup> 1 psi = 6.9 kN/m<sup>2</sup>.

of the experimental method. It was concluded after analyzing all the data that the values of  $\sigma_i$  and  $\sigma_c$  are not significantly influenced by the method of testing. One is, therefore, at liberty to use the one most convenient for the experimental facility.

**Pressure and Velocity Scale Effects.**—There was no compelling reason to be concerned about pressure or velocity scale effects for this model study since tests were conducted at prototype pressure and velocity conditions. However, to provide information useful for other applications, it was decided to study scale effects.

Pressure and velocity scale effects are not independent. They merely represent two different test procedures. For this study, they were both evaluated by



separate tests to help document that it makes no difference if cavitation is controlled by varying the velocity or pressure.

Results of the velocity scale effect studies for the 6-in. (152-mm) elbow are shown in Table 1. The values of  $\sigma_i$  and  $\sigma_c$  at 40 ft/sec (12.2 m/s) and 50 ft/sec (15.25 m/s) are identical. At 60 ft/sec (18.3 m/s) both values decreased slightly. It was not possible to test at higher velocities in the 6-in. (152-mm) pipe, and, therefore, it was not determined specifically if the variation was related to experimental accuracy or if it was an indication of a velocity scale effect at high velocities. However, based on additional tests and the fact that the  $\sigma$  variation was about the same as the uncertainty of the experimental procedure, it was concluded that there is not a velocity scale effect.

Tests conducted to evaluate the scale effect for the 6-in. (152-mm) elbow based on pressure are also summarized in Table 1. The variation in the values of  $\sigma_i$  and  $\sigma_c$  at the various pressure levels appear to be random. Numerous tests were also conducted with the 12-in. (305-mm) elbow at various pressures. For all tests, it was evident that there was no consistent variation of the cavitation limits with pressure or velocity. Such results are consistent with experimental work on orifices and sudden enlargements in pipelines (12). In contrast, pressure and velocity scale effects have been observed for various types of values (13,14,16).

**Size Scale Effects.**—One of the most significant scale effects found experimentally with closed conduit cavitation investigations is that associated with variation in size. Significant variations in  $\sigma_i$  and  $\sigma_c$  with pipe size have been found for orifices, sudden enlargements, and valves (12,13,15). Inspection of Fig. 2 demonstrates the same type of size scale effects for the long radius elbow. For the smallest elbow,  $\sigma_i$  is approx 2.4, and increases to 3.2 and 4.6 for the two larger elbows, respectively. For a size ratio of 1:4, the value of the incipient cavitation index almost doubles.

From the study, the experimental data, summarized in Table 2, were used to develop the following empirical relationships, which express the variations of  $\sigma_i$  and  $\sigma_c$  with elbow diameter.

$$\sigma_i = 1.44 \times D^{0.46}, \quad D \text{ in inches} \quad \dots \dots \dots (2)$$

$$\sigma_c = 1.38 \times D^{0.40}, \quad D \text{ in inches} \quad \dots \dots \dots (3)$$

These equations were evaluated by fitting an exponential equation to the data summarized in Table 2. The average values of  $\sigma$  for each pipe size were used to develop the equations.

Since there are no pressure or velocity scale effects, the prediction of  $\sigma_i$  and  $\sigma_c$  for any size geometrically similar elbow can be obtained directly from Eqs. 2 and 3. One limitation on these equations is that the elbow operated with a uniform approach velocity profile provided by the upstream chamber and nozzle. For fully developed flow approaching the elbow the value of  $\sigma_i$  and  $\sigma_c$  should be somewhat smaller. If the approach flow is disturbed by other elbows or other components, cavitation will probably occur at values of  $\sigma$  greater than those calculated by Eqs. 2 and 3.

In applying the size scale effect equations it is important to realize that the equations are inherently conservative. This is because of the way incipient and critical cavitation are defined. They are defined based on an absolute number

of cavitation events rather than on events per unit area or per unit volume of the pipe. Dynamic similarity would imply that the same percentage of nuclei would be cavitating in systems of different size. As a result, if one compared the cavitation conditions for a 3-in. (76-mm) and a 12-in. (305-mm) pipe with the same percentage of nuclei per unit volume of water growing into vapor cavities, and the velocity of flow were the same in both pipes, the larger system would be expected to have 16 times as many cavitation events per unit of time as the small one. The definition of inception as defined in this article requires both systems to operate at approximately the same number of events per unit of time. This forces the larger system to operate at a larger value of  $\sigma$ . This means that the incipient and critical cavitation conditions for different size pipes will sound about the same intensity but for a larger system the potential for vibration and erosion damage is less because there are fewer events per unit volume of flow.

TABLE 2.—Pressure Scale Effects Results

Size, in inches <sup>1</sup> (1)	$P_u$ , in psi <sup>2</sup> (2)	$\sigma_i$ (3)	$\sigma_c$ (4)	$\sigma_{ch}$ (5)
3	14.1	2.40	2.25	1.88
	25.0	2.40	2.20	1.88
	40.0	2.40	2.25	1.88
	60.0	2.40	2.30	1.92
6	14.1	3.30	2.75	1.87
	25.0	3.20	2.85	1.90
	40.0	3.15	2.50	1.93
	60.0	3.40	2.50	1.94
12	14.1	4.60	4.00	1.88
	25.0	4.60	4.00	—
	40.0	4.50	3.70	—

<sup>1</sup> 1 in. = 25.4 mm.

<sup>2</sup> 1 psi = 6.9 kN/m<sup>2</sup>.

It is important to realize that this does not account for all of the size scale effects. Larger systems operating at the same  $\sigma$  definitely produce more and a heavier degree of cavitation. For example, see Fig. 2 where  $\sigma$  equals 2.4. The 3-in. (76-mm) elbow is operating at inception and the accelerometer output is 320. The 6-in. (152-mm) is operating beyond  $\sigma_c$ , and the accelerometer level is about 2,400. The 12-in. (305-mm) is operating far beyond  $\sigma_c$ , and the accelerometer level is 11,000. The three cavitation levels, by ear, would probably be classified as very light, moderate, and heavy, respectively.

**Incipient Cavitation Damage.**—After several months of testing on the model elbow, it was removed and inspected for zones of cavitation damage. The interior of the elbow had been painted to protect against corrosion. Significant paint removal was observed on the inner curve of the elbow approx 90° from the inlet. Some of the paint was definitely removed by cavitation since pitting of the exposed steel was also observed.

To determine the incipient damage condition for the elbow and investigate

pressure scale effects, aluminum buttons were installed in the elbow in the zone of cavitation damage. The location and configuration of the buttons are shown in Fig. 1. The zone of maximum cavitation damage observed in the elbow was between locations 3 and 5 in Fig. 1.

Cavitation damage tests were conducted only with the 12-in. (305-mm) diameter elbow. Tests were carried out at three values of constant total upstream pressure, 5, 10, and 14.1 psi (34.5, 69, and 14.1 kN/m<sup>2</sup>). The variation of damage rate as a function of velocity is shown graphically in Fig. 3. With the semilogarithmic plotting, a linear variation in damage with increasing velocity is observed. This result is consistent with prior studies on valves, orifices, and sudden enlargements (1,8,10,11). At the defined incipient damage point of 1 pit/sq in./min on soft aluminum, the incipient damage condition,  $\sigma_{id} = 2.2$  for all pressures, indicating that there is no pressure scale effect.

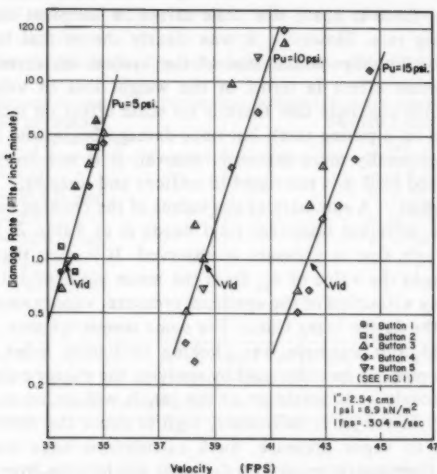


FIG. 3.—Determination of Incipient Damage Conditions

Prior tests on orifices and nozzles have shown slight pressure scale effect on  $\sigma_{id}$  (10,11). The work on the orifices and nozzles was more extensive and was carried out over a wider range of conditions. It is, therefore, possible that if a continuous strip of aluminum had been used in the elbow so the exact location of inception could have been determined, and, if the range of conditions had been increased, a slight pressure scale effect might have been found for the elbow. However, even for the orifice and nozzle, the pressure scale effect or incipient damage was rather minor.

The steepness of the slope of the lines in Fig. 3 is an indication of the sensitivity of damage rate to velocity. For example, increasing the velocity 10% beyond incipient damage increases the pitting rate by approx 20 times. It is, therefore, important to select an incipient damage value that is conservative

and not operate beyond that condition. The incipient damage definition of 1 pit/sq in./min on soft aluminum appears to provide the proper degree of conservatism. Prior tests on incipient damage in orifices (11) compared the damage rate of soft aluminum and mild steel at the incipient damage condition. A mild steel specimen was run for a 12-hr period at incipient damage, and the pitting rate was determined. The total number of pits which would have occurred on the aluminum specimen over the same amount of time was approx 150 times as many as were observed on the steel. This implies two things: first, the incipient damage definition is conservative since harder materials will experience far less damage; second, the definition is a good measure of incipient damage since even the harder materials experience some damage at that condition.

No size scale effects information was obtained during this research project. The only information currently available is for orifices and sudden enlargements in 3-, 6-, and 12-in. (76-, 152-, and 305-cm) diameter pipelines (1,10). These results show that there is not a size scale effect on incipient damage defined in terms of pitting rate. However, it was clearly shown that the size of the pits increased significantly as the size of the system increased. This would produce a size scale effect in terms of the weight loss of volume removal. These studies (1,10) conclude that there is no scale effect on incipient damage (as defined based on a pitting rate), but once damage begins the larger systems experience proportionally more material removal. It is not known if this can be generally applied or if it is restricted to orifices and nozzles.

**Choking Cavitation.**—A summary of the values of the choking cavitation index for the elbows at different upstream total heads is in Table 2. No consistent variation of  $\sigma_{ch}$  with size or pressure is observed. It is seen that there is less than 2% variation in the value of  $\sigma_{ch}$  from the mean value of 1.9. The choking condition is strictly a function of the upstream pressure, vapor pressure, velocity, and geometry of the device being tested. For some simple systems, this condition can be calculated. For example, the choking cavitation index for a nozzle discharging into a pipe can be calculated by applying the energy equation between the inlet to the nozzle and the throat of the jet. It will occur at the condition when the velocity of the jet is sufficiently high to cause the mean downstream pressure to drop to vapor pressure. Such calculations have been made and compared with experimental results (9) for a jet discharging from a nozzle and found to produce the same value of  $\sigma_{ch}$ . The difficulty in using that approach with most flow devices is that one is not sure of the cross sectional area of the jet at its vena contracta, and, consequently, one is not able to know the local maximum velocity. As a result,  $\sigma_{ch}$  must be determined experimentally.

#### APPLICATION OF DATA TO PROTOTYPE

Predictions of the prototype performance of the long radius elbow are summarized in Table 3. The data used as a reference are those data obtained from the 12-in. (305-mm) model using  $P_v = -12.2$  psi ( $-84.18$  kN/m<sup>2</sup>) and  $P_u = 14.1$  psi (97.29 kN/m<sup>2</sup>).  $P_u$  is the total upstream pressure head. The values of  $\sigma_i$  and  $\sigma_c$  for the prototype elbow were calculated using Eqs. 2 and 3, respectively.  $\sigma_{id}$  and  $\sigma_{ch}$  for the prototype elbow are identical to the model elbow since there are no size scale effects for these two cavitation limits. The values of the velocity for the prototype elbow were calculated using the definition

of  $\sigma$  with  $P_v = -14$  psi ( $-96.6$  kN/m<sup>2</sup>) and  $P_u = 14.1$  psi ( $97.29$  kN/m<sup>2</sup>).

The magnitude of the size scale effects on incipient and critical cavitation are easily observed by comparing the incipient and critical velocities for the two elbows. The size scale effects reduce the incipient and critical velocities by 29 and 24%, respectively, from the experimental values obtained with the 12-in. (305-mm) model. Ignoring the size scale effect for this study would have resulted in serious errors.

Analysis of the Kensico control structure for one valve fully open predicts that the long radius elbow would choke and establish a mean pipe velocity of 48.4 ft/sec (14.72 m/s). This was considered unacceptable and various schemes were considered to either reduce the cavitation or restrict operation of the system to an acceptable level. A description of these efforts is included in the project report (17).

Even though this study has evaluated four cavitation limits for the elbow, one must still use subjective judgement in selecting a safe operating condition.

TABLE 3.—Prototype Cavitation Characteristics Based on Model Scale Effects Tests

12-inch model (1)	64-inch prototype (2)
$\sigma_i = 4.57$	$\sigma_i = 9.75$
$V_i = 30.1$ ft/sec	$V_i = 21.4$
$\sigma_c = 3.9$	$\sigma_c = 7.28$
$V_c = 32.6$ ft/sec	$V_c = 24.7$
$\sigma_{id} = 2.2$	$\sigma_{id} = 2.2$
$V_{id} = 43.4$ ft/sec	$V_{id} = 45.0$
$\sigma_{ch} = 1.90$	$\sigma_{ch} = 1.9$
$V_{ch} = 46.7$ ft/sec	$V_{ch} = 48.4$

Notes:  $\sigma = P_u - P_v / \rho V^2 / 2$ .  $P_v = 12.2$  psi ( $-84.18$  kN/m<sup>2</sup>) for all model data.  $P_v = -14$  psi ( $-96.6$  kN/m<sup>2</sup>) for all prototype data.  $P_u = 14.1$  psi ( $97.29$  kN/m<sup>2</sup>) (total pressure head) for all velocity calculations. 1 in. = 25.4 mm. 1 ft/sec = 305 mm/s.

The region of uncertainty lies between critical and incipient damage. Table 3 shows that for the 64-in. (1,626-mm) elbow the velocity increases almost 100% between  $V_c$  and  $V_{id}$ . Most installations operating at  $V_c$  or  $\sigma_c$  would be too conservative. The decision must, therefore, be made as to how far beyond critical levels the system can operate successfully. In a large system, it is likely that the noise and vibrations would become intolerable before damage begins. More research is needed to quantify this point. As of now, one must arbitrarily decide how far beyond critical cavitation one dares operate.

## CONCLUSIONS

1. Using model cavitation data to predict prototype performance requires that the influence of scale effects be determined experimentally. The intensity of cavitation at a constant  $\sigma$  value generally increases with increased size, pressure, or velocity.

2. For the long radius elbow, the value of the cavitation index,  $\sigma$ , evaluated

at incipient, critical, incipient damage, or choking cavitation does not vary with velocity or pressure.

3. The cavitation index at incipient and critical cavitation increases significantly with elbow size as shown by Eqs. 2 and 3. The choking cavitation index was found to be independent of size. No study was made of size scale effects on incipient damage.

4. The critical cavitation limit is suggested as the practical design value for essentially cavitation-free operation. The incipient point is too conservative.

5. For most systems, the practical design limit lies between critical and incipient damage. As one operates beyond  $\sigma_c$ , the noise and vibrations increase rapidly. More research is needed to quantify acceptable noise and vibration levels and their dependence on velocity and size.

6. The model study determined that the velocities through the prototype system were sufficient to cause the elbows to operate in choking cavitation. A second phase of the study was conducted to investigate means of extending the non-cavitating range of the elbows and other problems uncovered by the model study.

#### APPENDIX I.—REFERENCES

1. Ball, J. W., Tullis, J. P., and Stripling, T., "Predicting Cavitation in Sudden Enlargements," *Journal of the Hydraulics Division*, ASCE, Vol. 101, No. HY7, July, 1975, pp. 857-870.
2. Baquero, F., "Cavitation Damage in Elbows," thesis presented to Colorado State University, at Ft. Collins, Colo., in 1977, in partial fulfillment of the requirements for the degree of Master of Science.
3. Daily, J. W., and Baller, H., "Cavitation Noise from Underwater Projectiles," *Hydro Machinery Laboratory Report No. 26*, California Institute of Technology, Mar., 1945.
4. Hammitt, F. G., "Cavitation Damage Scale Effects—State of Art Summarization," *Journal of the International Association of Hydraulics Research*, Vol. 13, No. 1, 1975, pp. 1-17.
5. Holl, J. W., and Wislicenus, G. F., "Scale Effects on Cavitation," *Journal of Basic Engineering, Transactions, American Society of Mechanical Engineers*, Sept., 1961, pp. 385-398.
6. Knapp, R. T., "Recent Investigations of the Mechanics of Cavitation and Cavitation Damage," *Transactions, American Society of Mechanical Engineers*, Oct., 1955, pp. 1045-1054.
7. Knapp, R. T., Daily, J. W., and Hammitt, F. G., "Cavitation," McGraw-Hill Book Co., Inc., New York, N.Y., 1970, 578 pp.
8. Rahmeyer, W. J., "Cavitation Pressure Scale Effects and Damage for Butterfly Valves," thesis presented to Colorado State University, at Ft. Collins, Colo., in 1975, in partial fulfillment of the requirements for the degree of Master of Science, 63 pp.
9. Smith, P. E., "Supercavitation in Pipe Flow," thesis presented to Colorado State University, at Ft. Collins, Colo., in 1976, in partial fulfillment of the requirements for the degree of Master of Science.
10. Stripling, T. E., "Cavitation Damage Scale Effects: Sudden Enlargements," thesis presented to Colorado State University, at Ft. Collins, Colo., in 1975, in partial fulfillment of the requirements for the degree of Doctor of Philosophy, 135 pp.
11. Sweeney, C. E., "Cavitation Damage in Sudden Enlargements," thesis presented to Colorado State University, at Ft. Collins, Colo., in 1974, in partial fulfillment of the requirements for the degree of master of Science, 81 pp.
12. Tullis, J. P., and Govindarajan, R., "Cavitation and Size Scale Effects for Orifices," *Journal of the Hydraulics Division*, ASCE, Vol. 99, No. HY3, Mar., 1973, pp. 417-430.
13. Tullis, J. P., "Cavitation Scale Effects for Valves," *Journal of the Hydraulics Division*, ASCE, Vol. 99, No. HY7, July, 1973, pp. 1109-1128.

14. Tullis, J. P., "Testing Valves for Cavitation," *Proceedings of the Conference on Cavitation*, held in Edinborough, Scotland, Institute of Mechanical Engineers, London, Sept., 1974.
15. Tullis, J. P., and Ball, J. W., "Cavitation Data for Valves and Its Application," *Proceedings of the Conference on Cavitation*, held in Edinborough, Scotland, Institute of Mechanical Engineers, London, England, Sept., 1974.
16. Tullis, J. P., Ball, J. W., and Rahmeyer, W. J., "Report of Model Tests for the Improvement of Flow Control at Kensico South Effluent Chamber of the Delaware Aqueduct," prepared for the Board of Water Supply of the City of New York, Hydro Machinery Laboratory Report No. 68, Colorado State University, Ft. Collins, Colo., Oct., 1976.
17. Tullis, J. P., "Report on Model Tests for the Improvement of Flow Control at Kensico South Effluent Chamber of the Delaware Aqueduct: Phase 2," prepared for the Board of Water Supply of the City of New York, Hydro Machinery Laboratory Report No. 97, Colorado State University, Ft. Collins, Colo., Nov., 1978.

## APPENDIX II.—NOTATION

*The following symbols are used in this paper:*

- $c$  = critical;
- $ch$  = choking;
- $D$  = elbow diameter;
- $i$  = incipient;
- $id$  = incipient damage;
- $P_u$  = total pressure head upstream from elbow;
- $P_v$  = liquid vapor pressure;
- $V$  = mean pipe velocity;
- $\rho$  = liquid density; and
- $\sigma$  = cavitation index.





## PHYSICAL MODELING OF ROTTERDAMSE WATERWEG ESTUARY

By Herman N. C. Breusers<sup>1</sup> and Ad G. van Os<sup>2</sup>

### INTRODUCTION

Modeling estuaries, as characterized by the complex interaction of river discharge, tidal movement, and density differences, is still a difficult operation. Exchange of information on the experience with hydraulic scale models of estuaries therefore seems necessary and useful. The model of "Europoort" and the "Rotterdamse Waterweg" estuary has a long history and was therefore subjected to a far-reaching evolution in the philosophy of estuarine models. Improvement in knowledge of the hydrodynamic phenomena and technical possibilities has resulted in major changes in the model and its operation.

The present contribution describes both this evolution and the final state of the model, together with the related aspects of calibration, verification, operation, and data processing. The model was built and operated by the Delft Hydraulics Laboratory under contract by Rijkswaterstaat, Ministry of Transport and Public Works, which not only provided the necessary funds but also closely participated in the design and calibration of the model and provided field data and technical assistance.

### PROBLEM STATEMENT: PURPOSE OF MODEL

**Problem Statement.**—The continuous extension of the Rotterdam harbor culminated in the construction of the Europoort harbor, situated at the seaboard end of the Rotterdamse Waterweg, one of the branches of the Rhine River. The increase in size of oil tankers and ore carriers called for the construction of a deep water port close to the sea. This was realized by building a harbor basin with a new inlet on the tidal flats south of the existing entrance of the Rotterdamse Waterweg (Fig. 1).

As large tankers and ore carriers are greatly affected by cross currents during

<sup>1</sup>Coordinator of Basic Research, Delft Hydraulics Lab., Delft, The Netherlands.

<sup>2</sup>Head, Density Currents and Transport Phenomena Branch, Delft Hydraulics Lab., Delft, The Netherlands.

Note.—Discussion open until April 1, 1982. Separate discussions should be submitted for the individual papers in this symposium. To extend the closing date one month, a written request must be filed with the Manager of Technical and Professional Publications, ASCE. Manuscript was submitted for review for possible publication on March 9, 1981. This paper is part of the Journal of the Hydraulics Division, Proceedings of the American Society of Civil Engineers, ©ASCE, Vol. 107, No. HY11, November, 1981. ISSN 0044-796X/81/0011-1351/\$01.00.

their stopping and entrance maneuvers, a careful study of the flow field was required. The first harbor basins had to be used in the early stages of the harbor construction with a temporary entrance. For that reason, means had to be provided to evaluate the changes in the flow field due to the construction of the harbor moles and to prepare the harbor pilots for these changes. Also, changes in the inner part of the harbor area had to be studied with respect to their influence on navigation.

The increase in harbor area and the continuous deepening of the estuary to provide sufficient sailing depth was detrimental to the salinity intrusion. The Rhine River already carries large amounts of salt from the mines in France and Germany which causes high salinity levels during low river flows. Any additional increase in salinity due to intrusion from the sea is harmful to the existing water inlets in and east of Rotterdam. These inlets provide water for

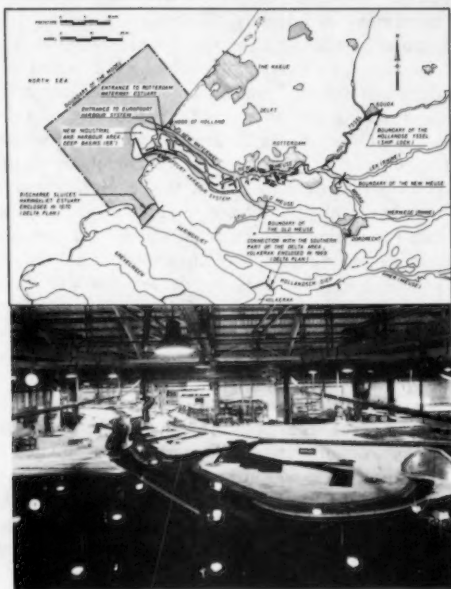


FIG. 1.—General Information

households, industry, and agriculture—i.e. for flushing the polders in the western part of the Netherlands which lie up to 6 m below sea level and suffer from saline seepage.

Before the construction of Europoort harbor, a critical situation was already extant so that further salinity intrusion had to be avoided and salinity intrusion had to be reduced, if possible. The increasing salinity intrusion and the extension of harbor facilities also caused an increase in siltation. Present dredging activities are in the order of 20,000,000 m<sup>3</sup> annually. The dumping of the spoil causes

problems because the spoil is strongly polluted by heavy metals such as PCB, due to the discharge of industrial effluents in the Rhine.

With reference to these problem areas, the following aspects have to be covered by a model:

1. Navigational aspects: reproduction of the flow field, both depth averaged and vertical flow distribution.
2. Salinity intrusion: reproduction of salinity distribution under the influence of tides and river discharges; possibilities of reducing salinity intrusion.
3. Transport of pollutants and silt; possibilities of reducing siltation.

This requires the reproduction of the driving mechanisms tidal movement, river discharge, and density difference between sea and river water, with resulting flow phenomena such as: (1) Tidal elevation and currents, displacing and mixing water masses; (2) estuarine circulations induced by density differences; (3) mixing by turbulence generated by bed shear and wall roughness (groynes, harbor entrances), and mixing due to exchange currents between harbors and estuary and the confluence of tidal branches; and (4) erosion, transport, and deposition of sediments. It will be clear that no model provides an exact reproduction of all relevant phenomena. A discussion of reproductive capabilities and possible scale effects will therefore be necessary.

The required accuracy of a model in the reproduction of natural phenomena will depend on the type of investigation. Three are considered:

1. Comparative tests, in which various alternatives are compared mutually or with the original situation; the required accuracy will be determined by the detectability of changes in practice. Moreover, this type of test requires a very easy and stable model control.
2. Absolute tests, in which velocity and salinity have to be predicted for a certain condition (tide, river discharge) at a certain location; here the accuracy of the model results will depend also on the measurability of the present situation in nature because this determines the accuracy of the model calibration.
3. Fundamental research, or giving information to improve the understanding of physical phenomena which is necessary to develop both hydraulic (scale) models and mathematical models. The accuracy of the results must be sufficient to detect the effect of the various parameters during this type of research.

#### RELATION TO OTHER SOLUTION METHODS

In general, the following methods are available:

1. Field studies.
2. Physical (scale) models.
3. Mathematical (analytical and numerical) models.

For all methods, information on accuracy, possibilities, and limitations is required. Each method has to start with a definition and schematization of the problem area, and boundary conditions have to be defined.

Salinity intrusion in estuaries is the result of a complicated interaction between

several mechanisms. Both mathematical and scale models have to be validated by field data. However, each method is limited, so that in general only a combination of all methods will lead to results. In the case of field data, information can be obtained only for the existing situation. Systematic changes in the variables (depth etc.) are not possible. Sufficiently complete sets of field data are essential for obtaining physical insight. Mathematical models are based on the knowledge of the physical processes involved such as turbulent mixing, boundary resistance, etc. Their predictive ability depends on the degree of schematization of the physical processes. The ideal model is a three-dimensional one with a good turbulence modeling, representing the influence of density differences on the turbulence structure as well. This type of model has not yet left the research stage and is presented only for ideal situations, for example with a simple representation of the eddy viscosity (5,8).

Two-dimensional models (two horizontal space dimensionals) cannot be used here because the estuary is partly mixed and an accurate representation of the salinity and velocity distribution is required. Moreover, these models are limited in reproducing areas with recirculating flows and, in general, turbulence generated by shear stress in a vertical plane. These models are useful, however, in providing boundary conditions for scale models. Two-dimensional models (one horizontal, one vertical space dimension) are being developed with reasonable success (4,9) for estuaries in which lateral variations are insignificant. In these models an empirical correction for the influence of stratification on the mixing length of eddy viscosity is used; their predictive ability is therefore limited. Application for the present estuary is questionable, due to the effects of groynes, harbors, and a confluence of two branches which can be introduced only as lumped parameters. The model therefore cannot predict effects of changes in wall roughness, harbor configuration, etc., but can be useful to obtain more insight into the physical phenomena.

In one-dimensional models, the effect of velocity and density distribution is very crudely reproduced by a dispersion coefficient. This means that the effect of highly two or three-dimensional mechanisms (e.g. gravitational circulation, exchange with harbors, or lateral irregularities) has to be schematized by a gradient-type dispersion modeling. Tuning of the model constants on a range of prototype measurements is therefore essential. Even then, however, the predictive capacity of this kind of model is very limited (6). These models can be used, however, to obtain boundary conditions for the inland boundaries of the model, if the scale model does not cover the whole area with tidal influences.

Summarizing, it can be said that mathematical models do not yet yield the possibilities to predict the flow velocity and salinity field in sufficient detail. Therefore, the main tool for estuarine problems at present is the physical (scale) model, although this type of model also has certain limitations (effects of distortion and Reynolds number).

For the study of transport of pollutants and sediments the situation is different. The initial stages (near field) of pollution dispersion generally cannot be modeled properly in a distorted physical model, while sediment transport characteristics like flocculation, erosion, etc., are difficult to model physically. However, if the three-dimensional velocity field is known, a fair prediction of pollutant concentration is possible if a reasonable value of the diffusion coefficient can

be given, because in many cases the influence of advection is predominant. The knowledge of the physical processes of sediment transport is so limited that reproduction, both in mathematical and scale models, is based on empirical knowledge only so that no preference can be expressed for any of these methods.

#### MODEL DESIGN AND CONSTRUCTION

**Introduction.**—In discussing the present Europoort model it must be realized that the first design was made in 1965, when the available knowledge (physical processes and field data) and the technical tools (instrumentation and mathematical models) were far less available than at present. In 1974 it was decided to construct a new sea-boundary control system and to adapt the model to new requirements, especially related to the study of salinity intrusion. This new model "sea" was completed in 1976. Recently, in early 1979, it was decided to extend the model inland with a threefold aim:

1. To extend the range of fresh water flows where the model can be used (especially low fresh water discharge giving a high salinity intrusion).
2. To extend the area of possible research in inland direction.
3. To reproduce the tide-affected part of the estuary.

This extension of the model will be combined with the reconstruction of the existing model which was greatly damaged by a fire.

The model had to serve several purposes, each of which makes special demands on the selection of the model boundaries and scales: (1) Studies for the influence of the harbor extension on the flow field near the entrance of the Rotterdamse Waterweg and the consequences with respect to navigation; (2) studies on the salinity intrusion in the estuary, as a result of changes in the geometry of the Rotterdamse Waterweg and Oude Maas; (3) studies on dispersion of sediment, heat, and pollutants. The emphasis of the model studies gradually shifted from the first to the second aspect, with occasional studies on the third aspect. At the start of the model study, most attention was paid to the reproduction of the flow field around the entrance. Parallel to the Europoort model also a schematized estuary model was built called the "tidal salinity flume," which is extensively used to obtain basic knowledge on the physical processes related to salinity intrusion and on the reproduction of these processes in a distorted scale model (10).

**Definition of Model Area.**—The choice of the model boundaries depends on the physical phenomena to be reproduced. The sea boundaries have to be chosen in such a way that the conditions at these boundaries are not affected by changes in the problem area and that the fresh water discharge of the river leaves the model in a correct way. The salinity distribution in the estuary and near the harbor mouth should not be affected by the conditions at the boundaries (13). Flow conditions near the harbor mouth are governed by tidal and density currents. The tidal range is from 1.35 (neap tide) to 1.75 m (spring tide). The fresh water discharge through the Rotterdamse Waterweg ranges from 400 to 4,000  $\text{m}^3/\text{s}$  (average 1,000  $\text{m}^3/\text{s}$ ). The salinity of the North Sea is about 33 ppt. The tidal flow pattern at sea is nearly parallel to the coast with high-water slack at sea at 3.5 hr after high water at Hook of Holland.

In view of this tidal flow pattern it was decided to take a closed western model boundary (Fig. 1) parallel to the dominant flow direction and to have two control boundaries (north and south) at some 10–15 km from the entrance, perpendicular to the main flow direction. The distance of the western boundary to the coast was roughly estimated from a potential flow computation on the influence of the proposed harbor extension. This estimate was verified later with two-dimensional tidal flow calculations which showed that the influence of the closed western boundary was within the experimental accuracy limits. The initial choice of the river boundaries was a compromise between cost and accuracy. Since attention was concentrated on the harbor entrance, only the salinity-affected part of the estuary was reproduced.

This means, however, that tidal discharges and fresh water discharges have to be known at the river boundaries. This is a weak point because the scale model becomes dependent on a mathematical model. The other possibility, the extension of the model up to the limits of tidal influence, is costly but makes the model self-supporting. In both cases, however, calibration is necessary to obtain accurate values for the discharges.

**Selection of Model Scales.**—Selection of model scales, defined here as the ratio of quantities in nature and model, involves finding a compromise between cost and accuracy. This holds also for mathematical models. Several aspects are of importance (7):

1. Length and depth scales should be large to reduce model dimensions, discharges, and use of salt. In the present case, tidal discharges up to 250,000 m<sup>3</sup>/s have to be simulated, which certainly presents a lower limit to the scales.

2. Reproduction of tidal flow phenomena requires Froude scaling—(velocity scale = length scale<sup>1/2</sup>).

3. Reproduction of density-influenced flow and mixing requires at least reproduction of the internal Froude number which means, in combination with the previous requirement, a one-to-one scaling of densities.

4. The distortion of the model, the ratio of length to depth scale, has to be limited because: (a) Slopes are exaggerated in a distorted model but should remain below a certain value to avoid flow separation; (b) the correct reproduction of vertical mixing becomes increasingly difficult with augmenting distortion; (c) distortion means an increase in roughness. The Darcy-Weisbach friction factor in the model has to be increased in the same ratio as the distortion. Bed roughness (cubes and strips) is preferred in the present model, which gives an upper limit to the model friction factor; and (d) dimensions of instruments require a minimum water depth.

5. Accuracy of the model and the instrumentation give maximum values for the model scales. The required accuracy for water levels and flow velocities presented no special problems here, but the salinity intrusion had to be reproduced in such an accurate way that special measures were necessary.

Consideration of all aspects and previous experience with tidal models has led to the following scales: Length scale = 640; depth scale = 64 (distortion 10); velocity scale = 8; (discharge scale 327,680).

Several aspects were not considered nor reproduced:

1. Waves: the effect of waves on vertical mixing can be neglected in general.
2. Wind: wind can change the tide-averaged circulation (drift) in the North Sea which is in the order of 5 cm/s to the north under normal conditions. If necessary, storm effects can be reproduced by changing the boundary conditions of the model.
3. Coriolis acceleration: neglecting the effects of the wrong representation of the Coriolis acceleration in models causes deviations in water levels and flow direction in general. Simulation of these effects requires rotation of the model or the use of rotating cylinders, where the lift force (Magnus effect) can simulate the Coriolis acceleration effects (11). Tidal computations have shown that in the present case Coriolis acceleration only affected water levels but not the flow velocity and direction. Only correction of water levels is therefore necessary in comparing water levels in model and nature.
4. Reproduction of sediment transport was not considered at the start of the model. Preliminary tests have shown that the model can be of some use for studying sediment transport but not all aspects are reproduced correctly.

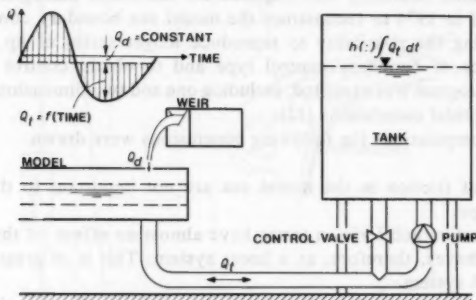


FIG. 2.—River Boundary Control

**Model Boundary Control Systems.**—For the river boundaries, a discharge control was chosen. The fresh-water discharge was regulated independently to obtain sufficient accuracy. The tidal flow was generated with a constant supply and a controllable underflow. The resulting tidal discharge was measured with a propeller current meter some distance from the inlet. When calibrating the model, the underflow gate is controlled in such a way that the flow velocity is in accordance with the prototype data. Once the movement of the gate is known, only this movement is reproduced. This system is stable but it is very time-consuming to find a new calibration. This was not a problem for the Europoort harbor studies, but the system was not flexible enough for salinity intrusion studies. Therefore, it was decided to switch to a volumetric discharge control, where the tidal discharge is stored in a large tank and the water level in the tank is used as a control variable (Fig. 2). These tidal discharges on the river boundary are calculated with a one-dimensional mathematical model of the whole estuary.

For the sea boundaries, a discharge control was chosen in 1965 because



experience had shown that for a relatively small sea, a water level control on all boundaries gives an unstable and inaccurate control of velocities in the sea area. This is especially true if the effects of resistance and the phase differences between the boundaries are small (6). The north boundary was divided in 5 sections and the south boundary in 7 sections, each with an overflow gate. The tidal discharge was roughly produced with a central pumping station and by-pass channels, whereas the fine control was done with the overflow gates. The resulting tidal discharges were measured with a large propeller current meter close to the model boundary. This system will not give a good water level reproduction, in view of inaccuracies in prototype data and the model. Therefore, one of the gates of the north boundary, the farthest away from the shore, was used to control the water level at Hook of Holland which was used as the reference level for the model.

Although this system was able to reproduce the tidal movements (discharges and levels) to the required accuracy, it lacked flexibility because introducing a new tide was very time-consuming and the reproduction of time series was impossible. Since flexibility was required for the water management studies, it was decided in 1974 to reconstruct the model sea boundary control system, thereby creating the possibility to reproduce longer series of up to 30 days. For the choice of boundary control type and to obtain control procedures, an extensive program was executed, including one and two-dimensional analytical and numerical tidal calculations (12).

From the computations the following conclusions were drawn:

1. Effects of friction in the model sea are not important to the choice of the control type.
2. The advective acceleration terms have almost no effect on the flow field. The model behaves, therefore, as a linear system. This is of great importance for the control system.
3. Closing the western boundary has only a minor effect on the velocities near the entrance of the estuary if the discharge through the western boundary is correctly compensated for on the north and south boundaries. Because more field data were available in 1975, it was found that a slight rotation of the western boundary gave better results than the existing boundary.
4. Omission of the Coriolis acceleration does not affect the flow field, but only the water levels.
5. Water level control for both the north and south boundaries gives unacceptable inaccuracies because of the small phase difference between the two boundaries. Tide-averaged discharges cannot be generated with a water level control system and have to be independently generated.
6. The most stable solution is a water-level control at one side, and a discharge control at the other boundary. Possible errors in one of the boundary conditions do not influence the other boundary.

A review of existing tidal models in other laboratories showed that for long—relative to the length of the tidal wave—estuaries, a water level control at the mouth of the estuary gives good results. For short sections of estuaries, generally one discharge and one water level control is applied.

Although a discharge control for both boundaries requires very great accuracy



to obtain a reasonable water balance and water level control, this type of control was chosen also because it can be used to simulate tide-averaged discharges (drift in northerly or southerly direction). The tidal discharges at the sea boundary are obtained as follows: The outgoing discharge is pumped from the model into a reservoir under the model. The flow into the model is supplied by the existing by-pass circuit (Fig. 3). Discharges are measured with electro-magnetic flowmeters which are very accurate. This fact, and the large number of control sections, give a very good overall water balance. The remaining error in the water level at Hook of Holland is very small and can be easily compensated for with a "fine water-level control" of limited capacity. This "fine water-level control" is a feedback system where the difference between desired and realized

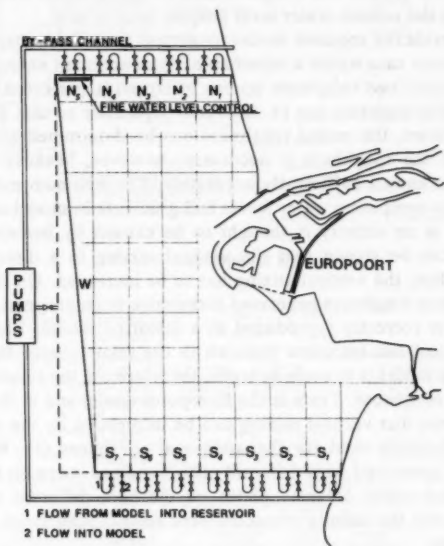


FIG. 3.—Sea Boundary Control

water level at Hook of Holland is translated in a correction of the discharges at Section N5.

Special attention had to be given to the influence of the salinity distribution along the model boundaries. Field data show density gradients both in the vertical direction as well as perpendicular to the coast. An exact reproduction of this distribution is almost impossible. It was therefore decided to generate a well mixed outflow, with water jets, and a uniform density of the incoming water, and to study the effect of this change in boundary condition on the salinity distribution in the estuary itself.

In one test, a temporary closed boundary parallel to the western boundary, half way the model sea, was constructed leaving all other conditions the same.

In another test, additional fresh water was introduced near the model boundaries (in the same order as the river discharge). Neither change affected the salinity distribution in the Rotterdamse Waterweg to a measurable extent, and it was therefore decided that the proposed salinity control at the model boundary was sufficiently accurate.

**Roughness and Mixing.**—The distortion of estuary models necessitates the adjustment of roughness and mixing. The roughness can be separated into wall and bed roughness. Wall roughness effect due to groynes, harbor entrances, and other protrusions is reproduced correctly, because their shape is reproduced geometrically similarly. The distortion is not significant here because these protrusions are already sharp in nature (the flow will separate from the protrusion). The friction factor for the bed roughness has to be increased with the distortion factor to obtain the correct water level shapes.

Means to provide the required model roughness are cubes, strips, and vertical bars. In the present case where a reasonable reproduction of velocity and salinity profiles is required, bed roughness (cubes or strips) is preferred. The effective roughness of these elements can be measured separately so that if the prototype roughness is known, the model roughness can be determined also. In general, a calibration of the roughness is necessary, however, because the prototype roughness is not known sufficiently accurately. The optimum model roughness is determined by comparing water levels and gradients in model and nature.

If all mixing in an estuary is thought to be caused by bed-shear generated turbulence, it can be shown that the vertical mixing in a distorted model is too small (2). Thus, the vertical mixing has to be increased. On the other hand, mixing due to wall-roughness generated turbulence from groynes, harbor inlets, or confluence, is correctly reproduced in a distorted model. This was proved in the systematical salt intrusion research in the tidal salinity flume. Whether the mixing in the model is to scale depends, therefore, on the relative importance of wall and bed roughness. Tests in the Europoort model and in the tidal salinity flume have shown that vertical mixing can be influenced by the choice of type of roughness elements used for the additional roughness (1). With the same total roughness, generated with different means such as strips on the side walls, vertical bars, and cubes or small plates on the bed, different values for the vertical mixing and the salinity intrusion were found. Wall strips produced the maximum mixing.

The conclusion is, therefore, that in reproducing the roughness, lack of knowledge of the prototype roughness is the weak point, but that calibration of the model will provide a sufficient solution. For the turbulent mixing, the model acts more or less as a "black box" and has to be calibrated also. The choice of the type of roughness element is here a calibration parameter. In the present model, additional mixing can be provided by air-bubble screens, with almost no effect on the roughness.

**Model Construction.**—The model was constructed in a traditional way. The sea bottom was constructed by prestressed concrete plates following the sea bed contours, leaving a reservoir for water storage under the floor. The river sections were constructed with sand and mortar using wooden profiles for the cross section. To keep the model sea at constant density, brine is injected in the by-pass circuit. The brine is produced with a special installation with a maximum capacity of 4,000 kg NaCl/hr.

## MODEL OPERATION AND CONTROL, INSTRUMENTATION AND DATA PROCESSING

**Operation and Control.**—In the original conception of the model, the sea boundaries were controlled by overflow weirs with feedback control on the velocity along the boundary or, if the reproduction of the tide was completed, by control on the position of the weirs. The desired programs were created on special analog programmers and the model was trimmed by trial and error.

In 1977, a new, computer-based, Rijnmond Model Control System (RMCS) was developed in combination with a data-acquisition system, by PANDATA for use on a PDP computer (3). Discharges for the model boundaries are computed

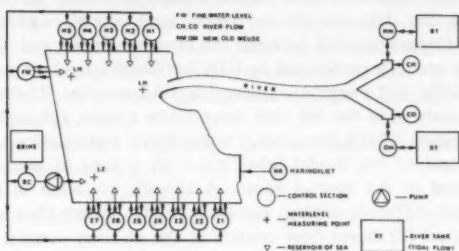


FIG. 4.—Computer System

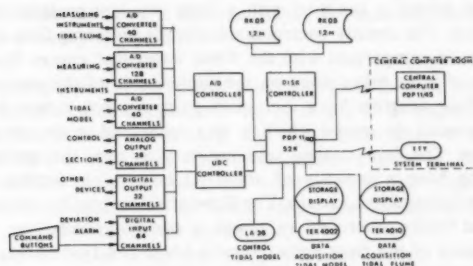


FIG. 5.—Tidal Model Control

from simultaneous 13 hr prototype measurements along the model boundaries. These raw data need correction to obtain a water balance and to compensate for the closing of the western model boundary. The corrected data are used to compute the model discharges for the 12 control sections. For time series, discharges are predicted with the aid of continuous records in a few points in nature. River boundary discharges are computed with a one-dimensional mathematical model, IMPLIC of the estuary.

The purpose of the model control is to accurately generate tides in the model to enable the execution of experiments under strictly defined conditions. Taking into account the deficiencies of the original model control, five areas of improvement were identified:

1. Faster adjustments, preferably automated as much as possible.
2. Better operational control, ease of use and flexibility.
3. Reproducibility of tides without a need to readjust.
4. A library of tides, to make possible tests under different tidal conditions.
5. Improvement of accuracy.

The adjustment process no longer should be a trial-and-error method, but flexible methods should enable the operator to perform adjustments of new tides. The model is controlled by a PDP 11/40 running under the RSX-11D operating system. The total hardware configuration is shown in Fig. 4. The model computer is connected to a central computer facility of the laboratory. In this remote facility, data analysis and data plotting take place after experiments have been run. Communication between the process control and data collection equipment of the model is performed by UDC hardware (standard process control hardware for PDP's) and a separate analog/digital controller. The analog/digital channels are mainly used for the data acquisition system although five analog channels are used by RMCS for sensing water-levels and salinity.

Operator control of the model takes place by means of push-buttons and a control terminal in the control room. A specific situation in the model is generated by four different control mechanisms: (1) Direct flow control along the sea boundaries; (2) direct flow control at the up-river control sections; (3) supervisory control of the water-level at a central location in the model; and (4) density difference control between fresh and salt water. The set-up is shown schematically in Fig. 5.

Flow into the model is supplied with a large constant-pressure by-pass and a pumping station. The density control maintains the incoming flow at a constant relative density, in comparison with the fresh water that comes from the river ends. Injection of brine takes place on the suction side of the pumping station. The outgoing flow controls have their own pumps which return the water to a large sump beneath the model which is also connected to the aforementioned pumping station. The flow control sections vary in size; the sections nearest to the coast-line have a capacity of about 80 L/s, while further away from the coast, sizes of about 260 L/s exist. The flows are measured by electro-magnetic flow meters and finally controlled by means of control valves.

The flow control of the river ends, Nieuwe Maas and Oude Maas, is divided into two different functions. One control is used for simulating the tidal movement by setpoint control of the level in a storage tank. The other one, the upper river discharge, is mostly a constant value during one experiment and is set by hand.

The RMCS also takes care of the start-up of the model and the adjustments of the discharges to obtain the required vertical tide at Hook of Holland. Several adjustment procedures are available. In one of these procedures the difference between the actual and required water level is measured continuously and used to compute a small correction in the discharges of all control sections. Another procedure ensures a constant mean sea level during the experiments. Set points for the control section are computed every 7.5 real-time (model) seconds with linear interpolation to obtain set points each 0.1 real time second. Water levels are also measured every 7.5 real-time seconds and, if necessary, used for the adjustment procedures by the operator.

The task of the operator is of a supervisory nature. He must ensure that the tide is generated as required for the experiment. His actions are limited and include checking that the model is functioning properly, sequence control of the phases of model operation, setting up equipment such as cameras and water level recorders, and acting in exceptional situations. The most essential part of the operator task is during the adjustment of a new tide. Tides which have been satisfactorily adjusted can be stored by the user in the model library.

The RMCS software was developed under the Digital Equipment RSX-11D operating system which has many features for real-time system development. In total, the system is comprised of over 100 Fortran programs (7,500 executable statements in all) and three programs written in PDP 11—Assembler. Experience has shown that the system permits fast and flexible adjustments. Usually a new tide can be adjusted within one or two days. The reproducibility of the water levels is accurate within 0.1 mm (for comparable times in different tidal cycles). The difference between desired and realized water level is generally less than 0.2 mm at any time.

**Instrumentation and Data Processing.**—The standard instrumentation of the model comprises the following:

1. Water level followers (vibrating-needle principle) with an error  $< 1$  cm prototype.
2. Propellor current meters, fixed or rotating, with a vane to measure flow direction (error  $< 2$  cm/s prototype or  $3^\circ$ ).
3. Conductivity and temperature probes to measure density (total error  $< 0.25$  kg/m<sup>3</sup> for measurements at different days); for measurements at the same day, a greater accuracy is possible.

There is also the possibility of special measurements: Overall stream patterns are recorded by photographing floats (5 m, 10 m and 15 m length). To measure lateral forces and moments on a ship, due to currents along a certain sailing line, a towed plate is used. For tanker simulation, a plate of 300 m  $\times$  15 m is used and smaller plates are used for coasters, etc. Although these plates give only a crude simulation of the actual ships, the instrument is very useful in comparing various situations or sailing lines.

The accuracy of water level and velocity measurements is sufficient, for all practical purposes, but the measurement of density deserves special attention. The accuracy required by the contractor for the determination of the salinity intrusion ( $\pm 100$  m prototype) corresponds to an accuracy in the density measurements of 0.1 kg/m<sup>3</sup>. Therefore, special methods are necessary here. Data processing started with line-following of paper records with computations and plotting by computer, but since 1974 a computer-based data acquisition system (up to 168 channels) is used. Computational and plotting programs are available to produce vertical and longitudinal profiles, vertical and profile-averaged values, discharges, dispersion coefficients etc.

#### MODEL CALIBRATION AND VERIFICATION

**Model Sea.**—Possibilities for calibration and verification of the model sea are limited. The information on tidal discharges at the sea boundaries and the

water level at Hook of Holland are used to control the model. The only variables left are the roughness of the model and the way the discharges of the closed western boundary are compensated. Velocities in the inner part of the model sea are hardly affected by changes in the bed roughness. Only water level differences can be influenced, but the roughness cannot be checked accurately because measurements in the open sea are not reliable. It was therefore assumed

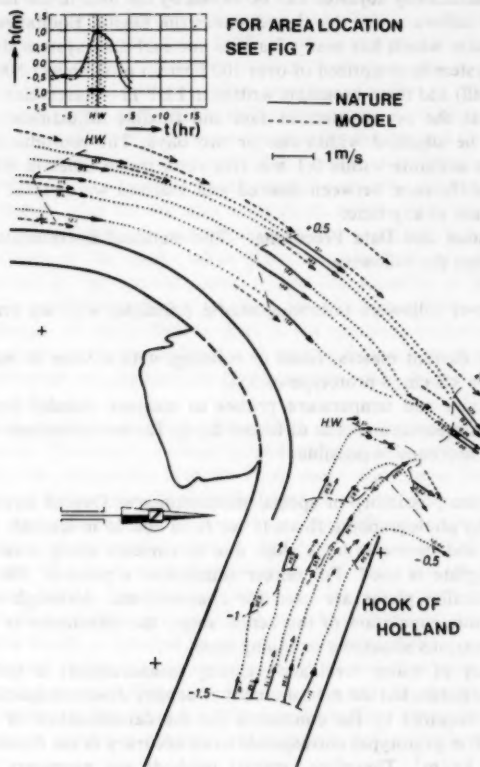


FIG. 6.—Comparison of Float Patterns in Model and Nature Around Europoort

that reproduction of a reasonable estimated value of the prototype roughness was sufficient.

By applying several ways of compensating the discharges through the western boundary, either by a 40%–60% distribution over the northern and southern boundary or a 100% compensation on the northwestern part of the boundary, as far away from the project area as possible (Fig. 3), and making a comparison of resulting velocities in the model and a few measuring points in nature, it

was concluded that preference had to be given to the second procedure. The first procedure proved to be wrong because it affected the two-dimensional flow pattern at sea. As a verification, float measurements near the entrance were used. Comparison of flow pattern obtained for floats with a length of 5 m for both neap, average, and spring tides showed a good similarity. As an example, results for an average tide are given in Fig. 6, which shows that



FIG. 7.—Measuring Positions for Verification Tests

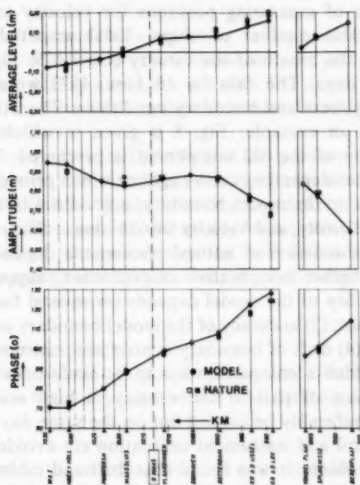


FIG. 8.—Verification of Tidal Propagation on River, 22-06-1974

even the complicated, density influenced, flow pattern near the mouth of the estuary is correctly reproduced in the model.

**River System.**—The most important feature of the river is the salinity intrusion, but tidal propagation and velocities have to be similar as well. For calibrating tidal propagation two parameters are of importance for the Europoort model: (1) The model roughness; and (2) the river boundary conditions. The longitudinal distributions of amplitude and phase of the M2 component of the water levels



were used as parameters for calibration. From sensitivity tests with the model it was found that the change in amplitude and phase over a certain section was almost linearly related to the amount of additional roughness. The use of these parameters therefore provides a good means to obtain the optimum roughness in the model.

On the other hand, it was found that relatively small changes in the boundary conditions had an influence of the same order as appreciable changes in the model roughness. The river boundary condition has a limited accuracy both for discharges measured in nature (limited number of measuring points and inaccuracy of instruments) and for the discharges computed with mathematical models (neither the analog DELTAR nor the numerical model IMPLIC account for density differences and have to be calibrated also with discharges and water levels in nature). Differences in the tidal discharge at the river boundary sections up to 20% and phase differences up to 30 min are possible. Calibration of the model is therefore always possible, though uncertain, by a combination of changes in the roughness and changes of the boundary conditions within the accuracy limits.

For the calibration, two sets of measurements in nature were available: 16 and 17 June, 1973, and 22 and 23 June, 1974. The measurement took two days because the number of measuring positions for velocity and salinity was too large for the available number of ships. Tidal amplitudes were measured continuously and at the mouth of the estuary (km 1,029, Fig. 7) measurements were done all four days. The data for 16 June, 1973 were used to obtain an optimum set of roughness and boundary conditions. The other days were used for verification. As an example, Fig. 8 is given in which mean water level, amplitude, and phase of the M2 component is presented. The prototype data show some differences depending on the agency which provided the data. Except for the stations close to the model boundary, a good similarity is obvious.

**Salinity Intrusion, Density, and Velocity Distribution.**—The required capabilities of a model for the simulation of natural phenomena depend on the nature of the investigation, whether comparative or predictive, support of fundamental research. The capability of the model depends on several factors: (1) Accuracy of boundary conditions; (2) accuracy of the model boundary control; (3) accuracy of instruments; and (4) drift of boundary control and instruments.

For the tests in which a comparison has to be made between two situations, for example deepening of part of the estuary, a high accuracy is required. These tests should preferably be carried out on the same day because incidental errors in model control and instrument calibration are avoided. From tests with constant control conditions it was found that drift and other errors were small ( $<0.07 \text{ kg/m}^3$ ); density changes larger than this value can be detected.

This figure roughly corresponds to changes in salinity intrusion length of  $\pm 75 \text{ m}$  in nature. This seems to be sufficient for practical applications. For tests on different days, using the same boundary conditions, density variations up to  $0.25 \text{ kg/m}^3$  occur in the upstream part of the salinity intrusion. This corresponds roughly to changes in salinity intrusion of  $\pm 300 \text{ m}$ . For a completely new situation, the accuracy of salinity prediction is limited therefore, but this will be sufficient in general, in view of the large variations in boundary conditions in nature (variations in tides, river discharges, and wind effects).

A model like the Europoort model can provide useful information for funda-



mental research but only in the verification of theoretical results. Measuring techniques are generally not sufficiently accurate nor detailed to obtain gradients and fluxes of mass and momentum. Efforts to improve this do not seem to be very promising up to now. The salinity distribution and intrusion in the model can be influenced in the following ways, assuming tidal propagation has already been adjusted:

1. The type of roughness: From observations in the tidal flume and the present model it has been concluded that for the same total friction factor, the vertical mixing and salinity intrusion depend on the roughness type.

2. Additional mixing can be obtained by the injection of air. Experimentally it has been found that quantities up to  $20 \text{ cm}^3/\text{m}^2/\text{s}$  hardly affect the roughness but greatly enhance the vertical mixing and reduce the salinity intrusion.

3. The "history" effects of the tidal movement: It cannot be assumed that the salinity intrusion during a certain tide is independent of the preceding tides, e.g. a spring tide following a normal tide. In the model, the tides have to be made cyclic. Comparisons, where the measurement period of 12.5 hr (one tide) was part of a cycle of 25 hr (one preceding tide) or 75 hr (five preceding tides) showed that for practical application, normal tidal variations history effects can be neglected.

4. The density difference between river and sea water: In principle this difference is kept at a constant value, obtained from prototype measurements, but slight deviations during a test are possible. However, if the interpretation of the results is on the basis of the relative density distribution, these deviations have no significant effect.

5. River boundary conditions: The effect of this parameter was already obvious for the tidal propagation, but the effects on the salinity distribution are dramatic. From sensitivity tests both with the tidal flume and the present model it appears that to obtain an accuracy of  $\pm 100 \text{ m}$  in the salinity intrusion, for instance defined as the position of a point near the bed with a salinity of  $0.5 \text{ kg/m}^3$  at the time of maximum salinity intrusion, the following accuracy in the river boundary conditions is required:

For the average river discharge	: $\pm 1\%$
For the amplitude of the M2 component of the tidal discharge	: $\pm 1\%$
For the phase of the M2 component of the tidal discharge	: $\pm 1 \text{ min}$ (or $0.5^\circ$ )

It will be clear that these accuracies are not obtainable from measurements in nature or from mathematical models. This means that for absolute predictions of the salinity, a relatively large uncertainty margin is present. It also means that an absolute calibration of the model is impossible, because small changes within the limits of uncertainty in the model boundary conditions have such a dominant effect on the salinity intrusion. Extension of the model up to the tidal limit is only a partial solution because this extension also has to be calibrated with data from nature.

For the optimum condition with respect to the reproduction of tidal propagation, the velocity and density distribution were compared for model and prototype without any further adjustment of the model (no air injection, etc.). Some results

for the measuring station at km 1,015 are presented in Fig. 9. Fig. 9a shows a comparison of some velocity profiles, Fig. 9b the distribution of the relative density, i.e., the difference between the local density and the river water density divided by the difference in density between sea and river water. Fig. 9c shows the velocity averaged over the vertical. These velocities are averaged for each flow direction (ebb versus flood); thus the density currents round slack tide become visible. Fig. 9d shows the depth averaged salinity distribution at low

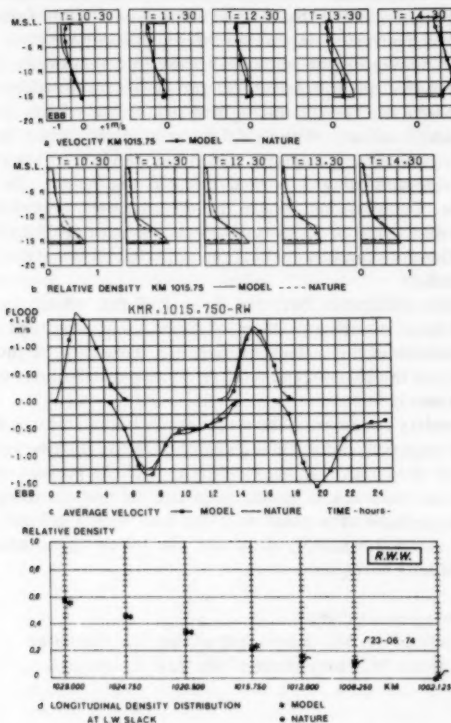


FIG. 9.—Verification of Density and Velocity Distribution, 22-06-1974

water slack. The river discharge during the period preceding the measurements in nature was relatively constant.

Further, it was proved before that the history effects of the tidal movement can be neglected for the salinity distribution in practical cases. Thus, it can be concluded that the prototype situation was a "quasi-steady state" which can be compared with the "cyclic-steady state" results of the model. The agreement is generally quite good. Further adjustments were not considered because of the uncertainties in the boundary conditions which have such a

great influence on the salinity intrusion. It may be concluded, however, that for the present model, a good reproduction of tidal propagation also gives a good reproduction of the salinity intrusion. For new situations, the knowledge of the boundary condition forms the weakest point in the accuracy of the model reproduction.

**Application of Model.**—Without going into detail, a short review of model applications will be given: The first part of the model studies was mainly related to navigational problems around the new Europoort harbor. The studies included the determination of the flow pattern and the hindrance for navigation during the various phases of construction of the harbor works. The effects of these works on the salinity intrusion was also studied. Later, the attention gradually shifted to the influence of modification of the inner estuary (removal or construction of groynes, deepening or shallowing of the river bed, modification of harbor entrances) on the salinity intrusion.

Special studies included the dispersion of cooling water from a large power plant in the Europoort area, exchange currents in harbors, and possible ways to reduce them in view of a reduction of sedimentation and the dispersion of pollutants in the river system. In all these cases, the model assisted in predicting the effects of these measures which are very difficult to predict in another way. It has proved to be very useful in supporting decisions related to the management of the estuary.

#### SUMMARY AND CONCLUSIONS

Salt intrusion and water quality modeling of a complicated estuary like the Rotterdamse Waterweg Estuary make high demands on the capabilities of modeling techniques. Increased environmental problems and the impact of the large infrastructural works have stressed the requirements. A thorough evaluation of research possibilities proved that, for the time being, only a complimentary approach with hydraulic and mathematical modeling is feasible. With respect to modeling of the estuary phenomena, the following can be concluded:

1. Mathematical models do not yet yield the possibility to predict in sufficient detail the flow velocity and salinity field. Therefore, the main tool for estuarine problems at present is the physical scale model. Mathematical models can be used successfully for the study of transport of pollutants and sediments.
2. Although the scaling of all phenomena in a hydraulic scale model is not yet completely understood, a situation which gives the model a partial black-box character, it proves to be the most powerful tool for the study of estuaries, provided certain requirements are fulfilled.
3. The hydraulic model should be calibrated very carefully with special emphasis on the influence of possible scale effects due to distortion and Reynolds number influences.
4. The verification tests of the physical model of the Rotterdamse Waterweg Estuary (a Froude scale model with a length scale 640 and a distortion 10) proved that reproduction of water levels and flow pattern is possible to the required accuracy if the proper boundary conditions are known. Once the tidal propagation in the river system was reproduced correctly, the simulation of salinity intrusion proved to be good.

5. The model should be provided with good boundary conditions. In the present case, the knowledge of the river boundary conditions is the weakest point in the accuracy of the model. This makes the verification of the salinity intrusion uncertain.

6. Mathematical models are useful in predicting discharges at model boundaries. However, for reasons of flexibility in model operation and accuracy of boundary control, an integrated system (extension of the model beyond the tidal limits) is preferable.

7. The model sea boundary should preferably be operated with discharge control, if the accuracy of the data permits this.

8. In the present case, where wall roughness is dominant, no additional mixing proved to be necessary after calibration of the total roughness on the tidal propagation with bed elements.

9. It is advisable to operate the model automatically both for the control of the boundary conditions as well as for the data processing. This permits flexible operation and increases the accuracy of the reproduction.

10. The purpose of the model research and the required accuracy have a large impact on the cost of research. A close cooperation between principal and laboratory in the problem definition phase is therefore essential.

#### APPENDIX.—REFERENCES

1. Abraham, G., Karelse, M., and Lases, W. B. P. M., "Data Requirements for One-Dimensional Mathematical Modelling of Salinity Intrusion in Estuaries," *Proceedings of the Sixteenth International Association for Hydraulic Research Congress*, Sao Paulo, Brazil, Vol. 3, 1975, pp. 275-283.
2. Abraham, G., "Evaluation of Applicability of Mathematical and Hydraulic Models," in Dutch, *Report S280-1*, Delft Hydraulics Lab., 1977.
3. Adriaanse, P., Caldwell, C. R., and Droppert, L. J., "Rijnmond Tidal Model Control System," *Journal A*, Brussels, Belgium, Vol. 19, No. 1, 1978, pp. 21-29.
4. Blumberg, A. F., "The Influence of Density Variation on Estuarine Tide and Circulation," *Estuarine and Coastal Marine Sciences*, Vol. 6, 1978, pp. 209-215.
5. Caponi, E. A., "A Three-Dimensional Model for the Numerical Simulation of Estuaries," *Advances in Geophysics*, Vol. 19, 1976, pp. 189-310.
6. Fischer, H. B., "Mixing and Dispersion in Estuaries," *Annual Review of Fluid Mechanics*, Vol. 18, 1976, pp. 107-133.
7. Hermann, F. A., Jr., "Overview of Physical Estuary Practice," *Modelling Techniques*, ASCE, New York, N.Y., Vol. 2, 1975, pp. 1270-1290.
8. Liu, S. K., and Leendertse, J. J., "Multidimensional Numerical Modeling of Estuaries and Coastal Seas," *Advances in Hydrosience*, Vol. 11, 1978, pp. 95-164.
9. Perrels, P. A. J., and Karelse, M., "A Two-Dimensional Model for Salt Intrusion in Estuaries," *Proceedings of the Ninth Liège Colloquium on Ocean Hydrodynamics*, Nihoul, J. C. J., ed., Elsevier, Amsterdam, The Netherlands, 1978, pp. 107-125.
10. Roelfzema, A., and van Os, A. G., "Effect of Harbours on Salt Intrusion in Estuaries," Delft Hydraulics Laboratory, Publication No. 204, 1978.
11. Schoemaker, H. J., "Influence of Earth Rotation in Hydraulic Tests," *De Ingenieur*, Vol. 70, 1958, p. A608.
12. Van der Kuur, P., and Verboom, G. K., "Computational Analysis for Optimum Boundary Control of Two-Dimensional Tidal Models," *Proceedings of the Sixteenth International Association for Hydraulic Research Congress*, Sao Paulo, Brazil, Vol. 1, 1975, pp. 304-310.
13. Van Rees, A. J., van der Kuur, P., and Strobband, H. J., "Experiences with Tidal Salinity Model Europoort," *Proceedings of the Thirteenth International Conference on Coastal Engineering*, Vancouver, B. C., Canada, Vol. 3, 1972, pp. 2355-2378.

## HEATED DISCHARGE IN AN ESTUARY: CASE STUDY

By James B. Nystrom,<sup>1</sup> George E. Hecker,<sup>2</sup> M. ASCE,  
and Han C. Moy<sup>3</sup>

### INTRODUCTION

A series of physical model studies, field surveys, and analyses were conducted to develop an outfall structure and to assist in evaluating the environmental impact of once-through condenser cooling at Consolidated Edison Company's Indian Point Station. This station, located on the Hudson River about 30 miles (48 km) north of New York City, has three nuclear units with a total rated capacity of 2,100 MW and uses a condenser circulating water flow rate of 4,590 cu ft/sec (130 m<sup>3</sup>/s) at a temperature rise of 15° F (8.3° C). The studies had the basic objective of predicting temperature rise patterns in the Hudson River due to plant operation with various possible discharge structures and at different river discharges.

Two model studies used to investigate recirculation and temperature rises will be emphasized in this paper. An undistorted 1-75 scale model, simulating approx one-half the river width 2,000 ft (610 m) and approx 4,600 ft (140 m) longitudinally, was used to determine near field thermal patterns, including direct recirculation, at Indian Point. Near field is defined as that area in which the initial momentum of the discharge governs the hydrodynamics of the thermal plume. Steady ambient current speeds up to 2 ft/sec (0.61 m/s) in both ebb and flood directions and transient currents from 0.2 ft/sec (0.06 m/s) ebb to 0.2 ft/sec (0.06 m/s) flood were simulated. A distorted scale model of a 15-mile (24-km) reach of the river simulated cumulative temperature patterns and total recirculation, including the effects of two additional fossil stations. In this intermediate-far field region, initial thermal patterns have an effect on overall thermal patterns, but the initial discharge momentum has been dissipated and surface heat transfer, buoyancy, and convective effects dominate. The river

<sup>1</sup>Lead Research Engr., Alden Research Lab., and Instr., Mech. Engrg., Worcester Polytechnic Inst., Holden, Mass.

<sup>2</sup>Dir., Alden Research Lab., and Assoc. Prof., Civ. Engrg., Worcester Polytechnic Inst., Holden, Mass.

<sup>3</sup>Senior Engr., Mech. Engrg. Dept., Consolidated Edison Co. of New York, Inc., New York, N.Y.

Note.—Discussion open until April 1, 1982. Separate discussions should be submitted for the individual papers in this symposium. To extend the closing date one month, a written request must be filed with the Manager of Technical and Professional Publications, ASCE. Manuscript was submitted for review for possible publication on March 9, 1981. This paper is part of the Journal of the Hydraulics Division, Proceedings of the American Society of Civil Engineers, ©ASCE, Vol. 107, No. HY11, November, 1981. ISSN 0044-796X/81/0011-1371/\$01.00.

was modeled at a horizontal scale of 1-400 and a vertical scale of 1-80. The model scaled average tidal-stage and velocity variations, and various constant fresh-water runoffs. Model river currents and tides were compared to field data taken for verification purposes.

Results from these models presented herein include near field temperature rise patterns for a constant ambient velocity, and far field temperature rise

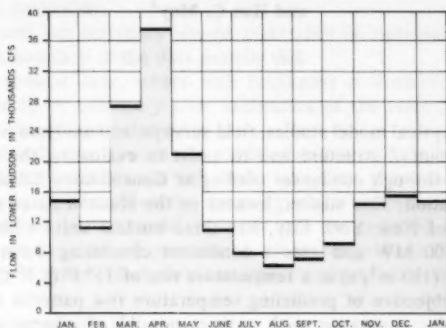


FIG. 1.—Monthly Average Freshwater Flow Rate (1,000 cu ft/sec =  $28.3 \text{ m}^3/\text{s}$ ) (4)

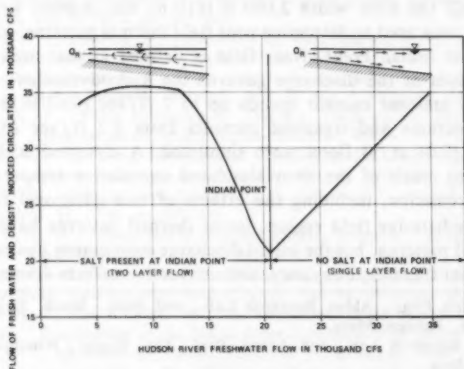


FIG. 2.—Density Induced Circulation (1,000 cu ft/sec =  $28.3 \text{ m}^3/\text{s}$ ) (8)

patterns at intervals in the tide cycle for two types of discharge structures. A comparison of physical model results to comprehensive measurements and a one-dimensional time-averaged analytic study is provided. The results are evaluated in terms of restrictions to complete similitude requirements and to model operation limits. Basic conclusions and techniques may be of value to other model investigations of hydrothermal phenomena.

## SITE DESCRIPTION

**Hydraulics of Hudson River Estuary Near Indian Point.**—At the Indian Point site, tidal flows dominate the hydraulics of the Hudson River. The average tidal range is about 3 ft, and average maximum tidal flow rate and current speed are 300,000 cu ft/sec (8,500 m<sup>3</sup>/s) and 2.0 ft/sec (0.61 m/s), respectively. Average fresh water runoff is less than 20,000 cu ft/sec (566 m<sup>3</sup>/s), or at least an order of magnitude less than tidal flows. The character of the river changes from broad and shallow, 10,000 ft (3,050 m) width and 15 ft (4.6 m) average depth, downstream of the plant site in Haverstraw Bay to relatively narrow and deep, 3,000 ft (914 m) width and 65 ft (20 m) average depth, upstream of the plant site at Bear Mountain Bridge. Ninety degree bends occur both upstream and downstream of the plant site, and the bends, together with the rapidly varying cross section, cause complex flow patterns.

Since ocean water is more dense than fresh water due to its salt content,

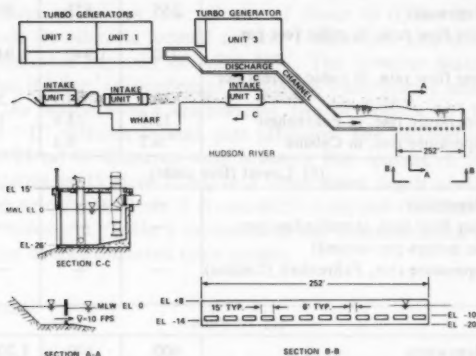


FIG. 3.—General Arrangement of Circulating Water Structures (1 ft = 0.3048 m)

a net upstream movement of ocean water, or density induced circulation, occurs in the lower layers. This phenomenon may affect the dilution and mixing of surface effluents since a corresponding increased oceanward flow occurs in the upper layer. In the Hudson River, vertical mixing is relatively strong, with vertical density gradients only a few parts per thousand, and thus the river is classed as partially stratified (11) in the salt intrusion region. The location of the maximum upstream intrusion of salt is dependent on the magnitude of the fresh-water runoff. At fresh water runoff flowrates in excess of about 20,800 cu ft/sec (589 m<sup>3</sup>/s), the salt intrusion front is driven downstream of Indian Point (1), and at lower fresh water flowrates, net density induced flow occurs at the site. The monthly average fresh-water flowrate (Fig. 1) indicates that the fresh water runoff is less than 20,800 cu ft/sec (589 m<sup>3</sup>/s) during a substantial part of the year; therefore, density induced circulation is an important feature of the river hydraulics. For predictive studies, a quantitative measure of the strength of the net density-induced circulation is required. Fig. 2 was developed

by evaluating the results of nine current meter surveys conducted in the Hudson River at times of different fresh-water runoff (8). River cross sections were instrumented with current meters placed at various lateral and vertical locations, and currents in the upper and lower layer, if any, were integrated over the section for a tide cycle. This procedure yielded the net nontidal flow exchange in addition to the known fresh-water runoff. Fig. 2 indicates that, when salt is present at Indian Point (fresh water flowrates less than 20,800 cu ft/sec ( $589 \text{ m}^3/\text{s}$ )), the total circulation increases substantially with decreasing fresh-water flowrate.

TABLE 1.—Plant Parameters

Power plant characteristics (1)	Unit 1 (2)	Unit 2 (3)	Unit 3 (4)	Total (5)
(a) Indian Point				
Capacity, in Megawatts	265	873	965	2,103
Circulating water flow rate, in cubic feet per second	710	1,940	1,940	4,590
Circulating water flow rate, in cubic meters per second	20.1	54.9	54.9	413
Condenser temperature rise, in Fahrenheit	12.0	14.6	16.0	14.8
Condenser temperature rise, in Celsius	6.7	8.1	8.9	8.2
(b) Lovett (five units)				
Capacity, in Megawatts	—	—	—	503.5
Circulating water flow rate, in cubic feet per second (cubic meters per second)	—	—	—	710 (20.1)
Condenser temperature rise, Fahrenheit (Celsius)	—	—	—	14.8 (8.2)
(c) Bowline				
Capacity, in Megawatts	600	600	1,200	
Circulating water flowrate, in cubic feet per second	855	855	1,710	
Circulating water flowrate, in cubic meters per second	24.2	24.2	48.4	
Condenser temperature rise, Fahrenheit	15	15	15	
Condenser temperature rise, Celsius	8.3	8.3	8.3	

**Meteorology.**—Due to surrounding topography, the prevailing winds at the plant site tend to follow the direction of the river center line with average wind speeds of about 5.5 miles/hr (2.5 m/s). Mean ambient air temperatures vary from 28° F (−2° C) in January to 75° F (24° C) in July, while mean water temperatures vary from 29° F (−1° C) to 72° F (22° C). Typical heat-transfer coefficients for average summer and winter conditions are in the range of 200 and 100 Btu/sq ft/Day/F (300 and 150 Kcal/m<sup>2</sup>/Day, C), respectively.

**Station Characteristics.**—The Indian Point Station is located approx 30 miles (48 km) north of New York City on the eastern side of the Hudson River, and consists of three nuclear units with a total generating capacity of 2,100 MWb. Each unit has a separate intake structure located at the shoreline (Fig.



3). Condenser circulating water is withdrawn over a depth of approx 26 ft (8.2 m) at a combined flowrate of 4,590 cu ft/sec (130 m<sup>3</sup>/s). The circulating water temperature is increased by about 14.8° F (8.2° C) and is returned to the river via a common discharge channel and outfall structure located on the shoreline approx 500 ft (152 m) southeast (downstream) of the Unit 3 intake structure. The outfall structure consists of 12 rectangular ports, 4 ft (1.22 m) high by 15 ft (4.57 m) long, located on 21 ft (6.40 m) centers with centerline submergence 12 ft (3.66 m) below mean low water. Ten of the 12 ports have manually operated gates so that a discharge velocity of approx 10 ft/sec (3.05 m/s) can be maintained regardless of condenser flowrate.

Two additional stations using once-through condenser cooling are located on the western shore of the river within 7 miles (11 km) downstream of Indian Point. Both of these stations are fossil fueled. Lovett station, located about 2 miles (3.2 km) downstream and rated at 500 MW, withdraws condenser circulating water through a shoreline intake at a rate of 721 cu ft/sec (20.1 m<sup>3</sup>/s). The circulating water, heated 14° F (7.8° C), is returned via two shoreline surface discharge structures at a velocity of about 10 ft/sec (3.05 m/s). The second station, Bowline, is located approx 7 miles (11 km) downstream and has a two-unit rated capacity of 1,200 MW. The Bowline Station withdraws 1,710 cu ft/sec (48.4 m<sup>3</sup>/s) condenser circulating water from a small embayment and returns the water with a temperature rise of approx 15° F (8.3° C) via a submerged "T" diffuser located just offshore. The diffuser consists of 16 ports, 3 ft (0.91 m) in diameter, with a center line spacing of 25 ft (7.62 m). Port submergence is 15 ft (4.57 m) in a total water depth of 21 ft (6.40 m). The discharge velocity is about 15 ft/sec (4.57 m/s) and the discharge direction is 5° above horizontal. Table 1 summarizes the characteristics of all stations included in the overall distorted scale model.

#### SIMILITUDE CRITERIA

Various physical phenomena control the hydrodynamics of a heated effluent as it is transported from the outfall to the main receiving water body, and a single model cannot correctly scale all phenomena simultaneously. The three regions of interest are (1) The near field region, in which the effluent momentum and buoyancy, in conjunction with ambient currents, govern the discharge trajectory, and dilution; (2) an intermediate region, where buoyant forces become predominant and control, for example, plume spreading and depth; and (3) a far field region, where convection, dispersion, and heat transfer to the atmosphere control the discharge characteristics.

A prime requirement in all regions is similitude of ambient flow patterns. The basis for similitude of free surface flow is equality of the Froude number in model and prototype.

The Froude number,  $F$ , represents the ratio of inertia to gravity forces, and is usually written

$$F = \frac{V}{\sqrt{gy}} \dots \dots \dots (1)$$

For similitude

$$F_m = F_p \dots \dots \dots (2)$$

$$\text{or } F_r = \frac{F_m}{F_p} \frac{V_r}{\sqrt{g_r y_r}} = 1 \dots \dots \dots (3)$$

in which  $V$  = a representative horizontal velocity;  $y$  = a representative vertical length; and  $g$  = the gravitational constant. Subscripts  $m$ ,  $p$ , and  $r$  refer to model, prototype, and the ratio of a given variable between model and prototype, respectively.

Assuming the gravitational constant is equal in model and prototype, the velocity ratio,  $V_r$ , is given by

$$V_r = \sqrt{y_r} \dots \dots \dots (4)$$

Equality of Froude numbers is necessary but not sufficient to achieve kinematic similitude. The ratio of inertia to viscous forces, indicated by the Reynolds number,  $R$ , must also be considered due to its influence on flow patterns and mixing processes. The Reynolds number for open channel flow may be defined as:

$$R = \frac{Vy}{\nu} \dots \dots \dots (5)$$

$$\text{and } R_r = \frac{R_m}{R_p} = \frac{V_r y_r}{\nu_r} \dots \dots \dots (6)$$

in which  $\nu$  is the kinematic viscosity.

Since the Froude criteria determines the velocity scale ratio, and the kinematic viscosity is essentially equal in the model and prototype, the Reynolds number in the model will be less than the prototype  $R$  by the factor  $y_r^{3/2}$ .

Generally, prototype Reynolds numbers are large, approx 1,000,000, which is well within the fully turbulent regime, indicating that the effect of viscosity on flow patterns and mixing is small. To assure the model operates in the turbulent flow regime requires a model channel Reynolds number to be greater than about 500-1,000. This requirement usually sets a lower limit on the vertical scale ratio which can be used.

The effect of buoyancy on flow patterns and mixing is indicated by the densimetric Froude number,  $F'$ , the ratio of inertia to buoyant forces,

$$F' = \frac{V}{\sqrt{\left(\frac{\Delta\rho}{\rho}\right)gy}} \dots \dots \dots (7)$$

in which  $\Delta\rho$  = the density difference between the layers; and  $\rho$  = the density of the heavier layer.

To achieve similitude of the influence of buoyancy, the densimetric Froude number must also be equal in model and prototype.

$$F'_r = \frac{V_r}{\sqrt{\left(\frac{\Delta\rho}{\rho}\right)g_r y_r}} = 1 \dots \dots \dots (8)$$

Since both free surface and density phenomena have to be simultaneously scaled, there can only be one velocity ratio. Substituting Eq. 4 into Eq. 8, and using  $g_r = 1$ , yields

$$\left( \frac{\Delta \rho}{\rho} \right)_r = 1 \dots \dots \dots (9)$$

Water density is a nonlinear function of temperature, particularly at lower temperatures. Since the density ratio must be unity throughout the modeled area, it is possible to strictly satisfy Eq. 9 over the entire area of varying temperatures only if temperatures in the model are the same as temperatures in the prototype. The temperature scale ratio is the same. Therefore, unity and temperatures as well as temperature rises should be equal in model and prototype. At high ambient temperatures, water density becomes nearly linear with temperature. Therefore, for a given temperature difference, the density ratio is essentially independent of ambient temperature, and ambient temperature does not have to be scaled directly.

In the near field region, a submerged outfall usually imparts considerable horizontal momentum to the effluent. The effluent also possesses potential energy due to the buoyancy induced by its elevated temperature, causing vertical acceleration. To maintain kinematic similitude, horizontal and vertical scales must be equal, i.e., the model must be undistorted in scale. The discharge velocity decays rapidly with distance, and the effluent forms a surface layer, so that the nearfield encompasses a relatively small area. Heat flux to the atmosphere over the limited near field area is relatively small in comparison to the total thermal flux, and simulation of heat transfer is not required in this region.

An additional consideration in the nearfield model is the influence of Reynolds number on the jet entrainment or dilution. No research has been conducted on Reynolds number effects of multiple jets, but work with a single round horizontal jet indicates the model tests should be conducted with as high a Reynolds number as practicable (6). These data show that while entrainment prior to impingement of the jet on the surface decreased with increasing Reynolds number, the total entrainment after impingement was relatively constant for Reynolds numbers greater than 10,000. Studies of a single vertical buoyant jet indicated that no apparent Reynolds number effects occurred beyond  $R$  greater than 1,200 (20).

These scaling considerations indicate decrease in scale effects with increasing model size, but, in the design of a near field model, possible scale effects must be balanced against the practical considerations of space and flow capabilities. For the Indian Point study, to assure the offshore model boundary was sufficiently removed from the expected plume, approx one-half the river width was simulated. Flow occurs in both upstream and downstream directions, so that sufficient length was required in both directions to assure that the initial jet momentum was dissipated and that the buoyant surface plume was fully developed. A length approximately equal to the width modeled was chosen for each direction, resulting in scaling an area about 2,000 ft (610 m) wide  $\times$  4,600 ft (1,400 m) long. A scale ratio of 1-75 satisfied the practical considerations of available space and flow capacity of an existing pump to achieve the maximum

2.0 ft/sec (0.61 m/s) current speed. The model jet Reynolds number was about 10,000 and the model river Reynolds number was greater than 500 for currents greater than about 0.5 ft/sec (0.15 m/s).

For the far field model, the similitude requirements of the initial discharge were relaxed while heat transfer to the atmosphere became a controlling factor. Calculations showed that about 35% of the heat discharged by the three plants was dissipated to the atmosphere within the model boundaries. The concept of a heat transfer coefficient,  $K$ , summarizing the heat transfer phenomena of evaporation, conduction, and radiation, has been widely applied (2,19) and may be used to determine a heat transfer scaling criterion given by

$$K_r = \frac{y_r^{3/2}}{x_r} \dots \dots \dots (10)$$

in which  $x_r$  is the horizontal scale ratio. Since the model was located in an atmospherically controlled building where high humidity and zero wind conditions

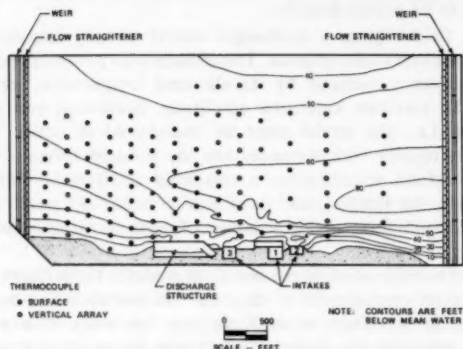


FIG. 4.—Uniform Scale Model General Arrangement (1 ft = 0.3048 m)

prevail, the model heat transfer coefficient was less than the prototype coefficient, and varied from about 60–90 Btu/sq ft/°F/Day (90 and 136 Kcal/m<sup>2</sup>/Day/°C). Prototype heat transfer coefficients vary with seasonal conditions and throughout the day. Typical values are between 100 and 200 Btu/sq ft/°F/Day (150 and 300 Kcal/m<sup>2</sup>/Day/°C), indicating a heat transfer scale ratio of between 0.40 and 0.67 was desirable.

The similitude requirements of equal Froude number and densimetric Froude number, and the need for a minimum Reynolds number for the river flow remain in force. To satisfy the Reynolds number criterion in the far field model, the vertical scale must be similar to that used in the near field model. A horizontal scale less than the vertical scale is required to satisfy the heat transfer scale criterion determined by the expected coefficient values in field and model. Space requirements and flow capacities dictated final values for the horizontal and vertical scales. In this study, a 1–400 horizontal scale and a 1–80 vertical scale were chosen to allow construction of the model in a 75 × 200 ft (23 × 61 m) building. The heat transfer scale ratio is then 0.56–1, which satisfies the

heat transfer coefficient scaling criteria based on typical model and field coefficients.

Other similitude considerations in model design evolved around the scaling of both turbulent and convective transport of momentum and heat, which tend to mix the tracer with ambient water. Evaluation of the extent to which such mixing is scaled in a physical model by use of one-dimensional or two-dimensional dimensionless convection-dispersion equations may be misleading in that these equations approximate and combine the effects of relative convection (dispersion) and turbulence (diffusion). Since the physical model will basically scale the three-dimensional velocity variations with time, depending on the degree of geometric scale distortion, the scaling of "ambient mixing" revolves around the scaling of turbulent diffusion, and how well the spacial and temporal velocity

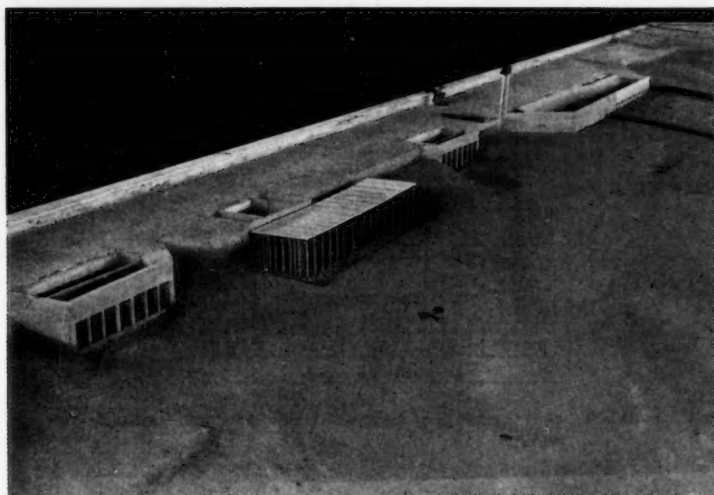


FIG. 5.—Uniform Scale Model Circulating Water Structures

variations are scaled. Excessive geometric scale distortions are undesirable in that the increase in velocity and tracer gradients may affect both dispersion and diffusion. The limitations in scaling diffusion involve the assumption that similitude of the scales of turbulence exists if Reynolds number is sufficiently high. It may be shown by use of the dimensionless three-dimensional diffusion equation, with Fickian heat transport assumed, that the ratio of model to prototype diffusivity coefficients is proportional to the velocity scale times the length scale. Experimentally determined diffusivity coefficients have been found to be proportional to the velocity and characteristic length such that the scaling requirement may be satisfied (18). Despite these formulations, the complete structure of turbulence cannot be modeled, due to the effect of geometry on the upper limit of the turbulence scale and the effect of viscous energy dissipation on the lower limit of turbulence scale. However, turbulent diffusion is unimportant

relative to the dispersion caused by velocity gradients and the relative displacement (mixing) of mass due to large scale eddies caused by river shape (3). The relative importance of convective transport, or dispersion, versus diffusive transport may be estimated by noting that the typical value of dispersion coefficient required in one-dimensional mathematical modeling is about two to three orders of magnitude greater than a typical diffusion coefficient (7). In the case of the Hudson River at Indian Point, the two bends in the river cause complex current patterns that increase the importance of the relative convection terms. Although the cumulative effect of diffusion will be of importance over large

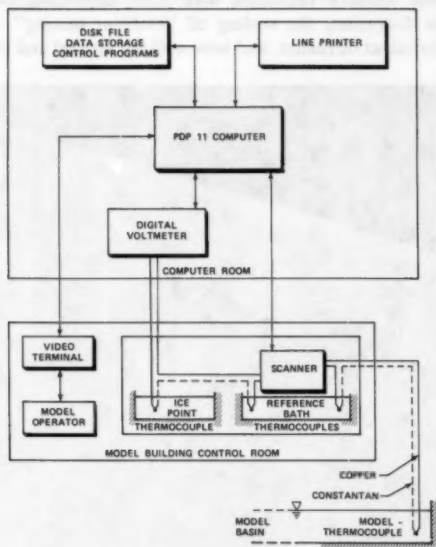


FIG. 6.—Data Acquisition System

distances, the convective transport far outweighs diffusive effects in the limited reaches simulated in the distorted scale model.

Other factors, usually not simulated in a physical model, include natural density gradients caused by thermal and salt stratifications. Natural thermal stratification is considered of secondary importance, but density induced circulation caused by salt gradients may significantly affect mixing by suppressing turbulence in the vertical direction and increasing net convection in both upper and lower layers.

#### MODEL DESCRIPTION

**Uniform 1/75 Scale Nearfield Model.**—The near field model was constructed at a 1-75 scale in a 31 × 65 ft (9.4 × 19.8 m) basin formed by 2-ft (0.61-m)

high concrete walls. The scaled river section, including a width of about 2,000 ft (610 m) from the eastern shore and about 4,600 ft (1,400 m) longitudinally, is shown in Fig. 4. Wooden templates were constructed from topographic data and located and leveled in the basin. The templates were perpendicular to the river center line, and spaced 300 ft (91 m) (prototype) apart except in areas near the discharge and intakes where a 150 ft (45.7 m) (prototype) spacing was used. The basin was then filled with compacted sand to within 1-2 inches (25-51 mm) of the top of the templates and concrete topping was subsequently added to form a watertight bottom. Topographic details near the intake and discharge structures between templates were interpolated using available information. Intake and discharge structures were constructed of treated wood to maintain control of dimensions. The multiple intake pumps were simulated by a manifold system which withdrew water at each pump location at scaled depths and velocities, and perforated plates simulated the rotating screens. Flow from each intake was individually metered and the combined flow was circulated through an oil fired boiler and variable electric immersion heaters to obtain the plant temperature rise. A head tank with an overflow was provided to allow diversion of intake flow into the sump. The oil offloading pier in front

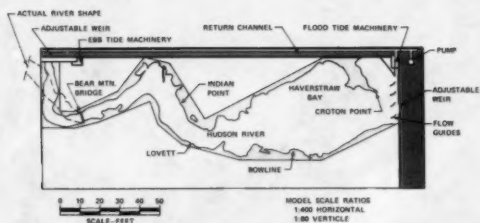


FIG. 7.—Distorted Scale Model—General Arrangement (1 ft = 0.3048 m)

of the Unit 1 intake was simulated such that the drag coefficient of individual piers at the lower model Reynolds number equalled that at the prototype Reynolds number.

A sufficient length of the discharge channel was modeled to assure the velocity distribution approaching the outfall structure was correctly simulated. Details of the prototype outfall structure were scaled to achieve similar flow contractions and, therefore, discharge velocity at the exit. Fig. 5 shows a portion of the completed model prior to instrumentation installations.

Ambient current speeds up to 2 ft/sec (0.61 m/s) prototype were attained in both directions. Flow entered the model via a flow distributor consisting of widely spaced vertical slots and a 35% open area perforated plate which provided a uniform lateral velocity profile. Flow was withdrawn over an adjustable weir at the opposite end of the model and returned to a large volume sump by gravity. An orifice meter in the supply line provided a means to set ambient currents quickly and accurately. Current velocity was measured by timing the traverse of an injected dye streak over a known distance. Water level was monitored with a point gage.

Since the primary purpose of data obtained from this model was to "calibrate" the distorted scale model under similar conditions, it was not required that the lateral velocity distribution in the river scale the field conditions. Therefore, a uniform lateral velocity profile was produced in the 1-75 scale model. A similar profile was produced in the distorted scale model, through the use of baffles and simulation of the uniform model offshore boundary during the calibration phase.

To maintain a constant ambient water temperature within the model, control of the atmosphere above the model was necessary. For heating, a hot air furnace was provided while cooling was accomplished through venting to the outside. General air circulation was forced by the heater, which constantly circulated

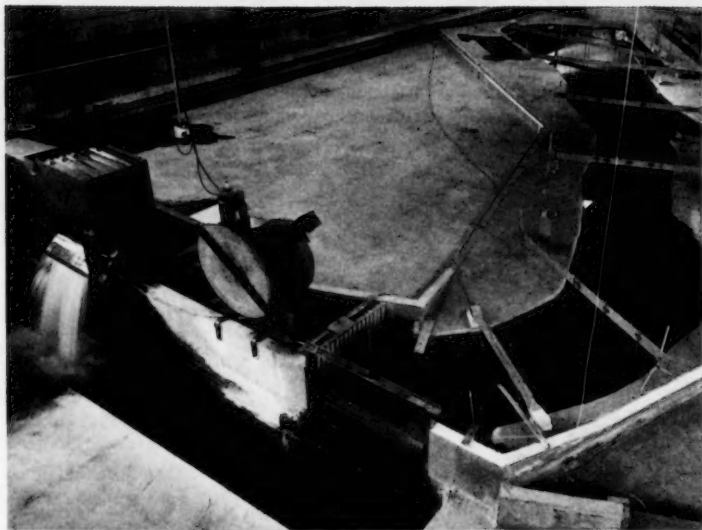


FIG. 8.—Tide Generation Machine;—Upstream Boundary of Distorted Scale Model

air even though the heat exchangers were cool. Sump water temperature was attained by either heating with a 50 hp boiler or cooling with water from an outside source.

Temperature measurement in the model was accomplished by a 216 probe matrix of copper-constantan thermocouples positioned as shown in Fig. 4. These probes measured near-surface temperatures, vertical cross-sectional temperatures, and critical temperatures for model operation, such as intake and discharge temperatures. Near-surface temperatures were measured with probes mounted on styrofoam floats to assure consistent measurement depth regardless of water level. Vertical arrays consisted of four probes equally spaced throughout the depth.



Thermocouple probe conjunctions were welded and insulated to prevent disturbance by stray electrical currents in the water, and were selectively switched into the measurement circuit by a scanner.

The thermocouples were interrogated by the Data Acquisition System shown as a block diagram (Fig. 6). The scanner-multiplexor received its addressing instructions from a mini-computer. Voltages generated in the measuring circuit were converted to digital form by the digital voltmeter and sent to the computer for conversion to temperatures and further processing. The accuracy of the measurement and conversion process was approx  $\pm 0.15^\circ \text{F}$  ( $\pm 0.08^\circ \text{C}$ ).

Reading the 216 probes and storing the data in a permanent disk storage file required approx 20 sec and was either manually controlled or controlled to scan at given time intervals automatically. Programming was available to retrieve the stored data and process it in various ways. Ambient probes could be specified and the data printed in tabular or various map forms, and averaging of any combination of scans was also possible. In map form, overall model



FIG. 9.—Comparison of Model and Field Velocity Patterns in Haverstraw Bay (1 ft/sec = 0.3048 m/s) (12)

surface temperatures were displayed in their correct spatial location. Either the actual temperature measured or a temperature difference relative to selected probes measuring ambient temperature could be displayed.

#### MODEL OPERATION

To initiate a test, the desired ambient temperature was obtained, a current speed set, and the water level set at mean tide level. Intake flow rates were set and the flow returned directly to the sump while the plant temperature rise was adjusted. Operation of the temperature sensors and data retrieval system were verified. When a constant ambient temperature was achieved throughout the model, the simulated condenser flow was diverted to the model and periodic scans were recorded until subsequent scans showed steady state had been reached, at which time three scans were recorded and averaged.

Preparations for varying current tests were similar to the constant velocity tests. A steady current of 0.2 ft/sec (0.06 m/s) was set, and sufficient time

with plant discharge elapsed to reach steady conditions. The current was then reversed by manually changing valves at the correct time scale while maintaining mean water level. Data were recorded automatically every 2 min (17.3 min prototype).

**Distorted Scale Model—Intermediate and Farfield.**—The overall distorted scale model simulated approx 15 miles (24 km) of the Hudson River from a point about 2 miles (3.2 km) upstream of Bear Mountain Bridge, to Croton Point in the south (Fig. 7). The horizontal and vertical scale ratios were 1:400 to 1:80, respectively, resulting in a geometric distortion of 5. The construction technique was the same as described for the uniform scale model.

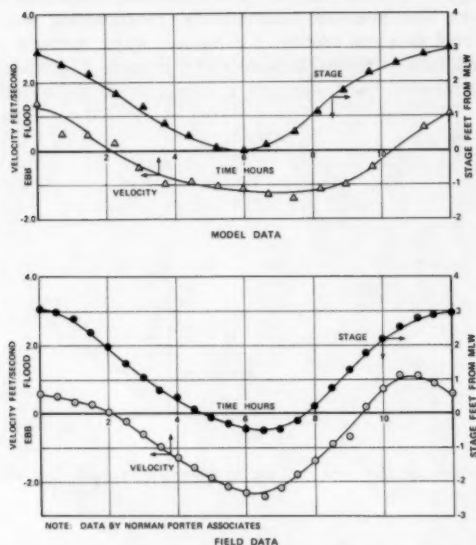


FIG. 10.—Comparison of Model and Field Current Speed at Indian Point (1 ft = 0.3048 m) (17)

To include a maximum river length in the available space, the plan shape of the river was altered upstream of Bear Mountain Bridge by adding bend, which allowed simulation of an additional 1.4 miles (2.3 km) of river. Since the tidal prism from the Indian Point Site reaches upstream only to Bear Mountain Bridge, the altered river alignment had no first order effect on effluent patterns at Indian Point. The additional river length upstream from the Bear Mountain Bridge insured that no plant induced heat was lost over the upstream model boundary due to dispersion during progressive tidal cycles.

A 1,300 cu ft (37 m<sup>3</sup>) sump provided a reservoir for the 10 hp (7.5 KW) vertical pump, which supplied inflow to constant head tanks at both ends of the model and mixed the sump water to maintain a uniform ambient temperature.

Sump temperature was raised to the desired ambient by heating with a 50 hp (37.5 KW) boiler. Tide controls were provided at both ends of the model and inflow to the model was controlled by a deflector riding under a slot orifice along the bottom of a constant head tank. Outflow was controlled by a movable sharp-crested weir. Both deflector and weir positions were controlled by cams rotating at 16.8 min/revolution, scaling the 12.5-hr tide cycle. The tide machinery in Fig. 8 was synchronized electrically once per tide cycle, and controls were designed to achieve average tidal values. The fresh water flow rate incorporated in the design of the tide machines was the minimum monthly average of 4,000 cu ft/sec (113 m<sup>3</sup>/s). This flowrate was checked and adjusted by the volumetric method. To model freshwater runoff flow rates greater than 4,000 cu ft/sec (113 m<sup>3</sup>/s), the required additional inflow was provided at the upstream model boundary by a separate constant metered flow from the head tank. An equal metered outflow was located at the downstream model boundary. Inflow boundary conditions were adjusted by means of vanes to provide a uniform velocity distribution.

At those times during the year when the fresh water runoff is low, significant

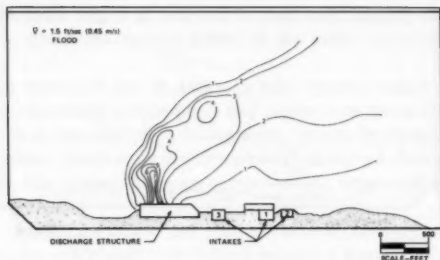


FIG. 11.—Surface Temperature Rise Patterns in Uniform Scale Model (Temperature Rises are in Fahrenheit, 1° F = 0.56° C) (1 ft = 0.3048 m)

levels of salt are present at the Indian Point site, indicating the presence of density induced circulation. To simulate vertical salinity gradients would require control of two flow rates and associated salinities at both ends of the model, and two independent reservoirs with salinity control would, therefore, be necessary. A system to separate the outflow from both ends of the model into components with the approximate salinity of the reservoirs would be necessary to conserve salt and water. Due to the complexity of design, construction, and operation of such a system, simulation of salinity gradients was not attempted.

The plant condenser temperature rise was achieved by variable current electrical immersion heaters. Time of travel of a particle of water from the intake through the heater system to the discharge structure was approximately equal to that of the actual plant so that recirculation was directly simulated. The effects of recirculation on discharge temperature and plume characteristics were, therefore, automatically reproduced, a factor which may be important for tidal flow variations. Intake structures were modeled to the distorted scale, and flow

was withdrawn at the scaled level. Individual orifice meters measured flowrate through each intake structure, and the flow was combined prior to entering the heaters.

A matrix of 340 thermocouples measured temperatures using the data acquisition system described above. Because of the high probe density and complex geometry, temperature rises were plotted manually. Several thermocouples were mounted on the downstream weir to determine the outflow water temperature and, therefore, the heat content of the water leaving the model.

The heat leaving the model was distributed in the sump by the mixing of the vertical pump. To maintain a constant ambient temperature throughout a test, a metered flow of water, cooler than ambient, was supplied to the sump. The inflow rate was manually adjusted to counteract the plant discharged heat leaving the model.

In cases of strong vertical mixing of the effluent with ambient water, such as with deepwater diffuser outfalls, water temperatures at the concrete forming the model boundaries could be greater than ambient temperature. Since the

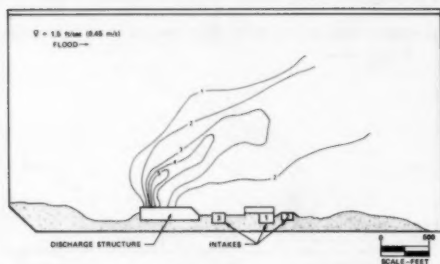


FIG. 12.—Surface Temperature Rise Patterns—Calibration of Distorted Scale Model (Temperature Rises are in Fahrenheit,  $1^{\circ}\text{F} = 0.56^{\circ}\text{C}$ ) (1 ft = 0.3048 m)

concrete and sand fill was carefully brought to ambient temperature prior to a test, the model boundary would represent a heat sink when river temperatures increased above ambient. Thermocouples were embedded at various levels in the sand and concrete to provide a measure of any heat transfer into the model.

Heat transfer to the atmosphere and equilibrium water temperature were measured by two insulated pans of water 2 ft  $\times$  4 ft  $\times$  1.5 in. (0.61 m  $\times$  1.22 m  $\times$  38 mm) deep. An investigation of the effect of pan size on equilibrium temperature and heat transfer coefficient showed no discernable effect over a range of sizes from 1.5–8 ft (0.46–2.44 m) square. Water depth was 1.5 in. (38 mm) in order to have the indicator react more quickly than the model. One pan had a constant energy input from an electrical immersion heater to cause an elevated temperature. Care was taken to assure that the rate of energy input was such that the pan temperature rise was similar to the average temperature rise in the model since heat transfer is dependent on water temperature. A heat transfer coefficient was defined as the heat input per unit area divided by the temperature difference between the heated and unheated pans.

Complete descriptions of the model are given in Hecker and Gurney (5) and

Hecker and Medeiros (6) as well as detailed test results for various plant conditions and outfall geometries.

#### TEST PROCEDURE

Prior to a test, the desired ambient temperature was set by heating or cooling the sump and allowing a steady unidirectional flow in the model. Room heaters, vents, and a roof sprinkler were controlled automatically by sensing temperature in the equilibrium pan and changing atmospheric conditions such that the equilibrium temperature equalled the ambient model river temperature. Sufficient time was allowed to achieve an equilibrium thermal condition between the ambient water, the atmosphere, and the thermal mass of the model. A physical check of all thermocouple probes assured correct location, and all thermocouples were scanned to verify electronic operation of the data acquisition system and initial temperature uniformity. Plant flow and temperature rises were set and the tide machinery started.

During a test, atmospheric conditions, equilibrium temperature, plant conditions, sump, and concrete temperatures were periodically monitored and plotted. If the sump temperature began to rise due to plant heat leaving the downstream end of the model, cooler water was added to the sump to achieve a constant ambient.

The model was operated for at least 10 tide cycles, which was normally sufficient to attain repeatable temperature rise patterns on successive tide cycles. Data were recorded at the same time during every tide cycle during the document transient phase. When steady state conditions were achieved, data were recorded each hour in four tide cycles. Data at corresponding times and positions were then averaged and plotted.

For some test conditions where the effluent was effectively mixed over the depth of the river, the model concrete bottom became a heat sink for the effluent. The model concrete and backfill temperatures were monitored, and the test was run until an equilibrium condition was attained, in which the heat loss to the model boundaries were minimized. In some cases, this required a 24-hr test. It was possible to calculate a thermal balance for the model since the plant heat input was known, and measurements of heat loss over the downstream weir, to the atmosphere, and to the bottom boundary, were made.

**Verification of Tidal Hydraulics.**—Basic design data for average tidal flows, river stage, and fresh-water runoff were obtained from historical records. To verify that overall current patterns and velocities were simulated adequately, two field surveys were conducted to obtain information in the vicinity of the Indian Point Station. The Alden Research Laboratory, ARL, conducted drouge studies in 1968 and 1969 to determine flow patterns and current speeds in Haverstraw Bay and near Indian Point (12). Sequential aerial photographs determined the path of several drouges for a time period of about one-half the tide cycle. Similar measurements were conducted in the model using interrupted time exposure photographs of drouges with attached light sources. Fig. 9 shows that the flow patterns and velocities in the model compare favorably to those in the prototype in Haverstraw Bay. Another drouge study, conducted within 400 ft (122 m) of the intake (17), assisted in the verification of the velocity-stage phase relationship. Model velocities were determined by measuring

the time of travel of dye spots injected into the water at locations corresponding to the drouge tracks. Since the model was operated at average stage and velocity, the field data were multiplied by the ratio of the stage on the day of the survey to the average stage. Fig. 10 compares the relationship between velocity and stage for field and model. Field data indicate maximum river stage occurs approximately at maximum flood current. Detailed comparisons of the velocities at this location is not warranted due to difficulties of spacial resolution in the model. The model is seen to produce a similar tidal relationship of stage to current, and the influence of average river currents and stages on thermal patterns would be simulated in the model.

#### TYPICAL RESULTS

**Uniform Scale Model—Nearfield Results.**—The uniform scale model was used to determine near field temperature rise patterns for various steady currents in both ebb and flood directions and for a transient reversing current. These data indicated the maximum local surface temperature, provided for detailed comparison between the shoreline and diffuser discharge, and also provided information for calibration of the distorted scale model discharge structure.

Typical results for two unit operations with the shoreline discharge are shown in Fig. 11 for a 1.5 ft/sec (0.46 m/s) flood current. Dye injection showed that the initial plume trajectory opposed the flood current direction due to the geometry of the discharge channel. Flow leaving the first upstream discharge port had a considerable velocity component parallel to the face of the discharge structure due to the approach velocity in the discharge channel. This lateral component of velocity decreased in the downstream direction until the discharge was essentially perpendicular to the structure at the last port. The resulting net downstream momentum caused the initial thermal plume direction to oppose the flood current, therefore, producing a plume trajectory well-removed from the shoreline for flood currents and minimized direct recirculation. Due to the variation in port discharge direction along the discharge structure, the individual port discharges converged in front of the structure, causing the plume to have a minimum lateral width of only about 200 ft (61 m). Temperature rises in the flow away region, after the initial rapid dilution, were somewhat greater than 2° F (1.1° C) and maximum local temperature rises were about 8° F (4.4° C).

Similar temperature data were generated for steady currents of 0.5, 1.0, 1.5, and 2.0 ft/sec (0.15, 0.30, 0.46, and 0.61 m/s) in both ebb and flood directions. A transient current beginning at 0.5 ft/sec (0.15 m/s) and reversing to 0.5 ft/sec in the opposite direction was simulated to determine the effects of returning heat on near field temperatures. During the transient tests, boundary effects were significant, and, therefore, the results were used only qualitatively to verify the distorted scale model during similar transient tests.

#### Distorted Scale Model

**Nearfield Calibration.**—Ambient flow conditions in the distorted scale model were forced to approximate those used in the uniform scale model by the use of a false longitudinal wall and lateral flow straighteners. The outfall structure was then modified so that the resulting thermal patterns at various steady currents matched the patterns determined in the uniform scale model. The primary change

in the distorted scale model discharge structure needed to basically reproduce the near field plume characteristics measured in the uniform scale model was a fourfold decrease in discharge velocity from the direct scaled value. The discharge structure geometry was also modified in other minor ways to refine the thermal patterns. Resulting thermal patterns are in Fig. 12 for similar conditions as existing for the uniform scale model results in Fig. 11. General agreement of the plume trajectory and flow away temperature rises is indicated while nearshore temperature rises were somewhat greater in the undistorted model for this particular current. For all currents, the plume trajectory agreement was good, and, while distorted model isotherm areas did not match exactly in any case, they were typically similar to those determined in the uniform

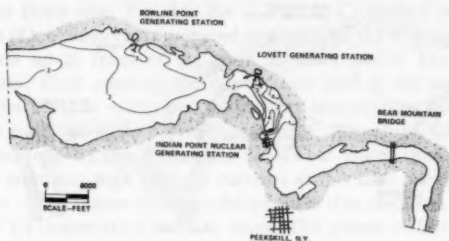


FIG. 13.—Overall Temperature Rise Patterns—Slack Tide Prior to Flood (Temperature Rises are in Fahrenheit,  $1^{\circ} F = 0.56^{\circ} C$ )

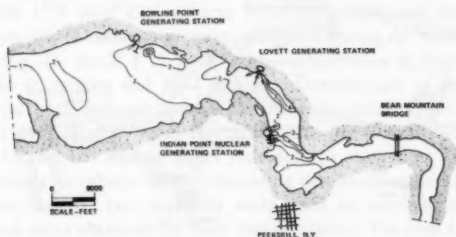


FIG. 14.—Overall Temperature Rise Patterns—Maximum Flood Tide (Temperature Rises are in Fahrenheit,  $1^{\circ} F = 0.56^{\circ} C$ )

scale model. Maximum temperature rises were less in the distorted scale model. Transient current tests conducted in the distorted scale model also indicated an adequate simulation of the uniform scale model results.

Complete agreement of thermal plumes in the near field in all aspects for all current cases was not obtained and was not a requirement since the purpose of the distorted scale model testing was to obtain intermediate and far field data. Agreement of the plume trajectory, depth, and temperature rises at the interface between near field and intermediate field was of greater significance than details of isotherm areas in the near field. These flow-away parameters

were reasonably approximated by the distorted scale model discharge structure, and, therefore, the calibration was sufficiently accurate to produce correct results in the intermediate and far field. The total heat flux, i.e., the flow and initial temperature rise, was scaled directly in both models such that a proper heat balance was obtained in the distorted scale overall model.

Similar calibration procedures were conducted for both the Bowline and Lovett stations. Uniform scale model test data (13) were used in the former case, while field data (15) were used in the latter case.

**Overall Temperature Rise Patterns.**—Surface and cross-sectional temperature-rise patterns were plotted at each hour in the tidal cycle. Selected typical results of surface patterns for two unit operation are shown at four times in the tide



FIG. 15.—Overall Temperature Rise Patterns—Slack Tide Prior to Ebb (Temperature Rises are in Fahrenheit,  $1^{\circ}\text{F} = 0.56^{\circ}\text{C}$ )

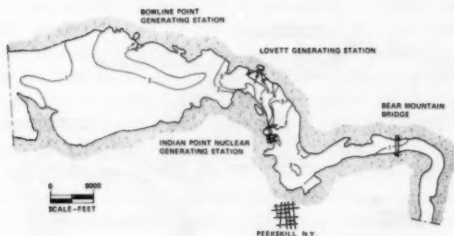


FIG. 16.—Overall Temperature Rise Patterns—Maximum Ebb Tide (Temperature Rises are in Fahrenheit,  $1^{\circ}\text{F} = 0.56^{\circ}\text{C}$ )

cycle to illustrate the variation of thermal patterns with tidal flow. Results shown are the average of four scans recorded at the same time in consecutive tide cycles after quasi-steady conditions had been attained. Freshwater runoff was 20,800 cu ft/sec (589 m<sup>3</sup>/s) and the measured heat transfer coefficient was approximately 140 Btu/sq ft/Day/°F (210 Kcal/m<sup>2</sup>/Day/°C), both parameters scaled to prototype values. Plant operation simulated conditions existing during a field survey to be detailed below, and only Units 1 and 2 were operating. Bowline operated at one-half capacity and Lovett operated at reduced load. Only surface temperature patterns will be shown to simplify the presentation.

Thermal patterns at slack water prior to flood are in Fig. 13. Ambient



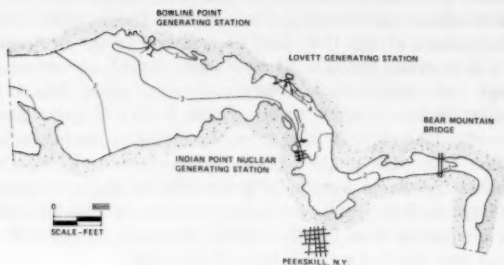
temperature water penetrated downstream nearly to Indian Point, and the 1° F (0.6° C) isotherm crosses the river near the plant site. The location of the farthest downstream movement of the 1° F (0.6° C) isotherm in the upstream reaches of the model was a strong function of freshwater runoff, as will be illustrated by tidal average and lateral average temperature rise plots. The 4° F (2.2° C) isotherm increased in area at slack water, and the 3° F (1.7° C) isotherm crossed the river diagonally, merging with the Lovett plume. Large temperature gradients existed at Indian Point due to the ambient ebb current while downstream of Lovett temperature gradients were small due to the mixing caused by the river bend, and the large surface areas, which allowed considerable atmospheric heat transfer. Heat originating from the Bowline discharge produced a 2° F (1.1° C) temperature rise near the downstream limit of the model.

At maximum flood tide, Fig. 14, the 1° F (0.6° C) surface isotherm moved about 2.5 miles (4 km) upstream compared to slack, and the 4° F (2.2° C) isotherm, which had built up in front of the plant at slack water, has separated and moved upstream. Flow entering the downstream end of the model has a heat deficit since the sump is controlled at ambient temperature and water leaving the model normally contains some excess heat. Therefore, the isotherms at the downstream end of the model are somewhat lower than would exist in the field. The relatively high ambient currents at this time provide rapid mixing and convection of the Indian Point discharge, such that the areas of 3° F (1.7° C) and 4° F (2.2° C) temperature rise are small. The plume at Lovett is restricted to the nearshore region.

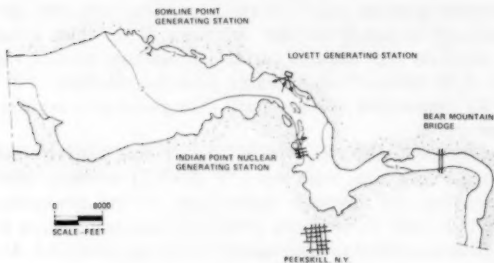
At slack water prior to ebb tide, Fig. 15, the thermal patterns reached their maximum upstream locations, with the 1° F (0.6° C) isotherm located about 2 miles (3.2 km) from the upstream model limit. At the downstream end of the model, the 1° F (0.6° C) isotherm penetrated upstream about halfway to the Bowline site due to ambient temperature flow entering the model. At maximum ebb current, Fig. 16, the 2° F (1.1° C) isotherm upstream of Indian Point rapidly dissipated due to mixing and heat transfer. Downstream at Indian Point, the 2° F (1.1° C) isotherm was continuous past Bowline, and a 4° F (2.2° C) isotherm crossed the river diagonally from Indian Point to the Lovett plume.

Since the 13 thermal pattern plots representing each hour in the tide cycle are cumbersome to evaluate when comparing discharge structures or the effect of fresh water runoff, two methods were used to summarize the numerous thermal pattern plots obtained for each test condition. The first type of summary was averaging the 13 hourly plots over the tidal cycle. From this tidal average data of surface temperature rises, a spatial average plot was calculated by averaging the lateral variation at each instrumented station along the river center line. The lateral average temperature was derived using the river width associated with individual thermocouples as a weighting factor. The lateral average temperature rise was plotted versus center line distance, and was useful for comparison to mathematical model predictions. The tidal average surface temperature plot and the lateral surface average versus center line distance plot will be used to illustrate the effects of plant loads at Indian Point, freshwater river flowrates, and discharge geometry.

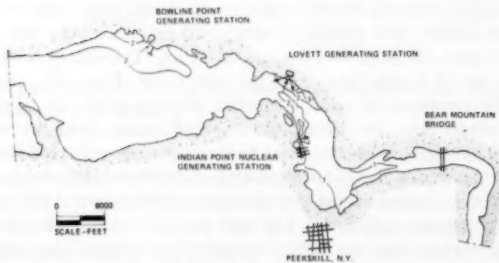
The effect of freshwater runoff on tidal average thermal patterns is shown in Fig. 17, where three runoffs are compared. The first runoff, 12,000 cu ft/sec (340 m<sup>3</sup>/s), simulated the value measured during a field survey; the second



TIDAL AVERAGE SURFACE THERMAL PATTERNS, TWO UNIT  
SHORELINE DISCHARGE, FRESHWATER RUNOFF = 12,000 FT



TIDAL AVERAGE SURFACE THERMAL PATTERNS, TWO UNIT  
SHORELINE DISCHARGE, FRESHWATER RUNOFF = 20,800 FT



TIDAL AVERAGE SURFACE THERMAL PATTERNS, TWO UNIT  
SHORELINE DISCHARGE, FRESHWATER RUNOFF = 35,000 CFS

**FIG. 17.—Tidal Average Overall Temperature Rise Patterns—Two Unit Operation with Shoreline Discharge (Temperature Rises are in Fahrenheit,  $1^{\circ} \text{F} = 0.56^{\circ} \text{C}$ )**

runoff, 20,800 cu ft/sec (589 m<sup>3</sup>/s), represents the minimum predicted net flushing, including density induced circulation, and the last runoff, 35,000 cu ft/sec (991 m<sup>3</sup>/s), represents the predicted net flushing flowrate due to density induced circulation at the 12,000 cu ft/sec (340 m<sup>3</sup>/s) freshwater runoff (Fig.

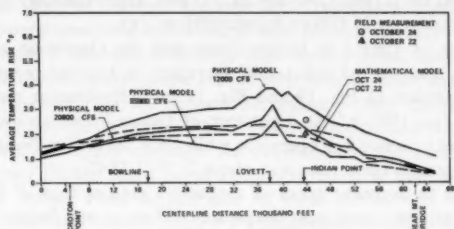


FIG. 18.—Comparison of Physical and Mathematical Model Predictions of Lateral Average Surface Temperature Rise Patterns (Temperature Rises are in Fahrenheit, 1° F = 0.56° C)

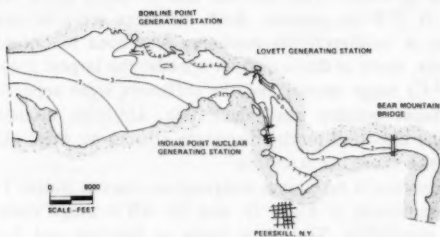


FIG. 19.—Tidal Average Overall Temperature Rise Patterns—Three-Unit Operation with Shoreline Discharge (Temperature Rises are in Fahrenheit, 1° F = 0.56° C)

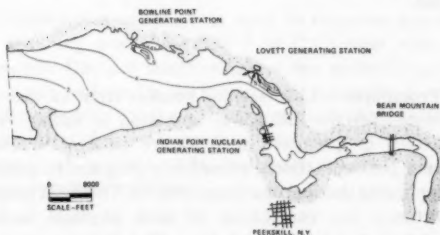


FIG. 20.—Tidal Average Overall Temperature Rise Patterns—Three-Unit Operation with Diffuser Discharge (Temperature Rises are in Fahrenheit, 1° F = 0.56° C)

2). The effect on average surface temperature values is dramatic, with all isotherms being displaced downstream and maximum temperatures decreasing with increasing flows. Temperature rises between Indian Point and Bowline decreased from

greater than 3° F (1.7° C) at 12,000 cu ft/sec (340 m<sup>3</sup>/s) to less than 2° F (1.1° C) at 35,000 cu ft/sec (991 m<sup>3</sup>/s). The lateral average surface temperature rises for the same cases are shown in Fig. 18. Temperature rises decrease almost 1° F (0.6° C) on the average for a change in freshwater river flow from 12,000 to 20,800 cu ft/sec (340–589 m<sup>3</sup>/s) and approximately 0.5° F (6.3° C) more for an increase to 35,000 cu ft/sec (991 m<sup>3</sup>/s).

The operation of Unit 3 at Indian Point and the Operation of Lovett and Bowline at full load caused substantial increases in average temperature rises, shown by comparison of Fig. 19 and Fig. 17 for a freshwater runoff flow rate of 20,800 cu ft/sec (589 m<sup>3</sup>/s). Upstream of Indian Point, an increase of 1° F (0.6° C) occurred over two unit operation while between Indian Point and Bowline, the increase in temperature rises was about 2° F (1.1° C).

In an attempt to decrease areas of isotherms greater than 4° F (2.2° C), an outfall system with two multiport deepwater diffusers was designed. A diffuser was designed for Units 1 and 3 having 35 three-foot (0.91 m) diameter ports on 25 ft (7.6 m) centers. This diffuser was located in about 55 ft (16.8 m) of water 340 ft (104 m) offshore of the existing structure. The Unit 2 diffuser was placed approx 3,000 ft (914 m) upstream of the existing structure, also in 55 ft (16.8 m) of water. This diffuser had 25 ports three feet (0.91 m) in diameter on 25 ft (7.6 m) centers. Both diffusers were oriented 45° to the current direction. A unidirectional discharge was used to optimize dilution at low current speeds, since at those current speeds, the largest areas of isotherms in the 4° F (2.2° C) range occur, and the diffusers were separated to attempt to decrease effluent buildup near slack tide. Uniform models tested were conducted and the distorted model discharge structures were calibrated in the same manner as the shoreline structure.

Substantial decreases in maximum temperature rises at Indian Point occurred, as shown by comparison of Figs. 19 and 20. All average rises 4° F (2.2° C) or greater were eliminated. Since heat loads at Bowline and Lovett remained constant, the changes in the vicinity of these plants were minimal. The diffusers were able only to decrease maximum temperature rises near Indian Point while overall patterns away from the discharge location remained similar to dissipate the given heat load.

#### FIELD PROGRAM

**Description of Procedures.**—Licenses and permits from various governmental agencies were granted for the full power operation of Indian Point Unit No. 2 partly on the basis of predicted temperature patterns. Provisions in the regulations require a post-operational monitoring program to demonstrate compliance with the applicable thermal discharge criteria. This field program provided an unusual opportunity for verification of both physical models, and the mathematical model to be described below. The field survey program was conducted between May, 1974 and October, 1976 (9,10).

Temperature measurements were made from two survey boats equipped with electronic range navigation systems and arrays of thermister temperature sensors. Automatic equipment recorded temperature and location on magnetic tape and a backup printer. Digital display allowed real time decisions to be made so that only the area of interest was surveyed. One boat was equipped to survey

to a depth of 20 ft (6.1 m) and that boat surveyed the plume in the vicinity of the outfall where plume depth was greatest. The second boat was equipped with a fixed sensor array to a depth of 6 ft (1.8 m) and was assigned to survey at greater distances from the outfall. Boat speed was varied from 2–8 knot (1–4 m/s), depending on the spacial temperature resolution required.

Ambient temperatures were measured at Bear Mountain Bridge at slack before flood and during ebb tide, and at Croton Point during flood, and at slack before ebb. At these locations, prior to the survey near Indian Point, detailed measurements of temperature, current speed, and salinity were conducted over the entire cross section. In the field, the ambient temperature is a spatially, as well as temporally, varying quantity. An evaluation of the measured ambients at Bear Mountain Bridge and Croton Point was made to estimate the ambient temperature at Indian Point at the time of each survey. To supplement the surface measurements, thermal imaginary measurements were conducted concurrently using infrared radiation scanning equipment in a light plane. The imaginary data were synoptic in nature and covered a significantly greater area than the surface measurements. However, the thermal imaginary data were not used

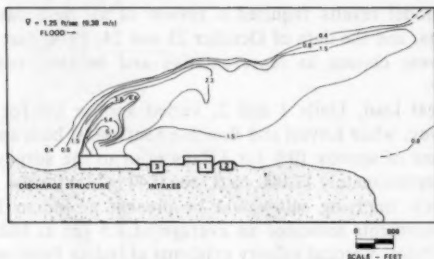


FIG. 21.—Field Measurement of Surface Temperature Rise Patterns (Temperature Rises are in Fahrenheit,  $1^{\circ}\text{F} = 0.56^{\circ}\text{C}$ ) (1 ft = 0.3048 m) (10)

extensively for field-model comparisons since its response was to a thin surface layer and the accuracy was about  $1.0^{\circ}\text{F}$  ( $0.5^{\circ}\text{C}$ ) even with several ground truth measurements. Detailed descriptions of the methodology and results of the field program may be found in the Indian Point report (8). To ensure maximum compatibility of conditions for the comparison, both physical and mathematical models were run after the field surveys using the applicable field values for input parameters, such as plant loads, freshwater runoff, ambient temperature, and surface heat transfer coefficient.

#### FIELD-MODEL COMPARISON

**Near Field.**—Near field data from the uniform scale model (Fig. 11) may be compared to field data taken on October 15, 1976 (9), shown in Fig. 21. During this particular survey, the plant temperature rise was greater than that used for the uniform scale model; therefore, to allow direct comparison, each field temperature rise was prorated by the ratio of model to field plant temperature

rise. Current speed was not measured, but predictions for Peekskill from the 1976 Tidal Current Table indicate a speed of approx 1.25 ft/sec (0.38 m/s). Initial plume trajectory and temperature gradients show reasonable agreement although the field plume does not travel quite as far offshore as the model plume. Isotherm areas show good agreement also, except the very near field, where the field data indicate larger areas. Some differences in model and field data are to be expected since conditions are not matched completely. In the field, more time was required to gather the data so that distortion of the plume is possible. Model data were an average of several scans to achieve better repeatability and a more representative result. The field current distribution and speed were not known accurately and were not uniform and steady as in the model. Therefore, the nearfield comparison appears reasonable in light of the approximations required.

**Overall Temperature Rise Patterns.**—Variability of far field data was considerable due to the intrinsic difficulty in obtaining synoptic field data and the variation in ambient conditions. Typically, tidal flows, freshwater flow, ambient temperature, and all meteorological parameters are changing, both temporally and spatially; therefore, detailed replication of results was not expected. To compare field results to model results required a review of all field data and use of typical field results, and the data of October 23 and 24, 1974, part of a four-day survey record, were chosen as representative and because conditions were reasonably steady.

Indian Point heat load, Units 1 and 2, varied approx 6% for 5 days prior to the chosen survey, while Lovett and Bowline heat loads, both approx one-half load, had variations of approx 10% for 3 days prior to the survey. Freshwater runoff averaged approximately 12,000 cu ft/sec (340 m<sup>3</sup>/s) for the 30-day period prior to the survey, implying salt would be present at Indian Point (Fig. 2) and salinity measurements indicated an average of 1.5 ppt at Indian Point and 4.2 ppt at Croton Point. Vertical salinity gradients at Indian Point were relatively strong, the bottom salinity being four times greater than the surface salinity. Average wind speed was less than 5 miles/hr (2.2 m/s) and air temperatures varied from 44.5° F (6.9° C) to 67° F (19.4° C) under clear skies. The average surface heat transfer coefficient was approx 105 Btu/sq ft/Day/°F (158 Kcal/m<sup>2</sup>/Day/°C) determined from measured meteorological conditions. Ambient water temperature decreased from approx 58° F (14.6° C) on the 22nd to 57° F (13.8° C) on the 25th. For the data presented, ambient water temperature was approximately constant at 57.8° F (14.3° C).

Thermal imaginary data were used to verify general model plume shapes near the plant site and agreement was found to be good. Thermal imaginary converted to temperature is illustrated in Fig. 22 for low water slack on October 24, 1975. The complex temperature distribution with large lateral and longitudinal temperature gradients, especially in the Haverstraw Bay area, indicate the difficulties involved in the analysis of field data. The infra-red data show the complexity of thermal patterns due to differential heating or cooling in shallow versus deep regions of the river and due to smaller artificial heat sources. Wind induced surface currents and small streams possibly further complicate the natural temperature patterns.

Model tests were conducted to simulate field conditions during the chosen survey period. Three test series were conducted to check on model consistency,

and the most representative model results were chosen for comparison. Other than plant loads, the only directly controlled variable in the model tests was the freshwater runoff. Since salt was present at Indian Point during all field surveys, density induced circulation existed, which could not be directly reproduced in the model. Although the complex phenomena occurring due to density induced circulation affects the dissipation of the plant effluent in many subtle

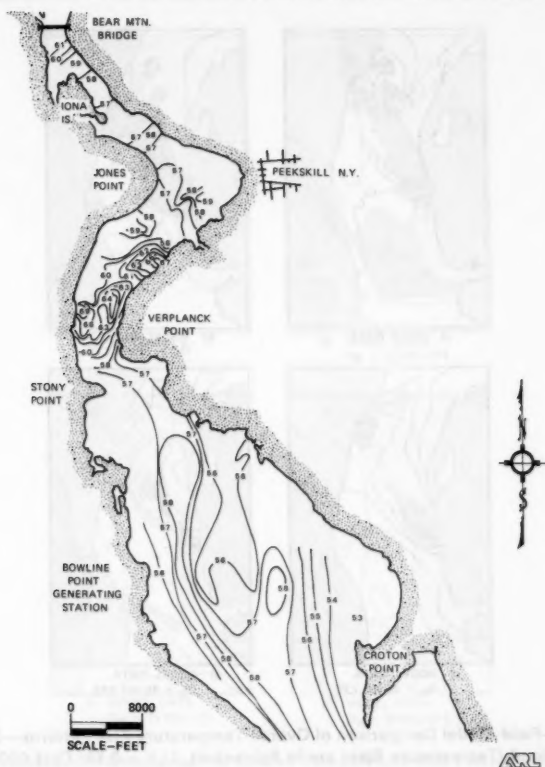


FIG. 22.—Field Surface Temperature Rise Patterns from Infra-Red Aerial Survey (Temperature Rises are in Fahrenheit,  $1^{\circ} \text{F} = 0.56^{\circ} \text{C}$ )

ways, the main effect is to increase the net through flow available for mixing. As a first order approximation, therefore, an attempt to simulate the effect of the density induced net flushing was made by increasing the freshwater runoff. The freshwater flow was distributed over the entire cross section of the river, whereas density induced circulation causes an upstream migration of flow in a lower layer and an equal downstream flow in addition to the

freshwater flow in an upper layer. This basic difference in the two phenomena makes simulation of density induced flow by increased freshwater runoff uncertain. Three flow rates were used; the actual measured value, the minimum predicted density induced circulation (20,800 cu ft/sec [ $589 \text{ m}^3/\text{s}$ ], Fig. 2), and 35,000 cu ft/sec ( $991 \text{ m}^3/\text{s}$ ), the predicted density induced circulation for the measured freshwater runoff flow rate.

Field data show that at slack before flood (low water slack), Fig. 23(a),

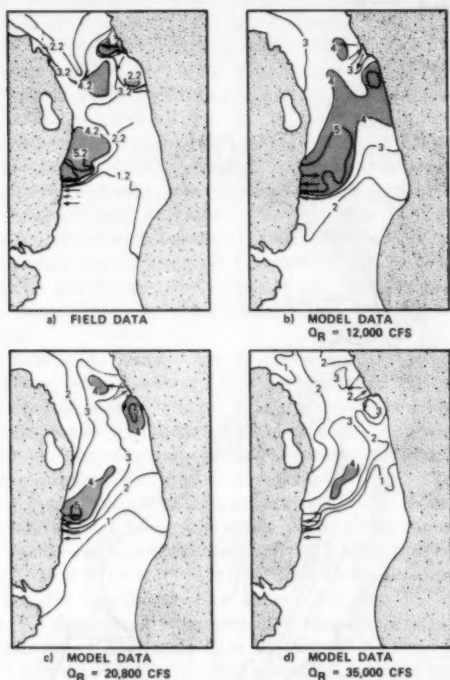


FIG. 23.—Field-Model Comparison of Overall Temperature Rise Patterns—Slack Tide Prior to Flood (Temperature Rises are in Fahrenheit,  $1^\circ \text{F} = 0.56^\circ \text{C}$ ) (1,000 cu ft/sec =  $28.3 \text{ m}^3/\text{s}$ )

the Indian Point plume occupied approx one-half the river width with strong upstream temperature gradients. A large  $5^\circ \text{F}$  ( $2.8^\circ \text{C}$ ) isotherm had built up in front of both Indian Point and Lovett. The  $4^\circ \text{F}$  ( $2.2^\circ \text{C}$ ) isotherm nearly crossed the river from Indian Point to merge with the Lovett plume. The  $1^\circ \text{F}$  ( $0.6^\circ \text{C}$ ) isotherm crossed the river near Indian Point. Model data at this time show similar plume shape and temperature gradients, regardless of freshwater flow. In the 12,000 cu ft/sec ( $340 \text{ m}^3/\text{s}$ ) case Fig. 23(b), the  $4^\circ \text{F}$  ( $2.2^\circ \text{C}$ ) and  $5^\circ \text{F}$  ( $2.8^\circ \text{C}$ ) isotherms were considerably larger than the field results, while



for largest flow, Fig. 23(d), temperature rises were generally too small. Temperature rises near Indian Point were approximately correct in the 20,800 cu ft/sec ( $589 \text{ m}^3/\text{s}$ ) case. At Lovett, model temperatures are lower than field results.

At maximum flood current, field data indicate the Indian Point plume occupied almost the entire river width, Figure 24(a). Temperature gradients were relatively strong on both sides of the plume and the plume was relatively limited in its longitudinal extent. The influence of Lovett was not well defined, but  $3^\circ \text{ F}$

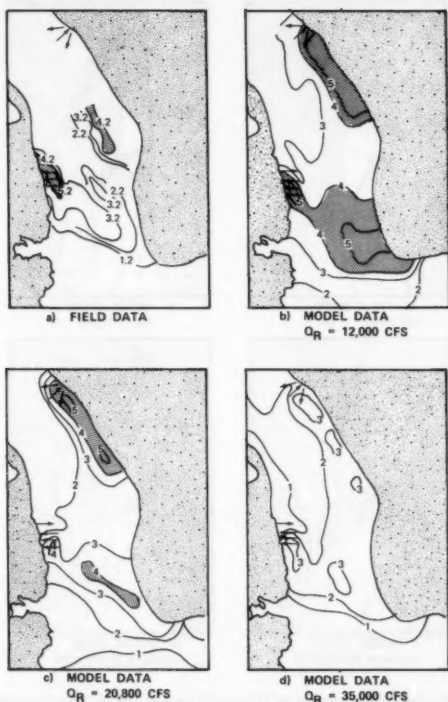


FIG. 24.—Field-Model Comparison of Overall Temperature Rise Patterns—Maximum Flood Tide (Temperature Rises are in Fahrenheit,  $1^\circ \text{ F} = 0.56^\circ \text{ C}$ ) ( $1,000 \text{ cu ft/sec} = 28.3 \text{ m}^3/\text{s}$ )

( $1.7^\circ \text{ C}$ ) and  $4^\circ \text{ F}$  ( $2.2^\circ \text{ C}$ ) isotherms were evident opposite the Indian Point site. Model temperature gradients and plume shape show reasonable similarity. The 12,000 cu ft/sec ( $340 \text{ m}^3/\text{s}$ ) case, Fig. 24(b), showed good agreement of near field temperature rises, but overestimated temperatures farther from the plant. The 20,800 cu ft/sec ( $589 \text{ m}^3/\text{s}$ ) case, Fig. 24(c), underestimated nearfield temperature rises, but more nearly matched temperature rises farther from the plant. In the model, the Lovett plume did not travel upstream as far as the

field results showed, but temperature rises were similar for the two lower freshwater flowrates.

At slack before ebb (high water slack), field data, Figure 25(a), indicated the Indian Point plume had the minimum size of the four tidal phases measured. The 3° F (1.7° C) isotherm occupied one-half the river width and was limited in longitudinal extent. Model data indicated lateral penetration into the river was somewhat greater than in the field in all cases. The 35,000 cu ft/sec (991

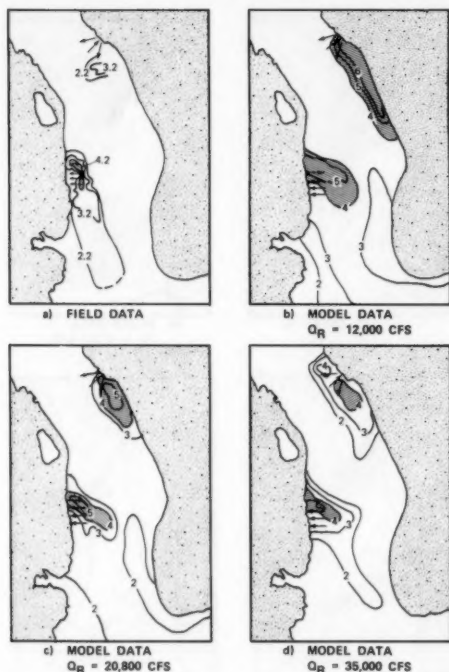


FIG. 25.—Field-Model Comparison of Overall Temperature Rise Patterns—Slack Tide Prior to Ebb (Temperature Rises are in Fahrenheit, 1° F = 0.56° C (1,000 cu ft/sec = 28.3 m<sup>3</sup>/s)

m<sup>3</sup>/s) case, Fig. 25(d), had best agreement of temperature rise areas while the lower freshwater flow rates overestimated temperature rises.

During ebb flow, Figure 26(a), field data indicated the 4° F (2.2° C) isotherm from Indian Point merged with the Lovett plume. A large 5° F (2.8° C) isotherm occurred due to the buildup of heat on the turn of tide and the return of heat from upstream. Lack of data near Lovett made definition of the extent of the 3° F (1.7° C) isotherm uncertain. Model data showed that, as in other cases, the 12,000 cu ft/sec (340 m<sup>3</sup>/s) case, Figure 26(b), overestimated while the

35,000 cu ft/sec ( $991 \text{ m}^3/\text{s}$ ) case, Figure 26(d), underestimated temperature rises near Indian Point. The 20,800 cu ft/sec ( $589 \text{ m}^3/\text{s}$ ) case overestimated the  $5^\circ \text{F}$  ( $0.8^\circ \text{C}$ ) isotherm at Lovett, but underestimated it at Indian Point. Model plume shape and temperature gradients showed agreement with the field data.

In summary, the density induced circulation present during the field surveys caused model simulation to be uncertain. Use of 12,000 cu ft/sec ( $340 \text{ m}^3/\text{s}$ )

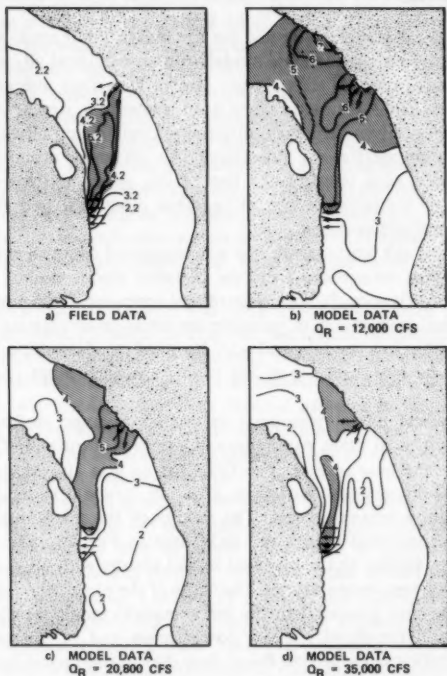


FIG. 26.—Field-Model Comparison of Overall Temperature Rise Patterns—Maximum Ebb Tide (Temperature Rises are in Fahrenheit,  $1^\circ \text{F} = 0.56^\circ \text{C}$ ) ( $1,000 \text{ cu ft/sec} = 28.3 \text{ m}^3/\text{s}$ )

freshwater flow overestimated temperature rises and use of 35,000 cu ft/sec ( $991 \text{ m}^3/\text{s}$ ) generally underestimated temperature rises. From the data, it would appear that a freshwater runoff of somewhat less than 20,800 cu ft/sec ( $589 \text{ m}^3/\text{s}$ ) would best reproduce field results. This conclusion is based on a single data set and is, therefore, tentative. Simulation of density induced circulation effects through use of increased freshwater flow in the model produced better agreement with field data, but the a priori choice of the required magnitude of freshwater runoff was not possible. Small changes in the measured field ambient could substantially change the conclusion since isotherm areas are

extremely sensitive to ambient temperatures. Other uncertainties affecting results are the differences in heat transfer coefficients, tidal flow variations in the field, and wind effects on plume shapes. Also, the model data tend to mask turbulent fluctuations relative to field measurements by the use of longer sensor time constants, larger sensor sampling volumes (spatial averaging), and averaging of several scans.

#### MATHEMATICAL MODEL

The mathematical model developed for the Indian Point study was a multisegment, one-dimensional steady state model with an empirical adjustment to relate the cross-sectional average temperature rise to a surface average temperature rise (14). Twenty-eight segments were used allowing a similar number of sets of input parameters (river geometry, dispersion coefficient thermal stratification, and heat transfer coefficient) describing the physical processes. Boundary conditions include zero temperature rise at the upper and lower ends of the river, equality of temperature rise at segment junctions, and conservation of energy at intermediate sections.

The surface average temperature rise was computed using an empirical thermal stratification factor determined from the physical model studies in conjunction with thermal stratification factors determined from the field temperature data. The mathematical simulation is valuable to assist in evaluating the boundary effects in the physical model, and can be used to determine the sensitivity of the average thermal response of the river to various input parameters, such as heat transfer.

The mathematical model was used to predict average surface temperature rises using the physical input parameters determined during the October survey period. The surface heat transfer coefficient used was 105 Btu/sq ft/Day/°F. The longitudinal dispersion coefficient, 2,257 sq ft/sec (210 m<sup>2</sup>/s), was determined from salinity measurements. The results of the mathematical model are compared to the physical model and field data in Fig. 18. The characteristics of the curves are similar to the physical model results without the peaks caused by high local discharge temperatures. The slope of the physical model temperature rise data is somewhat greater than the mathematical model results at both ends of the river reach simulated. At the downstream end of the physical model, a distinct heat deficit occurred on flood flow due to the model boundary, which caused the lowered temperature rises. At the upstream end, the temperature rises were sufficiently low at all times that a heat deficit was not evident in the physical model. The boundary effects in the physical model would appear to be sufficiently small such that the temperature rises near Indian Point would be essentially unaffected.

Mathematical predictions bracket the model temperature rises for 20,800 cu ft/sec (589 m<sup>3</sup>/s) runoff supporting the conclusions reached by the field model comparison. Field measurements at Indian Point, which are the average of the four tidal phases measured, show slightly higher temperature rises than the mathematical predictions.

#### SUMMARY AND CONCLUSIONS

Two physical model studies were conducted to assist in the evaluation of

the environmental impact of once-through condenser cooling at the Indian Point Nuclear Generating Station of Consolidated Edison Company of New York. Tidal flows dominate the hydraulics of the receiving water body, the Hudson River, which is classed as a partially stratified estuary. Salt from the ocean intrudes into the estuary past the Indian Point site for freshwater flow rates less than about 20,800 cu ft/sec (589 m<sup>3</sup>/s) and relatively strong vertical mixing causes vertical salinity gradients to be relatively weak.

The Indian Point Station required 4,590 cu ft/sec (413 m<sup>3</sup>/s) of condenser cooling water at a temperature rise of 14.8° F (8.2° C) at full power for three units. The discharge structure is located on the shoreline and has 12 rectangular jets at a submergence of 12 ft (3.66 m). Two additional fossil fueled power generating stations, utilizing once-through condenser cooling, are located within 7 miles (11 km) downstream of the Indian Point site.

Similitude criteria are developed for the design of models to predict near-field temperature patterns, i.e., in the area where the initial momentum and buoyancy of the effluent govern the plume trajectory and dilution, and intermediate-far-field thermal patterns, that is where buoyant forces, convection, and surface heat transfer control. These similitude criteria are applied in conjunction with practical considerations, such as enclosure size, to determine scale ratios for the two models.

The undistorted near-field model was constructed to a scale of 1-75. Near-field thermal patterns were obtained to evaluate maximum temperature rises, direct recirculation, and to calibrate the distorted scale model outfall structure. The distorted scale model, constructed to a horizontal scale of 1-400 and a vertical scale of 1-800, was used to determine thermal patterns in the intermediate-far-field. Construction techniques and instrumentation common to both models are described. The distorted scale model hydraulic behavior was verified by comparison to two field current pattern surveys.

Near-field model results compared favorably to field data. The "calibrated" nearfield thermal patterns in the distorted model approximated the uniform scale model results sufficiently well to allow confidence in predicted intermediate and far-field distorted model results. Distorted scale model results illustrated synoptic thermal patterns at 4 of the 13 times in the tidal cycle that data were taken. Summary plots showing the tidal average thermal patterns illustrated the effect of freshwater runoff, plant load, and discharge structure design.

Due to difficulties in obtaining meaningful field data at distances greater than about 2 miles from the plant, model-field comparisons could only be made relatively near the plant site, in which area the mixing was predominantly influenced by tidal currents as compared to more complex far-field phenomena influenced by salinity induced circulation. Direct comparisons in the far-field were not possible, but were indirectly evaluated by far-field effects on near-field results.

Field surveys were conducted at times when salt intruded past Indian Point, causing a density induced circulation, affecting the assimilative capacity of the river, which could not be directly reproduced in the model. Therefore, field data were compared to model data for various fresh-water runoffs simulating the increase in assimilative capacity. Model results showed general agreement of plume trajectory and shape for all freshwater runoff values, but isotherm areas tended to be a relatively strong function of freshwater runoff. Best agreement

of isotherm areas occurred for the 20,800 cu ft/sec ( $589 \text{ m}^3/\text{s}$ ) freshwater runoff tests, as compared to the 12,000 cu ft/sec ( $340 \text{ m}^3/\text{s}$ ) measured in the field.

Results from a multisegment, one-dimensional steady state mathematical model were compared to the lateral average physical model results and to field results. Mathematical model results indicated upstream and downstream boundary effects in the physical model were reasonably small.

Use of physical models provided an effective tool in the analysis of the thermal patterns resulting from discharge of a heated effluent into an estuary. Sensitivity of results to changes in outfall geometry, plant load, and fresh-water runoff were easily demonstrable. The most severe limitation in the case of a partially stratified estuary is the inability to simulate directly density-induced circulation. Other limitations include nonvariable surface heat transfer coefficients and tidal flows, and wind-induced surface currents. However, carefully designed and operated model can provide important information on temperature rise patterns that may be used in the design of outfall systems. Greater predictive detail and reliability was provided by the undistorted near-field model as compared to the overall distorted scale model.

#### ACKNOWLEDGMENTS

The writers wish to acknowledge the contributions of Peter A. Larsen, formerly of the Alden Research Laboratory, who supervised the design, construction, and initial testing of the far-field model, and conducted some of the field studies to determine river flow patterns near the site.

The field thermal survey data included in the paper are a portion of an extensive field measurement program conducted by Dames and Moore and Lawler, Matusky and Skelly developed the mathematical model used in the comparison of average cross-sectional temperature rises.

#### APPENDIX I.—REFERENCES

1. Busby, M. W., "Flow, Quality, and Salinity in the Hudson River Estuary," *Hudson River Ecology*, Hudson River Commission of New York, New York, N.Y., 1966.
2. Edinger, J. E., Brady, D. K., and Geyer, J. C., "Heat Exchange and Transport in the Environment," *Report No. 14*, Cooling Water Discharge Research Project (RD 49), Electric Power Research Institute, Nov., 1974.
3. Fischer, H. B., "The Effect of Bends on Dispersion in Streams," *Water Resources Research*, Vol. 5, No. 2, 1969, pp. 496-506.
4. Giese, G. L., and Barr, J. W., "The Hudson River Estuary, A Preliminary Investigation of Flow and Water Quality Characteristics," State of New York Conservation Department, Water Resources Commission, *Bulletin No. 61*, 1967.
5. Hecker, G. E., and Gurney, G. T., "Hydrothermal Model Studies for Indian Point Units 1 and 2," Alden Research Laboratory, Worcester Polytechnic Institute, Report No. 24-72/M118F, Mar., 1972.
6. Hecker, G. E., and Medeiros, W., "Reynolds Number Affects Dilution of Turbulent Buoyant Jets," Preprint of paper presented at 24th Annual Specialty Conference, Hydraulics Division, ASCE, August 1976, available from Alden Research Laboratory, Worcester Polytechnic Institute.
7. Holley, E., Harleman, D. R. F., and Fischer, H. B., "Dispersion in Homogeneous Estuary Flow," *Journal of Hydraulic Division*, ASCE, Aug., 1970, pp. 1691-1709.
8. Indian Point Unit No. 3, "Testimony of John P. Lawler on the Effect of Indian

- Point Units 1 and 2 Cooling Water Discharge on Hudson River Temperature Distribution," Environmental Report, Appendix EE, April 5, 1972.
9. Indian Point Nuclear Generating Station Intensive Thermal Survey Program, Dames & Moore and Consolidated Edison Company of New York, Inc., New York, N.Y., Aug., 1974 and Oct., 1974.
  10. Indian Point Nuclear Generating Station Thermal Survey Program, Routine Monthly Thermal Monitoring October, 1976 Survey, Consolidated Edison Company of New York, Inc., Feb., 1977.
  11. Ippen, A. T., "Estuary and Coastline Hydrodynamics," McGraw-Hill Book Company, Inc., New York, N.Y., 1966.
  12. Larsen, P. A., "Hydraulic Survey of Hudson River, the Haverstraw Bay Area," Alden Research Laboratory, Worcester Polytechnic Institute, Feb., 1970.
  13. Larsen, P. A., "Indian Point Cooling Water Studies, Tests with Bowline—Undistorted and Distorted Models," Alden Research Laboratory, Worcester Polytechnic Institute, Aug., 1970.
  14. Moy, H., Paretsky, L., Navarrete, R., and Szeligowski, J., "Thermal Plume Evaluation Program of Indian Point Nuclear Power Plant," Proceedings of the Conference on Waste Heat Management and Utilization Conference, Miami Beach, Florida, May 9-11, 1976.
  15. Neale, L. C., and Hecker, G. E., "Model Versus Field Data on Thermal Plumes from Power Stations," International Symposium Stratified Flows, Novosibirsk, USSR, 1972.
  16. Nystrom, J. B., and Hecker, G. E., "Hydrothermal Model Studies of Existing Shoreline Outfall and Offshore Diffusers for Indian Point Units 1 through 3," Alden Research Laboratory, Worcester Polytechnic Institute, Report No. 61-74/M118CF, June, 1974.
  17. Norman Porter Associates, Unpublished Transmittal to Consolidated Edison Company of New York, Inc., New York, N.Y.
  18. Okoye, J., "Characteristics of Transverse Mixing in Open Channel Flows," Report KH-R-23, Keck Laboratory of Hydraulics and Water Resources, California Institute of Technology, Pasadena, Calif., 1970.
  19. Ryan, P. J., and Harleman, D. R. F., "An Analytic and Experimental Study of Transient Cooling Pond Behavior," Report No. 161, Ralph M. Parsons Laboratory, Department of Civil Engineering, Massachusetts Institute of Technology, Cambridge, Mass., Jan., 1973.
  20. Ungate, C. D., "Temperature Reduction in a Submerged Vertical Jet in the Laminar Turbulent Transition," thesis presented to the Massachusetts Institute of Technology, in 1974, in partial fulfillment of the requirements for the degree of Master of Science.

## APPENDIX II.—NOTATION

*The following symbols are used in this paper:*

- $F$  = Froude number;  
 $F'$  = densimetric Froude number;  
 $f$  = friction factor;  
 $g$  = gravitational constant;  
 $K$  = heat transfer coefficient;  
 $m$  = subscript denoting model;  
 $p$  = subscript denoting prototype;  
 $Q_R$  = freshwater runoff;  
 $R$  = Reynolds number;  
 $r$  = subscript denoting ratio;  
 $S_E$  = energy gradient slope;  
 $T$  = temperature;  
 $\Delta T$  = temperature rise above ambient;

- $V$  = average velocity;  
 $x$  = horizontal distance;  
 $x_r$  = horizontal scale ratio;  
 $y$  = vertical distance;  
 $y_r$  = vertical scale ratio;  
 $\nu$  = kinematic viscosity;  
 $\rho$  = density; and  
 $\Delta\rho$  = density difference.



## INSTRUMENTATION FOR AERATED FLOW ON SPILLWAYS

By Paul Cain<sup>1</sup> and Ian R. Wood,<sup>2</sup> M. ASCE

### INTRODUCTION

This, the first of two papers, describes instrumentation developed to obtain measurements of the most important flow parameters within self-aerated flows on the spillway of Aviemore Dam and recommendations are made for future instrumentation. The second paper describes the spillway, the measurements, and their analysis.

### FLOW DESCRIPTION

Self-aeration in open channel flow is the natural phenomenon whereby atmospheric air is drawn into and mixed with the water, creating a characteristic white appearance.

For flow over a large spillway, self-aeration commences at the point where the turbulent boundary layer intersects the free surface.

When the transverse turbulent velocities are sufficiently strong near the water surface clumps of water burst through the surface into the air. These fall back by gravity into the main stream, breaking into spray and entraining air. This action intensifies until further downstream the surface has developed into a highly irregular and turbulent wave system bounded by a continuous air-water interface. The dimensions of the surface waves (spacing and amplitude) are of the same order as the depth of flow. Overturning waves are continuously entraining air beneath the water surface. This is broken into bubbles which are dispersed by the intense turbulence. The spray projected from the violently agitated water surface may extend a considerable height above the main flow, although it contributes little to the total water discharge.

Measurements in very aerated regions of flow on the spillway of Aviemore dam indicate the distribution of air bubbles shown in Fig. 1. The flow near the water surface (*A*) is very aerated with air concentrations (defined as the

<sup>1</sup>Engr., New Zealand Electricity Div., Ministry of Energy, Wellington, New Zealand.

<sup>2</sup>Prof. of Civ. Engrg., Univ. of Canterbury, Christchurch 1, New Zealand.

Note.—Discussion open until April 1, 1982. Separate discussions should be submitted for the individual papers in this symposium. To extend the closing date one month, a written request must be filed with the Manager of Technical and Professional Publications, ASCE. Manuscript was submitted for review for possible publication on September 5, 1980. This paper is part of the Journal of the Hydraulics Division, Proceedings of the American Society of Civil Engineers, ©ASCE, Vol. 107, No. HY11, November, 1981. ISSN 0044-796X/81/0011-1407/\$01.00.

volume of air/unit volume) frequently in the range 0.5–0.9. The largest bubbles within this surface region are about 10 mm–20 mm dimension. Away from the surface (*B*) the flow is less aerated, and the bubbles have been sheared down to about 0.5 mm–3 mm dimension. This range is thought to result from an equilibrium between the agitation of the flow and a bubble's resistance to deformation due to surface tension.

It is apparent from this description that a probe in position *P* will traverse from a region of spray between the waves through the very aerated region to a region which contains little or no air. It is also important to note that the air water mixture is compressible and that the velocity of sound in aerated flow becomes very small. It has been shown by Cain (1) that for an air concentration of 0.5 the velocity of sound is 20 m/s. For velocities in excess of this there is the possibility of shock waves being formed in front of a probe.

#### INITIAL COMBINED VELOCITY AND AIR CONCENTRATION PROBE

**General Description.**—Straub, Killen and Lamb (11) developed an instrument which timed the movement of a slug of salt between two electrodes. However most worker's have predicted the velocity from measurements of air concentration and stagnation pressure.

Keller (4) attempted to obtain measurements on Aviemore Dam using this approach in 1972 and a probe based on this principle was designed Fig. 2. The air concentration was measured between the two electrodes by an electrical resistance method first adapted for self-aerated flows by Lamb and Killen (6). This method was reliable and had been verified and was therefore chosen in preference to the many other techniques available. It will be discussed in the next section.

The stagnation pressure was measured by a pressure transducer connected to the stagnation point by a fluid filled pressure inlet tube about 140 mm long.

Both measurements refer to almost the same stream tube. The region of stagnation pressure measurement is limited to the cross section of the pressure inlet tube which is 6 mm diam. The air concentration is measured in the electric field set up between the two electrodes. The measurement region is mainly within a volume about 12 mm diam.

The concept of measurements at a "point" is important. The dimensions of the measurement regions were made small compared with the velocity, stagnation pressure and air concentration gradients expected in the 200 mm–350 mm depths of flow. It was initially expected that the bubbles would be in the range 1 mm–3 mm dimension, as reported by Straub and Lamb (12) and Killen (5). In this case, the flow beneath the water surface would all appear homogeneous to the probe. It was not until the final field tests that bubbles as large as 20 mm were measured near the water surface. Such large bubbles in fact appear nonhomogeneous to the probe, and complicated the interpretation of the air concentration signals measured at Aviemore.

#### Measurement of Stagnation Pressure

**Effects of Probe Geometry.**—In order to investigate the effect of the geometry of the probe on the stagnation pressure measurement, aerated flows were produced in a simulator Cain (1). The simulator produced an almost steady and almost

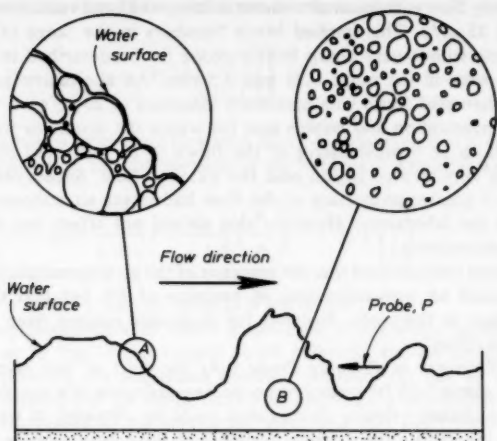


FIG. 1.—Structure of Turbulent Aerated Flow on Spillway

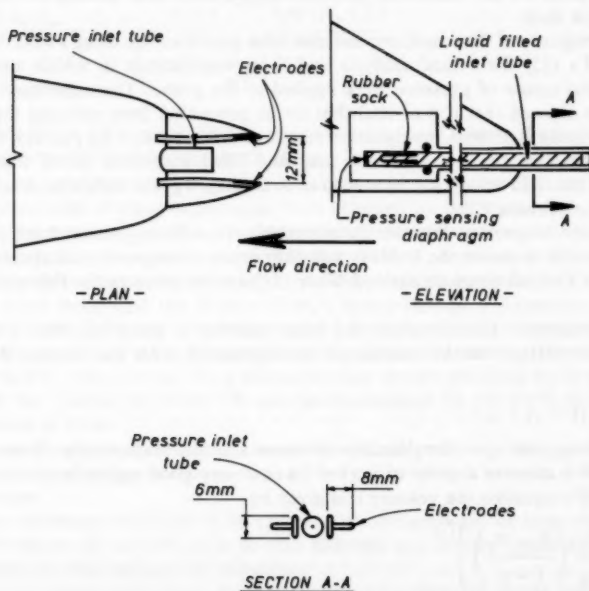


FIG. 2.—Combined Pressure Air Concentration Probe

uniform bubbly flow with mean air concentrations  $\approx 0.15$  and velocities of between 13 m/s and 25 m/s. This implied Mach Numbers in the range of 0.4 to 1.0. Measurements with a very sharp bubble probe (to be described later) showed the bubbles were in the range 0.25 mm–1.5 mm. An alternative configuration produced nonaerated flows with maximum velocities of 20 m/s.

The air concentration and bubble size for which the simulator was designed were thought to be representative of the flows to be measured on Aviomore except in the very aerated region near the water surface. Subsequent measurements show a greater proportion of the flow had larger air concentration than produced in the laboratory. However this should not affect the accuracy of the final measurements.

The simulator tests showed that the presence of the air concentration electrodes probably caused an over-estimation of pressure of 5% but that the ratio of the bubble size to the probe diameter for diameters ranging from 1.1 mm–19 mm had little effect.

*Dynamic Response of Pressure Probe.*—At the start of this investigation it was hoped to obtain high frequency response measurements of stagnation pressure from which turbulent velocity fluctuations could be obtained. It was therefore necessary to investigate the dynamic response of the pressure probe. Variations in pressure cause movement of the fluid so that the inlet tube acts as a viscous damper (Fig. 2). The dynamic response of the transducer and inlet tube will then depend on the transducer parameters, the inlet tube dimensions and the inlet tube fluid.

The response of the transducer and inlet tube was estimated using a modification of Wad's (13) theoretical analysis and from experiments in which step and sinusoidal inputs of pressure were applied to the probe. The experiments and analysis showed that it was vital that air be prevented from entering the inlet tube because it altered the dynamic response dramatically. To prevent this an inlet tube 0.69 mm I.D., 130 mm long and filled with SAE 30 oil was used for the final field tests. This resulted in an overdamped probe with a flat frequency response to about 1 Hz.

*Velocity Stagnation Pressure Relationship.*—In a homogeneous bubbly flow with no slip between the bubbles and the water, a range of assumptions can be made and relationships derived. Four of these are given in the following:

1. In subsonic flow in which the Mach number is much less than 1.0, the air-water mixture can be considered incompressible with the mixture density of

$$\rho_m = \rho_w(1 - c) + \rho_a c \quad \dots \dots \dots (1)$$

in which  $\rho_w$  and  $\rho_a$  = the densities of water and air, respectively. Since  $\rho_a \rho_w \approx 1/700$  a mixture density of  $\rho_w(1 - c)$  is a very good approximation. From Bernoulli's equation the velocity  $u$  is given by

$$u = \left[ \frac{2}{\rho_w} \left( \frac{P_s - P_0}{1 - c} \right) \right]^{1/2} \quad \dots \dots \dots (2)$$

in which  $P_s$  = the stagnation pressure; and  $P_0$  = the static pressure.

2. For isothermal flow which is either subsonic or supersonic with shock-free

deceleration to the stagnation point it can be shown that

$$u = \left\{ \frac{2}{\rho_w} \left[ P_s - P_0 + \frac{c}{1-c} P_0 \ln \left( \frac{P_s}{P_0} \right) \right] \right\}^{1/2} \dots \dots \dots (3)$$

3. In subsonic or supersonic flow with shock-free deceleration to the stagnation point, and for which the compression of the bubbles is adiabatic we get

$$u = \left( \frac{2}{\rho_w} \left\{ P_s - P_0 + \frac{c}{1-c} P \frac{\gamma}{\gamma-1} \left[ \left( \frac{P_s}{P_0} \right)^{\gamma-1/\gamma} - 1 \right] \right\} \right)^{1/2} \dots \dots \dots (4)$$

in which  $\gamma = 1.4$ , the ratio of specific heats for air.

4. For supersonic flow in which a detached shock wave forms in front of the probe as in Fig. 3 the normal shock relations can be applied from 1-2 and the expression for stagnation pressure recovery (2) can be applied from 2-3. This assumed that the shock relaxation processes are completed at 2 before the flow decelerates to the stagnation point and that the flow is isothermal. It can be shown that this leads to

$$u = \frac{\left\{ \frac{2}{\rho_w} \left[ P_s - M^2 P + \frac{c}{1-c} P_0 \ln \left( \frac{P_s}{M^2 P_0} \right) \right] \right\}^{1/2}}{\left( 1 - c + \frac{c}{M^2} \right)} \dots \dots \dots (5)$$

in which  $M^2 = [u^2 \rho_w c (1-c)] / P_0$ ; and in which  $u$ ,  $c$ ,  $M$  refer to the undisturbed flow upstream of the normal shock. (Cain, (1)).

The only published experimental data known to the writer that are suitable for comparison of these expressions were obtained by Eddington (2) who used a total pressure tube to measure the stagnation pressure for each of five flow conditions. His measurements are shown in Table 1, together with the corresponding velocities predicted by Eqs. 1-4. The velocities range from 45 m/s-102 m/s, much larger than the 12 m/s-22 m/s later measured at Aviemore.

Sterlini and Trotignon (10) have reported similar measurements at velocities from 10 m/s-25 m/s and 40 m/s-60 m/s for air concentrations from 0.5-0.55 and 0.8-0.85, respectively. They stated that their results indicated Eq. 3 overestimated the velocity by about 5% and underestimated by 2%-3.5% in each of the range of flows.

These discrepancies between the measured and predicted velocities can be attributed to the phenomenon of slip and thermal exchanges between the bubbles and water.

The maximum velocities to be expected on the spillways of large structures will be about 25 m/s-50 m/s so that although not strictly applicable, Eq. 3 provides the best estimate of velocity.

Eq. 3 is satisfactory for a homogeneous bubbly flow but in the self-aerated flow there will be regions of air gaps between the bubbly regions. If the proportion of the time the probe is in the bubbly flow is  $T$  (the intermittency parameter)

then the mean water velocity can be obtained as

$$\bar{u} = \left\{ \frac{2}{\rho_w} \left[ \frac{(\bar{P}_s - P_a)}{T} + \left( \frac{T - (1 - \bar{c})}{1 - \bar{c}} \right) P_a \ln \left( \frac{(\frac{\bar{P}_s - P_a}{T} + P_a)}{P_a} \right) \right] \right\}^{1/2} \quad (6)$$

in which  $P_a$  the atmospheric pressure is assumed equal to  $P_0$ .

**Conclusion.**—If the stagnation pressure, the air concentration and the intermittency can be measured then the best estimate of the mean velocity is obtained from Eq. 6. The best estimate of the accuracy of this measurement is  $-2.5\%$ – $+5\%$ .

TABLE 1.—Comparison of Measured and Predicted Velocity [ $P_0 = 98 \text{ kN/m}^2$  (abs)]

Measured by Eddington (1967)			Predicted			
Stagnation pressure $P_s$ , MN/m <sup>2</sup> (abs)	Air concentration $c$	Velocity $u$ , m/s	Velocity Eq. 2	Velocity Eq. 3	Velocity Eq. 4	Velocity Eq. 5
(1)	(2)	(3)	(4)	(5)	(6)	(7)
0.99	0.435	45	56	46	48	48
1.95	0.46	65	83	65	67	69
2.8	0.475	79	101	77	80	84
3.5	0.485	90	115	87	89	95
4.4	0.49	102	130	97	100	107

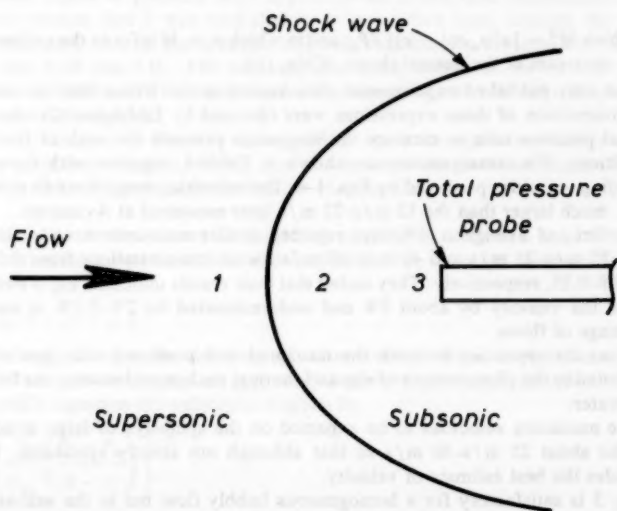


FIG. 3.—Shock Wave in Front of Pressure Probe

### Measurement of Air Concentration

**Operating Principle.**—This technique is based on an equation derived by Maxwell (7) for the specific resistivity of a suspension of spheres. This assumed the spheres to be the same diameter, and their spacing large compared with this diameter. By taking the conductivity of air as zero, Lamb and Killen (6) showed Maxwell's equation could be reduced to an expression for the air concentration of a suspension of air bubbles in water

$$c = \frac{\frac{R_E}{R_{EO}} - 1}{\frac{R_E}{R_{EO}} + 1} \dots \dots \dots (7)$$

in which  $R_E$  = the resistance of the air-water mixture between two electrodes. The term  $R_{EO}$  is the resistance of the water alone, measured between the same electrodes.

In spite of the assumptions concerning sphere size and spacing, Lamb and Killen (6) obtained excellent agreement between a probe utilizing this method and a mechanical sampler in a series of tests in self-aerated flows. Lamb and Killen measured the resistance in a bridge circuit using an a.c. (alternating current) source of e.m.f. in order to minimize the effects of polarization and electrolysis at the electrodes. This circuit can be represented by Fig. 4 in which the impedance between the electrodes is simulated by a capacitor  $C_E$  and resistor  $R_E$  in parallel. It is not possible to formulate a simple relationship between the measured potential difference  $V_E$  and  $R_E$  for this circuit.

Lamb and Killen actually analysed a simpler circuit in which the impedance between the electrodes has been assumed to be purely resistive, strictly valid only for a d.c. (direct current) source as shown. Analysis of this circuit combined with Eq. 7 yields the simple relationship

$$c = \frac{2\alpha \|V_E\|}{3(\alpha - 1) + (3 - \alpha) \|V_E\|} \dots \dots \dots (8)$$

in which  $\alpha = 1 + (R_{EO}/R_R)$ ; and  $\|V_E\|$  = the measured potential difference scaled so that it varies between 0.0 and 1.0 corresponding to  $C = 0.0$  and 1.0, respectively. Values of  $R_E$  and  $C_E$  obtained under simulated aerated flow conditions showed that for the 20.1 kHz source frequency, both circuits predicted the same relationship between  $\|V_E\|$  and  $R_E$ .

Eq. 8 is therefore valid for the circuit of Fig. 4. Using the measured value  $R_{EO} = 15.8 \text{ k}\Omega$ – $16.1 \text{ k}\Omega$ , and  $R_R = 10 \text{ k}\Omega$   $\alpha = 2.6$  and Eq. 8 reduces to

$$c = \frac{13 \|V_E\|}{12 + \|V_E\|} \dots \dots \dots (9)$$

The electronic measuring circuit Fig. 5 was designed in consultation with DAVCO Electronics and measures the component of  $V_E$  in phase with  $V_s$ . It was therefore necessary to experimentally relate the output from this electronic measuring circuit to the potential difference  $V_E$ . This was done by connecting both the measuring circuit and an R.M.S. voltmeter (Hewlett-Packard 3,400A R.M.S. Voltmeter) to the probe. Variations in air concentration were simulated

by slowly submerging the electrodes in water. The output signals gave the relationship between  $\|V_e\|$  and the scaled voltage from the electronic measuring circuit  $\|V_{em}\|$ . Combining this relationship with Eq. 9 yielded

$$c = 1.0 - 1.008 (1.0 - \|V_{em}\|)^{0.741} \quad (10)$$

The frequency response of the electronic circuit was flat to 1 kHz. Thus, it is apparent that the frequency response of the probe was limited by its physical size.

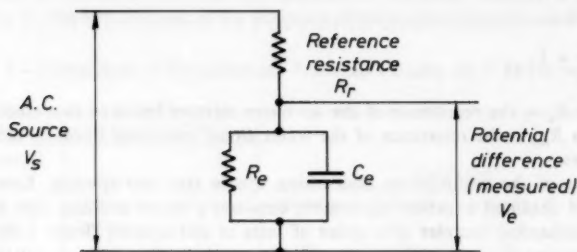


FIG. 4.—Circuit Diagram for an A.C. Source

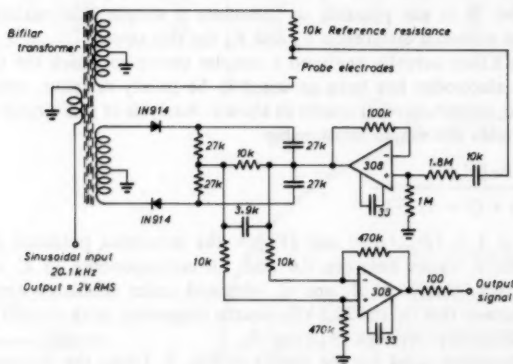


FIG. 5.—Air Concentration Measuring Circuit

**Frequency Response of Air Concentration Probe.**—The maximum frequency response possible is limited by the dimensions of the measurement region relative to the dimensions of the fluctuations being measured. For example, variations in air concentration whose dimensions are much smaller than the measurement region between the electrodes will be damped.

An approximation for the frequency response of the air concentration probe can be obtained by assuming a uniform electric field between the electrodes,



and sinusoidal air concentration variation in the direction of flow only. This implies

$$Z = \frac{u}{\pi f L} \sin \left( \frac{\pi f L}{u} \right) \dots \dots \dots (11)$$

in which  $Z$  = relative amplitude, of the measured air concentration fluctuation to real air concentration fluctuation;  $f$  = frequency of the air concentration fluctuations at the central point between the electrodes;  $u$  = velocity; and  $L$  = length of the measurement region. Eq. 11 has been evaluated by assuming

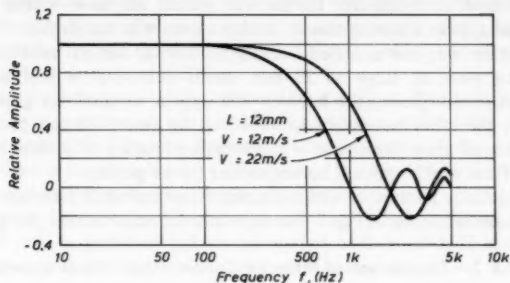


FIG. 6.—Response of Air Concentration Probe to Frequency of Air Concentration Variations

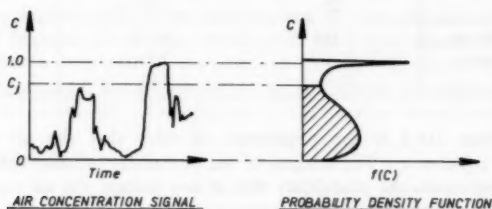


FIG. 7.—Schematic of Probability Density Function in Self Aerated Flow

a conservative value of 12 mm for  $L$ , and is plotted in Fig. 6 for  $u = 12$  m/s and 22 m/s. This shows a flat frequency response up to 100 Hz–200 Hz, less than the 1 kHz of the electronics developed for this probe.

**Air Concentration Probe Verification.**—As noted, Lamb and Killen (6) experimentally verified this measurement technique. However in spite of the confidence in Eq. 8 a direct check on the accuracy of the probe was made in the laboratory flow simulator using a gamma radiation technique which measures the mean air concentration in the path of the beam of  $\gamma$ -rays. This method is accurate to within plus or minus 1%.

The mean air concentrations from the two methods are in excellent agreement; the difference between them is on average only about 0.01 Table 2. The differences

between the measurements are within the accuracy of the signal fluctuations [0.01].

*Intermittency Parameter Measurements from Air Concentration Signal.*—The concept of an intermittency parameter  $T$  was introduced to improve the accuracy of mean velocity predictions from the stagnation pressure and air concentration measurements.

The intermittency parameter was initially defined as the proportion of time the measurement region of the combined pressure air concentration probe was within the water surface. The dimensions of the probe were chosen so that the measurement region was larger than the 1 mm–3 mm bubble size that was initially expected at Aviemore. If this was so, all the flow within the water surface would appear a homogeneous bubbly mixture to the probe.

This condition was not satisfied because as noted, the air bubbles near the water surface were as large as 20 mm. Such bubbly flow will not appear homogeneous to the probe; the bubbles will appear as small air gaps in wavy flow. It was therefore necessary to redefine the intermittency parameter as the proportion of time the probe's measurement region is within bubbly (or nonaerated) flow which appears homogeneous to the probe.

The intermittency parameter was estimated from probability density functions of the air concentration signal Fig. 7. For a given air concentration  $c$ , the probability

TABLE 2.—Comparison of Mean Air Concentration Measurements

Variables (1)	Test		
	$D$ (2)	$E$ (3)	$F$ (4)
Gamma radiation	0.164	0.154	0.149
Combined probe	0.16	0.16	0.17
Difference	0	0.01	0.02

density function  $f(c_j)$  is the proportion of time that the air concentration signal is equal to  $c_j$ . The integral of the probability density function from  $c = 0 - c_j$  represents the probability that at any instant, the air concentration will be less than or equal to  $c_j$ . If the frequency response of the air concentration instrument was infinite, any large air bubbles which obscured one or both of the electrodes would produce an output signal  $c = 1.0$ . Instead, the limited frequency response causes the output signal to fluctuate rapidly, frequently without attaining the level  $c = 1.0$ .

This complicates the interpretation of most of the plots of probability density function, i.e., the value of  $f(c)$  at say  $c = 0.8$  could be caused entirely by large bubbles which are inaccurately recorded. Alternatively, it could be caused entirely by a homogeneous mixture of small bubbles for which  $c = 0.8$ . In general, both sources will contribute to the value  $f(c)$ . Their individual contributions cannot be distinguished.

Under these circumstances, it was thought the intermittency parameter could be estimated most accurately as the integral of  $f(c)$  from  $c = 0 - 0.7$ . This assumes that the air concentration within homogeneous mixtures of small bubbles will rarely exceed 0.7.

The choice of 0.7 is rather arbitrary and cannot be justified with experimental evidence. For this reason the velocity calculations using Eq. 6 were repeated for values of  $T$  calculated as the integral from  $c = 0 - 0.6$ , and  $c = 0 - 0.8$ . These different values of  $T$  had little effect on the calculated velocities.

#### BUBBLE SIZE PROBE

This was a resistivity probe similar to those used by Neale and Bankoff (8) for measuring local parameters in mercury nitrogen flows. It consisted of a sharpened rod which is insulated except for its tip and set into a metal supporting tube. The electrical circuit applies a constant voltage over the probe and its series resistance. When the probe tip is in contact with water, current will flow between the tip and the supporting metal tube; when it is in contact with air as in Fig. 8(a) no current will flow.

The output is the potential difference over the resistor. This will vary between two values corresponding to air and water, as shown in Fig. 8(b). This signal is in fact oversimplified because the poor wettability of the probe tip will result in an output as in the dashed curve [Fig. 8(b)]. Provided the velocity is known the bubble size and spacing can then be calculated.

In this particular case the tip of the probe was a chrome plated steel needle approx 0.05 mm in diameter and was insulated with Araldite D except for the last 0.25 mm.

The electrical circuit was similar to Fig. 8(a), using a 10 k $\Omega$  resistance and 9V battery. However the circuit between the probe tip and the negative battery terminal was via the metal probe supporting assembly. The current therefore had to travel about 100 mm through an irregular water path.

The probe worked well in the bubbly flow in both the laboratory and in the field but because of the long current path the output signals were difficult to interpret in the very aerated wavy surface remote from the spillway surface. Its performance could have been improved by placing an uninsulated needle adjacent to the probe and connecting this to the negative battery terminal.

#### CORRELATION VELOCITY PROBE

This probe incorporates two resistivity probes alined in the flow direction and utilizes a cross-correlation technique to calculate the velocity. It was developed independently of similar probes reported by Herringe and Davis (3) and Serizawa, et al. (9). It proved to be more accurate than the combined velocity air concentration probe. The principle of the probe is explained with reference to Fig. 8.

If the tips of two resistivity probes are alined in the direction of flow Fig. 8(a) then the water velocity can be calculated from the time of travel of an air-water interface between the probe tips. Ideally the two signals would be identical but separated by a time delay  $\tau_0$  Fig. 8(b). In practice they will differ because the upstream probe will disturb the flow. In this case the probable time delay can be found by cross-correlating the two signals. If the measured cross-correlation function is plotted against time delay, then  $\tau_0$  will correspond to the maximum correlation in the cross-correlogram of Fig. 8(c).

This method assumes firstly that the upstream probe does not alter the velocity

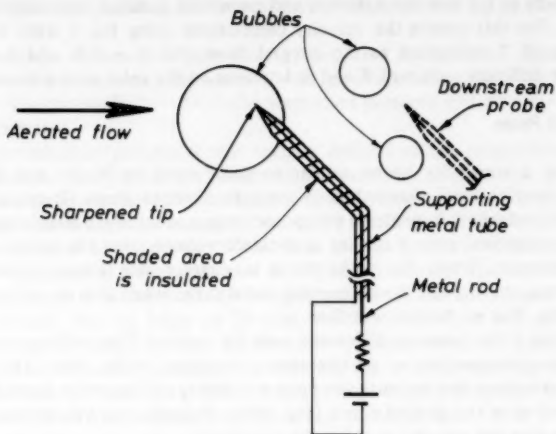
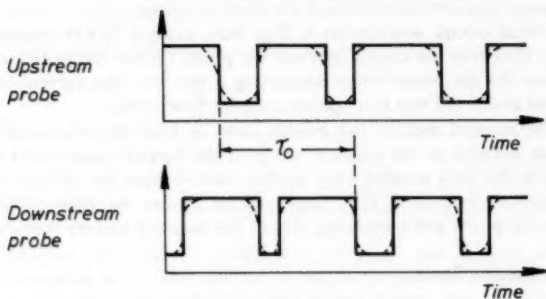
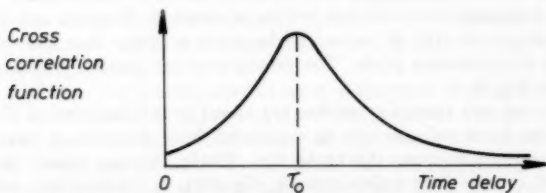
(a) RESISTIVITY & VELOCITY PROBE(b) IDEAL OUTPUT SIGNALS(c) TYPICAL CROSS-CORRELOGRAM

FIG. 8.—Resistivity Probe Used to Measure Bubble Size and Paired Resistivity Probes Used for Measuring Velocity

of the air-water interfaces between the probes, and secondly that this velocity is the same as the water velocity.

In designing a probe to use this principle, it is apparent the tip dimensions and spacing must be related to the dimensions of the air-water interface to

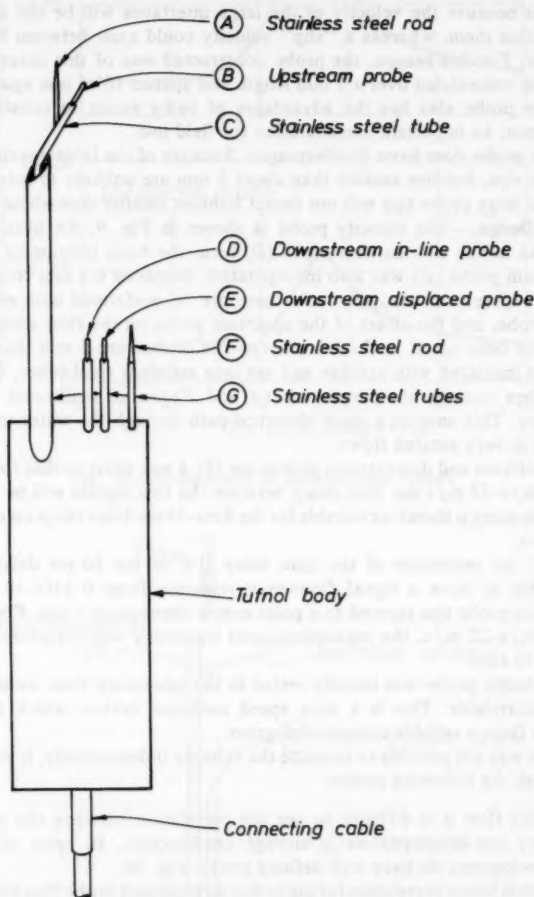


FIG. 9.—Plan of Velocity Probe

be measured. For instance, if it was intended to operate in a bubbly flow with a uniform bubble size, say 1 mm diam, then: (1) The probe tips must be much less than 1 mm diam to minimize the distortion and deflection of bubbles;

and (2) the tip spacing must not be greater than about 10 mm if bubbles intercepting the upstream tip are to intercept the downstream one.

Considering the nature of self-aerated flows it is apparent that a much larger probe will operate successfully by measuring the passage time not of small bubbles but of the large bubbles and air-water interfaces. This difference is important because the velocity of the large interfaces will be the same as the water within them, whereas a "slip" velocity could exist between bubbles and the water. For this reason, the probe constructed was of this latter type, with probe tips uninsulated over a 1 mm length and spaced 101.6 mm apart.

A large probe also has the advantages of being easier to construct and is more robust, an important consideration for field use.

A large probe does have disadvantages. Because of the large spacing between the probe tips, bubbles smaller than about 5 mm are unlikely to intercept them both. The large probe tips will not detect bubbles smaller than about 2 mm.

**Probe Design.**—The velocity probe is shown in Fig. 9. An upstream probe (*B*) and an in-line downstream probe (*D*) form the basic instrument. A second downstream probe (*E*) was also incorporated, displaced 6.4 mm from the first. The cross-correlation analysis could therefore be performed with either downstream probe, and the effect of the upstream probe on the flow directly behind it could be determined in the laboratory. The probes are 1 mm diam stainless steel rods insulated with araldite and set into stainless steel tubes, (*C* and *G*). These tubes and the sharpened rods (*A* and *F*) are all connected directly to the battery. This ensures a short electrical path through the water to the probe tips even in very aerated flows.

The upstream and downstream probes are 101.6 mm apart so that for velocities from 12 m/s–22 m/s the time delay between the two signals will be 4.6 ms–8.5 ms. This spacing is therefore suitable for the 0 ms–10 ms delay range on commercial correlators.

For 0.1 ms resolution of the time delay (1% of the 10 ms delay range) it is desirable to have a signal frequency response from 0 kHz–10 kHz. The uninsulated probe tips tapered to a point over a distance of 1 mm. For velocities from 12 m/s–22 m/s, the maximum signal frequency will therefore be limited to about 10 kHz.

The velocity probe was initially tested in the laboratory flow simulator using a DISA correlator. This is a slow speed analogue device, which took about 25 min to form a reliable cross-correlogram.

While it was not possible to measure the velocity independently, it was possible to establish the following points:

1. In this flow it is difficult to see the correlation between the two signals when they are displayed on a storage oscilloscope. In spite of this, the cross-correlograms do have well defined peaks. Fig. 10.
2. There is better correlation for the in-line downstream probe than the displaced one.
3. The in-line and displaced probes predicted the same time delay to within about 0.1 ms (this is the claimed accuracy of the correlator, i.e., 1% of the 10 ms delay range). As a result of these tests, the downstream in-line probe was used in the final field tests.

As no high speed cross-correlators were available for on-line analysis of the

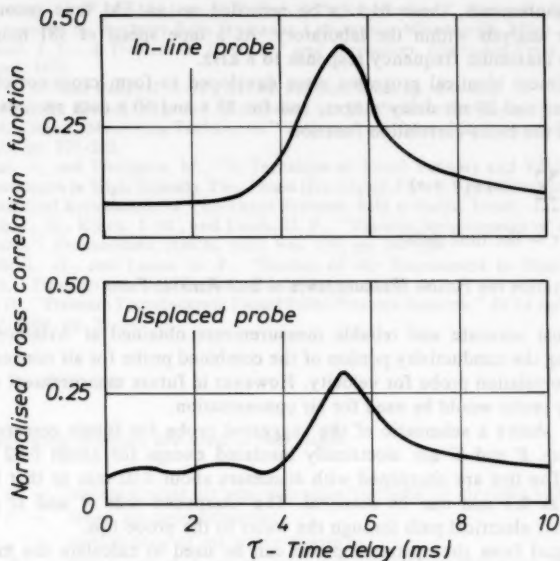


FIG. 10.—Comparison of Downstream Probes

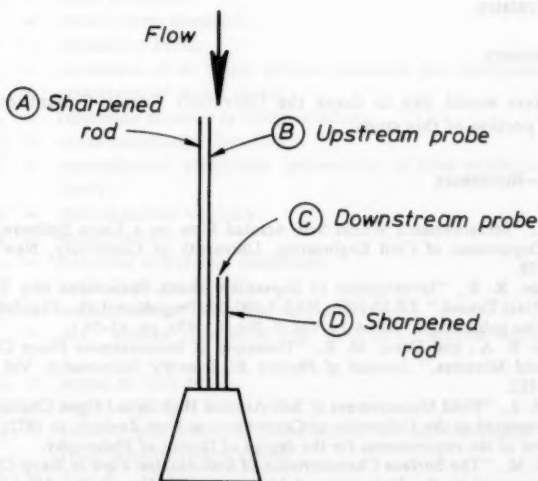


FIG. 11.—Schematic of Proposed Velocity Air Concentration Probe

field measurements, these had to be recorded on an FM tape recorder for computer analysis within the laboratory. At a tape speed of 381 mm/s this limits the maximum frequency response to 8 kHz.

Four almost identical programs were developed to form cross-correlograms with 10 ms and 20 ms delay ranges, and for 15 s and 60 s data records. These evaluated the cross-correlation function

$$R_{xy}(\tau) = \sum_{n=1}^N x(n)y(n+\tau) \dots \dots \dots (12)$$

in which  $\tau$  = the time delay.

#### INSTRUMENTATION FOR FUTURE MEASUREMENTS IN SELF AERATED FLOW

The most accurate and reliable measurements obtained at Aviemore were those using the conductivity portion of the combined probe for air concentration and the correlation probe for velocity. However in future measurement a single resistivity probe would be used for air concentration.

Fig. 11 shows a schematic of the suggested probe for future research. The two probes *B* and *C* are electrically insulated except for about 0.02 mm at the tips. The tips are sharpened with diameters about 0.02 mm so that bubbles as small as 0.1 mm can be detected. The sharpened rods *A* and *D* provide a very short electrical path through the water to the probe tips.

The signal from the upstream probe can be used to calculate the mean air concentration plus details of bubble size, spray size and the spacing of the waves.

The signals from both probes can be used to calculate the velocity using a cross-correlator.

#### ACKNOWLEDGMENTS

The writers would like to thank the University Grants Committee for the support of portion of this study.

#### APPENDIX I.—REFERENCES

1. Cain, P., "Measurements Within Self Aerated Flow on a Large Spillway," *Report 78-18*, Department of Civil Engineering, University of Canterbury, New Zealand, Apr., 1978.
2. Eddington, R. B., "Investigation of Supersonic Shock Phenomena in a Two-Phase (Liquid-Gas) Tunnel," *TR 32-1096*, NAS 7-100, Jet Propulsion Lab., Pasadena, Calif., 1967. (Also published in: *AIAA J.*, Vol. 8, No. 1, 1970, pp. 65-74.)
3. Herringe, R. A., and Davis, M. R., "Detection of Instantaneous Phase Changes in Gas-Liquid Mixtures," *Journal of Physics E: Scientific Instruments*, Vol. 7, 1974, pp. 807-812.
4. Keller, R. J., "Field Measurement of Self-Aerated High Speed Open Channel Flow," thesis presented to the University of Canterbury, at New Zealand, in 1972, in partial fulfillment of the requirements for the degree of Doctor of Philosophy.
5. Killen, J. M., "The Surface Characteristics of Self-Aerated Flow in Steep Channels," thesis presented to the University of Minnesota, at Minneapolis, Minn., in 1968, in partial fulfillment of the degree of Doctor of Philosophy.
6. Lamb, O. P., and Killen, J. M., "An Electrical Method for Measuring Air Concentration



- in Flowing Air-Water Mixtures," Technical Paper Number 2, Series B, University of Minnesota, St. Anthony Falls Hydraulic Laboratory, Minneapolis, Minn., 1950.
7. Maxwell, J. C., *A Treatise on Electricity and Magnetism*, Clarendon Press, Oxford, England, 1873.
  8. Neal, L. G., and Bankoff, S. G., *AIChE Journal*, 1963, pp. 490-494.
  9. Serizawa, A., Kataoka, I., and Michiyoshi, I., "Turbulence Structure of Air-Water Bubbly Flow-I. Measuring Techniques," *International Journal Multiphase Flow*, Vol. 2, 1975, pp. 221-233.
  10. Sterlini, J., and Trotignon, M., "A Technique of Local Velocity and Void Fraction Measurement in High Velocity Two Phase Gas-Liquid Flows," presented at the 1971 International Symposium on Two-Phase Systems, held at Haifa, Israel.
  11. Straub, L. G., Killen, J. M., and Lamb, O. P., "Velocity Measurement of Air-Water Mixtures," *Transactions, ASCE*, 1954, Vol. 119, pp. 207-220.
  12. Straub, L. G., and Lamb, O. P., "Studies of Air Entrainment in Open Channel Flows," *Transactions, ASCE*, Vol. 121, 1956, pp. 30-44.
  13. Wad, G., "Pressure Transducers in Liquid Filled Pressure Systems," *DISA Information*, No. 7, 1969, pp. 25-29.

## APPENDIX II.—NOTATION

*The following symbols are used in this paper:*

- $c$  = instantaneous air concentration [volume of air/unit volume];
- $\bar{c}$  = mean air concentration;
- $c_E$  = capacitance of air water mixture;
- $f$  = frequency of air concentration at central point between electrodes;
- $L$  = length of measurement region for air concentration probe;
- $M$  = Mach Number =  $u^2 \rho_w c(1 - c)/p$ ;
- $P_0$  = static pressure;
- $P_a$  = atmospheric pressure;
- $P_s$  = stagnation Press;
- $R_E$  = resistance of air water mixture between two electrodes;
- $R_{EO}$  = resistance of water alone;
- $R_R$  = reference resistor in bridge circuit;
- $R_{xy}(\tau)$  = cross-correlation function;
- $T$  = intermittency parameter [proportion of time probe is in bubbly flow];
- $u$  = instantaneous velocity;
- $\bar{u}$  = mean velocity;
- $V_E$  = potential difference measured;
- $\|V_E\|$  = scaled voltage  $V_E/V_S$ ;
- $\|V_{em}\|$  = scaled voltage from measuring circuit;
- $V_s$  = A.C. source voltage in Fig. 6 or D.C. source voltage in Fig. 7;
- $x(n)$  = signal at time  $n$ ;
- $y(n + \tau)$  = signal at time  $n + \tau$ ;
- $Z$  = relative amplitude of variation of air concentration and signal from concentration probe;
- $\alpha$  =  $1 + R_{EO}/R_E$ ;
- $\rho_a$  = density of air;
- $\rho_w$  = density of water;

- $\gamma$  = specific heat ratio (i.e., specific heat at constant pressure divided by specific heat at constant volume);
- $\tau$  = time delay; and
- $\tau_0$  = delay time for maximum correlation.

## MEASUREMENTS OF SELF-AERATED FLOW ON A SPILLWAY

By Paul Cain<sup>1</sup> and Ian R. Wood,<sup>2</sup> M. ASCE

### INTRODUCTION

This is the second of two papers, the first of which describes instrumentation developed to obtain measurements in the developing region of self-aerated flow on the spillway of Aviemore Dam. This paper considers the measurements obtained and the analysis of results.

### EXISTING TEST FACILITIES AT AVIEMORE

Spillway bay 5 has test stations 501-505 located at 6.10 m intervals down the spillway (Fig. 1). At each station there is a steel box 460 mm × 460 mm × 460 mm set into the concrete with removable steel cover plate set flush with the spillway surface. The stations are connected to a recording hut adjacent to the spillway by cables below the spillway surface. Access to the test stations is by a "skip" which is lowered from the top of the dam. From the skip the cover plate is removed and the instrument and drive assembly (Fig. 2) are bolted to the box. The instrument probe mounted on the assembly was driven via a gear and chain mechanism by a stepper motor and the probes position was determined from the rotation of an intermediate drive shaft which was displayed on the control unit within the recording hut. The motor drive logic allowed the probe to be accurately positioned to within 0.5 mm to a maximum depth of 352 mm. The instrument assembly was first positioned at station 501 with the probe on the spillway surface and the spillway gate was opened first to 300 m and then to 450 mm. Following traverses at these two openings the gate was then closed and the probe moved downstream.

The gate opening was indicated on a dial at the top of the dam, but its graduations are too coarse to allow the gate to be accurately reset.

For the measurements of the final test series the gate was opened according

<sup>1</sup>Engr., Pearson Bridge Ltd., P.O. Box 137, St. Leonards, N.S.W. 2065, Australia.

<sup>2</sup>Prof. of Civ. Engrg., Dept. of Civ. Engrg., Univ. of Canterbury, Private Bag, Christchurch 1, New Zealand.

Note.—Discussion open until April 1, 1982. Separate discussions should be submitted for the individual papers in this symposium. To extend the closing date one month, a written request must be filed with the Manager of Technical and Professional Publications, ASCE. Manuscript was submitted for review for possible publication on September 5, 1980. This paper is part of the Journal of the Hydraulics Division, Proceedings of the American Society of Civil Engineers, ©ASCE, Vol. 107, No. HY11, November, 1981. ISSN 0044-796X/81/0011-1425/\$01.00.

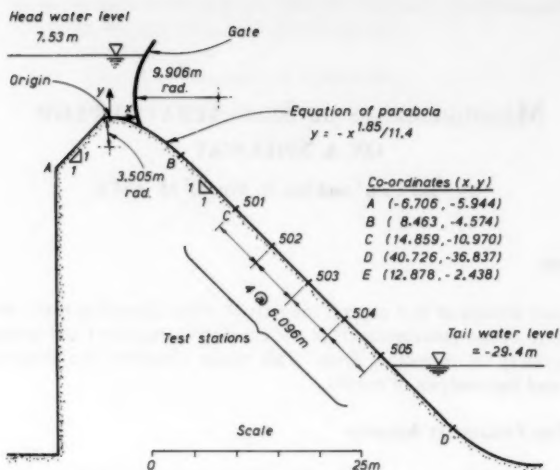


FIG. 1.—Section through Spillway at Aviemore Dam

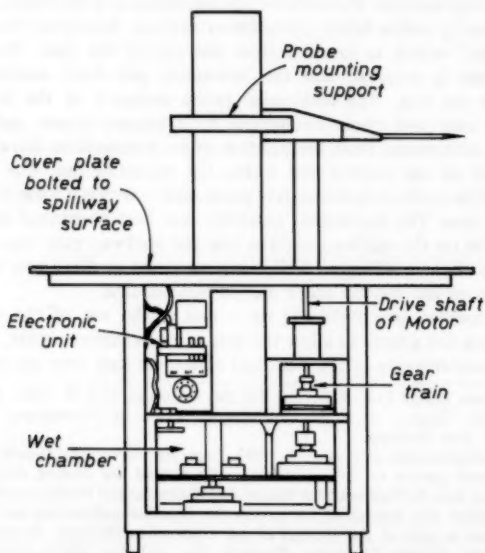


FIG. 2.—Instrument and Drive Mechanism on Spillway

to the dial firstly to 300 mm and then a further 150 mm–450 mm. These two openings were marked on a separate measuring frame as 196 mm and 290 mm, respectively. For all subsequent measurements the gate opened until the pointer

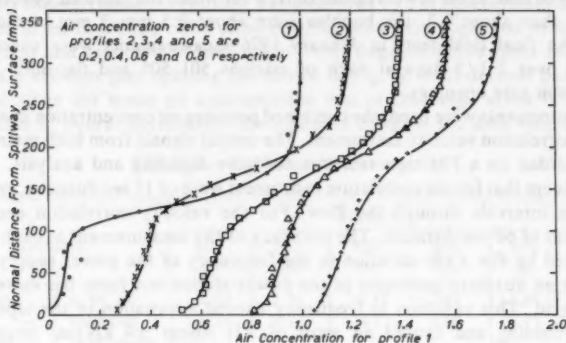


FIG. 3.—Measured Air Concentration Profiles (Gate Open 300 mm)

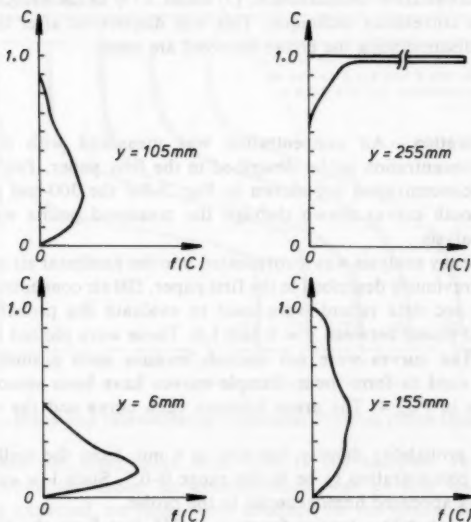


FIG. 4.—Sample Probability Density Functions Station 504 (Gate Opening 300 mm)

was within 2 mm of the above ( $<1\%$  FS). Thus the movement of the gate from its position on the compressible rubber seal was accurately set. However the rebound of the compressible seal created problems which will be considered later.

The initial field tests took place in April 1975 when the flooding of the Waitaki River first made water available for measurement. The instrument development was then incomplete and the tests were only partially successful. However they showed that, in the lower regions of flow for which the mean air concentration was less than about 0.2, the bubbles were about 0.5 mm–3 mm in dimension (3). In the final field tests in January 1976 measurements were successfully obtained over 2 1/2 days at each of stations 501–505 and for both 300-mm and 450-mm gate openings.

Two instruments were used, the combined pressure air concentration instrument and the correlation velocity instrument. The output signals from both instruments were recorded on a FM tape recorder for later digitising and analysis. Output signals except that for the correlation instrument were of 15 sec duration, recorded at 10 mm intervals through the flow. For the velocity correlation each fifth sample was of 60 sec duration. The accuracy of the measurement at each station was limited by the  $\pm 1\%$  variation in the frequency of the power supply which was from an auxillary generator in the power station not from the more stable national grid. This variation in frequency caused a variation in the tape speed during recording and caused an error of: (1) About  $\pm 4 \text{ kN/m}^2$  uncertainty for any stagnation pressures measurement. This corresponds to  $\pm 2\%$  of the maximum mean stagnation pressure measured; (2) about  $\pm 0.015$  uncertainty for any air concentration measurement; (3) about  $\pm 1\%$  of the velocity calculated with the cross correlation technique. This was discovered after the final tests and although disappointing the errors involved are small.

#### DATA ANALYSIS

**Air Concentration.**—Air concentration was measured with the combined pressure air concentration probe described in the first paper. Profiles of mean values of air concentration are shown in Fig. 3 for the 300-mm gate opening only. The smooth curves drawn through the measured points were used for subsequent analysis.

An intermittency analysis was incorporated into the nonlinear air concentration data analysis previously described in the first paper. 500 air concentration samples from each 14 sec data record were used to evaluate the probability density function at 100 points between  $c = 0$  and 1.0. These were plotted on the visual display unit. The curves were not smooth because such a small number of samples were used to form them. Sample curves have been smoothed by eye and are shown in Fig. 4. The areas between each curve and the vertical axes are identical.

The plot of probability density function at 6 mm from the spillway surface shows the air concentration to be in the range 0–0.5. Such low values suggest the flow always appeared homogeneous to the probe.

The plot of probability density function at 255 mm from the spillway have peaks at  $c = 1.0$ . These are caused mainly by the large air gaps between waves. The largest bubbles could also contribute to these peaks.

Between these two extremes at 155 mm from the spillway the value of  $f(c)$  at  $c = 0.8$  could be interpreted as being caused by large bubble incorrectly recorded because of the probe size or being caused by a homogeneous mixture for which  $c = 0.8$ . As reviewed in the first paper, the intermittency parameter

was estimated as the integral of  $f(c)$  from  $c = 0$  to  $c = 0.7$ . Plots of this intermittency parameter for the 350-mm gate opening are shown in Fig. 5 and suggest that the waves extend over the top third of the flow.

**Velocity Measurements.**—Velocity was measured by a cross-correlation method described in the first paper. The cross-correlograms were displayed on the visual display unit and recorded in hard copy form. Representative plots for station 503 with a 450-mm gate opening are shown in Fig. 6. Well defined peaks were obtained when the mean air concentration was in the range about 0.3–0.9. In the regions of poorer correlation, the analyses using 60 sec data samples often

TABLE 1.—Discharge Measurements

Variable (1)	Station					Mean
	501 (2)	502 (3)	503 (4)	504 (5)	505 (6)	$q$ (7)
300-mm gate opening — $q, \text{m}^2/\text{s}$	2.02	2.36	2.12	2.32	2.34	2.23
variation from mean	-0.21	0.13	-0.11	0.09	0.11	
450-mm gate opening — $q, \text{m}^2/\text{s}$	2.91	3.26	3.11	3.16	3.32	3.15
variation from mean	-0.24	0.11	-0.04	0.01	0.17	

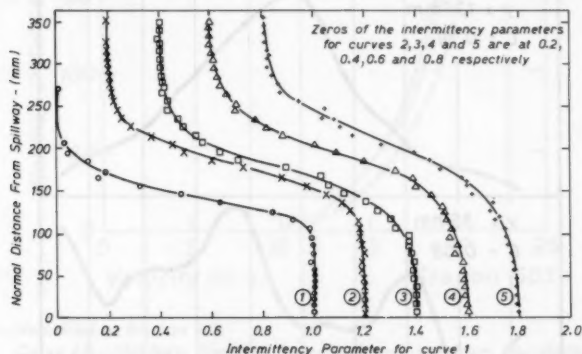


FIG. 5.—Measured Intermittency Parameter Profiles, (Gate Open 300 mm)

indicated peaks not discernable with only 15 sec samples. Peaks were not discernable when the mean air concentration was outside the range about 0.05–0.98. As expected, no peaks were obtained for the almost nonaerated flow at station 501 with a 450-mm gate opening.

The mean velocities were calculated from the time delays to the peaks.

The profile computed from the series of measurement similar to those in Fig. 6 at station 503 for the 300-mm gate opening is shown on Fig. 7 curve AB.

Profiles of mean values of stagnation pressure were also obtained but have not been reproduced here.

The smoothed profiles of mean stagnation pressure  $\bar{P}_s$  and air concentration  $\bar{C}$  plus the smoothed intermittency profiles were used to calculate mean velocity

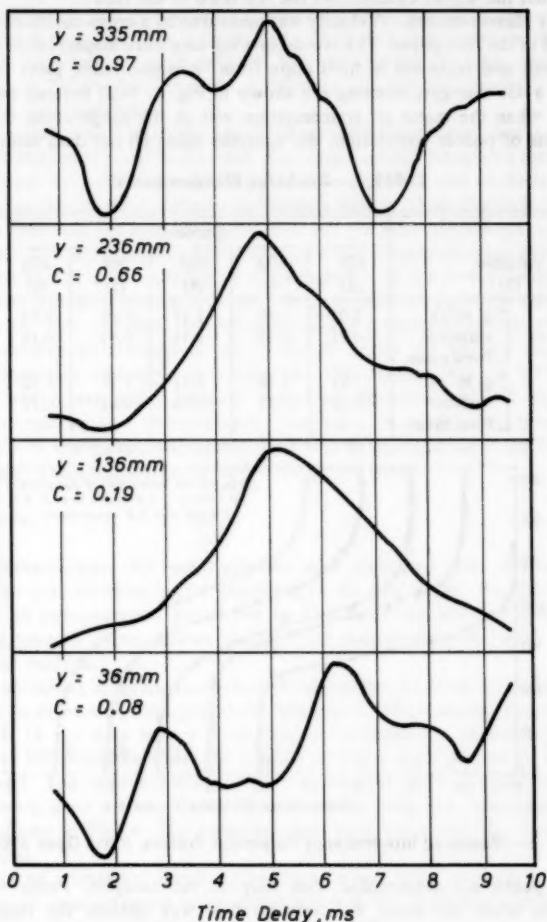


FIG. 6.—Cross-Correlograms, Cross-Correlation Functions have been Scaled to Fit Vertical Arcs and in Order to Smooth Curves 9 Point Moving Averages have been Used

profiles using the Eq. 6 of the first paper. Fig. 7 also shows the velocity profile obtained from this equation (AD). If the correlation velocity probe is taken as being correct then the results from all velocity profiles show that the stagnation



pressure air concentration method over estimates the velocity with an error which rises to 15% as the air concentration rises to 20%. This error remains approximately constant until the air concentration reaches 75%. Above this the error appears to increase. This increase is not surprising in that it can be shown that equations of the form of Eq. 6 of the first paper, are at high air concentration extremely sensitive to small errors in the stagnation pressure.

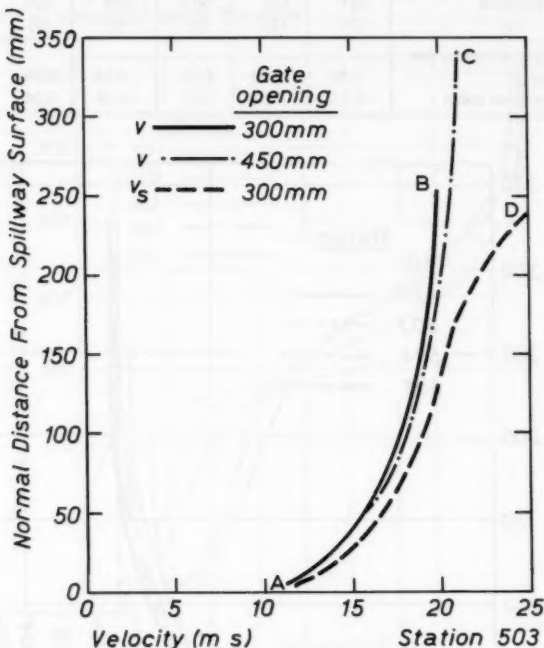


FIG. 7.—Velocities at Station 503

Curve AB—300-Gate Opening Velocity Computed from Correlation Technique

Curve AC—450-mm Gate Opening Velocity Computed from Correlation Technique

Curve AD—300-mm Gate Opening Velocity from Stagnation, Air Concentration Probe

The smoothed velocity profiles for the 300-mm gate opening obtained from the correlation probe have been superimposed in Fig. 8.

#### DISCHARGE MEASUREMENTS

The water discharge was calculated by integrating with depth the product of the velocity and  $(1 - c)$  up to the limit of  $c = 0.95$ .

TABLE 2.—Difference in Water Discharge  $\delta q$  and Variations from Mean  $\delta q$ 

Variable (1)	Station					Mean
	501 (2)	502 (3)	503 (4)	504 (5)	505 (6)	$\delta q$ (7)
$\delta q$ , in square meters per second	0.89	0.90	0.99	0.84	0.98	0.92
variation from mean	-0.03	-0.02	0.07	-0.08	0.06	

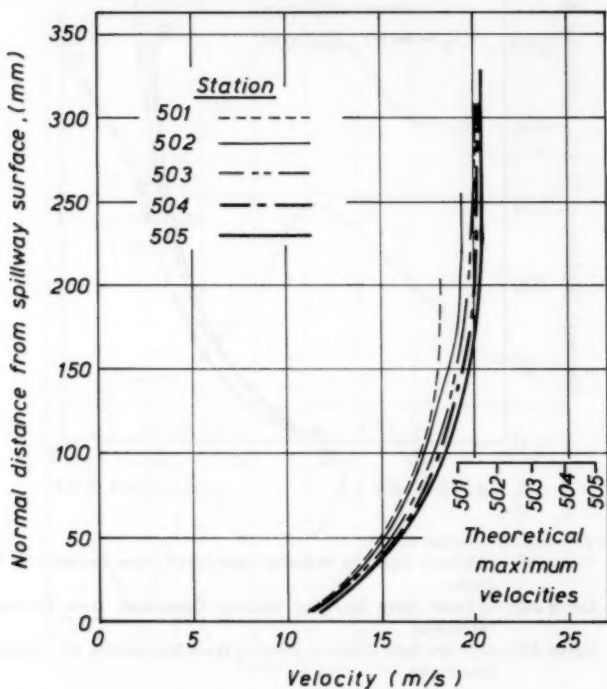
300mm GATE OPENING

FIG. 8.—Velocity Profiles Obtained using Correlation Technique for Stations down Spillway

The choice of  $c = 0.95$  was dictated by the maximum air concentration measured at station 505 with a 450-mm gate opening. This choice is not critical for discharge calculations because the proportion of water from this point to the highest measurement point was less than 1% of the total. The results are shown in Table 1. The errors expected in this calculation were expected to be—velocity— $\pm 1\%$ , air concentration— $\pm 2.5\%$ , a depth of gate opening— $\pm 1\%$ . Thus the maximum error expected was between 4 and 5%. The errors in the stations downstream of station 501 are of this order.

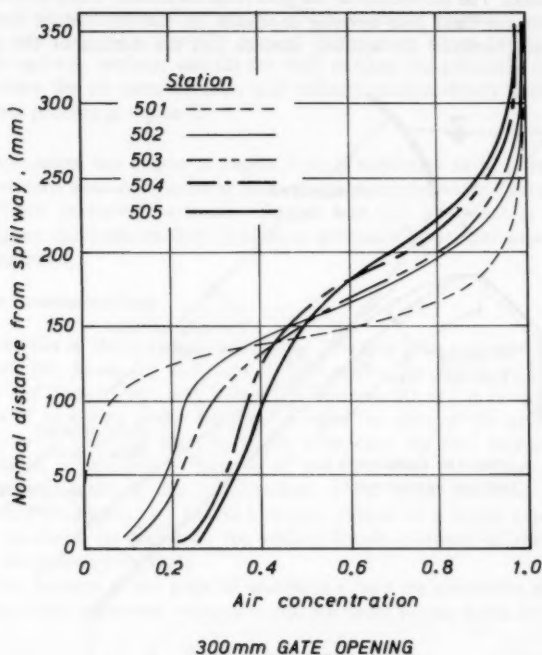


FIG. 9.—Final Air Concentration Profiles

However at station 501 the error was considerably larger. This was investigated further by examining the differences between the discharges ( $\delta q$ ) at the two gate settings. Table 2.

Measurements on model studies indicate an almost linear relationship between the gate opening and discharge. The difference in discharge  $\delta q$  between the discharge for the 300-mm and 450-mm gate openings should therefore be identical for all stations, regardless of the gate's initial closed position. It follows that any variations between the calculated values of  $\delta q$  can be attributed to errors in the measured  $u$  and  $\bar{c}$  profiles. For all cases including station 501 the errors in Table 1 are relatively small and can be accounted for by the error estimates

in the velocity air concentration and depth. This indicates an error in the measurement at station 501. This was attributed to the behavior of the gate seal.

This rubber in this seal deforms under the weight of the gate, its compression increasing with time due to creep. The rubber will rebound when the gate is opened so that when the gate is reclosed the rubber will again deform and start to creep. As the gate was closed for several weeks prior to the first measurements, the rubber was initially compressed more than for the subsequent measurements. The movement of the gate from its initially compressed position was set but the final gate opening depended on the rebound of the rubber. The distance between the spillway surface and the bottom of the gate was

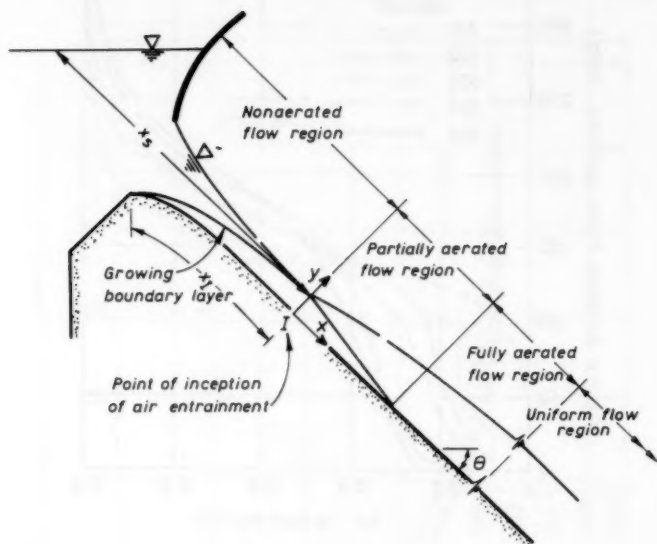


FIG. 10.—Regions of Flow

therefore smallest for the first measurements. This was reflected in the water discharge which were about 10% less than for the following ones.

In order to investigate the development of air entrainment down the spillway the water discharge must be identical for the tests at each station. There was almost no difference between the velocity profiles for the 300-mm and 450-mm gate openings (Fig. 7). It was therefore possible to use the measured discharges and to interpolate between the air concentration profiles to obtain the concentration profiles appropriate to the average discharges of 2.23 m/s and 3.16 m<sup>3</sup>/s. The set of adjusted profiles for the 300-mm gate opening is shown in Fig. 9 and the water discharge per unit width calculated from these profiles is constant to 1%.

## REVIEW OF RESULTS

Before considering the results in detail it is necessary to describe the regions of flow. These are (Fig. 10):

1. Nonaerated flow from the spillway gate to the point of inception of air entrainment.
2. The final uniform flow region in which the air concentration and the velocity profile do not change with distance down the spillway.
3. The gradually varied flow region which connects regions 1 and 2. This region consists of: (1) A partially aerated flow region where the air does not reach the spillway surface; and (2) the fully aerated but gradually varied flow region where the air concentration and velocity profile slowly change to the equilibrium profiles in region 2.

For dam design the extent of region 3 (a) is important as it determines the greatest velocity next to the spillway in the pure nonaerated water. This determines the maximum cavitation parameter. Region 2 is also important in that for a long spillway the uniform flow conditions determine the input condition into the stilling basin.

## REGION OF NONAERATED FLOW

The behavior in the region of nonaerated flow has been reviewed by Michels and Lovely (8), Bauer (1), Ealbronn (5), Campbell, Cox and Boyd (3), Cassidy (5), Rao and Kobus (10), and Keller and Rastogi (8) and it is apparent that the point of inception is the distance  $x_i$  from the start of the growth of the boundary layer over the crest to where it reaches the free surface Fig. 12. This distance is primarily a function of the flow over the spillway crest,  $q$ , (In an ungated spillway this is equivalent to the height over the crest) and the spillway roughness,  $k_s$ . It will however depend to a lesser extent on the spillway geometry (in particular the surface length upstream of the crest and whether the spillway is gated).

Thus the distance to the point of inception  $x_i$  and the properties at the point of inception (the maximum velocity  $v_i$  and the depth  $y_i$ ) are given by

$$\frac{x_i}{k_s}, \frac{y_i}{k_s}, \frac{v_i k_s}{q} = \Phi \left[ F_*, \frac{q}{\nu}, \frac{a}{k_s}, \frac{a}{b} \right] \dots \dots \dots (1)$$

in which  $F_* = q/[gS k_s^3]^{1/2}$ ;  $gS$  = the spillway slope component of gravity slope;  $\nu$  = the kinematic viscosity; and  $a, b$ , = linear dimensions of the spillway crest.

The Reynolds number on the spillways will always be large and the spillway's are relatively rough. Thus the effects of Reynolds number are likely to be negligible. The work of Campbell, et al., (3), Cassidy (4), and Rao and Kobus (9) applies to an ungated crest designed to the specification of the United States Army Corps of Engineers and thus takes into account the geometry of this particular crest. The earlier work of Bauer (1) and Halbronn (5) by assuming that the length over the spillway surface over which the developing boundary layer is computed may be approximated by the slope distance  $x_s$  defined as

in Fig. 12 neglects the effect of the spillway geometry. This approximation will be reasonable provided the point of inception of air entrainment is a reasonable distance down the spillway (i.e., provided  $x_I/a \gg 1$  in which  $a$  is a typical crest dimension). Under these conditions Halbronn and Bauer show that the

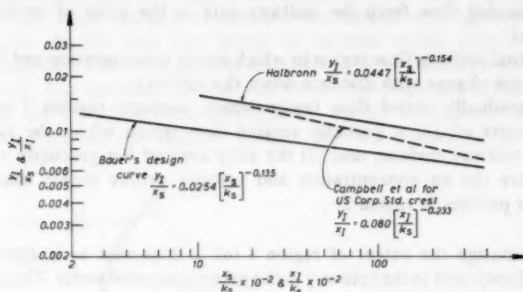


FIG. 11.—Design Curves for Point of Inception Obtained by Bauer, Halbronn and Campbell, et al.

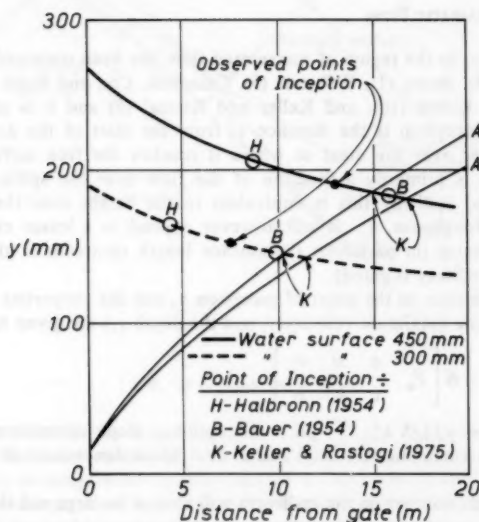


FIG. 12.—Comparison of Observed and Computed Points of Inception  
experimental results should be of the form

$$\frac{y_I}{x_s} = \alpha \left[ \frac{x_s}{k_s} \right]^{-\beta} \quad \dots \dots \dots (2)$$

Based on a boundary layer analysis Halbronn suggests a design curve with  $\alpha = 0.0447$  and  $\beta = 0.154$ . However Bauers experimental result yield  $\alpha = 0.0254$  and  $\beta = 0.135$ . Halbronn and Bauers curves are plotted on Fig. 11. Also plotted in this figure is Campbell, et al. design curve, plotted as  $Y_1/x_1 = \alpha_1 [x_1/k_s]^{-\beta_1}$ . This curve approaches that of Bauer's for their larger value of  $x/k_s$  when  $x_1$  tends to  $x_s$ .

If at these large distances down the spillway Bauer's approach is used and the velocity distribution at the point of inception is assumed to be

$$\frac{u}{u_1} = \left[ \frac{y}{y_1} \right] \frac{1}{n} \quad \dots \dots \dots (3)$$

in which  $u_1$  = the surface velocity at the point of inception;  $y_1$  = the inception depth; and  $n$  = a constant. Then Eq. 2 may be combined with Bernoulli's equation applied to the

$$\frac{x_s}{k_s} = \left[ \frac{n+1}{\alpha n \sqrt{2}} \right]^{1/1.5-\beta} [F_*]^{1/1.5-\beta} \quad \dots \dots \dots (4)$$

$$\frac{y_1}{k_s} = [\alpha]^{1/3-2\beta} \left[ \frac{n+1}{n \sqrt{2}} F_* \right]^{2[1-\beta]/3-2\beta} \quad \dots \dots \dots (5)$$

$$\frac{v_1 k_s}{q} = \sqrt{2} \alpha^{-1/3-2\beta} \left[ \frac{n+1}{n \sqrt{2}} \right]^{[1/3-2\beta]} F_*^{-2(1-\beta)/3-2\beta} \quad \dots \dots \dots (6)$$

The terms in the equation are all design parameters and enable the direct computation of the position and properties at the inception point. It is apparent from these expressions and the order of magnitude of  $\beta$  and  $n$  that all the inception point values have only a very small dependence on  $k_s$  and  $n$ .

This together with the large value of  $x_s/y_1$  (150) makes it reasonable to compare the observed result with those obtained by Bauer, and Halbronn.

For gate openings of 300 mm and 450 mm the position point of inception was determined from photographs of the flow. Locating the exact position of this point was complicated by the presence of surface aeration upstream of this point. This was caused by vortices originating behind the spillway gate and these appeared as long white lines in the flow direction. The point of inception was taken as that point where additional whiteness appeared. These first bursts of additional whiteness appeared at 7.7 and 2.3 m upstream of station 501 for the 300-mm and 450-mm gate openings, respectively.

The air concentration profiles were plotted at the stations down the spillway and the air concentration contours were drawn. These were used to estimate of the depth at the inception point. These results are given in Table 3, where  $x_G$  is the distance measured from the gate. The depth and position at the point of inception are compared with the prediction of Halbronn and Bauer in Fig. 12. Also shown are the computations of Keller and Rastogi (7). They used a program which computes the velocity distribution in the boundary layer and the water depth. The two curves  $A$  and  $A'$  determine the limits of the region in which turbulent flow occurs. Fig. 14 shows that for both gate openings the boundary layer intercepts the free surface about 3 m downstream of the observed point of inception.

## FINAL UNIFORM FLOW REGION

In the air entrained region downstream of the point of inception we define a characteristic depth  $y_{c=90}$  as the depth normal to the spillway surface where the air concentration is 90%. (The value of  $y_{c=90}$  was selected as it could be determined from all experimental measurements with reasonable accuracy.) A mean depth that would exist if the flow was without entrained air can also be defined as

$$d = \int_0^{\infty} (1 - c) dy \quad \dots \dots \dots (7)$$

This leads to an average concentration over the depth  $y_{c=90}$  of

$$\bar{c} = 1 - \frac{d}{y_{c=90}} \quad \dots \dots \dots (8)$$

and an average velocity of the water

$$\bar{u}_w = \frac{q}{d} = \frac{q}{(1 - \bar{c}) y_{c=90}} \quad \dots \dots \dots (9)$$

TABLE 3.—Point of Inception Data

Gate opening, in millimeters (1)	$x_G$ , in meters (2)	$y_I$ , in millimeters (3)	$v_I$ , in meters per second (4)
300	18.4	152	16.0
450	23.8	194	18.2

The value of  $y_{c=90}$ ,  $u_w$ , and  $\bar{c}$  in effect give the characteristics of a uniform concentration fluid of depth  $y_{c=90}$  with same discharge and the mean air concentration as the nonuniform flow. It is also convenient to define the velocity at the characteristics depth  $y_{c=90}$  as  $u_{c=90}$ .

Far downstream from the point of inception the flow will become uniform and the velocity distribution (and therefore the mean velocity), the air concentration distribution (and thus the mean air concentration) and of course the depth [say  $y_{c=90}$ ] will be independent of any upstream geometry and will thus depend only on the slope and roughness. The discharge and terms like  $q/[qS k_s]^{1/2}$  will of course determine the distance down the spillway at which the uniform flow occurs but as in uniform flow in a normal open channel there will be a relationship between the uniform flow parameters, i.e.

$$\bar{c}_u, \frac{u_{uc=90}}{\sqrt{gS y_{uc=90}}}, \frac{u_{uw}}{\sqrt{gS y_{uc=90}}} = \Phi \left[ \frac{y_{uc=90}}{k_s}, S \right] \quad \dots \dots \dots (10)$$

in which the subscript  $u$  implies a measurement in the uniform flow region. This together with Eq. 9 implies that for the uniform flow region



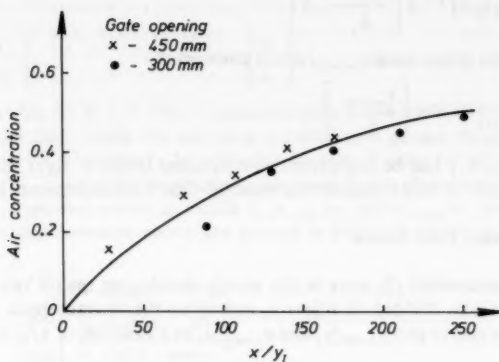


FIG. 13.—Variation of Mean Air Concentration with Dimensionless Distance  $[x/y_I]$  Measured from Point of Inception

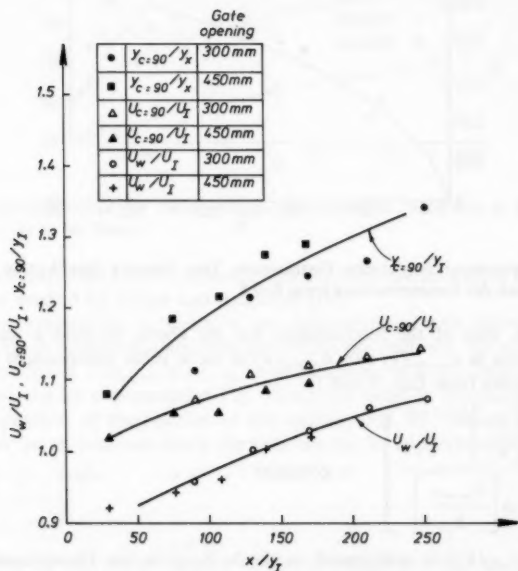


FIG. 14.—Variation of Dimensionless Depth  $y_{c=90}/y_I$  and Velocities  $v_{c=90}/v_I$ ,  $v_w/v_I$  with Dimensionless Distance  $x/y_I$  Measured from Point of Inception

$$q = d_u y_{uc=90} [gS]^{1/2} \phi \left[ \frac{y_{uc=90}}{k_s}, S \right] \dots \dots \dots (11)$$

For a constant slope since  $y_{uc=90}/d$  is a constant  $K$

$$\frac{q}{[y_{uc=90}^3 gS]^{1/2}} = K \phi \left[ \frac{y_{uc=90}}{k_s} \right] \dots \dots \dots (12)$$

The  $\phi [y_{uc=90}/k_s]$  can be interpreted as equivalent to the  $\sqrt{8g/f}$  in the normal Darcy equation. It was apparent that none of Cain's measurements (2) reached.

#### GRADUALLY VARIED FLOW REGION

Cain's measurement (2) were in the slowly developing region and in plotting the results it was decided to select  $y_l$  and  $v_l$  as the characteristic length and velocity scale and to plot  $y_{c=90}/y_l$  and  $u_{c=90}/u_l$  as a function of  $x/y_l$ , the distance

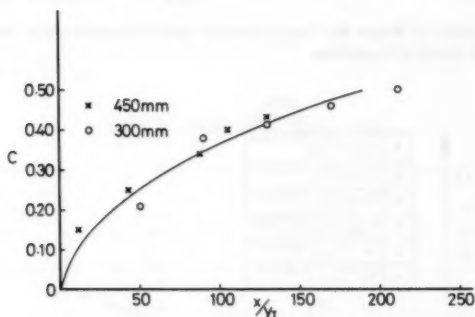


FIG. 15.—Dimensionless Velocity Distribution. This Velocity Distribution holds for Range of Mean Air Concentrations from 0–0.5

downstream. One of the requirements for the above to yield a single curve for each slope is  $y_{uc=90}/y_l$  and  $u_{uc=90}/u_l$  to have value independent of  $y_l$  and  $k_s$ . This implies from Eqs. 5 and 12

$$\frac{y_{uc=90}}{y_l} = \frac{\left[ \frac{y_l}{k_s} \right]^{\beta/2(1-\beta)}}{\phi \left[ \frac{y_{uc=90}}{k_s} \right]} = \text{constant} \dots \dots \dots (13)$$

If the  $\phi [y_{c=90}/k_s]$  is interpreted as the  $\sqrt{8g/f}$  in the Darcy equation and it is assumed that the effects of roughness in the air entrained flow is similar to that in a nonaerated flow then at the high Reynolds numbers we write

$$\phi \left[ \frac{y_{uc=90}}{k_s} \right] = \left[ \frac{y_{uc=90}}{k_s} \right]^m \dots \dots \dots (14)$$

where from the experimental work of Nikuradse  $m$  varies from 0.10–0.20. This implies

$$\frac{y_{uc=90}}{y_l} \sim \left[ \frac{y_l}{k_s} \right]^{\beta-2m[1-\beta]/[1-\beta](3+2m)} \sim \left[ \frac{y_l}{k_s} \right]^{\epsilon} \quad (15)$$

This implies that for  $\beta = 0.135$   $\epsilon$  varies between 0.014 and 0.037. These small values suggest that, within the accuracy required in a normal design,  $y_{uc=90}/y_l$  may be taken as a constant. In a similar manner it may be shown that for a fixed slope  $u_{uc=90}/u_l$  will also be almost constant. It therefore seems reasonable to look for a general curve in which  $\bar{c}$ ,  $y_{c=90}/y_l$  and  $u_{c=90}/u_l$  are functions of  $x/y_l$ . The experimental curves are plotted in Figs. 13 and 14. It is apparent

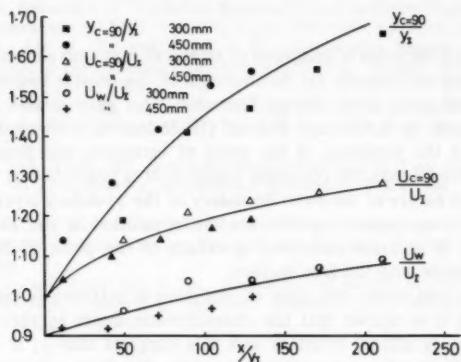


FIG. 16.—Dimensionless Air Concentration Distributions. Variation in Shape with Position  $x/y_l$  is to be Noted

from these curves that Cain's measurements are some distance from the uniform flow region studied by Straub and Anderson (10).

It is now appropriate to examine the distribution of the velocity and air concentration at nondimensional distances down the spillway. We would expect the distributions  $c$ ,  $u/u_{c=90}$ ,  $y/y_{c=90}$  to be functions of  $x/y_l$ . This is certainly the case for the air concentration Fig. 16 but the velocity distribution appears to be independent of the position of the spillway Fig. 15. Indeed the velocity distribution for all positions down the spillway can be approximated by

$$\frac{u}{u_{c=90}} = \left[ \frac{y}{y_{c=90}} \right]^{0.1584} \quad (16)$$

This implies that the air in suspension has a negligible effect on the velocity distribution of the air water interfaces and this contrasts with the work of most previous investigators. It is however reasonable to expect that with the constant interchange of water droplets from the mean flow into the air these droplets will retain the water velocity for the relatively short time of projection and hence the velocity distribution will not greatly differ from the nonaerated

flow distribution. It is apparent from Fig. 16 that the air concentration becomes more uniform with distance downstream and that the progression of the curves with the nondimensional distance ( $x/y_i$ ) for the larger values of  $x/y_i$  is regular. At small values of  $x/y_i$  (45 and 51) an irregularity occurs. This is almost certainly caused by the presence of a longitudinal vortex in the measurement at  $x/y_i = 45$ . These vortices are irregular features in the flow and with the small average air concentrations at these small  $x/y_i$  values, the presence of one of these air entraining eddies has a major effect.

It is also important to notice that the value  $x/y_i$  of approx 100 the air concentration has reached 10% at the spillway surface. This should set the downstream limit for cavitation.

## CONCLUSIONS

Observation of the point of inception of air entrainment has shown that provided this point occurs sufficiently far downstream of the crest a minor modification of Bauer's work gives direct design formulae. This gave results as reasonable as those obtained by Keller and Rastogi (7). Indeed in both of these methods the estimate of the positions of the point of inception was approx 2 m-3 m further downstream than the observed position. It is possible that this is caused by the unsteady nature of the outer boundary of the boundary layer. This results in turbulence being present outside the mean position at the outer boundary layer resulting in aeration occurring upstream of the point of intersection of the boundary layer with the free surface.

Also for the case where the point of inception is sufficiently far downstream from the crest it is shown that the characteristic depth in the uniform flow region  $y_{uc=90}/y_i$  is almost constant and this suggests that  $y_i$  is a convenient characteristic depth when presenting the results. Similarly a convenient characteristic velocity is  $u_i$ . The results presented in this manner show that for the 45° slope:

1.  $x/y_i = 212$  is still in the developing region of the air entraining flow and that at this point  $\bar{c} = 0.5$ ;  $y/y_i = 1.3$ ; and  $u_{c=90}/u_i = 1.1$ .
2. Significant air concentrations reached the spillway surface at  $x/y_i = 100$ . This implies that cavitation is not likely to occur downstream of this position.
3. That the shape of the velocity of air water interfaces is given by  $u/u_{c=90} = [y/y_{c=90}]^{0.158}$  for average air concentration ranging from 0-0.5.
4. That the air concentration becomes progressively larger and more uniform with increasing values of  $x/y_i$ .

## ACKNOWLEDGMENTS

The writers would like to thank K. P. McCool, L. Newbury, and G. Symes of the N. Z. Electricity Division of the Ministry of Energy for arranging the release of water over Aviemore spillway; S. M. J. Smith and J. Crawford of the Ministry of Works and Development for providing the equipment which gave access to the spillway and to W. K. Kennedy of the University of Canterbury, Electrical Engineering Department who assisted with the data analysis. The suggestions of a referee are also acknowledged.

## APPENDIX I.—REFERENCES

1. Bauer, W. J., "Turbulent Boundary Layer on Steep Slopes," *Transactions, ASCE*, Vol. 119, Paper No. 2719, 1954, pp. 1212-1232.
2. Cain, P., "Measurement Within Self-Aerated Flow on a Large Spillway," thesis presented to the University of Canterbury, at Christchurch, New Zealand, in 1978, in partial fulfillment of the requirements for the degree of Doctor of Philosophy.
3. Campbell, F. D., Cox, R. G., and Boyd, M. B., "Boundary Layer Development and Spillway Energy Losses," *Journal of the Hydraulics Division, ASCE*, Vol. 91, No. HY3, Proc. Paper 4331, May, 1965, pp. 149-163.
4. Cassidy, J. J., discussion of "Boundary Layer Development and Spillway Energy Losses," by Frank B. Campbell, Robert G. Cox, and Marden B. Boyd, *Journal of Hydraulics Division, ASCE*, Vol. 92, No. HY2, Proc. Paper 4331, Mar., 1966, pp. 370-372.
5. Halbronn, G., discussion of "Turbulent Boundary Layer on Steep Slopes," by William J. Bauer, *Transactions, ASCE*, Vol. 119, Paper 2719, 1954, pp. 1234-1242.
6. Keller, R. J., Lai, K. K., and Wood, I. R., "Developing Region in Self-Aerated Flows," *Journal of the Hydraulics Division, ASCE*, Vol. 100, No. HY4, Proc. Paper 10501, Apr., 1974, pp. 553-568.
7. Keller, R. J., and Rastogi, A. K., "Prediction of Flow Development on Spillway," *Journal of Hydraulics Division, ASCE*, Vol. 101, No. HY9, Proc. Paper 11581, Sept., 1975, pp. 1171-1183.
8. Michels, V., and Lovely, M., "Some Prototype Observations of Air Entrained Flow," *Proceedings of the Minnesota International Hydraulics Convention*, Part IV, 1953, pp. 403-414.
9. Rao, N. S. L., and Kobus, H. E., "Characteristics of Self-Aerated Surface Flows, Water and Waste Water," *Current Research and Practice*, Vol. 10, Erich Schmidt, Verlag, Berlin.
10. Straub, L. G., and Anderson, A. G., "Experimental Studies of Air Entrainment in Open Channel Flow," *Journal of Hydraulics Division, ASCE*, No. HY7, Proc. Paper 1890, Dec., 1958, pp. 456-481.

## APPENDIX II.—NOTATION

The following symbols are used in this paper:

- $a, b$  = linear dimensions of spillway crest;  
 $c$  = air concentration, as a percentage;  
 $\bar{c}$  = mean air concentration;  
 $d$  = mean flow depth defined by  $d = \int_0^\infty (1 - c) dy$ ;  
 $F_*$  = Froude number base on design quantities defined by  $q / [gS k_s^3]^{1/2}$ ;  
 $f$  = Darcy's function factor;  
 $g$  = acceleration of gravity;  
 $h$  = vertical distance from Spillway station to water level behind dam;  
 $k_s$  = equivalent sand roughness of spillway;  
 $n$  = constant;  
 $P_a$  = atmospheric pressure;  
 $P_s$  = mean stagnation pressure;  
 $q$  = discharge/unit width, in cubic meters per meter-second;  
 $S$  = spillway slope =  $\sin \theta$ ;  
 $u_i$  = velocity of surface streamline at point of inception;  
 $u_s$  = surface velocity;  
 $\bar{u}_w$  = average water velocity defined by  $g/d$ ;  
 $u_{c=90}$  = velocity where air concentration is 90%;

- $u_{uc=90}$  = velocity in uniform flow region where air concentration is 90%;  
 $\bar{u}_{uw}$  = mean velocity in uniform flow region;  
 $x$  = distance measured downstream from point of inception;  
 $x_G$  = distance measured downstream from gate;  
 $x_f$  = distance from start of growth of boundary layer to point where it reaches flow surface (point of inception of air entrainment);  
 $x_s$  = slope distance used as an approximation for  $x$ , and defined in Fig. 10;  
 $y$  = distance measured normal to spillway surface;  
 $y_s$  = depth to surface of flow;  
 $y_{c=90}$  = depth to position where air concentration is 90%;  
 $y_{uc=90}$  = depth in uniform flow region to position where air concentration is 90%;  
 $\alpha$  = constant;  
 $\beta_1$  = constant;  
 $\delta q$  = change in  $q$  between two gate openings;  
 $\rho_w$  = density of water; and  
 $\nu$  = kinematic viscosity.

## BED LOAD DISCHARGE COEFFICIENT

By Peter Engel<sup>1</sup> and Y. Lam Lau<sup>2</sup>

### INTRODUCTION

When flow conditions are in the dune regime, the flow separates at the dune crests, creating a wake zone extending some distance downstream to the point of reattachment on the back of the next bed form. This results in a velocity along the bed in the upstream direction within this zone. Therefore, the material contributing to the average bed load discharge must be obtained from the region between the point of flow reattachment and the first crest downstream. This contention is supported by observations of Raudkivi (8), Yalin (11), and Vanoni and Hwang (9).

The fact that bed load transport occurs only between the point of flow reattachment and the next crest was a basic consideration in the development of an equation by Crickmore (1) and Engel and Lau (3) to compute bed load from bed profile records of migrating dunes. A basic requirement of this equation is a definition of the bed elevations on the bed forms at which there is zero transport, and this was taken to be at the point of flow reattachment. Analysis of data by Jonys (6) for a large number of dunes showed that the point of maximum pressure (minimum velocity) could be taken above the trough elevation in the lee of the bed forms by an amount equal to 0.17, the bed-form height.

A review of the literature could not confirm the above value for the position of zero transport, nor was it possible to determine this position theoretically. Therefore, an experimental study was conducted to reveal the relationship between the position of zero transport, bed-form height, bed-form shape, grain size, and flow conditions. The results are used to produce a bed load discharge coefficient for use with the equation presented by Engel and Lau (3).

### ANALYTICAL CONSIDERATIONS

**Background.**—The equation given by Engel and Lau (3) to compute bed-load discharge from migrating dunes is given by

<sup>1</sup>Research Engr., Environmental Hydr. Sect., Hydr. Div., National Water Research Inst., Burlington, Ontario, Canada.

<sup>2</sup>Head, Environmental Hydr. Sect., Hydr. Div., National Water Research Inst., Burlington, Ontario, Canada.

Note.—Discussion open until April 1, 1982. To extend the closing date one month, a written request must be filed with the Manager of Technical and Professional Publications, ASCE. Manuscript was submitted for review for possible publication on December 10, 1980. This paper is part of the Journal of the Hydraulics Division, Proceedings of the American Society of Civil Engineers, ©ASCE, Vol. 107, No. HY11, November, 1981. ISSN 0044-796X/81/0011-1445/\$01.00.

$$G_s = 1.32 \gamma_s (1 - P) \bar{\xi} U_w \quad (1)$$

in which  $G_s$  = submerged weight of bed load per unit width per unit time;  $\gamma_s$  = submerged unit weight of sediment;  $P$  = porosity of sediment;  $\bar{\xi}$  = average departure of the bed elevations about the average of all the elevation,  $\bar{\eta}$  in the profile record; and  $U_w$  = speed of the migrating dunes. In developing Eq. 1, it was assumed that the dunes were triangular in shape. An additional requirement was to define the distance between the elevation of zero transport,  $\eta_o$ , and the lowest point in the trough,  $\eta_t$ , for the dunes (Fig. 1). From data by Jonys (6), an average value of this distance in terms of dune height,  $\Delta$ , was determined as  $(\eta_o - \eta_t) = 0.17 \Delta$ . This value, together with the assumption of triangular dune shapes, lead to the final value of 1.32 given in Eq. 1. Reasonably good results were obtained when bed load discharge computed with Eq. 1 was compared with data from flume experiments.

**Bed Load Discharge Coefficient.**—The coefficient of 1.32 in Eq. 1 may be regarded as a particular value of a general bed-load coefficient. This general coefficient can be obtained from the equation given by Engel and Lau (3) as

$$q_{sa} = (\bar{\eta} - \eta_o) U_w \quad (2)$$

in which  $q_{sa}$  = average volumetric transport rate per unit width including the

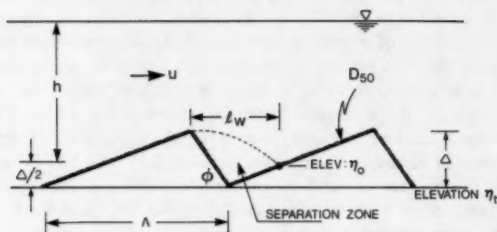


FIG. 1.—Definition Sketch

voids,  $U_w$  = average dune migration speed, and  $\eta$  = bed elevation. Eq. 2 can be rewritten as

$$q_{sa} = [(\bar{\eta} - \eta_t) - (\eta_o - \eta_t)] U_w \quad (3)$$

If one now writes  $(\bar{\eta} - \eta_t) = \alpha \Delta$ ;  $(\eta_o - \eta_t) = k \Delta$ ; and  $\Delta = a \bar{\xi}$ ; in which  $\Delta$  = height of the bed forms, then upon substituting into Eq. 3, one obtains

$$q_{sa} = a(\alpha - k) \bar{\xi} U_w = K \bar{\xi} U_w \quad (4)$$

in which  $\bar{\xi}$  = average departure of the bed elevation about the mean bed elevation. The quantity  $a(\alpha - k)$  is the bed-load discharge coefficient, and will be denoted as  $K$ . If the dunes are assumed to be triangular in shape, the coefficients,  $a$  and  $\alpha$ , can be shown to be equal to 4 and 0.5, respectively. Willis and Kennedy (10) have stated that the assumption of triangular dunes is sufficiently accurate for computation of bed load transport rates. Fredsoe (5) used both triangular and sinusoidal forms for calculating the variation of shear stress along the dune, and found that the triangular shape gave more accurate results. Therefore, the



triangular dune shape was used for this study and the bed load discharge coefficient,  $K$ , may be written as

$$K = 4(0.5 - k) \quad (5)$$

**Dimensional Analysis.**—In order to have good control of the variables defining the dune height and length, it is convenient to use a rigid bed composed of artificial dunes. Under these conditions, considering two-dimensional flow in a straight uniform channel,  $k$  can be expressed as

$$k = f(\Delta, \Lambda, \phi, D_{50}, h, U, \rho, \mu, g) \quad (6)$$

in which  $\Lambda$  = length of bed forms, crest to crest;  $\Delta$  = height of dunes, trough to crest;  $\phi$  = angle of inclination of downstream face of dunes;  $D_{50}$  = median grain diameter;  $h$  = average depth of flow;  $U$  = average flow velocity;  $\rho$  = density of the fluid;  $\mu$  = viscosity of the fluid; and  $g$  = acceleration due to gravity. The symbols are schematically defined in Fig. 1. Using the  $\pi$  theorem for dimensional analysis and simplifying, Eq. 6 can be written in dimensionless form as

$$k = f_1 \left( \frac{\Delta}{\Lambda}, \phi, \frac{D_{50}}{\Delta}, \frac{h}{\Delta}, \frac{U \Delta \rho}{\mu}, \frac{U}{\sqrt{gh}} \right) \quad (7)$$

Measurements by Etheridge and Kemp (4) have shown that flow in the separation zone is insensitive to the flow in the corner region at the foot of a reverse rectangular step. This suggests that quite crude modelling of ripples and dunes in the region between crest and downstream toe is justifiable. Therefore, the angle  $\phi$  is not an important parameter in Eq. 7, and can be omitted from further consideration. For large Reynolds number, the effect of viscosity will also not be important, and the term  $U \Delta \rho / \mu$  can be deleted. Analysis of the experimental data obtained by Engel (2) also indicated that within the experimental error,  $k$  is virtually independent of the Froude number,  $U / \sqrt{gh}$  and, at most, only weakly dependent on  $h / \Delta$ . Therefore, the consideration of  $k$  is reduced to revealing the form of the relationship

$$k = f_2 \left( \frac{\Delta}{\Lambda}, \frac{D_{50}}{\Delta} \right) \quad (8)$$

The coefficient,  $k$ , depends on  $\eta_o$ , the elevation of zero transport, which was taken to be at the point of flow reattachment. In this study the position of  $\eta_o$  was obtained by measuring the length of the flow separation  $l_w$  defined in Fig. 1. The value of  $k$  could then be simply computed from the relationship

$$k = \frac{l_w - \Delta \cot \phi}{\Lambda - \Delta \cot \phi} \quad (9)$$

The variation of  $k$  and, thus, the discharge coefficient,  $K$ , with the hydraulic parameters and its effect on the computation of bed-load discharge have been investigated.

#### EXPERIMENTAL EQUIPMENT AND PROCEDURE

Experiments were conducted in a tilting flume rectangular in cross section, 20 m long and 1 m wide. Discharges were measured at the downstream end

using a weir box. The flow leaving the flume was split into three parts of equal width, and only the flow from the central portion was measured in the weir box. By working only with the nearly two-dimensional flow in the center portion of the flume, the effect of the side walls was practically eliminated. The flows were always uniform with Froude numbers not exceeding 0.5.

The dune roughness was obtained by using artificial bed forms fabricated from plywood and covered with sand. Four different bed form shapes,  $\Delta/\Delta$ , each with different sand roughnesses ( $D_{50}$ ), as well as the smooth bed forms ( $D_{50} \approx 0$ ) were used. All bed forms had a height of 30 mm with a downstream toe angle of  $\phi = 30^\circ$ , and were placed over the full length of the flume. The sand was fixed to the bed forms by first covering these with "Mactac," self adhesive vinyl covering. Then a thin layer of varnish was brushed on, and the sand was sprinkled on top so that the "Mactac" was completely covered (7). After drying overnight, the excess sand was washed off, and a uniform layer of sand was left on the dunes. To change over to another sand roughness, the "Mactac" was stripped off and the process repeated. Each bed form was tested with one or more sand sizes before a new one was placed in the flume. In all, three different sand sizes were used having median diameters of 0.62, 1.20, and 2.60 mm, respectively. Thus, each sand size was approximately twice as large as the one preceding it. Tests on the plane bed forms were conducted using the smooth surface of the "Mactac" only.

The flow separations in all cases were observed using Potassium Permanganate solution as a tracer. A 100-ml hypodermic syringe with a needle 450 mm long and 1 mm inside diameter was attached to a traversing mechanism on a movable carriage, which travelled on the rails on top of the flume walls. This permitted movement of the syringe in both the vertical and horizontal direction. The tip of the hypodermic needle was ground off at an angle of  $30^\circ$  with the vertical. This made it possible to place the needle so that the dye was always injected at right angles to the main flow, and ensured that no momentum in the streamwise direction was imparted to the dye. Once a given flow was set up, the syringe was filled with the dye and positioned on the center line of the flow and then lowered so that the needle was about 1 mm or less above the dune surface.

The location of the point of flow reattachment was obtained by the following two steps. In both steps, dye was injected into the flow in small short pulses, and these were observed to note their direction of movement. In the first step, the syringe was always positioned well downstream of the anticipated separation zone so that there was a clear and distinct movement of dye pulses downstream. The syringe was then moved in small increments to new positions upstream, and, in each case, the behavior of the dye pulses was carefully noted. The progressive upstream positioning continued until it was observed that some of the dye tended to travel upstream. This point was defined as the downstream edge of the region in which the point of flow reattachment occurs. The concept of a region was adopted since due to the turbulent fluctuations it would not be possible to define a precise point, but rather an average. In the second step of the procedure, the syringe was placed at the toe of the bed form in the separation zone being considered. At this point, the dye pulses clearly moved upstream and up the steep face of the dune. The syringe was then placed at different positions, each being about 3-4 mm further downstream than the previous one, and the movement of the dye observed. This was continued until,

once again, a portion of the dye pulse was entrained in the downstream flow. This point was taken to be the upstream edge of the region for the point of flow reattachment. All positional measurements were related to the crest of the dune upstream of the separation zone, and, thus, the probable average location of the point of flow reattachment was simply the average of the measured pairs. Several pairs of such measurements were made for a given flow condition to ensure a reasonably reliable position for the point of reattachment. The variation between values of the length of flow separation for the different pairs of measurement was less than 10%. In all, data for 291 runs were obtained (2) in which dune length, flow depth, sand size, and the discharge were the basic variables that were varied.

#### DATA ANALYSIS

Average values of  $k$  were computed with Eq. 9 and plotted in Fig. 2 as a function of  $\Delta/\Lambda$  using  $D_{50}/\Delta$  as a parameter. The variation of  $k$  is shown as a family of curves, which diverge in a nonlinear fashion from a near common value at  $\Delta/\Lambda = 0.07$  to form separate branches for each value of  $D_{50}/\Delta$ , as  $\Delta/\Lambda$  decreases toward the lowest tested value of  $\Delta/\Lambda = 0.02$ . For each curve, values of  $k$  decrease as  $\Delta/\Lambda$  decreases, with the rate of change in  $k$  increasing as  $\Delta/\Lambda$  decreases. The curves also show that, for small values of  $\Delta/\Lambda$ , the effect of change in grain size is more significant for a given dune height,  $\Delta$ , than for larger values of  $\Delta/\Lambda$ . This effect is virtually negligible when  $\Delta/\Lambda < 0.06$ . Next, values of  $k$  were obtained by interpolation for even

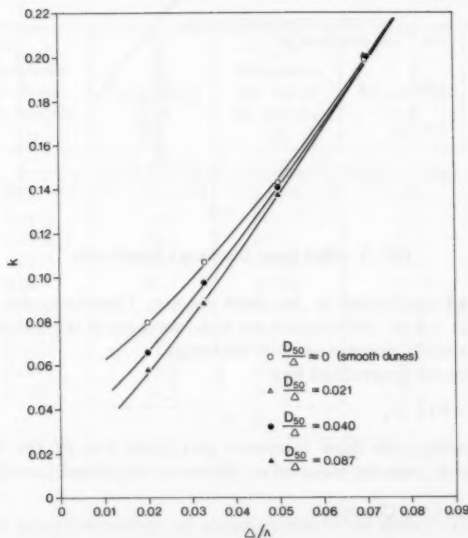


FIG. 2.—Variation of  $k$  with Dune Steepness

values of  $D_{50}/\Delta$  for each value of  $\Delta/\Lambda$  from Fig. 2, and these were used to compute  $K$  from Eq. 5. These values of  $K$  were then plotted in Fig. 3 as a function of the  $\Delta/\Lambda$ , using  $D_{50}/\Delta$  as a parameter. The family of curves displays similar characteristics to that in Fig. 2, except that  $K$  decreases as  $\Delta/\Lambda$  increases, which is a direct consequence of the application of  $k$  to Eq. 5.

Upon examining Fig. 2, it can be seen that the value of  $k = 0.17$  used by Engel and Lau (3) to obtain the value of  $K = 1.32$  in Eq. 1 corresponds to a dune steepness of approx 0.06. The value of  $\Delta/\Lambda = 0.06$  is the maximum value that is likely to occur for dunes (12), and is approximately the value for the data of Jonys (6) used by Engel and Lau (3). In this range, as can be seen from Fig. 3, there is always an effect on  $K$  due to the grain size of the bed material. Fig. 3 also shows that  $K = 1.32$  is the minimum value

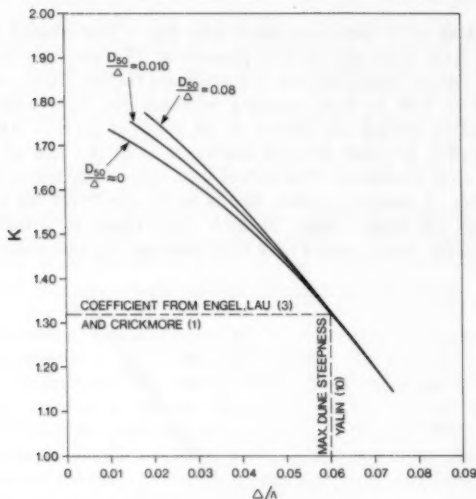


FIG. 3.—Bed Load Discharge Coefficient

of the bed load coefficient in the dune regime. Therefore, the use of  $K = 1.32$ , when  $\Delta/\Lambda < 0.06$ , will result in an underestimate of the bed load discharge and this error should increase as  $\Delta/\Lambda$  decreases.

Eq. 1 can now be generalized into

$$G_s = K \gamma_s (1 - P) \bar{\xi} U_w \quad (10)$$

in which  $K$  varies with dune steepness and grain size of the bed material. Values of  $\bar{\xi}$  and  $U_w$  can be obtained as shown by Engel and Lau (3).

#### APPLICATION OF BED LOAD COEFFICIENT

Existing data used by Engel and Lau (3) were used as a preliminary test to assess the effect of using  $K$  from Fig. 3 when computing bed-load discharge

with Eq. 1. The dune lengths,  $\Lambda$ , were obtained by dividing the length of the bed profile record consisting of a number of complete dunes divided by the number of dunes. The dune heights,  $\Delta$ , were obtained as the difference between

TABLE 1.—Computed Bed Load Using  $K$ 

Run number (1)	$\bar{\xi}$ in meters (2)	$U_w$ times $10^4$ meters per second (3)	$G_{sm}$ in kilograms per meter per second (4)	$\Delta/\Lambda$ (5)	$D_{50}/\Delta$ (6)	$K$ (7)	$G_{sc}$ in kilograms per meter per second (8)	$E$ , as a percentage (9)
1	0.0201	6.02	0.0166	0.062	0.018	1.30	0.0143	-14.0
3	0.0191	6.25	0.0161	0.049	0.020	1.45	0.0157	-2.5
4	0.0164	5.37	0.0089	0.052	0.020	1.42	0.113	27.5
5	0.0175	6.52	0.0177	0.044	0.025	1.51	0.0156	-11.5
6	0.0185	10.87	0.0336	0.041	0.024	1.54	0.0281	-16.4
7	0.0162	4.20	0.0107	0.039	0.023	1.56	0.0096	-9.9
8	0.0207	7.33	0.0171	0.045	0.024	1.50	0.0206	20.8
13	0.0147	6.75	0.0128	0.050	0.026	1.45	0.0131	2.0
14	0.0179	7.79	0.0153	0.048	0.026	1.47	0.0186	21.5
15	0.0179	9.09	0.0174	0.054	0.021	1.40	0.0207	18.8

TABLE 2.—Effect of Bed Load Coefficient

Run number (1)	$G_{sc}$ in kilograms per meter per second (2)	Percentage of $E$ (3)	$G_{sc}$ in kilograms per meter per second (4)	Percentage of $E$ (5)	$G_{sm}$ in kilograms per meter per second (6)
(a) $K = 1.32$ ; $K = K(D_{50}/\Delta, \Delta/\Lambda)$					
1	0.0145	-12.7	0.0143	-14.0	0.0166
3	0.0143	-11.2	0.0157	-2.5	0.0161
4	0.0106	19.1	0.113	27.5	0.0089
5	0.0137	-22.6	0.0156	-11.7	0.0177
6	0.0237	-29.5	0.0281	-16.4	0.0336
7	0.0083	-22.4	0.0096	-9.9	0.0107
8	0.0182	6.4	0.0206	20.8	0.0171
13	0.0119	-7.0	0.0131	2.0	0.0128
14	0.0167	9.2	0.0186	21.5	0.0153
15	0.0195	12.1	0.0207	+18.8	0.0174
(b) $\bar{E}$					
		-5.9		+3.6	

the crest and trough elevation of clearly identifiable dunes. The final values of  $\Lambda$  and  $\Delta$  were taken as the arithmetic mean obtained from at least 15 profiles for each flow condition. More sophisticated methods are available, but the present

procedure was deemed to be sufficient for a preliminary assessment of the discharge coefficient,  $K$ . The data are given in Table 1. Values of  $K$  were obtained for the appropriate values of  $\Delta/\Lambda$  and  $D_{50}/\Delta$  for each of the 10 runs and the bed load discharge  $G_{sc}$  computed. These computed values of  $G_{sc}$  were compared with the measured values  $G_{sm}$  by computing the relative percent error defined as

$$E = \frac{G_{sc} - G_{sm}}{G_{sm}} \times 100\% \quad (11)$$

The computed values of  $G_{sc}$  and  $E$  are given also in Table 1. In order to assess the effect of  $K$ , the computed bed load discharge errors in Table 1 were compared with the percent errors obtained by Engel and Lau (3) when  $K = 1.32$ . The computed bed load discharge and the corresponding percent errors for the two cases of  $K$  are given in Table 2.

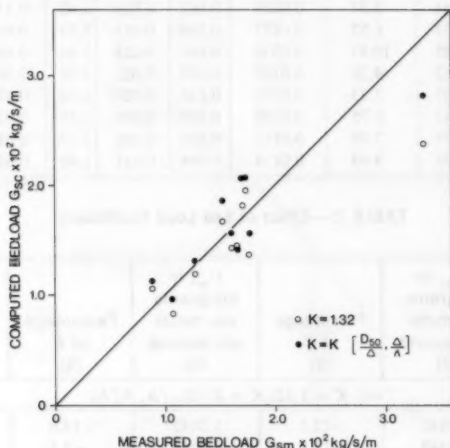


FIG. 4.—Effect of Bed Load Coefficient

The values of the computed bed load were plotted in Fig. 4 versus the measured transport rate for the two cases of  $K = 1.32$  and those obtained from Fig. 3. Upon comparing the two sets of plotted data, it can be seen that the effect of  $K$  has been to reduce the negative errors and to increase the positive errors over the range of  $\Delta/\Lambda$  from 0.039–0.062 used. However, the reduction in the negative errors was greater than the increase in the positive errors. The net effect of this was a change in overall average error from  $-5.2$ – $+3.6\%$ . The overall average absolute error changed from  $15.2$ – $14.5\%$ .

The use of the bed load coefficient,  $K$ , has resulted in an overall improvement. However, the limited data indicates that the improvement is small because the value of  $K$  depends heavily on the bed form parameters,  $\Delta$ , and  $\Lambda$ , both of which are known to have large sampling variances. This is particularly true

for the bed-form height,  $\Delta$ . Since it has been shown in Fig. 3 that  $K$  is quite sensitive to changes in  $\Delta/\Lambda$ , then it is quite clear that values of  $K$  cannot be more reliable than the measured values of  $\Delta$  and  $\Lambda$ .

## CONCLUSIONS

The results from experimental data (2) resulted in the following conclusions:

1. The position of zero transport on the back of a dune varies with the steepness of the dunes and the grain size of the bed material.
2. The bed load coefficient defined in Eq. 4 is quite sensitive to changes in dune steepness and, to a lesser degree, to changes in grain size of the bed material. When dunes are flat, the effect of grain size on the bed load coefficient is significant. When dunes are steep, the coefficient depends on dune steepness only.
3. The use of the bed load coefficient resulted in some improvement by decreasing the overall average error in a set of 10 separate flume tests.
4. The value of the bed load coefficient  $K = 1.32$  used by Engel and Lau (3) appears to be a special case representing the value for maximum dune steepness of 0.06.

## ACKNOWLEDGMENTS

All the measurements and photographs were made by J. Dalton assisted by D. Doede. The writers are grateful for their dedication to this project.

## APPENDIX I.—REFERENCES

1. Crickmore, M. G., "Effect of Flume Width on Bed Form Characteristics," *Journal of the Hydraulics Division*, ASCE, Vol. 96, No. HY2, Proc. Paper 7077, Feb., 1970.
2. Engel, P., "Bed Load Discharge Coefficient for Migrating Dunes," Unpublished Report, Hydraulics Division, National Water Research Institute, Burlington, Ontario, Canada, Apr., 1980.
3. Engel, P., and Lau, Y. L., "Computation of Bed Load Using Bathymetric Data," *Journal of the Hydraulics Division*, ASCE, Vol. 106, No. HY3, Proc. Paper 15255, Mar., 1980.
4. Etheridge, D. W., and Kemp, P. H., "Velocity Measurements Downstream of Rearward Facing Steps with Reference to Bed Instability," *Journal of Hydraulics Research*, International Association of Hydraulics Research, Vol. 17, No. 2, 1979.
5. Fredsoe, J., "Dimensions of Stationary Dunes," Progress Report No. 49, Institute of Hydrodynamics and Hydraulic Engineering, Technical University of Denmark, Aug., 1979, pp. 3-10.
6. Jonys, C. K., "An Experimental Study of Bed Form Mechanics," thesis, presented at the University of Alberta, Alberta, Canada, in 1973, in partial fulfillment of the requirements for degree of Doctor of Philosophy.
7. Lau, Y. L., and Krishnappan, B. G., "Transverse Dispersion in Rectangular Channels," *Journal of the Hydraulics Division*, ASCE, Vol. 103, No. HY10, Nov., 1979.
8. Raudkivi, A. Y., "Study of Sediment Ripple Formation," *Journal of the Hydraulics Division*, ASCE, Vol. 89, No. HY6, Proc. Paper 3692, Nov., 1963, pp. 15-33.
9. Vanoni, V. A., and Hwang, L. S., "Relation Between Bed Forms and Friction in Streams," *Journal of the Hydraulics Division*, ASCE, Vol. 95, No. HY4, Apr., 1967.
10. Willis, J. C., and Kennedy, J. F., "Sediment Discharge of Alluvial Streams Calculated from Bed Form Statistics," International Association of Hydraulics Research Report

- No. 202, Iowa Institute of Hydraulic Research, The University of Iowa, Iowa City, Iowa, 1975.
11. Yalin, M. S., "Mechanics of Sediment Transport," 2nd ed., Pergamon Press, Inc., New York, N.Y., 1977.
  12. Yalin, M. S., "Geometric Properties of Sand Waves," *Journal of the Hydraulics Division*, ASCE, Vol. 90, No. HY5, 1964.

## APPENDIX II.—NOTATION

*The following symbols are used in this paper:*

- $a$  = a dimensionless coefficient;
- $D_{50}$  = median grain diameter;
- $E$  = relative percent error;
- $f$  = a symbol denoting a function;
- $G_{sc}$  = computed submerged weight of bed load;
- $G_{sm}$  = measured submerged weight of bed load;
- $g$  = acceleration due to gravity;
- $h$  = average depth of flow;
- $K$  = bed-load discharge coefficient;
- $k$  = dimensionless difference between elevation of point of reattachment and the dune trough;
- $l_w$  = length of flow separation;
- $P$  = porosity of the bed material;
- $U$  = average flow velocity;
- $U_w$  = migration speed of the dunes;
- $\alpha$  = dimensionless coefficient;
- $\Delta$  = height of the dunes;
- $\bar{\xi}$  = average departure of bed elevation about the mean bed elevation;
- $\gamma_s$  = submerged unit weight of bed load;
- $\Lambda$  = length of the dune;
- $\mu$  = viscosity of the fluid;
- $\phi$  = angle of repose of bed material;
- $\eta_a$  = elevation of point of reattachment;
- $\eta_t$  = elevation of lowest point in the trough in the lee of the dune crest;  
and
- $\rho$  = density of the fluid.



## PARTICLE COUNTER FOR SEDIMENT TRANSPORT STUDIES

By John P. Downing, Jr.<sup>1</sup>

### INTRODUCTION

The direct measurement of bed load transport in oceanic and riverine flows is a difficult problem because the movement of sediment particles, as bed load, is confined to a thin region at the water-sediment interface. In the case of sand-bedded transport systems, the layer of moving grains is usually less than 0.4 in. (1.0 cm) thick, and, therefore, conventional instrumentation is too large to measure the process without disturbing it. For this reason, existing acoustic bed load sensors are operated away from the bottom and respond to indirect phenomena associated with particle motion on the bed, such as self-generated noise (5,1,7). This paper reports the development of an acoustic instrument that measures bed load transport by responding to the direct impacts of sand-sized sediment particles entrained in the bed load layer. The instrument consists of an electromechanical transducer for the detection of particle impacts, and an electronic circuit that shapes the transient signals produced by impacts into digital pulses and counts them. The transducer is rugged, physically small, and preliminary field evaluations indicate that the instrument is potentially useful for measuring bed load transport rates in natural flows.

The idea of using an impact-sensitive transducer to measure particle flux in suspensions is not a new one. Sensors were developed for the studies of particle dispersion in pipe flows, and the movement of wind-blown sand on beach dunes, by Sharp and O'Neill (8), and Wilson, et al. (10), respectively. The basic operating principle of all impact sensors is inherently simple. A sediment particle entrained in a moving fluid of lesser density will strike a small elastic object, hereafter called the target, and cause it to vibrate. The impact event is detected by converting the mechanical vibration of the target to an analog electrical signal with a suitable transducer. An obvious advantage of this detection method is that silt and clay particles and biological debris, which are not of primary interest in many studies, have insufficient inertia to be detected; this is also the case for entrained gas bubbles. Soulsby's (9) analytical assessment

<sup>1</sup>Doctoral Candidate, Dept. of Oceanography, Univ. of Washington, Seattle, Wash. 98198.

Note.—Discussion open until April 1, 1982. To extend the closing date one month, a written request must be filed with the Manager of Technical and Professional Publications, ASCE. Manuscript was submitted for review for possible publication on December 10, 1980. This paper is part of the Journal of the Hydraulics Division, Proceedings of the American Society of Civil Engineers, ©ASCE, Vol. 107, No. HY11, November, 1981. ISSN 0044-796X/81/0011-1455/\$01.00.

of target design parameters showed that: (1) The maximum energy transfer from a particle to a target occurs when the mass of the target equals that of the particle; (2) the probability of a particle impacting the face of a disk-shaped target in its path increases as the target diameter decreases; and (3) multiple impacts of a single particle with the target become less likely with a decreased target diameter. Collectively, these effects dictate that the target must be made as small as is practical in order to optimize sensitivity to impacts, and to reduce the likelihood of multiple counts being generated by a single particle striking the target.

In this report, analytical errors and statements of precision are expressed as  $\pm$  one standard deviation and  $100\times$  (Standard Deviation:Average Value), respectively.

#### SENSOR DESCRIPTION

Fig. 1 shows a photograph of the transducer. The target is a stainless steel wire, 0.04 in. (1.0 mm) in diameter, by 2.0 in. (50 mm) long. The acoustic

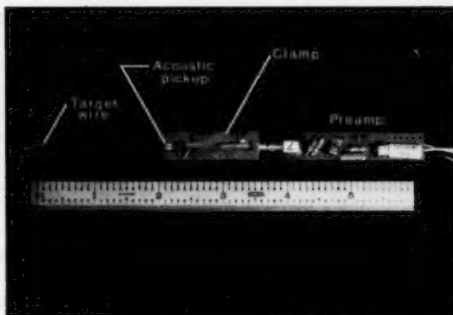


FIG. 1.—Transducer and Preamplifier

pickup consists of two pairs of piezo-ceramic (PZT) disks (Sonotite<sup>R</sup> 101 Lead Zirconate Titanate) 0.12 in. (3.0 mm) in diameter, by 0.02 in. (0.51 mm) thick connected in parallel (Fig. 2). Each pair of disks has a nominal resonant frequency in the thickness mode of 1.95 MHz providing adequate bandwidth to resolve the frequencies associated with grain impacts. The target and PZT disks are acoustically coupled by a 0.12 in. (3.0 mm) square steel block, silver-soldered to the target. PZT disk pairs are compressed against opposing faces of the coupling block by a small clamp, and the transducer and preamplifier are electrically connected with a miniature coaxial connector. The transducer and preamplifier are sealed in a water-tight housing (Fig. 3).

#### ELECTRONICS

The electronic circuit for counting transient impact signals includes: (1) A signal conditioner stage (amplification and filtering); (2) a pulse shaper which

generates a +12 v digital pulse for each detectable impact event; and (3) a 12-bit digital counter that sums the output pulse stream for a preset time interval.

Fig. 2 is a simplified schematic diagram of the circuit. The transducer output is amplified once by a field-effect transistor input preamplifier [gain of 16 (Fig.

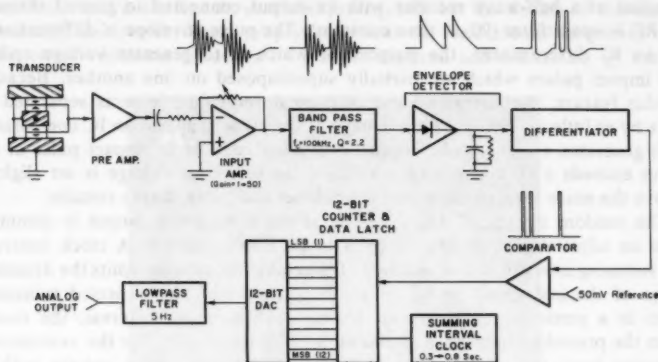


FIG. 2.—Simplified Schematic of Impact Pulse Counter Circuit

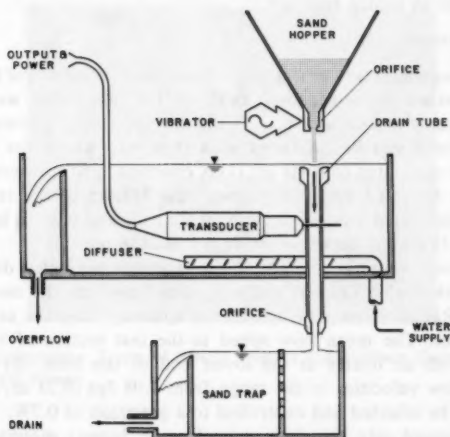


FIG. 3.—Instrument Calibration Apparatus

1)), and again by a variable gain (1-50) integrated circuit amplifier. Gain adjustments to the latter amplifier permit compensation for sensitivity variations among individual transducers. Noise in the transducer output produced by ambient flow turbulence, target strumming, and intergranular collisions is attenuated

with an active bandpass filter. The filter consists of two cascaded second-order multiple feedback sections with a center frequency of 100 kHz,  $Q$  of 2.2, and a gain of 15.

Wave forms of the impact pulses at various points in the circuit are shown in Fig. 2. The first stage of the shaper circuit is an envelope detector that consists of a half-wave rectifier with its output connected to ground through an RC lowpass filter (90  $\mu$ s time constant). The pulse envelope is differentiated by an IC differentiator, the purpose of which is to generate voltage spikes for impact pulses which are partially superimposed on one another. Because of this feature, the instrument can distinguish individual impacts separated in time by as little as 100  $\mu$ s. The last stage of the pulse shaper is an IC comparator that generates a digital pulse when the leading edge of an impact pulse at its input exceeds a 50 mv reference voltage; the reference voltage is set slightly above the noise level of the signal conditioner and pulse shaper circuits.

The random stream of digital pulses at the comparator output is summed over an adjustable time interval by a 12-bit ripple counter. A clock controls the summing interval, and adjustment of the clock frequency permits the dynamic range of the instrument to be set in accordance with the expected transport rates in a particular environment. During each summing interval, the count from the preceding interval is stored on a 12-bit data latch. For the evaluations reported here, the digital count was converted to an analog voltage with a 12-bit digital to analog converter and lowpass filtered ( $-3$  dB point at 5 Hz). This particular scheme proved convenient because the instrument output could be monitored on an analog recorder.

#### LABORATORY APPARATUS

Laboratory experiments to characterize the transient response of the transducer to sediment-particle impacts and to calibrate the instrument were conducted using the apparatus shown in Fig. 3. With this apparatus, known mass fluxes of sand and water can be produced in a tube into which the sensor target is inserted. The apparatus consists of: (1) A constant-head reservoir; (2) a Plexiglas drain tube mounted vertically through the bottom of the reservoir [tube I.D. and cross-sectional area are 0.50 in. (1.27 cm), and 0.20 sq in. (1.27 cm<sup>2</sup>), respectively]; (3) a sand dispenser; and (4) a sand trap.

During test runs, water is supplied to the reservoir through a diffuser, enters the drain tube through a circular spillway, and flows into the sand trap below the reservoir. Radial vanes attached to the spillway suppress secondary flow in the drain tube. The mean flow speed in the test section of the drain tube is controlled with an orifice at the lower end of the tube. By this method, steady mean flow velocities in the range from 1.08 fps (0.33 m/s) to 5.76 fps (1.76 m/s) can be selected and controlled to a precision of 0.7%.

Sand is dispensed into the drain tube from a hopper mounted above the spillway. The mass flux of sand is controlled with an orifice inserted into the bottom of the sand hopper, and a steady flow of sand is maintained with an electric vibrator. The mass flux of sand,  $\phi_s$ , can be preset in the range from  $0.44$ – $50.8 \times 10^{-3}$  lb/sec (0.20–23.1 g/s) and controlled to a precision of 1.1%. The drain plumbing on the sand trap is hinged and activates a microswitch when moved. This feature allows times samples of the test suspension to be obtained for the calibration of the apparatus.

## ACOUSTIC RESPONSE OF TRANSDUCER

Because it is a complex electromechanical system, the response of the transducer to particle impacts could not be determined analytically in a straightforward manner. A clear understanding of several acoustic properties of the transducer, however, was an essential prerequisite for the design of the signal processing electronics. These properties include the fundamental frequency and duration of vibrations produced by particle impacts, and the factor,  $Q$ , which

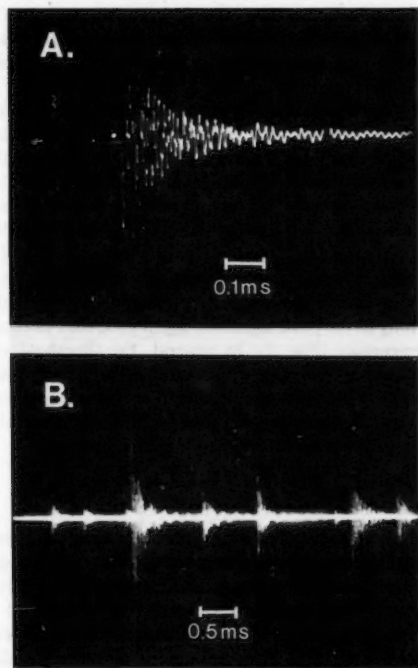


FIG. 4.—(a) Oscilloscope Trace of Single Impact Pulse Wave Form (b) Sequence of Several Impact Pulses

represents the quality of the transducer as a harmonic oscillator. To determine these properties, the transducer target was subjected in the test apparatus (Fig. 3) to flows with low concentrations of beach sand. A range of grain sizes  $5.9\text{--}19.7 \times 10^{-3}$  in. (0.15–0.50 mm), and flow velocities 1.84–2.95 fps (0.56–0.90 m/s) were investigated. It was assumed in the laboratory work that the grain velocity prior to impact with the target equaled the average flow velocity in the drain tube, plus the still water fall velocity of the test grains; but no attempt was made to account for velocity variations across the diameter of the tube.

Fig. 4(a) shows the signal wave form produced by a  $1.97 \times 10^{-2}$  in. (0.50 mm) diameter sand grain impacting the target with a velocity of 2.89 fps (0.88 m/s). Numerous other wave forms representing a range of grain sizes and velocities were photographed, and all of them displayed a similar shape and had the same fundamental frequency. Analysis of these photographs indicated that grain impacts excite damped free vibrations with a fundamental frequency of  $100 \pm 3$  kHz in the transducer and that it has a quality factor,  $Q$ , of approx 12. The approximation,  $Q = \pi/\delta$  (4) was used to estimate  $Q$  in which  $\delta$  is the logarithmic decrement of the pulse waveform envelope (obtained from photographs).  $Q$  is an important parameter because it sets an upper limit on the rate of grain impacts that can be discriminated by the transducer. In this sense, a low  $Q$  value is a desirable property because the vibrations produced by an individual impact will decay rapidly and be less likely to superimpose on those produced by succeeding impacts. Analysis of several impact pulse sequences (Fig. 4(b)) indicates that, for a particular grain size and velocity, the peak amplitudes of individual pulses are random and highly variable; the coefficient of variation of peak amplitude is typically 90%. The time interval between pulses is also random, as was expected; but the duration of pulses is relatively constant,  $350 \pm 170$   $\mu$ s, for the range of conditions investigated.

In natural sediment transport systems, grains moving as bed load will have a range of sizes and speeds (grain momentum), depending on the sorting of the bed material and flow conditions. A grain can be detected, regardless of its momentum, as long as the peak signal voltage it produces exceeds the reference voltage of the comparator (Fig. 2). In general, the threshold of detection for bed material is related to: (1) The noise level of the electronics; (2) the size of the material; and (3) the flow conditions. To evaluate potential uses of the instrument, the interaction of some of these factors was determined empirically by laboratory calibrations with natural sedimentary material.

#### LABORATORY CALIBRATION RESULTS

Laboratory calibrations were conducted with beach sand because the instrument was originally designed for littoral transport studies. The sand grains have a mean diameter and standard deviation of  $9.21 \times 10^{-3}$  in. (0.23 mm), and  $2.50 \times 10^{-3}$  in. (0.063 mm), respectively. Because it was anticipated that both mass flux,  $\phi_s$ , and grain velocity,  $U_g$ , would influence the instrument output,  $\Delta V$ , calibration runs were made with 26 combinations of these variables. Moreover, triplicate runs for each of these combinations were made to determine instrument precision. The relative errors for 19 of the 26 triplicate analyses were one % or less, and the remainder ranged from 1.6–7.5%. From these results, it is concluded that instrument precision is of the same order as the precision of the experimental apparatus.

The calibration data form a family of curves of constant particle mass flux,  $\phi_s$  in  $\text{g}/(\text{s} \cdot \text{cm}^2)$ , on a plot of  $U_g$ , versus time-averaged differential voltage,  $\Delta V$  (Fig. 5). In both laboratory and field experiments,  $\Delta V$  is the difference between the time-averaged instrument outputs with and without sand entrained in the test flow. It is also the analog of the count rate in pulses per unit time, whereby one volt represents an average rate of 820 counts per second.

It is clear from the trend of the curves that, with particle flux held constant,

the count rate increases with grain velocity. This result was expected since, as grain velocity increases, a larger proportion of the grains have momentum in excess of the threshold value necessary for detection. Since an accurate determination of grain velocity is difficult to make in the field, the greatest source of uncertainty in particle flux measurements results from this characteristic of the instrument. In order to quantify this uncertainty, computations of the relative errors in flux estimates were made with the calibration data for a range of  $\Delta V$  and  $U_R$  values. Computed relative errors produced by a  $\pm 10\%$  uncertainty in  $U_R$  are given in Table 1. The tabulated values represent the plus or minus deviation expressed as a percentage of the flux computed for each pair of tabulated  $\Delta V$  and  $U_R$  values. It can be seen that the uncertainty in flux measurements is considerable when  $U_R$  and  $\Delta V$  are less than 2.0 fps

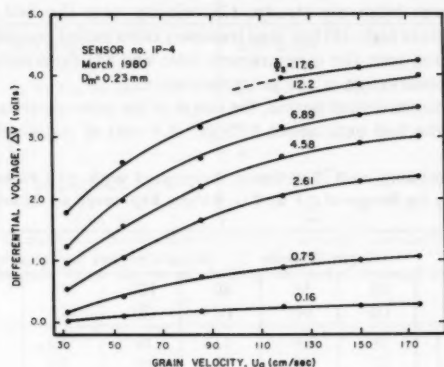


FIG. 5.—Laboratory Calibration Results

(0.60 m/s) and 0.5 v. For higher grain velocities and output voltages, the uncertainty in flux measurement is of the same order, or less than the uncertainty in  $U_R$ .

#### FIELD CALIBRATION

A precise field calibration of the instrument was impractical because no methods exist to determine grain velocity or to measure bed load transport independently with accuracy. Preliminary field experiments were conducted, however, to evaluate the response of the sensor to natural transport conditions on a sandy stream bed. For this work, a bed load trap was used to sample the sediment particles striking the target. This trap is a small version of the one described by Emmett (3), and has an entrance 22 mm wide by 19 mm high. Flow measurements were made with a ducted-impeller current meter (6), the sensor of which is 1.70 in. (4.32 cm) in diameter.

The experiments were conducted at Muddy Creek in western Wyoming on June 8, 1980. Dietrich, et al., (2) describe in detail the physical setting, flow

characteristics, and sediment transport regime at the site; the following brief description summarizes their discussion. Muddy Creek is a meandering tributary of the Upper Green River; it has a bankfull discharge, and a mean width and depth of 42.3 cfs ( $1.2 \text{ m}^3/\text{s}$ ), 18.0 ft (5.5 m), and 2.0 ft (0.6 m), respectively. The stream bed is composed largely of coarse to very coarse sand,  $D_{50}$  ranges from  $2.24\text{--}6.89 \times 10^{-2}$  in. (0.57–1.75 mm). This material is supplied to the channel by bank erosion of outwash terraces. At the time these experiments were carried out, a relatively high constant discharge was maintained by the irrigation runoff. For this reason, and because very little suspended sediment is carried by the stream, it is an excellent site for bed load transport studies.

Bed load and flow-speed measurements were made from a portable bridge over the gently sloping upstream face of a point bar. Compared with other locations in the channel, this site was best suited for such measurements because: (1) The flow was relatively steady; (2) velocity near the bed, and bed load transport rates were high; (3) bed load transport rates varied considerably because of dune migration past the measurement site; and (4) flow depth, 1.0 ft (0.30 m), permitted observation of the instrumentation.

During each measurement period, the target of the acoustic sensor was inserted vertically into the bed until about 0.75 in. (1.9 cm) of its length was exposed

TABLE 1.—Uncertainty in  $\Phi$ , Estimates, Associated with  $\pm 10$  Percent Uncertainty in Grain Velocity for Range of  $\Delta V$  and  $U_{*c}$  Values Expressed as  $\pm$  Percentage

$\Delta V$ , in volts (1)	Grain Velocity, $U_{*c}$ , (in centimeters per second)							
	35 (2)	40 (3)	60 (4)	80 (5)	100 (6)	120 (7)	140 (8)	160 (9)
0.1	38	28	16	12	10	9	8	7
0.5	37	27	15	12	10	9	8	7
1.0	12	12	12	12	11	9	9	8
2.0	11	11	12	11	12	11	11	8
3.0	— <sup>a</sup>	— <sup>a</sup>	11	11	12	11	11	11
4.0	— <sup>a</sup>	— <sup>a</sup>	— <sup>a</sup>	— <sup>a</sup>	— <sup>a</sup>	11	11	11

<sup>a</sup>Outside range of calibration.

to moving sand grains. At the same time, the bed load trap was placed on the bed about 2.0 in. (5 cm) downstream from the target to sample the particles striking it. For selected runs, a current meter was used to measure average flow velocity 2.0 in. (5.1 cm) above the bed. Operating the instrumentation in this manner, nine analog time series of the bed load sensor output, each 30 seconds long, were recorded with an oscillographic recorder. Bed load samples acquired concurrently were later weighed and sieved to determine the time-averaged bed load transport rates,  $\Phi_b$ , in g/s per cm width of bed, and the size distribution of bed load material.

## RESULTS AND ANALYSIS

Fig. 6 shows four sample time series of  $\Delta V$  that represent the range of bed load transport rates observed during the experiment. The time-averaged voltage



output,  $\Delta V$ , was computed for each record from samples taken at one second intervals; these values are indicated on the sample analog records by dashed horizontal lines. The start time, and  $\Phi_b$  value determined with the trap, are indicated above each record as well.

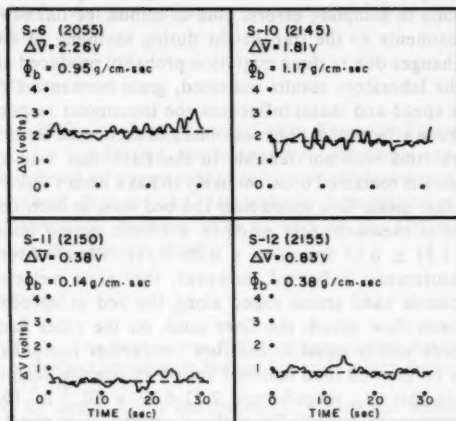


FIG. 6.—Four Sample Time Series of Analog Output Obtained in Muddy Creek, Wyoming

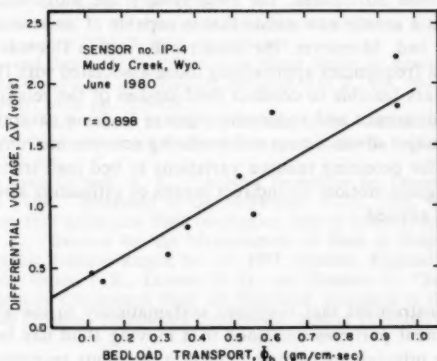


FIG. 7.—Scatter Plot of Measured Bed Load Transport,  $\Phi_b$ , Versus Time-Averaged Differential Voltage Output,  $\Delta V$

The  $\Delta V$  and  $\Phi_b$  data are presented on the scatter plot shown in Fig. 7. Although there is considerable scatter in the data, the results of the experiment indicate that the instrument responds systematically to variations in bed load

transport rate. The line on Fig. 7 is the least squares regression of  $\Delta V$  on  $\Phi_b$ ; and a correlation coefficient,  $r = 0.898$ , was computed for these data.

There are two sources of experimental error that contributed to the scatter of the data. First, there was considerable margin for operator error in the use of the bed load trap. Disturbance of the bed during the emplacement and retrieval of the trap results in sampling errors, plus or minus, of unknown magnitude. Moreover, adjustments to the trap height during sampling to compensate for bed elevation changes due to dune migration probably produced similar errors.

Second, as the laboratory results indicated, grain momentum (the combined effects of grain speed and mass) influences the instrument response to particle flux. Whereas these effects could be controlled and accounted for in the laboratory calibration work, this was not feasible in the field, nor was an assumption that grain momentum remained constant likely to have been valid. Flow measurements indicate that mean flow speed near the bed was, in fact, constant. Three 30-sec, streamwise measurements made in a 15-min period indicated a mean flow speed of  $1.51 \pm 0.03$  fps ( $0.46 \pm 0.01$  m/s). Visual observation of the streambed measurements indicated, however, that grain velocity was highly variable. The coarse sand grains rolled along the bed at speeds considerably less than the mean flow speed; the finer sand, on the other hand, moved by saltation at speeds nearly equal to the flow. A further complication was that the median size of the bed load material varied among the samples. The sieve analyses indicate that  $D_{50}$  ranged from  $2.22$ – $6.79 \times 10^{-2}$  in. ( $0.57$ – $1.74$  mm) during the measurement period. From these results, it is concluded that the effects of grain momentum on instrument performance remain untested in natural systems, but that better results from future experiments could be anticipated, if sites with well-sorted bed material are selected.

In spite of these difficulties, the field results are most encouraging; they demonstrate that a sensor now exists that is capable of measuring local particle flux and on the bed. Moreover, the sensor can resolve fluctuations in particle flux that occur at frequencies approaching those associated with flow turbulence; and it now appears feasible to conduct field studies of the relationship between boundary flow dynamics and sediment response in some natural systems. This is considered a major advancement since existing acoustic instrumentation (5,1,7) is only reliable for detecting relative variations in bed load transport rates and the initiation of grain motion; no indirect means of estimating absolute transport rates previously existed.

## CONCLUSIONS

An acoustic instrument that responds systematically to the absolute flux of sand-sized sediment particles entrained in a moving fluid has been developed. By virtue of the principle of particle detection, spurious response of the sensor to silt, clay, biological material, and air bubbles is negligible. The results of laboratory and limited field experiments indicate that the instrument has application to the problem of local bed load measurement in natural transport systems. Because of the difficulties resulting from the dependence of instrument output on grain momentum, the best results will be obtained in natural systems with: (1) Well-sorted bed material in the size range from  $9.75$ – $78.0 \times 10^{-3}$  in. ( $0.25$ – $2.0$  mm); (2) grain velocities exceeding  $2.0$  fps ( $0.60$  m/s); and (3) high transport

rates. Other applications for which the instrument would be well suited include laboratory studies of sediment transport in pipes and flumes, and investigations of wind-blown sand.

With minor modifications of the electronics, the output of the instrument could be transmitted in digital form. In this way, the count-rate values could be recorded directly, and more efficient processing of laboratory and field data would be possible.

#### ACKNOWLEDGMENTS

The author would like to thank Harvey Smith, Research Engineer, University of Washington, for conducting the laboratory calibration experiments. This research was supported by a grant to the University of Washington Oceanography Department National Oceanic and Atmospheric Administration University of Washington Contribution Number 1226 as part of the Office of Sea Grant Nearshore Sediment Transport Study.

#### APPENDIX.—REFERENCES

1. Anderson, M. G., "An Inexpensive Circuit Design for the Acoustic Detection of Oscillations in Bedload Transport in Natural Streams," *Earth Surface Processes*, Vol. 1, 1976, pp. 213-217.
2. Dietrich, W. E., Smith, J. D., and Dunne, T., "Flow and Sediment Transport in a Sand Bedded Meander," *Journal of Geology*, Vol. 87, 1979, pp. 305-315.
3. Emmett, W. W., "A Field Calibration of the Sediment-Trapping Characteristics of the Helley-Smith Bedload Sampler," United States Geological Survey Open File Report, 1979, no. 79-411.
4. Harris, C. M., and Crede, C. E., *Shock and Vibration Handbook*, 2nd ed., McGraw-Hill Book Co., Inc., New York, N.Y., 1976.
5. Johnson, P. and Muir, T. C., "Acoustic Detection of Sediment Movement," *Journal of Hydraulic Research*, Vol. 7, 1969, pp. 519-540.
6. Nece, R. E., and Smith, J. D., "Boundary Shear Stress in Rivers and Estuaries," *Journal of the Waterways and Harbors Division*, ASCE, Vol. 96, No. WW2, Proc. Paper 7280, May, 1970, pp. 335-358.
7. Richards, K. S., and Milne, L. M., "Problems in the Calibration of an Acoustic Device for the Observations of Bedload Transport," *Earth Surface Processes*, Vol. 4, 1979, pp. 335-346.
8. Sharp, B. B., and O'Neill, K. C., "A New Technique for Discrete Particle Study in Turbulent Flow," presented at the November 25-29, 1968, Third Australasian Conference on Hydraulics and Fluid Mechanics, held at Sydney, Australia.
9. Soulsby, R. L., "Sensors for the Measurement of Sand in Suspension," Institute of Oceanographic Sciences Report No. 27, 1977, Taunton, England.
10. Wilson, D. G., Guala, J. R., Palmer, H. D., and Blanton, J., "Sediment Transport Studies, Nearshore Continental Shelf off Maryland, presented at the May 3-6, 1976, Eighth Annual Offshore Technology Conference, held at Houston, Tex.



## BUOYANT SURFACE JETS

By Gerhard H. Jirka,<sup>1</sup> M. ASCE, E. Eric Adams,<sup>2</sup> A. M. ASCE,  
and Keith D. Stolzenbach,<sup>3</sup> M. ASCE

### INTRODUCTION

Buoyant surface jets are often encountered in environmental fluid mechanics. Their scales range from a few meters of horizontal extent for small inflows into treatment tanks, to several hundred kilometers for large rivers entering the ocean. A buoyant surface jet arises from a combined source of momentum and buoyancy injected at and parallel to the free surface of the receiving water body. Since the buoyant force acts normal to the surface, complicated distortions of the cross-sectional jet geometry take place. This fact, together with the buoyant damping of the jet turbulence, has prevented the development of relatively simple analytical solutions to the problem, as has been possible for several cases of the buoyant submerged jet. The presence of shallow receiving water near the discharge point and of ambient crosscurrents further complicates the physical situation.

A number of mathematical models for buoyant surface jet discharges have been developed during the past 10 yr. These, together with basic experimentation, have been aimed at an improved understanding of the mixing characteristics and environmental impacts of these discharges. State-of-the-art reviews of the mathematical and physical bases of these models have been prepared by Jirka, Abraham, and Harleman (16). Dunn, Policastro, and Paddock (10), Policastro and Dunn (29), and others. Briefly, most predictive models can be categorized into one-dimensional jet integral models and three-dimensional finite difference models.

The *jet integral models* consist of a set of ordinary differential equations derived from the cross-sectional (normal to the jet trajectory) integration of jet properties such as mass, momentum, and buoyancy fluxes. Empirical formulations for internal jet behavior such as buoyant damping of turbulence and cross-sectional distortion (lateral spreading) are included. The equation systems are parabolic and are solved by simple forward-marching numerical

<sup>1</sup>Asst. Prof., School of Civ. and Environmental Engrg., Cornell Univ., Ithaca, N.Y.

<sup>2</sup>Principal Research Engr. and Lect., Dept. of Civ. Engrg., Massachusetts Inst. of Tech., Cambridge, Mass.

<sup>3</sup>Assoc. Prof., Dept. of Civ. Engrg., Massachusetts Inst. of Tech., Cambridge, Mass.

Note.—Discussion open until April 1, 1982. To extend the closing date one month, a written request must be filed with the Manager of Technical and Professional Publications, ASCE. Manuscript was submitted for review for possible publication on July 24, 1980. This paper is part of the *Journal of the Hydraulics Division*, Proceedings of the American Society of Civil Engineers, ©ASCE, Vol. 107, No. HY11, November, 1981. ISSN 0044-796X/81/0011-1467/\$01.00.

schemes along the jet trajectory. Comparison with laboratory and field data (16) demonstrates that several of these jet integral models predict reasonably well the details of the induced velocity and density or pollutant fields, provided that certain phenomena are accounted for. These phenomena relate mainly to three factors: (1) The jet-like behavior ceases after a certain transition distance; (2) shallow receiving water causes bottom attachment; and (3) strong crosscurrents cause shoreline attachment downstream from the discharge.

*Three-dimensional numerical models* directly solve a finite difference (or finite element) approximation to the full Reynolds equations with various approximations for the turbulent shear and heat transport covariance terms. Several such models have been developed in recent years. So far, however, the successful comparison with laboratory or field data remains limited to some special conditions such as discharges into relatively enclosed regions or environments with strong ambient crossflows (e.g., rivers), in which the ambient turbulence level appears to dominate the mixing process (41).

Other situations, such as discharges into more quiescent receiving waters, have yet eluded a truly satisfactory simulation. Apparent reasons include (1) Lack of fully workable turbulence closure techniques under the influence of buoyancy while considering the full range of jet-induced to geophysical turbulence; (2) the difficult trade-off of modeling a large enough domain while providing sufficient resolution in a three-dimensional model (computer capacity and costs); and (3) the unknown nature of the open fluid boundary conditions which need to be specified as part of the elliptic equation system. These boundaries may contain a combination of stratified inflow and outflow, which appears to be inherently unsteady, as is discussed subsequently. For example, although recent numerical model studies by McGuirk and Rodi (24) and Raithby and Schneider (32) use detailed turbulence closure models including buoyancy production, for reasons of computational efficiency they still employ the boundary layer assumption, and lead to parabolic equation systems. Therefore, the quality of their predictions and the range of model applicability do not appear to be much improved over the simpler integral models.

In this paper, the fluid mechanical properties of buoyant surface jets entering various types of receiving waters are discussed. Then jet properties, such as mixing capacity (dilution) and geometric scale (vertical penetration, transition length, and trajectory), are defined using dimensional analysis and are then quantified through combined use of integral jet model predictions and field or laboratory observations.

This has two purposes. First, the relationships are useful as initial estimates to define discharge behavior, mixing efficiency, regions of influence, and parametric sensitivity of different discharge design alternatives. In some instances these simple measures should be sufficient for analysis and design; examples include the estimate of entrance mixing in cooling pond analysis (18) or the assessment of frontal dynamics in coastal plume analysis (5). Secondly, the results define limits of applicability of buoyant surface jet models, e.g., by establishing criteria on transition distance and on bottom and shoreline attachment, and thus can be used in the selection of appropriate predictive models.

#### STAGNANT DEEP RECEIVING WATER

**Physical Situation.**—The schematic structure of a three-dimensional buoyant

surface jet discharging into receiving water of sufficiently large horizontal and vertical extent (Fig. 1) can be synthesized from a number of laboratory observations (2,15,21,38,42,43), and some field data (13,23,26). This structure can be interpreted as an interplay of inertial and buoyant fluid forces. The relative action of these forces on a fluid element located at a distance,  $x$ , along the jet trajectory is measured by a local densimetric Froude number

$$F_r(x) = \frac{u}{(g'h)^{1/2}} \quad \dots \dots \dots (1)$$

in which  $u$  = characteristic horizontal velocity;  $h$  = characteristic depth;  $g' = (\rho_a - \rho)/\rho_a$  = reduced gravitational acceleration;  $\rho$  = characteristic density;  $\rho_a$  = ambient density; and  $g$  = gravitational acceleration. It can be assumed

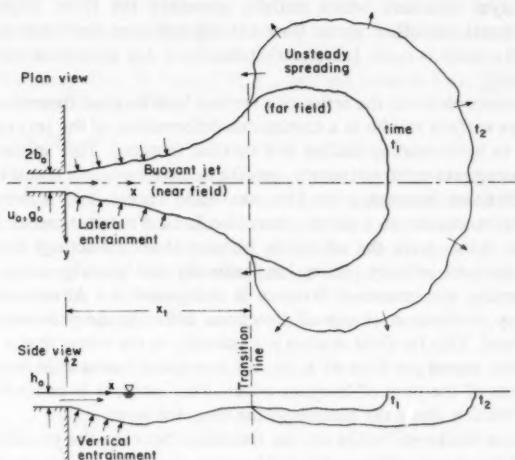


FIG. 1.—Structure of Buoyant Surface Jet in Stagnant Deep Receiving Water

that in an initial region (small  $x$ ) momentum will dominate over buoyancy, or  $F_r(x) \gg 1$ . Hence, density can be treated as a passive scalar, which, like jet momentum, is diffused in the cross section through turbulent exchange, giving rise to classical momentum jet patterns (3,34). The jet diffusion process is distinguished by two interrelated phenomena: (1) The linear growth of the jet, both laterally and vertically; and (2) the entrainment of ambient irrotational fluid into the turbulent region in a complicated, intermittent process, which, however, can be characterized by a small mean transverse velocity (entrainment velocity) (40). At larger distances from the source, buoyancy exerts an increasing influence on the jet behavior, as is seen by taking the axisymmetric jet solutions  $u \sim x^{-1}$ ,  $g' \sim x^{-1}$ , and  $h \sim x$  in Eq. 1, so that  $F_r \sim x^{-1}$ . Ultimately, buoyancy has a dramatic effect on the flow and is responsible for the gradual transition from jet-like flow, near the discharge, to a buoyant spreading regime at greater

distances, as shown in Fig. 1. Two heuristic interpretations are offered for this transition—one based on microscopic (turbulence) considerations and one based on macroscopic (mean flow) considerations.

On a microscopic scale, buoyancy affects the turbulent development of the jet. Near the discharge, jet growth is governed by the scale of the largest turbulent eddies which are in equilibrium with the mean shear flow from which they derive their energy, and with smaller eddies to which they transfer their energy (40). At greater longitudinal distances, however, gravitational stability damps vertical turbulent motion. The resulting two-dimensional structure hinders spectral energy transfer which relies on the mechanism of vortex stretching and on a three-dimensional eddy structure. As a result, the energy of the large horizontal eddies increases, contributing to jet meandering (particularly apparent for discharges into shallow water), and an ultimate outgrowth of the horizontal boundary layer structure which initially governed the flow. Experiments in two-dimensional stratified shear flow (11,30) indicate that vertical turbulent entrainment ceases as  $F_r \rightarrow 1$ , suggesting that  $F_r \approx 1$  is an approximate criterion for transition.

On a macroscopic level, the action of a vertical bulk buoyant force in conjunction with the free surface results in a continuous deformation of the jet cross-section, giving rise to horizontal spreading and vertical thinning. This spreading occurs at an increasing rate until, ultimately, jet-like behavior ceases. It can be reasoned that the transition between a jet-like, near-field region, and a density-driven, far-field region occurs at a point where the local Froude number is of order unity, since at this point the advective velocity (forward-acting) approximately equals the buoyant velocity (acting longitudinally and laterally-acting).

Subsequently, the transition distance is designated  $x_t$ . At distances beyond  $x_t$ , buoyancy results in motion in all directions, although the predominant motion is still forward. This far-field motion is unsteady, in the sense that a continuous supply of the mixed jet flow at  $x_t$  causes a gradual increase in length, width, and thickness of the pool of buoyant water. This increase is controlled through interfacial friction along the bottom of the buoyant layer.

As the layer thickness builds up, the transition between the jet-like, near-field region, and the density-driven, far-field region can become abrupt, in the form of a hydraulic jump. Furthermore, for extended times, the buoyant layer will also move inward toward the discharge point—accelerated by the near-field entrainment (2,12)—and ultimately the whole jet region may be immersed in its own mixed water. Of course, for sufficiently long periods of time, a steady-state based on a balance between heat loss to the atmosphere and heat addition through the discharge must result in both the near and far fields.

The following analysis is limited to the near-field aspects of the buoyant jet region, i.e., up to the point of transition. This implies that either a mechanism is present in the far-field which prevents a build-up, e.g., a weak ambient current, or the unsteady effects have little influence on the near-field behavior. Some support will be given for the latter assumption.

**Dimensional Analysis.**—The steady-state, near-field behavior of buoyant surface jets can be expressed in nondimensional form by choosing appropriate scales derived from the source conditions. This was first evident from the work of Stolzenbach et al. (37,38) who, through correlations of their integral model results, suggested expressions for the dilution and the maximum vertical jet penetration.



The concept of a "self-similarity of buoyant surface jets" was suggested by Jirka et al. (16), and additional jet properties were summarized. More recently, Baddour and Chu (4) have proposed another unified presentation of jet properties using a somewhat different normalization.

For discharge from a rectangular channel at high Reynolds number into infinite receiving water, under the Boussinesq assumption, the physical situation may be described solely by the source variables shown in Fig. 1, which include the discharge depth,  $h_o$ , the discharge half-width,  $b_o$ , the discharge velocity,  $u_o$ , and the discharge reduced gravity,  $g'_o$ . Hence if  $\Phi$  denotes a characteristic local property, e.g., longitudinal velocity, or an integral property, e.g., jet flow rate, then it may be a function of these variables and of distance,  $x$ , only, i.e.,

$$\Phi = f\{x, h_o, b_o, u_o, g'_o\} \quad (2)$$

Alternatively the flow may be characterized by an independent set of source flux variables including the kinematic momentum flux,  $M_o = u_o^2 b_o h_o$ , the kinematic buoyancy flux,  $B_o = u_o g'_o b_o h_o$ , and the volume flux,  $Q_o = u_o b_o h_o$ , plus the source depth,  $h_o$ . Thus

$$\Phi = f\{x, M_o, B_o, Q_o, h_o\} \quad (3)$$

It is noted (4) that the kinematic momentum force parameter  $u_o^2 b_o h_o + 0.5 g'_o h_o^2 b_o$  could be used in place of the kinematic momentum flux. Eq. 2 has historical precedence and the advantage that it preserves the physical dimensions of the source; however, Eq. 3 has the advantage that, under many conditions, one or more of the independent variables can be shown to be insignificant. In the following, Eq. 3 is used first and the results are then reinterpreted with respect to the more commonly recognized  $u_o$ ,  $b_o$ ,  $h_o$ , and  $g'_o$ .

Using  $M_o$  and  $B_o$  as repeating variables, Eq. 3 can be written

$$\Phi^* = \frac{\Phi}{M_o^\alpha B_o^\beta} = f^*(x M_o^{-3/4} B_o^{1/2}, M_o^{5/4} B_o^{-1/2} Q_o^{-1}, h_o^2 M_o Q_o^{-2}) \quad (4a)$$

in which  $\Phi^* = \Phi$  normalized by the appropriate combination of  $M_o$  and  $B_o$ ; exponents  $\alpha$  and  $\beta$  depend on the dimensions of  $\Phi$  and are given in Table 1. Expressed in terms of  $u_o$ ,  $g'_o$ ,  $h_o$ , and  $b_o$ , Eq. 4a becomes

$$\Phi^* = \frac{\Phi}{(u_o^2 b_o h_o)^\alpha (u_o g'_o h_o b_o)^\beta} = f^*\left[\frac{x g_o'^{1/2}}{u_o (h_o b_o)^{1/4}}, \frac{u_o}{g_o'^{1/2} (h_o b_o)^{1/4}}, \frac{h_o}{b_o}\right] \quad (4b)$$

Defining  $\ell_o = (h_o b_o)^{1/2}$ , and recognizing  $A = h_o/b_o$  as a discharge channel aspect ratio, and  $F_o' = u_o/(g_o' \ell_o)^{1/2} = F_o A^{1/4}$  as a densimetric Froude number with length scale,  $\ell_o$ , Eq. 4b may be rewritten

$$\Phi^* = \frac{\Phi}{\Phi_o F_o'^\gamma} = f^*\left(\frac{x}{\ell_o F_o'}, F_o', A\right) \quad (4c)$$

in which  $\Phi_o$  is a characteristic value of  $\Phi$  at the origin; the value of  $\gamma$  is a function of  $\alpha$  and  $\beta$  such that  $\Phi_o F_o'^\gamma = M_o^\alpha B_o^\beta$ . See Table 1.

Eqs. 4a, 4b, and 4c may often be simplified by noting that the second parameter

within brackets of each equation indicates sensitivity to be magnitude of the discharge flow  $Q_o$ , while the third parameter indicates sensitivity to the discharge channel shape or aspect ratio. Experience with other jet applications—e.g., submerged buoyant jets as analyzed by Wright (44) and submerged nonbuoyant jets with varying aspect ratio (45) as analyzed by Stolzenbach and Harleman (38)—suggest that, where high local dilutions are obtained, both of these influences diminish, resulting in

$$\Phi^* = f^* \left( \frac{x}{\ell_o F'_o} \right) \dots \dots \dots (5)$$

Furthermore, certain asymptotic jet properties such as stable dilution may be expected to be independent of  $x$ , in which case

$$\Phi^* = \text{constant} \dots \dots \dots (6)$$

The validity of these simplifications will be explored further in the following.

**Jet Properties.**—The dimensional analysis and physical reasoning presented above has suggested certain relationships between the dependent jet properties,

TABLE 1.—Normalization of Surface Jet Variables

Variable $\phi$ (1)	Dimension (2)	$\Phi_o$ (3)	$\alpha$ (4)	$\beta$ (5)	$\gamma$ (6)
$\ell$	length	$\ell_o = \sqrt{h_o b_o}$	3/4	-1/2	1
$u$	velocity	$u_o$	-1/4	1/2	-1
$Q$	volume flow rate	$u_o h_o b_o$	5/4	-1/2	1
$g'^a$	acceleration <sup>a</sup>	$g'_o$	-5/4	3/2	-1

<sup>a</sup>Jet variables which are proportional to  $g'$ —e.g., excess temperature or density deficit—scale similarly.

$\Phi$ , and the governing independent variables. In the following, these relationships are quantified (i.e., proportionality coefficients are estimated) through combined use of integral jet model predictions and laboratory and field data. The integral jet model which was used was developed by Stolzenbach and Harleman (38,39). This model was chosen because of the writers' familiarity with it; in many cases similar results could be obtained with other model formulations (16).

**Transition Distance  $x_t$ .**—Several criteria can be used to define the transition distance. In mathematical models, the distance where the centerline value of  $F_r \approx 1$ , or the position where strong lateral spreading occurs,  $db/dx \gg 1$ , in which  $b$  = jet half-width, can be used as indicators. It is noteworthy that in many integral models a singularity in the matrix of differential equations is reached at  $F_r \approx 1$ , indicating a mathematical transition between a region of jet-like flow and a region of buoyant spreading. In the Stolzenbach-Harleman model this singularity occurs at  $F'_o = 1.6$ , which is reached at a distance  $x_t$  given approximately by

$$\frac{x_t}{\ell_o F'_o} \approx 12 A^{-0.2} \dots \dots \dots (7a)$$

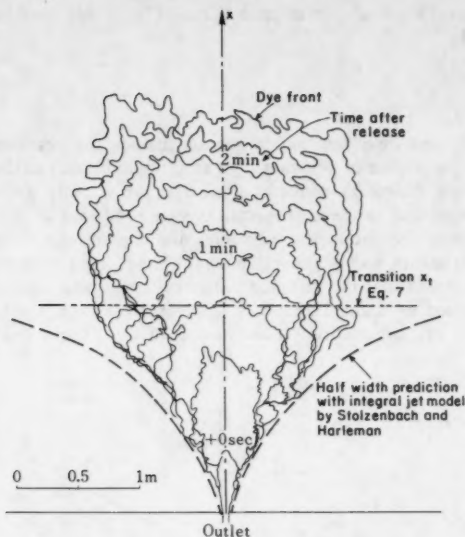


FIG. 2.—Unsteady Dye Fronts within Steady Buoyant Surface Jet Showing Nonlinear Spread and Transition. Experiments by Hayashi and Shuto (15) and Mathematical Model Predictions (38) for Jet Half-Width

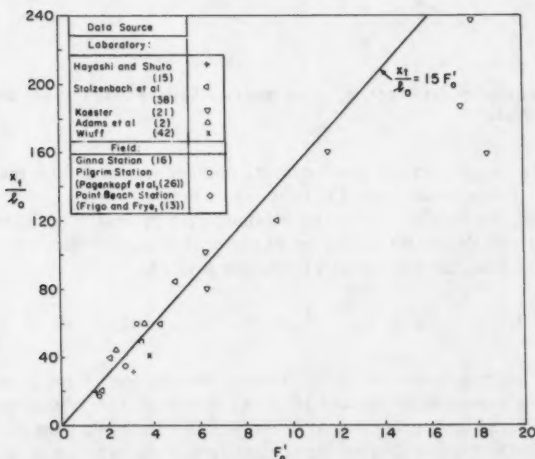


FIG. 3.—Transition Distance,  $x_t$ , for Buoyant Surface Jets in Deep and Shallow Receiving Water

For moderate values of aspect ratio  $0.1 \leq A \leq 2$  this may be approximated reasonably by

$$\frac{x_i}{\ell_o F_o'} \approx 15 \quad (7b)$$

Laboratory and field data indicators can include the occurrence of a stable dilution, i.e., a plateau of constant  $g'$  with little additional mixing, or excessive local spreading based on concentration, dye, or velocity patterns. Available data were examined in these respects, as suggested in Fig. 2, and are plotted in Fig. 3. Generally, the measured values are in good agreement with Eq. 7b. In their experiments with negatively buoyant jets along a solid bottom, Baddour and Chu (4) found that the distance to the collapse zone, somewhat analogous to the transition as defined above, was given by  $x_i/\ell_o F_o' \approx 5$  in the present notation. The proportionality is consistent with Eq. 7b; the lower value of the

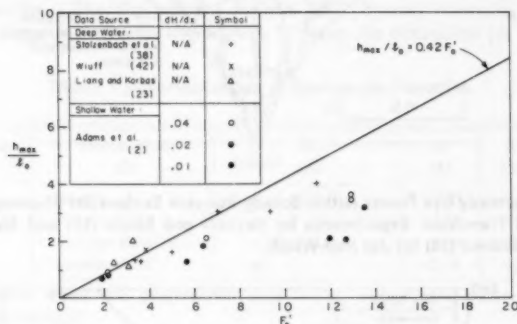


FIG. 4.—Maximum Jet Depth,  $h_{max}$ , for Buoyant Surface Jets in Deep and Shallow Receiving Water

coefficient may reflect the low Reynolds number jet conditions and the solid boundary effects which existed in their experiment.

**Maximum Jet Depth,  $h_{max}$ .**—The maximum jet penetration, defined by the depth at which excess jet excess buoyancy or temperature becomes negligible, is estimated from the Stolzenbach-Harleman model as

$$\frac{h_{max}}{\ell_o F_o'} \approx 0.42 \quad (8)$$

Few detailed measurements of the vertical distribution of jet properties are reported in experimental studies to date. However, the laboratory data by Stolzenbach and Harleman (38) and Wuiff (42), plus field data from the Millstone Nuclear Power Station (23), all show good agreement with Eq. 8, as indicated in Fig. 4. It should be mentioned that, in some of these references, the jet depth is measured in terms of the location where the excess temperature is one half of the center-line value; in these cases Stolzenbach and Harleman's

profile assumption is used to compute the maximum depth as 1.59 times the maximum half-depth. The location of the region of maximum penetration is given by the Stolzenbach-Harleman model as approximately

$$\frac{x_{\max}}{g'_o F'_o} \approx 5.5 \quad (9)$$

**Stable Center-Line Concentration,  $g'_{cs}$ .**—Since the mixing process beyond the transition distance,  $x_t$ , is rather inefficient, the excess temperature, and in particular its center-line value, reaches a stable plateau. This value is given by the model as

$$\frac{g'_{cs} F'_o}{g'_o} = \left(1 + \frac{1}{F_o'^2}\right)^{-1/2} \quad (10a)$$

For  $F_o' \geq 3$ , the approximation

$$\frac{g'_{cs} F'_o}{g'_o} \approx 1 \quad (10b)$$

is reasonable. The inverse of  $g'_{cs}/g'_o$  may be termed a stable center-line dilution,  $S_{cs}$ , which, for  $F_o' \geq 3$ , is thus

$$S_{cs} \approx 1.0 F_o' \quad (11)$$

Center-line dilution data for deep water conditions are summarized in Fig. 5, based on the same data sources, and employing the same symbols as used

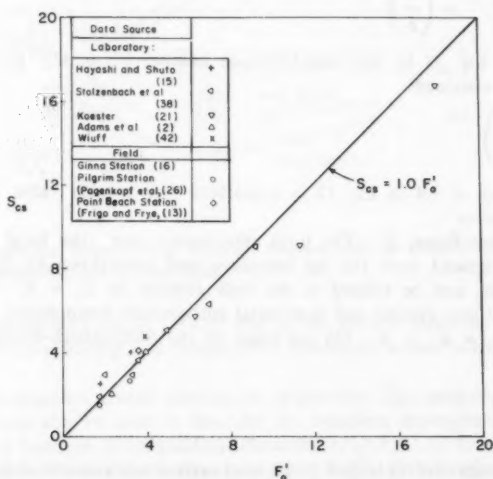


FIG. 5.—Maximum Stable Dilution,  $S_{cs}$ , for Buoyant Surface Jets in Deep Receiving Water

in Fig. 3. Excellent agreement with Eq. 11 is found. A distinct temperature plateau is observed in all reported cases, both laboratory and field, if the ambient conditions are reasonably stagnant. It is noted that the data of Baddour and Chu (4) indicate the same proportionality but lower dilution than Eq. 11. Their constant of proportionality is about 0.35, which is probably due to the aforementioned reasons.

**Stable Bulk Dilution,  $S_s$ .**—A bulk dilution or mixing ratio is defined as the ratio of local discharge to initial discharge,  $S = Q/Q_o$ . As with  $g'_{cs}$ ,  $S$  will attain as asymptotic stable value,  $S_s$ . This asymptotic value is an important characteristic of surface buoyant jets as it describes their total mixing capacity, i.e., the total amount of ambient flow entrained into the entire jet bulk. The computed quotient of bulk to center-line dilution is a constant which depends on the transverse velocity and temperature profiles. For the profiles used in the Stolzenbach-Harleman model, and for  $F'_o \geq 3$ , the constant is approximately 1.4 so that, from Eq. 11,

$$S_s \approx 1.4 F'_o \quad (12)$$

While Eq. 12 was derived from a mathematical model, it is interesting that  $S_s$  can be estimated reasonably well from simple physical arguments without considering the details of the entrainment process. The transition condition is characterized by a local Froude number of the order of unity. Taking the bulk flow at the transition as  $Q_s$  and assuming that the momentum and buoyancy fluxes are approximately equal to their initial values  $M_o$  and  $B_o$ , the result is

$$\frac{Q_s B_o^{1/2}}{M_o^{5/4}} \approx F'^{-1} = \left(\frac{h}{b}\right)^{-1/4} \quad (13)$$

Multiplying Eq. 13 by the initial Froude number  $F'_o = M_o^{5/4} Q_o^{-1} B_o^{-1/2}$ , the following is obtained:

$$S_s \approx F'_o \left(\frac{h}{b}\right)^{-1/4} \quad (14)$$

The constant of 1.4 in Eq. 12 is consistent with a local value of  $b/h = 4$  at the transition.

**Entrainment Rates,  $E$ .**—The total entrainment rate, (the local entrainment velocity integrated over the jet boundary and normalized by  $Q_o$ ), may be designated  $E_s$  and be related to the bulk dilution by  $E_s = S_s - 1$ .  $E_s$  can be separated into vertical and horizontal entrainment components,  $E_v$  and  $E_h$ , in which  $E_s = E_v + E_h$ . On the basis of the Stolzenbach-Harleman model for  $F'_o > 1$ ,

$$E_v \approx 1.2(F'_o - 1) \quad (15a)$$

$$E_h \approx 0.2(F'_o + 1) \quad (15b)$$

Eq. 15 indicates that for large  $F'_o$ , the total vertical entrainment at the jet bottom contributes much more to mixing than the total horizontal entrainment at the jet periphery. In the limit  $F'_o \rightarrow \infty$ ,  $E_v/E_h \approx 6$ . This suggests that, for moderate and large  $F'_o$ , far-field lateral recirculation should have a relatively minor effect

on jet mixing capacity, and that experiments which exhibit such recirculation should still agree relatively well with the steady-state predictive models as far as global dilution and center-line properties are concerned.

Conversely, far-field recirculation effects are expected to become significant for discharges with low  $F'_0$  or for discharges into shallow water, where bottom entrainment is inhibited. Not surprisingly, it is mainly in these later situations that dilutions predicted with integral jet analyses have not compared well with measurements (10). Eq. 15a has been proposed by Jirka et al. (17,19) for the analysis of entrance mixing in cooling impoundments in which the far-field

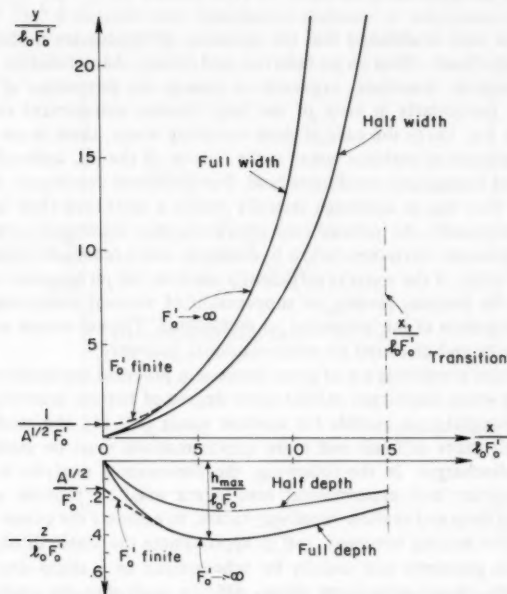


FIG. 6.—Self-similar Geometry of Buoyant Surface Jets in Deep Receiving Water Computed by Mathematical Model (38)

effects (recirculation) are so severe, due to the limited receiving water area, that the effective mixing and temperature reduction occurs solely at the jet bottom.

Eqs. 7-15 describe several distinct jet properties. The mathematical model can, of course, also be used to describe the complete dependence of any jet variable as a function of longitudinal distance,  $x/(L_0 F'_0)$ . As an example, the complete nondimensional jet geometry is given in Fig. 6, indicating both width and depth relationships. A unique self-similar presentation results for the point source condition  $F'_0 \rightarrow \infty$ . For finite source dimensions, the source geometry is usually felt for small distances,  $x/(L_0 F'_0)$ , and the aspect ratio,  $A$ , must

be included, giving an initial width,  $b_o/(\ell_o F_o') = A^{-1/2} F_o'^{-1}$ , and depth,  $h_o/(\ell_o F_o') = A^{1/2} F_o'^{-1}$ . For very small values,  $F_o' \sim 1$ , this nondimensional source size can become significant. For  $A > 1$ , this effect is particularly severe with respect to the jet depth. However, the hydrostatic pressure assumption made in the development of integral jet models becomes invalid in this extreme range. From an analysis of different data sets (16), it appears that probable limits of applicability for the jet property equations, Eqs. 7-15, are a sufficiently high Froude number  $F_o' \geq 3$  and a moderate aspect ratio  $A \leq 2$ .

#### EFFECTS OF SHALLOW RECEIVING WATER

It has been well established that the presence of boundaries in the receiving fluid has a significant effect on jet behavior and mixing characteristics. A shallow receiving water is, therefore, expected to change the properties of a surface buoyant jet, particularly in view of the large bottom entrainment contribution suggested by Eq. 15. In the case of deep receiving water, there is no restriction on the entrainment of ambient water at the bottom of the jet, induced velocities are small, and hydrostatic conditions hold. For shallower conditions, the bottom entrainment flow has to approach laterally within a restricted fluid layer under the jet. Consequently, the induced velocities are higher, leading to more frictional dissipation, pressure deviations below hydrostatic, and a reduced vertical entrainment flow. Finally, if the water is sufficiently shallow, the jet becomes completely attached to the bottom, leading to suppression of vertical entrainment and to frictional dissipation of the integrated jet momentum. The net results are reduced mixing capacity and distorted jet cross-sectional geometry.

Shallow water conditions are of great concern in practical applications. Indeed, most cooling water discharges exhibit some degree of bottom interaction. While there exist integral-type models for shallow water (1,9,14), the modeling task is significantly more difficult and more approximations must be made than for deep water discharges. In the following, the dimensional analysis is extended to shallow water, and experimental results are used to provide a criterion distinguishing deep and shallow receiving waters, to estimate the extent of bottom attachment (for sloping bottoms), and to approximate the stable dilution.

The bottom geometry can usually be schematized as a sharp drop-off to a constant depth,  $H$ , or as a linear slope,  $dH/dx$ , such that the ambient depth  $= H(x) = h_o + (dH/dx)x$ . In either case, an additional geometric parameter,  $H$  or  $dH/dx$ , enters the basic formulation of Eqs. 2 or 3, and Eq. 4c could therefore be replaced by either

$$\Phi^* = \frac{\Phi}{\Phi_o F_o'^\gamma} = f^* \left( \frac{x}{\ell_o F_o'}, \frac{dH}{dx}, F_o', A \right) \quad (16a)$$

$$\text{or } \Phi^* = \frac{\Phi}{\Phi_o F_o'^\gamma} = f^* \left( \frac{x}{\ell_o F_o'}, \frac{H}{\ell_o F_o'}, F_o', A \right) \quad (16b)$$

In principle, an additional parameter describing bottom resistance should be included in Eq. 16, but there is insufficient data to quantify the dependence. Again, under certain conditions, one or more of the independent parameters may be shown to be insignificant.



It is of interest to know if the jet will interact with the bottom and, if so, over what distance. For jets over a sloping bottom, bottom attachment begins at the source and the jet remains attached until such time as lateral buoyant forces succeed in contracting or uplifting the bottom of the jet. The experiments by Adams (2) are used in Fig. 4 to plot the maximum jet depth,  $h_{\max}$ , occurring at the point of detachment, versus  $\ell_o F'_o$ , as suggested by Eq. 16a. These results indicate that, unlike deep water cases in which  $h_{\max}/(\ell_o F'_o) \approx \text{constant}$ , bottom friction causes  $h_{\max}/(\ell_o F'_o)$  to decrease with increasing  $F'_o$ . Similar conclusions can be drawn from the data of Safaie (33). Bottom friction also results in smaller values of  $h_{\max}/(\ell_o F'_o)$  for smaller  $dH/dx$ . And, as is the case for deep water, the data of Fig. 4 suggest that detachment distance is independent of aspect ratio for moderate and high  $F'_o$ .

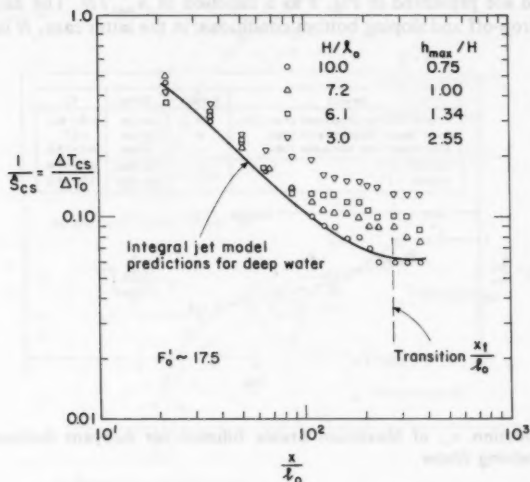


FIG. 7.—Effect of Shallowness,  $h_{\max}/H$ , on the Mixing Characteristics of Buoyant Surface Jets. Data from Koester (21)

For shallow water situations characterized by a step drop-off, it is physically appealing to contrast the ambient depth,  $H$ , with the maximum depth which would be predicted to occur in deep water. The parameter,  $H/(\ell_o F'_o)$ , in Eq. 16b may thus be replaced with  $h_{\max}/H$ . The parameter  $h_{\max}/H(x_{\max})$ , in which  $H$  = the water depth at the distance of maximum penetration,  $x_{\max}$  computed from Eq. 9, could also be used in place of  $dH/dx$  to characterize the depth of a sloping bottom.

Systematic experimental studies of the effects of shallow water on heated surface jets have been performed by Koester (21) and Adams et al. (2) for situations with a step drop-off and constant ambient depth,  $H$ . As an example, Fig. 7 shows Koester's results for normalized center-line temperature reduction for four experiments with constant  $F'_o$  ( $\approx 17.5$ ) but variable depth,  $H/\ell_o$ , ranging

from 3.0 to 10.0. In this case, the shallowness fact,  $h_{\max}/H$ , varied from 0.75 to 2.55. Fig. 7 shows a systematic pattern: For small  $h_{\max}/H$ , good agreement with the deep water model (38) is obtained; for larger  $h_{\max}/H$ , the induced temperatures are increased and the ultimate mixing, as measured by the observed plateaus of  $\hat{S}_{cs} = \Delta T_o / \Delta T_{cs}$ , is decreased.  $\Delta T_o$  = discharge temperature rise and  $\Delta T_{cs}$  = observed stable temperature rise. The ratio of the observed value  $S_{cs}$  to the predicted deep water value  $S_{cs}$ , given by Eq. 11, is defined as a shallow water dilution reduction factor.

$$r_s = \frac{\hat{S}_{cs}}{S_{cs}} \dots \dots \dots (17)$$

Data from Fig. 7 and from several other sources have been analyzed in this manner and are presented in Fig. 8 as a function of  $h_{\max}/H$ . The data include both step drop-off and sloping bottom conditions; in the latter case,  $H$  is replaced

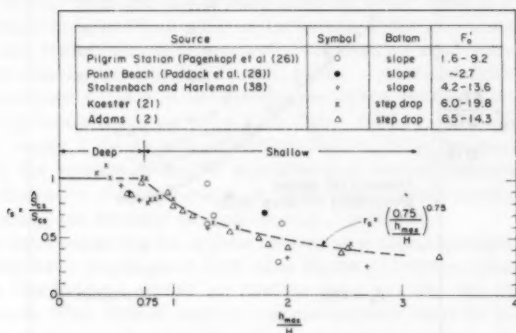


FIG. 8.—Reduction,  $r_s$ , of Maximum Stable Dilution for Buoyant Surface Jets in Shallow Receiving Water

by  $H(x_{\max})$ . Fig. 8 indicates a significant reduction in dilution for large  $h_{\max}/H$ . A breakpoint seems to occur at a value of  $h_{\max}/H \approx 0.75$ . Observed dilutions for  $h_{\max}/H < 0.75$  agree well with the deep water prediction  $S_{cs}$ , as can also be seen from Fig. 7. Thus, a simple criterion for shallow water conditions is proposed as

$$\frac{h_{\max}}{H} > 0.75 \dots \dots \dots (18)$$

Furthermore, the dilution reduction under shallow water conditions can be estimated from the visual best-fit line

$$r_s = \left( \frac{0.75}{\frac{h_{\max}}{H}} \right)^{0.75} \quad \text{for} \quad \frac{h_{\max}}{H} > 0.75 \dots \dots \dots (19)$$

Eq. 19 has been used by Jirka et al. (16) to adjust the model predictions of deep water models to yield satisfactory agreement with field and laboratory data.

#### EFFECTS OF CROSS-FLOWING RECEIVING WATER

Ambient currents influence both the near-field geometry and mixing of buoyant surface jets, and the advective and diffusive processes in the far field. However, the following analysis will concentrate only on the near-field aspects.

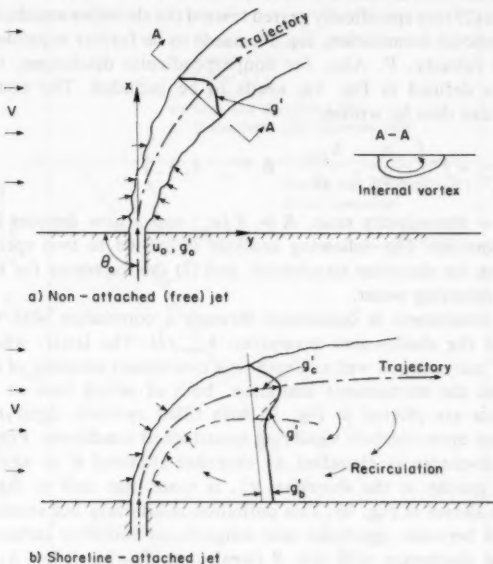


FIG. 9.—Behavior of Buoyant Surface Jets in Crossflow: (a) Nonattached Condition; (b) Shoreline Attachment

The depth of the receiving water is again an important factor. If deep water conditions prevail, then the crossflow causes a bent-over jet trajectory [Fig. 9(a)] by virtue of two force mechanisms: (1) An entrainment force due to transfer of ambient fluid momentum into the jet proper; and (2) a drag force due to shear and unequal pressure distributions on the jet boundary. Close to the discharge, mixing is similar to that for stagnant receiving water, but at greater distances, mixing increases as additional shear-induced entrainment and ambient diffusion come into play. Characteristically, buoyant surface jets in a crossflow do not have a transition zone with a stable limiting dilution.

In shallow receiving water, where the entering buoyant jet occupies a portion or all of the available water depth, the crossflow has even stronger effects. The ambient flow is blocked leading to higher stagnation pressures and a stronger

bending than in the deep case. At the same time, the entrainment on the downstream side of the jet is inhibited leading to further pressure changes. Eventually, the jet becomes partially attached to the shoreline and recirculation results with a build-up of excess temperature and reduced dilutions. Many practical discharge situations, particularly those into rivers, are shoreline-attached. A criterion for shoreline attachment is developed in the following, and its application should guide the selection of proper models for more detailed analysis. Several integral jet models (31,35,38) which include some crossflow force formulation, are strictly applicable only for nonattached conditions where they have shown good agreement with available data (16). On the other hand, ambient diffusion-based models (27) are specifically geared toward the shoreline attached conditions.

The dimensional formulation, Eq. 16, needs to be further expanded to include the ambient velocity,  $V$ . Also, for nonperpendicular discharges, the injection angle,  $\theta_o$ , as defined in Fig. 9a, needs to be included. The nondimensional formulation can thus be written

$$\Phi^* = \frac{\Phi}{\Phi_o F_o'} = f^* \left( \frac{x}{x_o F_o'}, \frac{h_{\max}}{H}, R, F_o', A, \theta_o \right) \quad (20)$$

in which  $R$  = the velocity ratio,  $R = V/u_o$ ; and  $x$  now denotes the distance from the shoreline. The following analysis is limited to two special aspects: (1) A criterion for shoreline attachment; and (2) the trajectory for nonattaching jets in deep receiving water.

Shoreline attachment is considered through a correlation with the velocity ratio,  $R$ , and the shallowness parameter,  $h_{\max}/H$ . The latter, which includes the effect of buoyancy as well as depth, is a convenient measure of the blocking condition and the entrainment limitation, both of which lead to attachment. Available data are plotted in Fig. 10 with filled symbols signifying attached conditions and open symbols signifying nonattached conditions. For the present purpose, a discharge is classified as shoreline-attached if at any section,  $x$ , the reduced gravity at the shoreline,  $g'_b$ , is more than half of the center-line value,  $g'_c$ , as shown in Fig. 9b. This definition is arbitrary but seems acceptable to distinguish between significant and insignificant shoreline influence. Fig. 10 indicates that discharges with low  $R$  (weak crossflow) and low  $h_{\max}/H$  (deep water) generally do not attach. In particular, jets into very deep water,  $h_{\max}/H < 0.1$ , do not seem to attach under any circumstance. This is corroborated by Keffer and Baines' wind tunnel data (20) which show nonattaching jets even for  $R \rightarrow 1$ . A visual best-fit line is shown in Fig. 10, giving

$$R > 0.05 \left( \frac{h_{\max}}{H} \right)^{-3/2} \quad (21)$$

as a criterion for shoreline attachment of surface buoyant jets with perpendicular,  $\theta_o = 90^\circ$ , discharge.

The trajectory of a deep water jet, discharging perpendicular to a crossflow, is expected to depend on  $M_o$ ,  $V$ , and  $B_o$ . Thus

$$\frac{y}{\frac{M_o^{1/2}}{V}} = f \left( \frac{x}{\frac{M_o^{1/2}}{V}}, \frac{B_o^{1/2}}{M_o^{1/4} V} \right) \quad (22a)$$

$$\text{or } \frac{yR}{\ell_o} = f\left(\frac{xR}{\ell_o}, (RF'_o)^{-1}\right) \dots \dots \dots (22b)$$

In exploring the functional form of  $f$  in Eq. 22, the limiting condition of  $B_o = 0$  is considered first. In analogy with nonbuoyant jets, two phases of the trajectory can be expected.

In the initial, weakly bent phase of the trajectory, the jet will behave like a pure momentum jet which is laterally advected by the crossflow. In the later, strongly bent phase it will behave like a line impulse which is gradually propagating

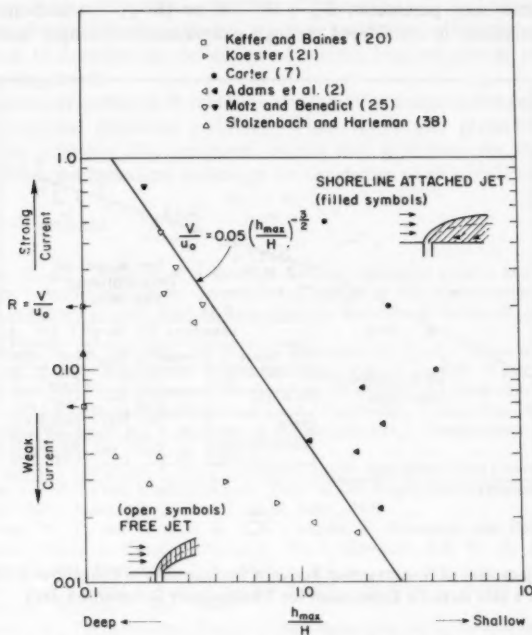


FIG. 10.—Shoreline Attachment for Buoyant Surface Jets as Function of Velocity Ratio,  $R$ , Shallowness,  $h_{\max}/H$

perpendicular to the crossflow. Similar analogies have been used in submerged jet analysis (6,36,44) giving in inverse form

$$\frac{xR}{\ell_o} = c_1 \left( \frac{yR}{\ell_o} \right)^{1/2} \quad (\text{initial phase}) \dots \dots \dots (23a)$$

$$\frac{xR}{\ell_o} = c_2 \left( \frac{yR}{\ell_o} \right)^{1/3} \quad (\text{final phase}) \dots \dots \dots (23b)$$

in which  $c_1$  and  $c_2$  = parameters to be determined from experiments and which, in the present case, should show some dependence on the initial buoyancy flux.

Buoyant surface jet trajectory data from several laboratory sources are summarized in Fig. 11 along with Wright's (44) best-fit expression,  $c_1 = c_2 = 2.0$ , for nonbuoyant, submerged jets. The data in Fig. 11 show some deviation from the nonbuoyant jet expression. Undoubtedly, some of the scatter is due to experimental effects (opposite wall effects in flumes, nonuniform ambient velocity, etc.), although the data sources have been carefully scrutinized to eliminate these errors. However, there appears also to be some systematic effect due to the buoyancy parameter,  $B_o^{1/2}/M_o^{1/4} V$ , or  $(Re'_o)^{-1}$ , which appears in Eq. 22. This effect is considered through examination of length scales. The

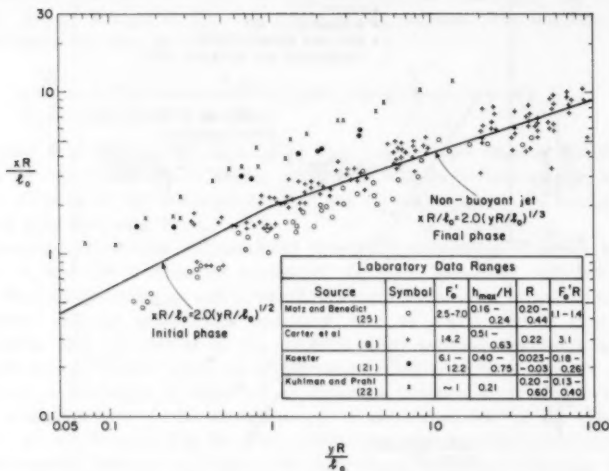


FIG. 11.—Trajectories of Nonattached Buoyant Surface Jets in Crossflow in Comparison to Wright's (44) Best-Fit Expression for Nonbuoyant Submerged Jets

length of buoyant influence is, of course, the transition length,  $x_t \sim L_o F_o'$ , as given by Eq. 7. The length for crossflow influence is  $x_c \sim L_o/R$ . The ratio  $x_t/x_c \sim F_o'R$  therefore provides an indication of the effect of buoyancy on the trajectory. If  $F_o'R \gg 1$ , then buoyancy should play a minor role as the crossflow deflection occurs more quickly than the buoyant influences. For  $F_o'R \leq 1$ , buoyancy should play a significant role. In particular, strongly buoyant surface jets,  $F_o'R \ll 1$ , are expected to penetrate more deeply into the receiving water than nonbuoyant jets, since both crossflow forces, entrainment and drag force, decrease. The data shown in Fig. 11 generally support the above argument.

## CONCLUSIONS

A combination of dimensional analysis, simple physical arguments, and data

inspection has been used to define distinct geometric properties and mixing characteristics within the near field of buoyant surface jets. For *deep stagnant* receiving water, the buoyant jet has a certain transition length which is used, in fact, to define the near field zone, a maximum penetration depth, and a limited dilution capacity which is predominantly met through bottom entrainment. These parameters are found to scale with a densimetric Froude number,  $F_\rho$ , based on kinematic momentum and buoyancy fluxes and characteristic source length. A definition for *shallow* receiving water conditions, Eq. 18, is given on the basis of observation of reduced entrainment. Increasing shallowness decreases the jet mixing capacity and increases the length of bottom contact. A criterion is presented to distinguish free and shoreline-attached buoyant surface jets in *crossflowing* receiving water. A simple trajectory relation, shown in Fig. 11, appears to describe the deflection of surface buoyant jets in *crossflowing deep* receiving water.

The relations given herein should be useful for initial design and impact estimates for environmental discharge problems. Whenever further predictive detail is needed, the relations also represent criteria and guidelines for the selection of appropriate mathematical models or for the design of physical models.

#### APPENDIX.—REFERENCES

1. Adams, E. E., "Analysis of a Buoyant Surface Discharge over a Shallow Sloping Bottom," *Proceedings of the Seventeenth Congress of the International Association for Hydraulics Research*, held at Baden-Baden, Republic of Germany, Vol. 1, Aug., 1977, pp. 363-370.
2. Adams, E. E., Stolzenbach, K. D., and Harleman, D. R. F., "Near and Far Field Analysis of Buoyant Surface Discharges into Large Bodies of Water," *Technical Report No. 205*, R. M. Parsons Lab. for Water Resources and Hydrodynamics, Dept. of Civ. Engrg., Massachusetts Inst. of Tech., Cambridge, Mass., Aug., 1975.
3. Albertson, M. L., et al., "Diffusion of Submerged Jets," *Transactions, ASCE*, Vol. 115, Paper No. 2409, 1950, pp. 639-697.
4. Baddour, R. E., and Chu, V. H., "Turbulent Gravity-Stratified Shear Flows," *Technical Report No. 78-3*, Fluid Mechanics Lab., Dept. of Civ. Engrg. and Applied Mathematics, McGill Univ., Montreal, Quebec, Canada, Sept., 1978.
5. Bowman, M. J., and Iverson, R. L., "Chapter 10: Estuarine and Plume Fronts," *Oceanic Fronts in Coastal Processes*, M. J. Bowman and W. E. Esaias, eds., Springer-Verlag, New York, N.Y., 1978.
6. Briggs, G. A., *Plume Rise*, U.S. Atomic Energy Commission Critical Review Series, Report No. TID-25075, Nov., 1969.
7. Carter, H. H., "A Preliminary Report on the Characteristics of a Heated Jet Discharging Horizontally into a Transverse Current-Part I, Constant Depth," *Technical Report No. 61*, Chesapeake Bay Inst., Johns Hopkins Univ., Baltimore, Md., Nov., 1969.
8. Carter, H. H., Schiemer, E. W., and Regier, R., "The Buoyant Surface Jet Discharging Normal to an Ambient Flow of Various Depths," *Technical Report No. 81*, Chesapeake Bay Inst., Johns Hopkins Univ., Baltimore, Md., Feb., 1973.
9. Dinelli, G., Colombo, A., and Sala, R., "Prévision de la Dispersion des Effluents Thermique dans la Méditerranée au Moyen d'un Modèle à Jet," *XIV<sup>e</sup> Journées de L'Hydraulique, Société Hydrotechnique de France*, Paris, France, 1976.
10. Dunn, W. E., Policastro, A. J., and Paddock, R. A., "Surface Thermal Plumes: Evaluation of Mathematical Models for the Near and Complete Field," *Report No. ANL/WR-75-3*, Argonne National Lab., Argonne, Ill., Aug., 1975.
11. Ellison, T. H., and Turner, J. S., "Turbulent Entrainment in Stratified Flows," *Journal of Fluid Mechanics*, Vol. 6, Part 3, 1959, pp. 423-448.
12. Engelund, F., "Hydraulics of Surface Buoyant Jet," *Journal of the Hydraulics Division, ASCE*, Vol. 102, No. HY9, Proc. Paper 12409, Sept., 1976, pp. 1315-1325.

13. Frigo, A., and Frye, D., "Physical Measurements of Thermal Discharges into Lake Michigan: 1971," *Report No. ANL/ES-16*, Argonne National Lab., Argonne, Ill., Oct., 1972.
14. Hansen, N. E. O., "The Surface Jet in Shallow Water," Progress Report 28, Inst. of Hydrodynamics and Hydraulic Engrg., Technical Univ. of Denmark, Apr., 1973, pp. 9-18.
15. Hayashi, T., and Shuto, N., "Diffusion of Warm Water Jets Discharged Horizontally at Water Surface," *Proceedings of the Twelfth Congress of the International Association for Hydraulic Research*, held at Fort Collins, Colorado, Vol. 4, Sept., 1967, pp. 47-59.
16. Jirka, G. H., Abraham, G., and Harleman, D. R. F., "An Assessment of Techniques for Hydrothermal Prediction," *Technical Report No. 203*, R. M. Parsons Lab. for Water Resources and Hydrodynamics, Dept. of Civ. Engrg., Massachusetts Inst. of Tech., Cambridge, Mass., July, 1975.
17. Jirka, G. H., and Harleman, D. R. F., "Cooling Impoundments: Classification and Analysis," *Journal of the Energy Division, ASCE*, Vol. 105, No. EY2, Proc. Paper 14779, Aug., 1979, pp. 291-309.
18. Jirka, G. H., and Watanabe, M., "Thermal Structure of Cooling Ponds," *Journal of the Hydraulics Division, ASCE*, Vol. 106, No. HY5, Proc. Paper 15412, May, 1980, pp. 701-715.
19. Jirka, G. H., et al., "Mathematical Predictive Models for Cooling Ponds and Lakes. Part A: Model Development and Design Considerations," *Technical Report No. 238*, R. M. Parsons Lab. for Water Resources and Hydrodynamics, Div. of Civ. Engrg., Massachusetts Inst. of Tech., Cambridge, Mass., Dec., 1978.
20. Keffer, J. F., and Baines, W. D., "The Round Turbulent Jet in a Crosswind," *Journal of Fluid Mechanics*, Vol. 15, Part 4, 1963, pp. 481-496.
21. Koester, G. E., "Experimental Study of Submerged Single-Port Thermal Discharges," thesis presented to the Massachusetts Inst. of Tech., at Cambridge, Mass., in 1974, in partial fulfillment of the requirements for the degree of Master of Science in Civ. Engrg.
22. Kuhlmann, J. H., and Pahl, J. M., "Laboratory Modeling of Surface Thermal Plumes," *Technical Report*, Division of Fluid, Thermal and Aerospace Sciences, Case Western Reserve Univ., Cleveland, Ohio, Aug., 1974.
23. Liang, H. C., and Korbas, G., "Operational Units 1 and 2 and Preoperational Unit 3 Hydrothermal and Infrared Imagery Surveys—July 1977, Millstone Nuclear Power Station," NERM-47, Stone and Webster Engrg. Corp., Boston, Mass., Sept., 1978.
24. McGuirk, J. J., and Rodi, W., "Mathematical Modeling of Three-Dimensional Heated Surface Jets," *Journal of Fluid Mechanics*, Vol. 95, Part 4, 1979, pp. 609-633.
25. Motz, L., and Benedict, B., "Heated Surface Jet Discharged into a Flowing Ambient Stream," *Report No. 4*, Dept. of Environmental and Water Resources Engrg., Vanderbilt Univ., Nashville, Tenn., Aug., 1970.
26. Pagenkopf, J. R., et al., "Oceanographic Studies at Pilgrim Nuclear Power Station to Determine Characteristics of Condenser Water Discharge (Correlation of Field Observations with Theory)," *Technical Report No. 183*, R. M. Parsons Lab. for Water Resources and Hydrodynamics, Dept. of Civ. Engrg., Massachusetts Inst. of Tech., Cambridge, Mass., Jan., 1974.
27. Paily, P. P., and Sayre, W. W., "Model for Shore-Attached Thermal Plumes in Rivers," *Journal of the Hydraulics Division, ASCE*, Vol. 104, No. HY5, Proc. Paper 13762, May, 1978, pp. 709-723.
28. Paddock, R. et al., "Temperature and Velocity Measurements and Predictive Model Comparisons in the Near-Far Region of Surface Thermal Discharges," *Report No. ANL/ES-25*, Argonne National Lab., Argonne, Ill., Oct., 1973.
29. Policastro, A. J., and Dunn, W. E., "Numerical Modeling of Surface Thermal Plumes," *Proceedings of International Advanced Course on Heat Disposal from Power Generation*, Dubrovnik, Yugoslavia, Aug., 1976.
30. Price, J. F., "On the Scaling of Stress-Driven Entrainment Experiments," *Journal of Fluid Mechanics*, Vol. 90, Part 3, 1979, pp. 509-529.
31. Prych, E. A., "A Warm Water Effluent Analysed as a Buoyant Surface Jet," *Serie Hydrologi. No. 21*, Sveriges Meteorologiska och Hydrologiska Institute, Stockholm, Sweden, 1972.
32. Raithby, G. D., and Schneider, G. E., "The Prediction of Surface Discharge Jets



- by a Three-Dimensional Finite-Difference Model," *Journal of Heat Transfer*, ASME, Vol. 102, Feb., 1980, pp. 138-145.
33. Safaie, B., "Mixing of Buoyant Surface Jet over Sloping Bottom," *Journal of the Waterway, Port, Coastal and Ocean Engineering Division*, ASCE, Vol. 105, No. WW4, Proc. Paper 14954, Nov., 1979, pp. 357-373.
  34. Schlichting, H., *Boundary Layer Theory*, McGraw-Hill Book Co., New York, N.Y., 1968.
  35. Shirazi, M. A., and Davis, L. R., "Workbook of Thermal Plume Predictions—Vol. 2, Surface Discharges," *Report No. EPA-R2-72-0056*, U.S. Environmental Protection Agency, Corvallis, Oreg., May, 1974.
  36. Slawson, P. R., and Csanady, G. T., "On the Mean Path of Buoyant, Bent-Over Chimney Plumes," *Journal of Fluid Mechanics*, Vol. 28, Part 2, 1967, pp. 311-322.
  37. Stolzenbach, K. D., Adams, E. E., and Harleman, D. R. F., "A User's Manual for Three-Dimensional Heated Surface Discharge Computations," *Technical Report No. 156*, R. M. Parsons Lab. for Water Resources and Hydrodynamics, Division of Civ. Engrg., Massachusetts Inst. of Tech., Cambridge, Mass., Sept., 1972.
  38. Stolzenbach, K. D., and Harleman, D. R. F., "An Analytical and Experimental Investigation of Surface Discharges of Heated Water," *Technical Report No. 135*, R. M. Parsons Lab. for Water Resources and Hydrodynamics, Division of Civ. Engrg., Massachusetts Inst. of Tech., Cambridge, Mass., Feb., 1971.
  39. Stolzenbach, K. D., and Harleman, D. R. F., "Three-Dimensional Heated Surface Jets," *Water Resources Research*, Vol. 9, No. 1, Feb., 1973, pp. 129-137.
  40. Townsend, A. A., *The Structure of Turbulent Shear Flow*, Cambridge University Press, New York, N.Y., 1976.
  41. Waldrop, W. R., and Farmer, R. C., "Thermal Effluent-River Interactions," *Proceedings of the Sixteenth Congress of the International Association for Hydraulic Research*, held in S. Paulo, Brazil, Vol. 3, July-Aug., 1975, pp. 221-229.
  42. Wiuff, R., "Experiments on Surface Buoyant Jet," *Journal of the Hydraulics Division*, ASCE, Vol. 104, No. HY5, Proc. Paper 13739, May, 1978, pp. 667-679.
  43. Wohlanski, E. J., and Banner, M. L., "Buoyant Surface Jet in Tidal Longshore Current," *Journal of the Hydraulics Division*, ASCE, Vol. 104, No. HY11, Proc. Paper 14186, Nov., 1978, pp. 1505-1519.
  44. Wright, S. J., "Mean Behavior of Buoyant Jets in a Crossflow," *Journal of the Hydraulics Division*, ASCE, Vol. 103, No. HY5, Proc. Paper 12944, May, 1977, pp. 499-513.
  45. Yevdjovich, V. M., "Diffusion of Slot Jets with Finite Length-Width Ratios," *Hydraulics Papers No. 2*, Colorado State Univ., Ft. Collins, Colo., 1966.



## HYDRAULIC EXPONENTS

By Ven Te Chow,<sup>1</sup> F. ASCE

### INTRODUCTION

For the computation of open-channel flows, the *hydraulic exponents* are the parameters  $M$  and  $N$  defined in the following equations by Chow (2,3,4):

$$Z^2 = Cy^M \quad \dots \dots \dots (1)$$

$$K^2 = Cy^N \quad \dots \dots \dots (2)$$

in which  $Z$  = the section factor for critical-flow computation, which is the product of the water area of the channel flow cross section and the square root of the hydraulic depth of the flow section;  $K$  = the conveyance of the channel flow cross section, being a measure of the carrying capacity of the section;  $y$  = the flow depth; and  $C$  = a coefficient which is different in nature between its value in Eq. 1 and Eq. 2.

For a flow cross section of water area  $A$ , top width  $T$ , and hydraulic depth  $D (= A/T)$ , the section factor for critical-flow computation is

$$Z = A\sqrt{D} = A\sqrt{\frac{A}{T}} \quad \dots \dots \dots (3)$$

The discharge  $Q$  of uniform flow in a channel is expressed by the product of the mean flow velocity,  $V$ , and the water area,  $A$ , or

$$Q = VA \quad \dots \dots \dots (4)$$

Most practical uniform-flow formulas, such as Manning's and Chézy's, can be expressed in the following general form:

$$V = CR^x S^y \quad \dots \dots \dots (5)$$

in which  $V$  = the mean flow velocity;  $R$  = the hydraulic radius;  $S$  = the energy slope, or channel slope, for uniform flow;  $x$  and  $y$  = exponents; and  $C$  = a factor of flow resistance, varying with the mean velocity, hydraulic radius, channel roughness, viscosity, and many other factors.

<sup>1</sup>Prof. of Civ. and Hydrosystems Engrg., Univ. of Illinois at Urbana-Champaign, Urbana, Ill. 61801.

Note.—Discussion open until April 1, 1982. To extend the closing date one month, a written request must be filed with the Manager of Technical and Professional Publications, ASCE. Manuscript was submitted for review for possible publication on December 10, 1980. This paper is part of the Journal of the Hydraulics Division, Proceedings of the American Society of Civil Engineers, ©ASCE, Vol. 107, No. HY11, November, 1981. ISSN 0044-796X/81/0011-1489/\$01.00.

Substituting Eq. 5 for  $V$  into Eq. 4

$$Q = CAR^x S^y = KS^y \quad (6)$$

in which the conveyance is expressed by

$$K = CAR^x \quad (7)$$

When the Chézy formula is used,  $x = 1/2$ ;  $C$  = Chézy's resistance factor; and Eq. 7 becomes

$$K = CAR^{1/2} \quad (8)$$

When the Manning formula is used,  $x = 2/3$ ;  $C = 1.49/n$  in which  $n$  = Manning's roughness coefficient; and Eq. 7 becomes

$$K = \frac{1.49}{n} AR^{2/3} \quad (9)$$

in which  $AR^{2/3}$  = the section factor for uniform-flow computation. In the following analysis, the Manning formula will be used.

Since  $M$  is a parameter which is useful in the computation of critical flow in open channels, it is called the hydraulic exponent for critical-flow computation. As  $N$  is mainly involved in the computation of uniform flow in open channels, it is called the hydraulic exponent for uniform-flow computation.

The significance of hydraulic exponents is in their application to the computation of flow profiles of a gradually varied flow in prismatic open channels. Their use will greatly simplify the otherwise complicated computation.

#### DERIVATION OF $M$

It should be noted that the relationships between  $Z$  and  $y$  and between  $K$  and  $y$ , as given by Eqs. 1 and 2, are empirical because these relationships for most channel flow cross sections, except infinitely wide rectangular sections and triangular sections, do not follow exactly the exponential forms of the equations throughout the full range of flow depth.

For most flow cross sections, the value of  $\ln Z$  plotted against  $\ln y$  will produce a curve  $P_1P_2$  as shown in Fig. 1. The curvature of this curve is somewhat exaggerated in the figure for the sake of demonstrating the idea of an approximation in applying the hydraulic exponent to the flow-profile computation. As an approximation, the curve  $P_1P_2$  may be replaced by a straight line  $P'_1P'_2$  for the range of flow depth to vary between  $y_1$  and  $y_2$  in the channel. The slope of  $P'_1P'_2$  is then assumed to be equal to that of the tangent to point  $P$  at an average depth,  $y$ , between  $y_1$  and  $y_2$ .

Taking logarithms on both sides of Eq. 1 gives

$$2 \ln Z = \ln C + M \ln y \quad (10)$$

This equation shows that if  $M$  is constant with reference to the approximated line  $P'_1P'_2$ , then Eq. 10 will plot as a straight line in Fig. 1 and this straight line may be represented by  $P'_1P'_2$ . Obviously, the slope of this line is

$$\frac{d(\ln Z)}{d(\ln y)} = \frac{M}{2} = \tan \alpha \quad (11)$$

in which  $\alpha$  = the slope angle of the line. Thus

$$M = 2 \frac{d(\ln Z)}{d(\ln y)} = 2 \tan \alpha \quad \dots \dots \dots (12)$$

In the meantime, taking logarithms on both sides of Eq. 3, and then differentiating the resulting equation with respect to  $\ln y$  give

$$\frac{d(\ln Z)}{d(\ln y)} = \frac{3y}{2} \frac{T}{A} - \frac{y}{2T} \frac{dT}{dy} \quad \dots \dots \dots (13)$$

Substituting Eq. 13 into Eq. 12 gives

$$M = \frac{y}{A} \left( 3T - \frac{A}{T} \frac{dT}{dy} \right) \quad \dots \dots \dots (14)$$

This is a general equation for the hydraulic exponent  $M$ , which is a function of the channel geometry and the flow depth. For a trapezoidal section,  $A = (b + zy)y$  and  $T = b + 2zy$ , in which  $b$  = the bottom width and  $z$  = the

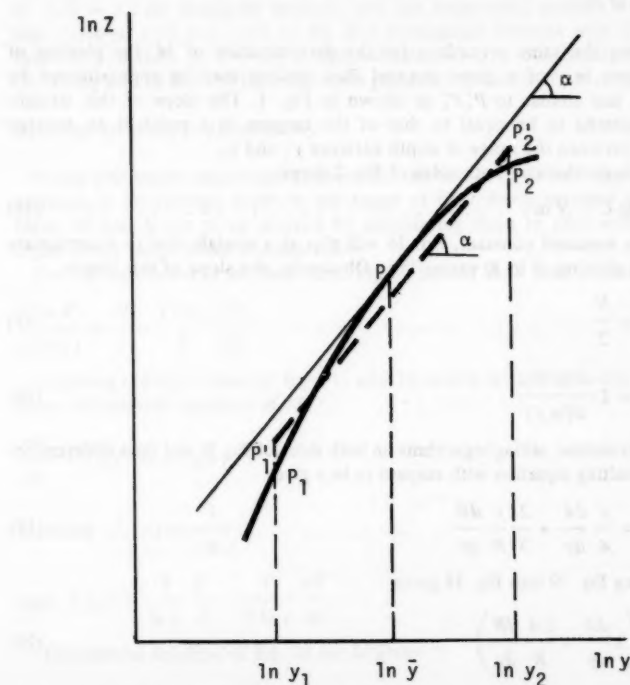


FIG. 1.—Plotting of  $\ln Z$  versus  $\ln y$

side slope (horizontal to 1 in vertical) of the section. Substituting these relations into Eq. 13, and simplifying

$$M = \frac{3 \left[ 1 + 2z \left( \frac{y}{b} \right) \right]^2 - 2z \left( \frac{y}{b} \right) \left[ 1 + z \left( \frac{y}{b} \right) \right]}{\left[ 1 + 2z \left( \frac{y}{b} \right) \right] \left[ 1 + z \left( \frac{y}{b} \right) \right]} \dots \dots \dots (15)$$

This equation indicates that the value of  $M$  for a trapezoidal section is a function of  $z$  and  $y/b$ . Thus, for a family of geometrically similar flow cross sections, the value of  $M$  remains the same. It can be seen in Eq. 15 that  $M$  approaches 3.0 for very low values of  $y/b$  (i.e.,  $y/b \rightarrow 0$ ), and 5.0 for very high values of  $y/b$  (i.e.,  $y/b \rightarrow \infty$ ). Further,  $M$  varies from a minimum of 3.0 for a rectangular section to a maximum of 5.0 for a triangular section. Similar equations for  $M$  may also be developed for some other geometrical flow cross sections.

#### DERIVATION OF $N$

Following the same procedure for the determination of  $M$ , the plotting of  $\ln N$  against  $\ln y$  of a given channel flow section may be approximated by a straight line similar to  $P'_1P'_2$  as shown in Fig. 1. The slope of this straight line is assumed to be equal to that of the tangent to a point at an average depth,  $y$ , between the range of depth between  $y_1$  and  $y_2$ .

Taking logarithms on both sides of Eq. 2 gives

$$2 \ln K = \ln C + N \ln y \dots \dots \dots (16)$$

Since  $N$  is assumed constant, Eq. 16 will plot as a straight line to approximate the actual plotting of  $\ln K$  versus  $\ln y$ . Obviously, the slope of this line is

$$\frac{d(\ln K)}{d(\ln y)} = \frac{N}{2} \dots \dots \dots (17)$$

$$\text{Thus } N = 2 \frac{d(\ln K)}{d(\ln y)} \dots \dots \dots (18)$$

In the meantime, taking logarithms on both sides of Eq. 9, and then differentiating the resulting equation with respect to  $\ln y$  give

$$\frac{d(\ln K)}{d(\ln y)} = \frac{y}{A} \frac{dA}{dy} + \frac{2}{3} \frac{y}{R} \frac{dR}{dy} \dots \dots \dots (19)$$

Substituting Eq. 19 into Eq. 18 gives

$$N = \frac{2y}{3A} \left( 3 \frac{dA}{dy} + \frac{2A}{R} \frac{dR}{dy} \right) \dots \dots \dots (20)$$

Since  $dA/dy = T$ ; and  $R = A/P$  in which  $P$  = the wetted perimeter; Eq. 20 becomes

$$N = \frac{2y}{3A} \left( 5T - 2R \frac{dP}{dy} \right) \dots \dots \dots (21)$$

which is a general equation for determining  $N$ .

For a trapezoidal channel section having a bottom width,  $b$ , and side slopes 1 on  $z$ ,  $A = (B + zy)y$ ;  $T = b + 2zy$ ;  $P = b + 2y\sqrt{1+z^2}$ ; and  $R = (b + zy)y/(b + 2y\sqrt{1+z^2})$ . Substituting these relations in Eq. 21 and simplifying,

$$N = \frac{10}{3} \frac{1 + 2z \left( \frac{y}{b} \right)}{1 + z \left( \frac{y}{b} \right)} - \frac{8}{3} \frac{\sqrt{1+z^2} \left( \frac{y}{b} \right)}{1 + 2\sqrt{1+z^2} \left( \frac{y}{b} \right)} \dots \dots \dots (22)$$

This equation indicates that  $N$  is a function of  $z$  and  $y/b$ , but it is not a function of  $y$  alone. This means that for geometrically similar flow cross sections,  $N$  will be the same. Eq. 22 shows that the value of  $N$  approaches a minimum of 2.0 for very narrow rectangular sections (i.e.,  $y/b \rightarrow \infty$ ), and a maximum of  $16/3 = 5.3$  for triangular sections, and for trapezoidal sections with a very high value of  $y/b$  (i.e.,  $y/b \rightarrow \infty$ ). For rectangular sections with a very low value of  $y/b$  (i.e.,  $y/b \rightarrow 0$ ),  $N$  approximates  $10/3 = 3.3$ . Similar equations for  $N$  may also be derived for some other geometrical channel flow cross sections.

#### DERIVATION OF $M$ AND $N$ VARYING WITH $y$

In the previously mentioned derivations, the values of  $M$  and  $N$  are assumed constant at an average depth in the range of flow depth between  $y_1$  and  $y_2$ . Here,  $M$  and  $N$  are to be derived by considering them to vary with the flow depth in the range under consideration.

For the derivation of  $M$ , therefore, Eq. 11 should have been written as

$$\frac{d(\ln Z)}{d(\ln y)} = \frac{M}{2} + \frac{y \ln y}{2} \frac{dM}{dy} \dots \dots \dots (23)$$

Equating the right sides of Eqs. 13 and 23 results in the following first-order linear differential equation of  $M$ :

$$\frac{dM}{dy} + f_1(y)M = f_2(y) \dots \dots \dots (24)$$

$$\text{in which } f_1(y) = \frac{1}{y \ln y} \dots \dots \dots (25)$$

$$\text{and } f_2(y) = \frac{3}{\ln y} \frac{T}{A} - \frac{1}{T \ln y} \frac{dT}{dy} \dots \dots \dots (26)$$

The general solution of Eq. 24 for  $M$  gives

$$M = e^{-\int f_1(y) dy} [\int f_2(y) e^{\int f_1(y) dy} dy + c] \dots \dots \dots (27)$$

in which  $c$  = an integration constant.

Substituting Eq. 25 for  $f_1(y)$  into Eq. 27 gives

$$M = \frac{1}{\ln y} [\int \ln y f_2(y) dy + c] \quad (28)$$

However, Eq. 28 cannot be solved directly except numerically, or for triangular and rectangular flow cross sections.

For a triangular flow cross section, Eq. 26 gives

$$f_2(y) = \frac{5}{y \ln y} \quad (29)$$

Substituting Eq. 29 for  $f_2(y)$  into Eq. 28, and noting that  $M = 5$  for triangular sections, and thus  $c = 0$ , Eq. 28 gives  $M = 5$ .

For a rectangular flow cross section, Eq. 26 gives

$$f_2(y) = \frac{3}{y \ln y} \quad (30)$$

Substituting Eq. 30 for  $f_2(y)$  into Eq. 28, and noting that  $M = 3$  for rectangular sections, and thus  $c = 0$ , Eq. 28 gives  $M = 3$ .

For the derivation of  $N$  varying with depth, Eq. 17 should have been written as

$$\frac{d(\ln K)}{d(\ln y)} = \frac{N}{2} + \frac{y \ln y}{2} \frac{dN}{dy} \quad (31)$$

Equating the right sides of Eqs. 19 and 31 results in the following first-order linear differential equation of  $N$ :

$$\frac{dN}{dy} + f'_1(y) N = f'_2(y) \quad (32)$$

$$\text{in which } f'_1(y) = \frac{1}{y \ln y} \quad (33)$$

$$\text{and } f'_2(y) = \frac{2}{A \ln y} \frac{dA}{dy} + \frac{4}{3 R \ln y} \frac{dR}{dy} = \frac{2}{3 A \ln y} \left( 5T - 2R \frac{dP}{dy} \right) \quad (34)$$

since  $dA/dy = T$  and  $R = A/P$ , in which  $P$  = the wetted perimeter. The general solution of Eq. 32 is

$$N = e^{-\int f'_1(y) dy} [\int f'_2(y) e^{\int f'_1(y) dy} dy + c] \quad (35)$$

in which  $c$  = an integration constant.

Substituting Eq. 33 for  $f'_1(y)$  into Eq. 35 gives

$$N = \frac{1}{\ln y} [\int \ln y f'_2(y) dy + c] \quad (36)$$

in which  $c$  = an integration constant. For most flow cross sections, Eq. 36 cannot be solved by direct integration but by numerical integration. However, triangular and rectangular cross sections are exceptions. For a triangular flow



cross section, Eq. 34 gives

$$f'_2(y) = \frac{16}{3y \ln y} \dots \dots \dots (37)$$

Substituting Eq. 37 for  $f'_2(y)$  into Eq. 36, and noting that  $N = 16/3$  for a triangular section, and thus  $c = 0$ , Eq. 36 gives  $N = 16/3 = 5.3$ .

For a rectangular flow cross section, Eq. 34 gives

$$f'_2(y) = \frac{2}{3y \ln y} \left( \frac{5b + 6y}{b + 2y} \right) \dots \dots \dots (38)$$

Substituting Eq. 38 for  $f'_2(y)$  into Eq. 36, and noting that  $N = 10/3$  for a rectangular section of very low flow depth, and thus  $c = 0$ , Eq. 36 gives

$$N = \frac{10}{3} - \frac{4 \ln(b + 2y)}{3 \ln y} \dots \dots \dots (39)$$

When  $N$  and  $M$  are considered to vary with  $y$ , it is equivalent to taking Eqs. 1 and 2 as exact representations of such relationships for a given channel flow cross section. Thus, the expressions for  $N$  and  $M$  can also be determined directly from the geometry of the section. For a rectangular section, e.g., Eq. 9 gives

$$K^2 = \left( \frac{1.49}{n} \right)^2 (by)^2 \left( \frac{by}{b + 2y} \right)^{4/3} \dots \dots \dots (40)$$

Equating the left side of Eq. 40 to that of Eq. 2, and then equating the terms on both sides which only contain  $y$ , Eq. 39 can also be obtained.

#### RELATIONSHIP BETWEEN $M(\bar{y})$ ; $N(\bar{y})$ AND $M(y)$ ; $N(y)$

When  $M$  and  $N$  are considered to vary with flow depth from  $y_1$  to  $y_2$ , they become different in a mathematical sense. In order to mark this difference, they may be denoted by  $M(y)$  and  $N(y)$ ; whereas  $M(\bar{y})$  and  $N(\bar{y})$  are used to denote  $M$  and  $N$  when depending only on the average of depths  $y_1$  and  $y_2$ .

It can be shown that the slope of a tangent to either the curve of  $\ln Z$  versus  $\ln y$ , or the curve of  $\ln K$  versus  $\ln y$ , can be computed by using the equations either for  $M(\bar{y})$  and  $N(\bar{y})$  or for  $M(y)$  and  $N(y)$  because all these equations are mathematically consistent.

As an illustration, consider a rectangular flow cross section with a bottom width of 10 units (i.e., either 10 m or 10 ft). For this cross section, with  $z = 0$  and  $b = 10$ , Eq. 22 gives

$$N(\bar{y}) = \frac{10}{3} - \frac{4y}{3(5 + y)} \dots \dots \dots (41)$$

The slope of a tangent to the curve of  $\ln y$  for this cross section at  $y = \bar{y}$  is given by Eqs. 17 and 41 as

TABLE 1.—Values of  $\tan \alpha$  Determined Graphically and by using Eqs. 42 and 43 for Different Flow Depths in Rectangular Channel

y (1)	Graphical Determination from Fig. 1		Using $N(\bar{y})$ by Eq. 42	Using $N(y)$ by Eq. 43	$N = 2 \tan \alpha$ (6)
	$\alpha^\circ$ (2)	$\tan \alpha$ (3)	$\tan \alpha$ (4)	$\tan \alpha$ (5)	
2	55.9	1.48	1.48	1.48	2.96
5	53.1	1.33	1.33	1.33	2.66
10	50.7	1.22	1.22	1.22	2.44

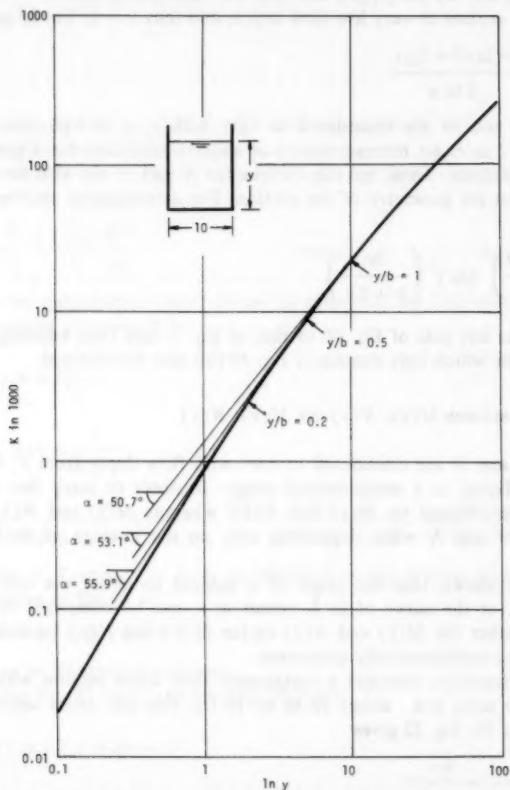


FIG. 2.—Plotting of  $\ln K$  versus  $\ln y$  for Rectangular Channel Section

$$\tan \alpha = \frac{N(\bar{y})}{2} = \frac{5}{3} - \frac{2y}{3(5+y)} \dots \dots \dots (42)$$

If  $N(y)$  is considered, the tangent slope  $\tan \alpha$  can be expressed by Eq. 31 in which  $N(y)$  is expressed by Eq. 39. Substituting Eq. 39 into Eq. 31 gives

$$\tan \alpha = \frac{5}{3} - \frac{4y}{3(b+2y)} \dots \dots \dots (43)$$

For  $b = 10$ , Eq. 43 becomes Eq. 42 exactly.

Further, the plotting of  $\ln K$  versus  $\ln y$  for the previously mentioned example is shown in Fig. 2. For  $y = 2, 5$ , and 10 units, the tangent slopes found graphically are compared with those determined by use of  $N(\bar{y})$  and  $N(y)$ , as shown in Table 1.

Similar relationships can be found between  $N(\bar{y})$  and  $N(y)$ , and also between  $M(\bar{y})$  and  $M(y)$ , for other geometrical flow cross sections.

#### APPLICATION OF HYDRAULIC EXPONENTS

The application of the hydraulic exponents is to simplify the computation of surface profiles of a gradually varied open-channel flow. For such a flow, the slope of the surface profile can be expressed by (2; p. 221):

$$\frac{dy}{dx} = S_0 \frac{1 - \left(\frac{K_n}{K}\right)^2}{1 - \left(\frac{Z_c}{Z}\right)^2} \dots \dots \dots (44)$$

in which  $y$  = the flow depth;  $x$  = the distance along the channel;  $S_0$  = the channel slope;  $K$  = the conveyance for the flow depth  $y$ ;  $K_n = K$  for the normal depth  $y_n$ ;  $Z$  = the section factor for the flow depth  $y$ ; and  $Z_c = Z$  for the critical depth  $y_c$ . Taking  $M$  and  $N$  as constants,  $K_n^2 = C_1 y_n^N$ ;  $K^2 = C_1 y^N$ ;  $Z_c^2 = C_2 y_c^M$ ; and  $Z^2 = C_2 y^M$ ; in which  $C_1$  and  $C_2$  = coefficients. Substituting these expressions into Eq. 44 gives

$$\frac{dy}{dx} = S_0 \frac{1 - \left(\frac{y_n}{y}\right)^2}{1 - \left(\frac{y_c}{y}\right)^2} \dots \dots \dots (45)$$

Let  $u = y/y_n$ . Then Eq. 45 may be integrated to express  $x$  as

$$x = \frac{y_n}{S_0} \left[ u - \int_0^u \frac{du}{1-u^N} + \left(\frac{y_c}{y_n}\right)^N \int_0^u \frac{u^{N-M}}{1-u^N} du \right] \dots \dots \dots (46)$$

in which  $\int_0^u (1-u^N)^{-1} du$  and  $\int_0^u [u^{N-M}/(1-u^N)] du$  are known as varied-flow functions. These functions can be easily evaluated by finding their values in prepared varied-flow function tables for a given value of  $y$  and for given values

of  $M$  and  $N$ . With the values of these functions known, Eq. 46 can be used to compute the surface profile of the gradually varied flow.

The aforementioned procedure can greatly simplify the computation of surface profiles of a gradually varied flow in a prismatic geometrical channel. This is a method of direct integration. The method involves an approximation as mentioned previously, but it has been found to produce reliable results in practical application.

It can easily be seen that the advantage of this simple method of direct integration cannot be attained if the values of  $M$  and  $N$  are taken to vary within the range of flow depth between  $y_1$  and  $y_2$ . If  $M$  and  $N$  are not treated as constants, they will contain flow depth as a variable. As a result, it will not be easy to integrate Eq. 46, and thus the advantage of the direct integration method will be lost.

## CONCLUSIONS

The determination of  $M$  and  $N$  has originally been given by Chow (2; 3, pp. 66 and 131; 4). Similar hydraulic exponents were also proposed by Bakhmeteff (1), and Mononobe (8), Lee (7), Von Seggern (11), and others. In fact, Eqs. 15 and 22 for trapezoidal sections have been developed by Chugaev (5, pp. 157-227), and graphical solutions of Eq. 22 were presented by Kirpich (6, p. 47), Pavlovskii (9, p. 515), and Rakhmanoff (10, pp. 75-114). However, no sufficiently detailed examinations have been given previously. This paper is intended to clarify the mathematical derivation of the hydraulic exponents and their implication in flow-computation applications.

The equations derived for  $M(\bar{y})$ ,  $N(\bar{y})$ ,  $M(y)$ , and  $N(y)$  are all mathematically consistent with each other as shown graphically by the example of a rectangular flow cross section.

The use of  $M(\bar{y})$  and  $N(\bar{y})$  in a flow-profile computation involves an approximation, which is to use the values of  $M(\bar{y})$  and  $N(\bar{y})$  at the average depth of the range of flow depth under consideration. This approximation will greatly simplify the computation by direct integration, and has been proven to produce reliable results for practical application.

The use of  $M(y)$  and  $N(y)$  would involve the variation of these values within the range of flow under consideration. Consequently, they would not be useful to achieve simplification in flow-profile computation by the method of direct integration.

## APPENDIX I.—REFERENCES

1. Bakhmeteff, B. A., *Hydraulics of Open Channels*, McGraw-Hill Book Co., Inc., New York, N.Y., 1932.
2. Chow, V. T., "Integrating the Equation of Gradually Varied Flow," *Proceedings, ASCE*, Vol. 81, Nov., 1955, pp. 1-32.
3. Chow, V. T., *Open-channel Hydraulics*, McGraw-Hill Book Co., Inc., New York, N.Y., 1959.
4. Chow, V. T., "Open-channel Flow," Section 24, *Handbook of Fluid Dynamics*, V. L. Streeter, ed., McGraw-Hill Book Co., Inc., New York, N.Y., 1961, pp. 24-1-24-59.
5. Chugaev, R. R., "About Some Questions Concerning Nonuniform Flow of Water in Open Prismatic Channels," (in Russian), *Transactions, All-Union Scientific Research Institute of Hydraulic Engineering*, Vol. 1, Leningrad, USSR, 1931.

6. Kirpich, P. Z., "Dimensionless Constants for Hydraulic Elements of Open-channel Cross-Sections," *Civil Engineering*, Vol. 18, No. 10, 1948.
7. Lee, M., "Steady Gradually Varied Flow in Uniform Channels on Mild Slopes," thesis presented to the University of Illinois, at Urbana, Ill., in 1947, in partial fulfillment of the requirements for the degree of Doctor of Philosophy.
8. Mononobe, N., "Back-water and Drop-down Curves for Uniform Channels," *Transactions*, ASCE, Vol. 103, 1938, pp. 950-989.
9. Pavlovskii, N. N., *Handbook of Hydraulics* (in Russian), Onti, Leningrad and Moscow, USSR, 1937.
10. Rakhmanoff, A. N., "On the Construction of Curves of Free Surfaces in Prismatic and Cylindrical Channels with Established Flow," (in Russian), *Transactions*, All-Union Scientific Research Institute of Hydraulic Engineering, Leningrad, USSR, Vol. 3, 1931, pp. 75-114.
11. Von Seggern, "Integrating the Equation of Nonuniform Flow," *Transactions*, ASCE, Vol. 115, 1950, pp. 71-88.

## APPENDIX II.—NOTATION

*The following symbols are used in this paper:*

- $A$  = water area of flow cross section;
- $b$  = bottom width of channel flow cross section;
- $C$  = coefficient; constant;
- $c$  = integration constant;
- $D$  = hydraulic depth =  $A/T$ ;
- $f_1(y), f_2(y)$  = functions of  $y$ ;
- $K$  = conveyance of channel flow cross section;
- $M$  = hydraulic exponent for critical-flow computation;
- $N$  = hydraulic exponent for uniform-flow computation;
- $P$  = wetted perimeter of channel flow cross section;
- $Q$  = discharge;
- $R$  = hydraulic radius;
- $S$  = energy slope of flow in channel;
- $S_0$  = bottom slope of channel;
- $T$  = top width of flow cross section;
- $u$  =  $y/y_n$ ;
- $V$  = mean flow velocity in channel flow cross section;
- $x$  = distance along channel; exponent;
- $y$  = flow depth; exponent;
- $y_1, y_2$  = flow depth;
- $\bar{y}$  = average flow depth between  $y_1$  and  $y_2$ ;
- $y_c$  = critical flow depth;
- $y_n$  = normal flow depth;
- $Z$  = section factor for critical-flow computation;
- $z$  = side slope of trapezoidal channel flow cross section; and
- $\alpha$  = slope angle of tangent to curve of  $\ln Z$  versus  $\ln y$ , or of  $\ln K$  versus  $\ln y$ .



## MODELING CIRCULATION IN DEPTH-AVERAGED FLOW

By Victor M. Ponce,<sup>1</sup> M. ASCE, and Steven B. Yabusaki<sup>2</sup>

### INTRODUCTION

There exists a class of open channel flow problems which can be adequately described in the context of depth-averaged, two-dimensional mathematical models. Essentially, these models are capable of resolving flow currents in two horizontal directions with the fluid and flow properties assumed to be invariant along the vertical. Such simplified representations of a three-dimensional phenomena are justified where turbulent mixing, due to bottom roughness, effectively generates a uniform velocity distribution over the flow depth.

Thermal effluents from cooling facilities, contaminant discharges from chemical processing plants, and sediment movement by local scouring are all evidence of a progressive industrialization which has the potential to tax the natural cleansing action of waterways to the point where serious environmental consequences may result. Knowledge of the effect of proposed modifications is vital to the safe development and utilization of waterways.

In this study, a fundamental investigation of the circulation phenomena in open channels is performed using a depth-averaged mathematical model. Circulation has been observed to have a primary influence on erosion and accretion processes, heat diffusion, and contaminant dispersion. Therefore, the clarification of the physical mechanisms leading to the generation of circulation in free surface flow is a much needed research endeavor.

### LITERATURE REVIEW

Prior to the development of efficient, high-speed computer hardware, two alternatives were available to the researcher interested in modeling free-surface flow: (1) analytical solutions; and (2) physical hydraulic models. Despite providing the most accurate results, analytical solutions are extremely rare and apply only in highly simplified situations. Conversely, physical hydraulic models are used widely and quite successfully. Most of the drawbacks associated with

<sup>1</sup>Assoc. Prof. of Civ. Engrg., San Diego State Univ., San Diego, Calif. 92182.

<sup>2</sup>Civ. Engr., Water and Land Resources Dept., Batelle, Pacific Northwest Laboratories, Richland, Wash.

Note.—Discussion open until April 1, 1982. To extend the closing date one month, a written request must be filed with the Manager of Technical and Professional Publications, ASCE. Manuscript was submitted for review for possible publication on August 20, 1980. This paper is part of the Journal of the Hydraulics Division, Proceedings of the American Society of Civil Engineers, ©ASCE, Vol. 107, No. HY11, November, 1981. ISSN 0044-796X/81/0011-1501/\$01.00.

physical models are of an economic nature owing to the high cost of construction and the time required to adequately simulate the prototype conditions. Lack of flexibility, however, is probably the largest deterrent to selecting a physical model since a change in configuration usually involves expensive modifications.

The increased efficiency of digital computers has triggered a strong research effort in the refinement of mathematical models. While offering almost unlimited flexibility in the simulation of various alternatives, these models have the additional appeal of smaller development and operating costs. Certain specialized problems still remain within the realm of physical modeling, but the use of mathematical models continues to grow.

Mathematical models of open channel flow exist at various levels of sophistication. The detailed description of flow phenomena is best accomplished in a three-dimensional spatial framework; however, the complexity of a formulation in three dimensions often requires tremendous amounts of computational effort. Where valid, the simplification to a two-dimensional representation can offer a considerable reduction in complexity and expense. This involves an integration of the three-dimensional equations of fluid dynamics over the flow depth. The two-dimensional depth-integrated system of equations is not without its pitfalls: there is a closure problem associated with the effective shear stresses which act tangentially on vertical sides of a fluid element. No rigorous relation between these stresses and the depth-averaged variables is currently available.

Hansen (6) is credited for being the first to outline the depth-averaged two-dimensional formulation. Later, several other researchers, most notably Leendertse (10,11), followed Hansen in applying two-dimensional modeling concepts to the study of estuarine and coastal hydrodynamics. In a detailed analysis of free-surface flow, Leendertse developed a computational model for long period wave propagation in well-mixed estuaries and coastal seas (10). Particular emphasis was given in Leendertse's work to the numerical properties of the two-dimensional model in the form of a linear stability and convergence analysis following the von Neumann approach.

Kuipers and Vreugdenhil (7) extended Leendertse's 1967 model to the realm of secondary flows. By imposing a steady condition at the open boundaries, they were able to use the unsteady character of Leendertse's model as an iterative technique to approach steady circulating flow under certain specified boundary conditions. A theoretical analysis of the vorticity-generating mechanisms was performed in order to throw additional light onto the causes of circulating flow in depth-averaged two-dimensional models. According to Kuipers and Vreugdenhil, if wind stresses are neglected, vorticity can be created either by the convective terms interacting with converging or diverging flow or through the effective shear stresses. Numerical experiments showed the necessity of including the convective inertia terms in order to model two-dimensional circulating flow. The observed circulation in the model is attributed to the combined effect of the convective inertia terms and the artificial viscosity, since no explicit account of the effective stresses was made.

In a companion report to that of Kuipers and Vreugdenhil, Flokstra (3) has directed attention to the importance of correctly modeling the effective shear stresses. Without actually resolving the closure problem associated with the modeling of these stresses, Flokstra made a detailed analysis of the relevant physical mechanisms contributing to the generation of circulation. According



to Flokstra's vorticity balance, it is theoretically impossible to generate circulating flow without modeling the effective shear stresses. In addition, Flokstra's analysis leads to the conclusion that a no-slip velocity condition at closed boundaries is essential to the generation of eddy flow patterns.

Abbott and Rasmussen (1) verified Kuipers and Vreugdenhil's conclusion that the convective inertia terms are necessary for the generation of circulation. Using physical reasoning, they attributed the circulating patterns to a direct consequence of the resistance effects dominating the inertial effects. Abbott and Rasmussen also concluded that "pseudo-circulations," occurring strictly due to the truncation errors of first order difference schemes, were possible in depth-averaged two-dimensional models.

The occurrence of nonlinear instability in two-dimensional numerical models was also studied by Flokstra (4). Three approaches were cited to handle this problem: (1) A spatial smoothing process similar to that used by Kuipers and Vreugdenhil; (2) the explicit introduction of an eddy viscosity term in the equations of motion; and (3) the use of a difference scheme affected with numerical viscosity.

McGuirk and Rodi (12) developed a depth-averaged velocity and contaminant distribution model of open channel flow which described the recirculation region immediately downstream of a side discharge into a flowing river. Considering the constant turbulent diffusion coefficient and nonexplicit representations of the turbulent structure too crude for the side jet phenomena, McGuirk and Rodi utilized an extension of Launder and Spalding's (8) two-dimensional turbulence model.

Lean and Weare (9) tested Flokstra's theoretically-based conclusions using a depth-averaged circulation model of flows past a breakwater. The effective stresses were shown to have contributions from shear layer turbulence and turbulence generated at the bed. Criteria is presented to delimit the conditions under which the shear layer turbulence will predominate. An observation of numerical circulation (5) similar to that experienced by Abbott and Rasmussen but caused by a coarse computational grid is reported.

At present, many uncertainties exist in the mathematical modeling of depth-averaged two-dimensional open channel flow. Several models which exhibit circulation and numerous theoretical reviews on the factors causing circulation are present in the literature. However, no comprehensive analysis of the various mechanisms leading to circulation has been attempted in conjunction with a numerical model. The objectives of this study are, thus, twofold: (1) The clarification of the physical processes which contribute to the generation of circulation; and (2) the identification of significant factors in the numerical specification of circulating flow problems.

#### GOVERNING EQUATIONS

The derivation of the equations governing depth-averaged free-surface flow is accomplished by the successive simplification of the general three-dimensional fluid flow equations, i.e., the Navier-Stokes equations. Four assumptions are basic to the equation set used in this study: (1) Water is incompressible; (2) vertical velocities and accelerations are negligible; (3) wind stresses and geostrophic effects are negligible; and (4) average values are sufficient to describe

properties which vary over the flow depth.

Fluid density effects are not considered in this study; thus, incompressibility is a limitation to the applicability of the model. The second assumption is a consequence of the relatively large magnitude of the gravitational body force which, in flows of shallow depth, simplifies the z-component of the motion equation to a statement of hydrostatic pressure distribution in the vertical. For the type of flow under consideration, i.e., open channel flow, the magnitude of the wind and geostrophic effects is insignificant compared to the driving forces found in the mean flow currents. These two terms can be easily incorporated into the model if desired, and their absence does not detract from the generality of the conclusions of this study. The most significant assumption is that an average value is capable of representing a property which normally varies over the flow depth. Until this assumption is made, the analysis is fundamentally three-dimensional. Due to the depth-averaging of the equation set, information on the vertical distribution of velocity is partially lost. Fortunately, the shallow waters found in rivers and well-mixed estuaries usually do not require such detailed information.

The resulting depth-averaged equations are:

$$\text{Conservation of mass} \quad \frac{\partial \eta}{\partial t} + \frac{\partial (h\bar{u})}{\partial x} + \frac{\partial (h\bar{v})}{\partial y} = 0 \quad (1)$$

$$\begin{aligned} \text{Conservation of momentum} \quad & \frac{\partial \bar{u}}{\partial t} + \bar{u} \frac{\partial \bar{u}}{\partial x} + \bar{v} \frac{\partial \bar{u}}{\partial y} + g \frac{\partial \eta}{\partial x} + \frac{1}{\rho h} \tau_{bx} \\ & - \frac{1}{\rho h} \frac{\partial}{\partial x} (hT_{xx}) - \frac{1}{\rho h} \frac{\partial}{\partial y} (hT_{xy}) = 0 \quad (2) \end{aligned}$$

$$\begin{aligned} & \frac{\partial \bar{v}}{\partial t} + \bar{u} \frac{\partial \bar{v}}{\partial x} + \bar{v} \frac{\partial \bar{v}}{\partial y} + g \frac{\partial \eta}{\partial y} + \frac{1}{\rho h} \tau_{by} - \frac{1}{\rho h} \frac{\partial}{\partial x} (hT_{xy}) \\ & - \frac{1}{\rho h} \frac{\partial}{\partial y} (hT_{yy}) = 0 \quad (3) \end{aligned}$$

in which  $\bar{u}$ ,  $\bar{v}$  = depth-averaged velocities;  $t$  = time;  $x$ ,  $y$  = coordinate directions;  $g$  = gravitational acceleration;  $\eta$  = water elevation ( $\eta = h + z_b$ );  $\rho$  = fluid density;  $\tau_{bx}$ ,  $\tau_{by}$  = bottom shear stresses; and  $T_{xx}$ ,  $T_{xy}$ ,  $T_{yy}$  = effective shear stresses defined as follows:

$$T_{xx} = \frac{1}{h} \int_{z_b}^{\eta} \left[ 2\rho\nu \frac{\partial u}{\partial x} - \rho \overline{u'^2} - \rho(u - \bar{u})^2 \right] dz \quad (4)$$

$$T_{xy} = T_{yx} = \frac{1}{h} \int_{z_b}^{\eta} \left[ \rho\nu \left( \frac{\partial u}{\partial y} + \frac{\partial v}{\partial x} \right) - \rho \overline{u'v'} - \rho(u - \bar{u})(v - \bar{v}) \right] dz \quad (5)$$

$$T_{yy} = \frac{1}{h} \int_{z_b}^{\eta} \left[ 2\rho\nu \frac{\partial v}{\partial y} - \rho \overline{v'^2} - \rho(v - \bar{v})^2 \right] dz \quad (6)$$

in which  $\nu$  = kinematic viscosity; and  $u'$  and  $v'$  = turbulent velocity fluctuations.

The foregoing equation set, although containing many approximations and

simplifications, is not closed. Historically, turbulent flow theory has suffered from an incomplete physical representation of the turbulent momentum transfer (Reynolds stresses), i.e., those stresses due to the correlations of turbulent velocity fluctuations. Depth-averaging the formulation further complicates the problem by creating an additional stress due to the nonuniform velocity distribution in the vertical. These two stresses and the viscous shear stress combine into the terms previously identified as the effective shear stresses.

Representing the effective shear stresses in terms of the mean flow variables is by far the largest impediment to the proper depth-averaged modeling of circulating flow. Since this problem remains to be solved, the use of empirical parameters and calibration techniques is indicated. In this study, the procedure developed by Kuipers and Vreugdenhil (7) is adopted. This particular technique does not explicitly include the effective shear stresses in the equation set, but introduces them in a velocity-averaging routine which effectively simulates the contribution of the effective stresses. In this routine, an averaging procedure occurs after each set of new dependent variables has been generated, as follows:

$$\bar{u}_{j,k}^* = \bar{u}_{j,k}(1 - \alpha) + \frac{\alpha}{4} (\bar{u}_{j-1,k} + \bar{u}_{j,k-1} + \bar{u}_{j,k+1} + \bar{u}_{j+1,k}) \dots \dots \dots (7)$$

$$\bar{v}_{j,k}^* = \bar{v}_{j,k}(1 - \alpha) + \frac{\alpha}{4} (\bar{v}_{j-1,k} + \bar{v}_{j,k-1} + \bar{v}_{j,k+1} + \bar{v}_{j+1,k}) \dots \dots \dots (8)$$

in which  $\bar{u}_{j,k}^*$  = spatially averaged  $\bar{u}_{j,k}$ ;  $\bar{v}_{j,k}^*$  = spatially averaged  $\bar{v}_{j,k}$ ;  $\alpha$  = weighting factor; and  $j, k$  = spatial indices. When these substitutions are made in the governing equations, closure terms appear such that

$$\frac{1}{\rho h} \left[ \frac{\partial}{\partial x} (hT_{xx}) + \frac{\partial}{\partial y} (hT_{xy}) \right] = \epsilon \left( \frac{\partial^2 \bar{u}}{\partial x^2} + \frac{\partial^2 \bar{u}}{\partial y^2} \right) \dots \dots \dots (9)$$

$$\frac{1}{\rho h} \left[ \frac{\partial}{\partial x} (hT_{xy}) + \frac{\partial}{\partial y} (hT_{yy}) \right] = \epsilon \left( \frac{\partial^2 \bar{v}}{\partial x^2} + \frac{\partial^2 \bar{v}}{\partial y^2} \right) \dots \dots \dots (10)$$

in which  $\epsilon = \alpha (\Delta x)^2 / 2 \Delta t$ ;  $\Delta x$  = spatial increment; and  $\Delta t$  = temporal increment.

The bottom shear stress, like the effective shear stress, has not been rigorously related to flow properties. However, years of experimentation has resulted in the development of several satisfactory empirical resistance equations. Any of the applicable resistance equations can be used to relate the bottom shear stress to the flow velocity, assuming the validity of a steady uniform flow roughness. The Chézy expression is preferred here for simplicity, due to the dimensionless friction factor  $f$ , associated with it, as follows:

$$\tau_{bx} = \rho f, \bar{u} (\bar{u}^2 + \bar{v}^2)^{1/2} \dots \dots \dots (11)$$

$$\tau_{by} = \rho f, \bar{v} (\bar{u}^2 + \bar{v}^2)^{1/2} \dots \dots \dots (12)$$

in which  $f = g/C^2$ ; and  $C$  = Chézy coefficient.

#### MATHEMATICAL MODEL

A finite difference approximation is used to represent the partial differential equation set in the numerical model. In order to visualize the computational

structure, the reader must imagine levels of horizontal  $x$ - $y$  grids layered in the vertical time dimension. Conceptually, the four variables,  $u$ ,  $v$ ,  $\eta$ , and  $z_b$ , should all be defined at every node location. However practical limitations in the computational procedure make it more convenient to define a separate grid system for each of these variables. These four grid systems are staggered in space in a form originally due to Platzman (13), as shown in Fig. 1. Normally, it is not necessary for  $\Delta x$  to be equal to  $\Delta y$ ; however, the representation of the effective shear stresses used in this model does hinge on this assumption.

Among the several types of finite difference schemes available, the central

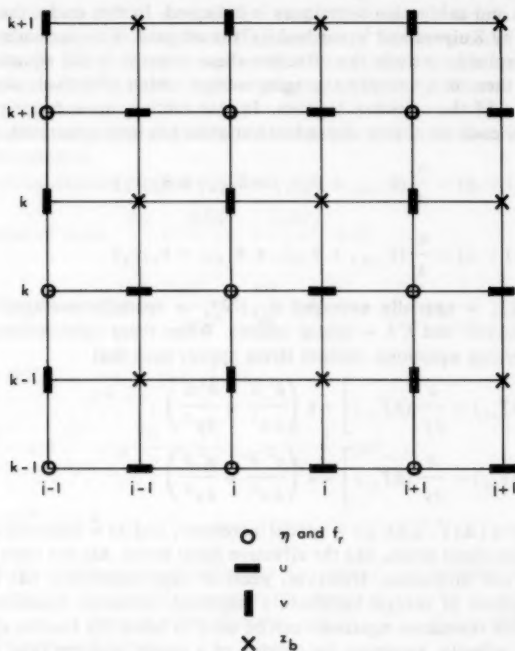


FIG. 1.—Typical Spatial Grid Configuration at Time Level  $n$

difference approximations provide second order accuracy. Generally speaking, spatial derivatives can always be expressed in a central difference format. However, unless iterations are performed, temporal derivatives cannot be represented by central difference schemes because two entire time levels of unknowns would be present. The additional computational effort required by an iterative formulation is normally not warranted. Consequently, a less accurate but more expedient first order difference scheme is preferred for the temporal derivatives.

Equations which are nonlinear with respect to the unknown variables present

formidable difficulties for an efficient numerical solution. Although the governing equations contain nonlinear terms, a judicious specification of known and unknown values in the finite difference equations results in a linear representation of the unknown variables. This equation set is then solved by an efficient matrix inversion algorithm.

The computational procedure used in this model is a multioperational solution mode based on the division of each time step  $\Delta t$  into two stages of half-time step each. Leendertse (10) modified the well-known "alternating-direction implicit" or ADI method, by including two explicit schemes in such a way that each stage contained an implicit scheme followed by an explicit scheme. The advantage of the ADI method, in addition to those attributable to implicit schemes, lies in the solution procedure which solves the x-momentum equation separately from the y-momentum equation, permitting the two-dimensional problem to be solved as a sequence of two one-dimensional problems. After each implicit step, a single dependent variable remains unknown and can be directly solved for by an explicit method. The numerical model is based on the set of governing equations derived earlier. Each of the three equations has a difference scheme centered about a unique location on the grid system. The x-momentum equation is referenced to the node occupied by  $\bar{u}_{j,k}$  while the y-momentum equation is centered about node location  $\bar{v}_{j,k}$ ;  $\eta_{j,k}$  is the reference location for the continuity equation (for simplicity, overbars are omitted hereafter).

In the mathematical model used in this study, the finite difference analogs of the various equations are, for the first stage:

$$\text{x-Momentum (Implicit)} \quad \left. \frac{\partial u}{\partial t} \right|_{u_{j,k}^{n+1/2}} = \frac{u_{j,k}^{n+1/2} - u_{j,k}^n}{\frac{1}{2} \Delta t} \quad \dots \quad (13)$$

$$u \left. \frac{\partial u}{\partial x} \right|_{u_{j,k}^{n+1/2}} = u_{j,k}^{n+1/2} \left[ \frac{u_{j+1,k}^n - u_{j-1,k}^n}{2 \Delta x} \right] \quad \dots \quad (14)$$

$$v \left. \frac{\partial u}{\partial y} \right|_{u_{j,k}^{n+1/2}} = \left[ \frac{v_{j,k-1}^n + v_{j+1,k-1}^n + v_{j,k}^n + v_{j+1,k}^n}{4} \right] \left[ \frac{u_{j,k+1}^n - u_{j,k-1}^n}{2 \Delta y} \right] \quad \dots \quad (15)$$

$$g \left. \frac{\partial \eta}{\partial x} \right|_{u_{j,k}^{n+1/2}} = g \left[ \frac{\eta_{j+1,k}^{n+1/2} - \eta_{j,k}^{n+1/2}}{\Delta x} \right] \quad \dots \quad (16)$$

$$f_r u \left. \frac{(u^2 + v^2)^{1/2}}{(\eta - z)} \right|_{u_{j,k}^{n+1/2}} = \left[ \frac{f_{rj,k} + f_{rj+1,k}}{2} \right] \frac{\left[ u_{j,k}^{n+1/2} \left[ (u_{j,k}^n)^2 + \left( \frac{v_{j,k-1}^n + v_{j+1,k-1}^n + v_{j,k}^n + v_{j+1,k}^n}{4} \right)^2 \right]^{1/2} \right]}{\left[ \frac{\eta_{j+1,k}^n + \eta_{j,k}^n}{2} - \frac{z_{b,j,k} + z_{b,j,k-1}}{2} \right]} \quad (17)$$

$$\text{Continuity (Implicit)} \quad \left. \frac{\partial \eta}{\partial t} \right|_{\eta_{j,k}^{n+1/2}} = \frac{\eta_{j,k}^{n+1/2} - \eta_{j,k}^n}{\frac{1}{2} \Delta t} \quad \dots \quad (18)$$

$$\frac{\partial}{\partial x} [(\eta - z_b)u] \Big|_{\eta_{j,k}^{n+1/2}} = \frac{\left[ \frac{\eta_{j+1,k}^n + \eta_{j,k}^n}{2} - \frac{z_{b_{j,k}} + z_{b_{j,k-1}}}{2} \right] u_{j,k}^{n+1/2}}{\Delta x} - \frac{\left[ \frac{\eta_{j,k}^n + \eta_{j-1,k}^n}{2} - \frac{z_{b_{j-1,k}} + z_{b_{j-1,k-1}}}{2} \right] u_{j-1,k}^{n+1/2}}{\Delta x} \dots (19)$$

$$\frac{\partial}{\partial y} [(\eta - z_b)v] \Big|_{\eta_{j,k}^{n+1/2}} = \frac{\left[ \frac{\eta_{j,k+1}^n + \eta_{j,k}^n}{2} - \frac{z_{b_{j,k}} + z_{b_{j-1,k}}}{2} \right] v_{j,k}^n}{\Delta y} - \frac{\left[ \frac{\eta_{j,k}^n + \eta_{j,k-1}^n}{2} - \frac{z_{b_{j,k-1}} + z_{b_{j-1,k-1}}}{2} \right] v_{j,k-1}^n}{\Delta y} \dots (20)$$

$$\text{y-Momentum (Explicit)} \quad \frac{\partial v}{\partial t} \Big|_{\eta_{j,k}^{n+1/2}} = \frac{v_{j,k}^{n+1/2} - v_{j,k}^n}{\frac{1}{2} \Delta t} \dots (21)$$

$$u \frac{\partial v}{\partial x} \Big|_{\eta_{j,k}^{n+1/2}} = \left( \frac{u_{j,k}^{n+1/2} + u_{j,k+1}^{n+1/2} + u_{j-1,k+1}^{n+1/2} + u_{j-1,k}^{n+1/2}}{4} \right) \left( \frac{v_{j+1,k}^n - v_{j-1,k}^n}{2 \Delta x} \right) \dots (22)$$

$$v \frac{\partial v}{\partial y} \Big|_{\eta_{j,k}^{n+1/2}} = v_{j,k}^{n+1/2} \left[ \frac{v_{j,k+1}^n - v_{j,k-1}^n}{2 \Delta y} \right] \dots (23)$$

$$g \frac{\partial \eta}{\partial y} \Big|_{\eta_{j,k}^{n+1/2}} = g \left[ \frac{\eta_{j,k+1}^{n+1/2} - \eta_{j,k}^{n+1/2}}{\Delta y} \right] \dots (24)$$

$$f_r v \frac{(u^2 + v^2)^{1/2}}{(\eta - z_b)} \Big|_{\eta_{j,k}^{n+1/2}} = \left( \frac{f_{j,k} + f_{j,k+1}}{2} \right) \left[ \frac{v_{j,k}^{n+1/2} \left[ (v_{j,k}^n)^2 + \left( \frac{u_{j,k}^n + u_{j,k+1}^n + u_{j-1,k}^n + u_{j-1,k+1}^n}{4} \right)^2 \right]^{1/2}}{\left( \frac{\eta_{j,k+1}^{n+1/2} + \eta_{j,k}^{n+1/2}}{2} - \frac{z_{b_{j,k}} + z_{b_{j-1,k}}}{2} \right)} \right] \dots (25)$$

Similar discretization techniques are applicable for the second stage: (1) y-momentum and continuity (implicit); and (2) x-momentum (explicit). See Ref. 14 for additional details.

Two boundary types can be specified in the numerical model: closed and open boundaries. At closed boundaries, the most convenient specification is the condition of zero mass flux (i.e., zero velocity) in a direction perpendicular to the boundary. At open boundaries, either mean velocity or water surface elevation may be specified, depending on the modeling needs.

Spatial central finite differences such as those used on this model require

information which lies outside the boundaries of the computational model. Although a zero velocity tangential to the wall is a realistic assumption (the no-slip velocity condition), a zero water level at the boundary can be grossly inaccurate and may lead to numerical stability problems. A satisfactory alternative appears to be the relocation of interior values. A simple relocation technique was chosen in which exterior values were defined to be equal to those interior values adjacent to the boundaries. This is tantamount to a perfect slip condition, a reasonable assumption in turbulent flows in which the viscous effects have little influence on the horizontal velocity distribution.

A pervasive problem in two-dimensional mathematical modeling is the lack of adequate theoretical numerical stability criteria. Linear stability theory classifies the multi-operational procedure as unconditionally stable. However, experience (15) has shown that it is only weakly stable.

## RESULTS

The objective of the numerical experimentation is the clarification of the circulation phenomena found in free surface flow. Two hypothetical configura-

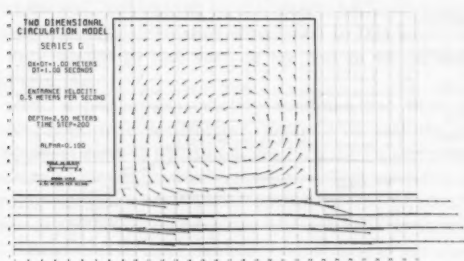


FIG. 2.—Channel-Pool Baseline Flow Pattern, Time Step 200

tions are tested under a gamut of initial and boundary conditions. In addition to a sensitivity analysis, experiments are performed in which more than one element is varied from the baseline in order to determine the interaction between several components of the problem.

The bulk of the testing program consists of experiments performed on a channel-pool configuration; channel dimensions are 4 m in width by 30 m in length, while the pool is a rectangle 14 m wide and 15 m long.

The first series of tests are performed with a 0.5 m/s velocity specified in the channel as an initial condition and at the upstream end as a steady boundary condition. A water depth of 2.5 m serves as both the initial condition and the steady downstream boundary condition. There is no velocity in the pool initially. Closed boundaries are represented by zero velocities perpendicular to walls. Without a bed slope, the water in the system is driven solely by the upstream entrance velocity. Numerical parameters used in the baseline run are: weighting factor  $\alpha = 0.1$ , friction factor  $f_r = 0.0045$ , spatial increment  $\Delta x = \Delta y = 1.0$  m, and temporal increment  $\Delta t = 1.0$  sec. Fig. 2 is a plot

of the baseline velocity vectors after 200 sec of simulation. A well-developed circulation appears in the pool area with little or no divergence from the mainstream flow. Water levels in the pool range from 2.50 m–2.52 m. Entrance levels, however, fall continuously from 2.50 m–2.44 m.

The necessity of modeling the effective shear stresses where physical circulation is present has been explained theoretically by Flokstra (3). In the present model, the representation of the effective shear stresses is not explicit in the discretized equation set; rather, the action of the effective shear stresses is simulated by a velocity averaging interphase which employs a weighting factor  $\alpha$  to control the magnitude of the effect. The first experiment performed on the channel-pool configuration omits the effective stress modeling by setting  $\alpha$  to zero. Transfer of turbulent momentum from the mainstream to the pool is insignificant in this case. With no flow divergence into the pool, the initial conditions are virtually preserved.

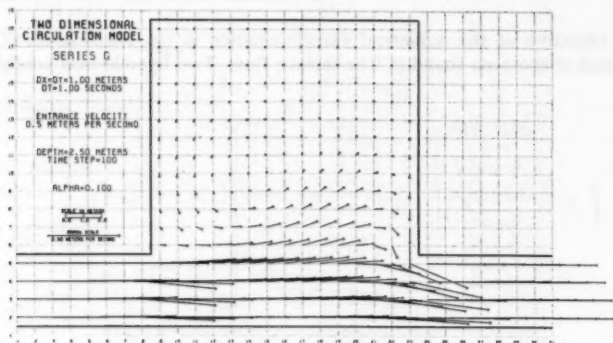


FIG. 3.—Flow Pattern Neglecting Convective Inertia, Time Step 100

The convective inertia terms,  $u \partial u / \partial x$ ,  $v \partial u / \partial y$ ,  $u \partial v / \partial x$ , and  $v \partial v / \partial y$ , are often neglected in numerical modeling because the nonlinearity of these terms introduces additional difficulties. Several authors have commented on the necessary presence of the convective inertia terms in the equation set when secondary flow is to be resolved. To test this conclusion, all four convective inertia terms were set to zero. The plot at 100 sec of simulation time is presented in Fig. 3. Divergence of the flow from the channel into the pool is strong; however, no circulation sets up. As water in the channel reaches the upstream end of the pool, flow immediately is directed into the pool along the boundaries, preventing circulation from occurring.

In the literature, the role of friction in circulation is not clearly defined. To shed more light on this subject, an experiment is performed wherein the friction terms,  $f_r u \sqrt{u^2 + v^2} / \eta - z_b$  and  $f_r v \sqrt{u^2 + v^2} / \eta - z_b$ , are eliminated from the computation. The results from this experiment, including detailed quantitative results are virtually indistinguishable from the baseline results, Fig. 2.

The effect of an increase in flow depth has been documented by Bengtsson



(2) following experiments performed on a lake model. His conclusion was that the influence of the horizontal turbulence terms was reduced with increasing depth. In this study, the horizontal dispersion of momentum is simulated by the effective stress closure terms,  $\epsilon (\partial^2 u / \partial x^2 + \partial^2 u / \partial y^2)$  and  $\epsilon (\partial^2 v / \partial x^2 + \partial^2 v / \partial y^2)$ . It is therefore, not obvious how depth should affect these terms. To investigate the effect of flow depth, depths ranging from 0.04 m–50 m were tested, with instability occurring only in the 0.04 m run. Results displayed the following trends: shallower depths show more divergence of flow from the channel, larger velocities in the shear layer, and faster set-up of circulation. In the extreme, however, the shallow depth is also subject to instability. Larger depths have less energy transfer to the pool and consequently little or no circulation.

The earlier experiments with friction appear to dismiss the importance attached to it by some authors. However, these tests were all performed on problems of relatively small scale. To test the effect of friction in a large scale problem, the size of the configuration was increased by setting  $\Delta x = \Delta y = 100$  m. Experience from the stability analysis testing led to the use of a time increment of 100 sec to accompany the length scale increase. In this test, the baseline friction value,  $f_r = 0.0045$ , was used. Flow diverged immediately into the pool near the upstream wall, penetrating to the center, before leaving the pool along the downstream wall. No circulation developed in this experiment. The flow pattern was very similar to that seen in the test in which convective inertia was neglected (Fig. 3).

In earlier tests, a perfect-slip velocity condition had been implemented at all closed boundaries with satisfactory results. To test the validity of this assumption, an experiment is performed in which the flow is subject to a no-slip velocity condition as closed physical boundaries. This condition can be approximated by setting all velocities located outside of the physical boundaries to zero. For this experiment, a bed slope  $S_0 = 0.0005$  is introduced into the channel-pool configuration. Open boundary conditions at the channel end points are water levels which correspond to the initial bed slope condition. Closed boundaries remain to be defined by zero perpendicular velocities. All other parameters are the same as in the velocity-specified baseline testing, i.e.,  $\alpha = 0.1$ ,  $\Delta x = \Delta y = 1.0$  m,  $\Delta t = 1.0$  sec, and  $f_r = 0.0045$ . The no-slip model experiences strong damping of velocity although the development of circulation is apparent after 190 sec of simulation.

Secondary flow in sudden expansions is of a slightly different nature than the channel-pool system treated earlier. This is due in part to the bending of currents into the expansion and the increased exposure of secondary currents to mainstream effects. Abbott and Rasmussen (1) developed a channel expansion model from which results and conclusions were presented. An attempt is made here to verify these conclusions using a similar geometry.

In this testing series, the configuration consists of an entrance channel 9 m wide and 7.5 m long while the expanded channel is 17 m wide and 22.5 m long. A fixed bed slope of  $S_0 = 0.0005$  in the direction of the entrance channel flow is specified for the entire configuration. The initial condition is a water surface slope parallel to the bed at a depth of 2.5 m. All velocities are set to zero at the beginning of the simulation. Open boundary conditions at both upstream and downstream ends are water levels which match the initial

conditions. Closed boundaries are zero velocities perpendicular to the walls. Friction in this model is governed by a dimensionless friction factor  $f_r = 0.0045$ . The weighting factor is set to 0.1 while the space increment is 1.0 m and the time increment is 1.0 sec.

Fig. 4 is a plot of the channel expansion baseline results after 100 sec of simulation. A well-developed circulation forms a zone of separation in the corner

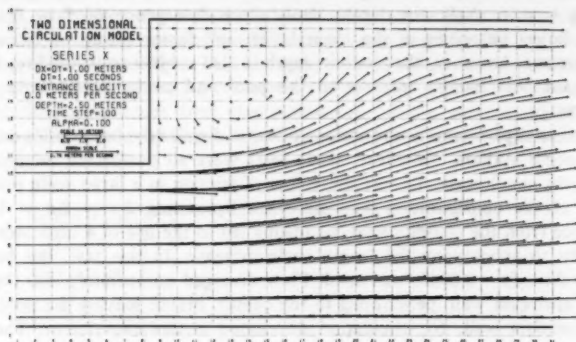


FIG. 4.—Channel Expansion Baseline Flow Pattern, Time Step 100

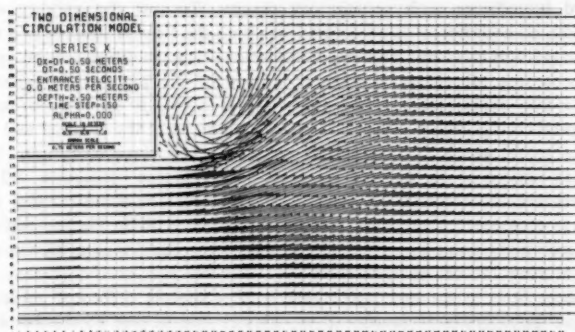


FIG. 5.—Channel Expansion Flow Pattern with Increased Spatial Resolution, Time Step 150

of the expansion. Entrance velocities range from 0.72 m/s at the bottom wall to 0.77 m/s at the top wall while exit velocities vary from 0.44 m/s–0.30 m/s, bottom to top. Water levels throughout the simulation are continuous and stable. Slightly lower elevations are found within the circulation pattern.

For the most part, the testing of the channel expansion produced results consistent with those of the channel-pool configuration. A discrepancy was found, however, when the slope-specified models were tested without modeling

the effective stresses. In the velocity-specified channel-pool model, the absence of the effective stresses resulted in no circulation being produced. Contrary to this result, both configurations, i.e., the channel expansion and the channel-pool system, are able to generate a spiraling secondary flow without the presence of the effective stresses if a bed slope is the driving force.

The question arose that the secondary currents which appear without the benefit of effective stress modeling may be of a strictly numerical nature. Theoretically, numerical effects should be minimized as the discretization of the problem domain is made exceedingly small. To this end, both space and time increments in the expansion model were reduced although the problem size remained constant. The values of these parameters for this test are  $\Delta x = \Delta y = 0.5$  m and  $\Delta t = 0.5$  sec.

A horizontal water surface without velocity is specified as the initial condition. As the simulation begins, the downstream water level is lowered in 40 time steps to a depth of 2.5 m, the same depth as the upstream boundary condition. Thus a line drawn through the end point water levels will be parallel to the bed slope. The weighting factor for this experiment is zero while the nondimensional friction factor is 0.0045. Fig. 5 is a plot of the velocity vectors after 150 sec of simulation. A strong spiraling "circulation," with a character similar to those observed in earlier slope-specified experiments, sets up in the expansion corner.

## EVALUATION

The testing program for this study is fairly extensive; therefore, only a limited discussion can be presented here. However, the analysis and evaluation of the numerical experiments is based on all the tests performed. For a more detailed description, the reader is referred to (14).

The use of specified water levels at the open boundaries proved to be a better boundary condition than the velocity specified in the early testing series. When a difference in water levels is the driving force for flow through the configuration, both velocity and water surface are steady and continuous, with few, if any, anomalies. This is in contrast to the velocity-specified model which requires a special initial condition before simulation can begin. In addition, oscillating water levels and velocities plague many of the velocity-specified simulations.

Specific differences in model behavior due to a change in boundary conditions are found only in the testing of  $\alpha$ , the weighting factor used in the velocity-averaging routine. In the velocity-specified model, circulation did not occur without the presence of the closure terms,  $\epsilon(\partial^2 u / \partial x^2 + \partial^2 u / \partial y^2)$  and  $\epsilon(\partial^2 v / \partial x^2 + \partial^2 v / \partial y^2)$ , in the computations. However, a spiraling secondary flow did appear in all sloping models when tested without the effective stresses being represented. It does not appear that this result is numerically-produced, as evidenced by the undiminished presence of this "circulation" in spite of increased grid resolution.

While acknowledging the "no-slip" velocity condition in nature, the testing of this model has been performed primarily with a "perfect slip" boundary specification. This is a reasonable assumption in models where the spatial resolution across a channel width is not very fine. In the experiment involving

the specification of zero velocities outside the boundary geometry, overwhelming resistance effects resulted. Obviously, any consideration of a no-slip boundary condition must be coordinated with an accompanying reduction in the bed resistance effects.

Results from the testing program are reasonable and encouraging, despite the presence of two flaws traceable to the representation of the effective stresses. First, there is yet to be found a physical basis by which to choose the appropriate weighting factor,  $\alpha$ , on the velocity averaging routine. There are instances in the literature where physical processes have been successfully replaced by numerical techniques in a general manner. Although the selection of the weighting factor is presently a manageable calibration task, a physical link to the turbulence process has yet to be advanced.

The second drawback in the effective stress representation is somewhat more serious than the first. Much of the success is fulfilling the required profile of traits by the closure terms is due to the effect of numerical viscosity. As the weighting factor is increased, the model reacts as if the fluid is becoming more viscous, thus increasing the exchange of lateral momentum and increasing viscous damping. Essentially, viscosity is used to model a turbulence effect. Therefore, care must be exercised when using the velocity averaging routine; a balance must be struck between the simulation of the effective stresses and the associated change in fluid properties.

This study has experimentally verified Flokstra's conclusion that true circulation, i.e., a flow pattern possessing a separation zone with closed circular streamlines, requires the modeling of the effective shear stresses. An order of magnitude analysis performed on the various terms in the equation of motion verifies the significance of the effective stresses in all instances where circulation occurs. Circulation requires a continuous exchange of turbulent energy across the shear layer to be maintained. Withdrawal of the effective stresses after a steady flow pattern has set up dissolves the circulation and ultimately leads to instability.

The order-of-magnitude analysis of terms found in the momentum equation shows that convective inertia is significant in the channel and shear layer for all instances where circulation occurs. The presence of inertia allows the flow to retain a uniform structure for a distance beyond the location of a configuration change, enabling the development of a separation zone adjacent to the free extension of uniform flow. Ultimately, this separation of flow develops into a local zone of circulating flow.

Merely including the convective inertia in the mathematical model will not ensure the generation of secondary flow. Even with the additional stipulation that the effective stresses and all other quantities be precisely described, circulation may yet be inhibited by frictional effects. In every case where secondary currents do not occur, the resistance term is significant and larger than the convective inertia terms.

This study has found that bottom friction is the largest deterrent to the existence of circulating flow. A competition seems to exist between convective inertia and bed resistance forces. The fact that convective inertia terms contain spatial gradients of velocity makes them particularly sensitive to scale effects. In small scale problems, lateral differences in velocity occur over relatively small distances, creating large velocity gradients. The large magnitudes of the convective inertia

terms render the bed resistance effects negligible. No reasonable friction factor can affect this mechanism. Conversely, large scale problems reduce the magnitude of both convective inertia and effective stresses to such a degree that the friction terms are promoted to the point where resistance effects totally inhibit the generation of secondary flow.

This model displays at least two different instability mechanisms: nonlinear and Courant. Nonlinear instability is theoretically described as the inability to resolve energy at scales smaller than twice the spatial grid increment. Physically, energy is "cascaded" to smaller and smaller scales by the action of the nonlinear terms in the governing equations. At the smallest scales, energy is dissipated by viscous effects. the discrete formulation of the numerical model interrupts the energy cascade at the resolution of the grid. Thus, energy accumulates at this scale and eventually spoils the computations.

Nonlinear instability is characterized by gradually developing water surface discontinuities accompanied by a similar behavior in the computed velocities. The process is usually slow, and can take as many as 100 time steps to develop. In this numerical model, nonlinear instability requires the velocity averaging technique to be present in all simulations although the weighting factor need not be large. Most runs were stable with  $\alpha = 0.1$ . Physically speaking, the use of the velocity averaging routine introduces a stronger viscous dissipation mechanism into the fluid. Energy no longer must be transferred to scales smaller than the grid resolution for viscous effects to act.

Courant instability occurs when the ratio of physical celerity to numerical celerity (defined as the Courant number) exceeds a characteristic value. The physical celerity for this model is the maximum channel velocity,  $U_{\max}$ , while the numerical celerity is defined as  $\Delta x/\Delta t = \Delta y/\Delta t$ . Thus, the criterion is of the form  $U_{\max} \Delta t/\Delta x \leq \xi$ , in which  $\xi$  is the characteristic limit. The two explicit stages contained in the multioperational procedure are presumably responsible for the Courant stability condition found in this model.

Courant instability is characteristically a very rapid process. The simulation proceeds without noticeable difficulty until a sudden discontinuity appears in one of the dependent variables. Within a few time steps the entire calculation is spoiled. In this study the limiting value of the Courant number is dependent upon the weighting factor used in the velocity averaging routine. This is to be expected since large weighting factors can smooth instabilities that would otherwise occur if smaller weighting factors were used. For  $\alpha = 0.1$ , the Courant number in this model must be less than or equal to 0.5.

#### CONCLUSIONS AND RECOMMENDATIONS

Major conclusions from this study are as follows:

1. Effective shear stress modeling is a necessary condition for the resolution of steady, closed-streamline circulation in depth-averaged mathematical models.
2. Convective inertia must be included in an analysis where secondary currents are being considered.
3. A competition seems to exist between convective inertia and the resistance effects at the bed. Circulating flow-barring wind forces is possible only where bed resistance is of minor influence, e.g., at small length scales.

4. The no-slip velocity condition at the physical boundaries is not absolutely necessary. However, if the no-slip condition is specified, the increased resistance effects may have to be corrected for by reducing the friction factor used in the modeling of bed resistance.

5. The type of boundary conditions has a significant effect on the resulting flow patterns for a given problem.

The following recommendations are offered for future research:

1. The greatest source of uncertainty is the modeling of the effective stresses. Although simplified methods of representing the effective stresses have yielded reasonable results, it is surmised that a higher level of sophistication is necessary in order to handle complex flow patterns. In such cases, a separate account of the three components of the effective stresses may be warranted. At present, individual closure assumptions are not available.

2. Additional studies are needed in order to identify the numerical effects of various discretization schemes and techniques used to represent the physical boundaries.

3. Although not directly benefiting the formulation of mathematical models, the compilation of physical data on various circulating flows would certainly be instrumental in the development and testing of management models capable of high accuracy simulation.

#### ACKNOWLEDGMENTS

This study was made possible by a National Science Foundation Grant No. CME-7805458. The support of this institution is gratefully acknowledged.

#### APPENDIX I.—REFERENCES

1. Abbott, M. B., and Rasmussen, C. H., "On the Numerical Modeling of Rapid Expansions and Contractions in Models that are Two-Dimensional in Plan," *Paper A104*, 17th Congress of the International Association for Hydraulic Research, Baden-Baden, Germany, Vol. 2, 1977, pp. 229-237.
2. Bengtsson, L., "Wind Induced Circulation in Lakes," *Nordic Hydrology*, Vol. 9, No. 2, Stockholm, Sweden, 1978, pp. 75-94.
3. Flokstra, C., "Generation of Two-Dimensional Horizontal Secondary Currents," *Reports S 163-II*, Delft Hydraulics Laboratory, Delft, The Netherlands, July, 1976.
4. Flokstra, C., "The Closure Problem for Depth-Averaged Two-Dimensional Flow," *Paper A106*, 17th Congress of the International Association for Hydraulic Research, Baden-Baden, Germany, Vol. 2, 1977, pp. 247-256.
5. Forester, C. K., "Higher Order Monotonic Convective Difference Schemes," *Journal of Computational Physics*, Vol. 23, 1977, pp. 1-22.
6. Hansen, W., "Hydrodynamic Methods Applied to Oceanographic Problems," *Proceedings of the Symposium on Mathematical-Hydrodynamical Methods of Physical Oceanography*, Institute für Meereskunde der Universität Hamburg, Hamburg, West Germany, 1962, pp. 25-34.
7. Kuipers, J., and Vreugdenhil, C. B., "Calculations of Two-Dimensional Horizontal Flows," *Report S 163-I*, Delft Hydraulics Laboratory, Delft, The Netherlands, Oct., 1973.
8. Launder, B. E., and Spalding, D. B., "The Numerical Computation of Turbulent Flows," *Computational Methods in Applied Mechanical Engineering*, Vol. 3, 1974, pp. 269-289.

9. Lean, G. H., and Weare, T. J., "Modeling Two-Dimensional Circulating Flow," *Journal of the Hydraulics Division*, ASCE, Vol. 105, No. HY1, Proc. Paper 14312, Jan., 1979, pp. 17-26.
10. Leendertse, J. J., "Aspects of a Computational Model for Long-Period Water Wave Propagation," *RM-5294-PR*, The Rand Corporation, Santa Monica, Calif., May, 1967.
11. Leendertse, J. J., "A Water-Quality Simulation Model for Well-Mixed Estuaries and Coastal Seas, Vol. I, Principles of Computation," *RM-6230-RC*, The Rand Corp., Santa Monica, Calif., Feb., 1970.
12. McGuirk, J. J., and Rodi, W., "A Depth-Averaged Mathematical Model for the Near Field of Side Discharges into Open Channel Flow," *Journal of Fluid Mechanics*, Vol. 86, Part 4, London, England, 1978, pp. 761-781.
13. Platzman, G. W., "A Numerical Computation of the Surge of 26 June 1954 on Lake Michigan," *Geophysics*, Vol. 6, No. 3-4, 1959, pp. 407-438.
14. Ponce, V. M., and Yabusaki, S. B., "Mathematical Modeling of Circulation in Two-dimensional Plane Flow," *Report CER79-80VMP-SBY59*, Civil Engineering Department, Engineering Research Center, Colorado State University, Fort Collins, Colo., June, 1980.
15. Weare, T. J., "Instability in Tidal Flow Computational Schemes," *Journal of the Hydraulics Division*, ASCE, Vol. 102, No. HY5, Proc. Paper 12100, May, 1976, pp. 569-580.

## APPENDIX II.—NOTATION

*The following symbols are used in this paper:*

- $C$  = Chézy resistance coefficient;
- $f_r$  = dimensionless friction factor;
- $g$  = gravitational acceleration;
- $h$  = flow depth;
- $j$  = x-coordinate nodal index;
- $k$  = y-coordinate nodal index;
- $n$  = t-coordinate nodal index;
- $T$  = effective stress;
- $t$  = time;
- $\Delta t$  = time increment;
- $U$  = channel velocity;
- $u$  = velocity component in x-direction;
- $u'$  = temporal velocity fluctuation in x-direction;
- $\bar{u}$  = depth-averaged velocity;
- $\bar{u}^*$  = spatially-averaged velocity;
- $v$  = velocity component in y-direction;
- $\bar{v}$  = depth-averaged velocity;
- $\bar{v}^*$  = spatially-averaged velocity;
- $x$  = coordinate direction;
- $\Delta x$  = space increment in x-direction;
- $y$  = coordinate direction;
- $\Delta y$  = space increment in y-direction;
- $z$  = coordinate direction;
- $z_b$  = bottom elevation;
- $\alpha$  = weighting factor;
- $\epsilon$  = eddy diffusivity;
- $\eta$  = water surface elevation;

- $\nu$  = kinematic viscosity;  
 $\xi$  = Courant number criterion;  
 $\rho$  = fluid density; and  
 $\tau$  = surface stress.



## APPROXIMATE ERROR BOUNDS FOR SIMULATED HYDROGRAPHS

By David C. Garen<sup>1</sup> and Stephen J. Burges,<sup>2</sup> M. ASCE

### INTRODUCTION

One of the more important aspects of watershed modeling is the explicit consideration of uncertainty in model output. The utility of the output of watershed models can be greatly enhanced if it is accompanied by measures of its accuracy. This can be important in model choice, decision-making, engineering design, data collection, and model refinement.

Errors in hydrologic models have been analyzed from many different viewpoints using a variety of approaches. An important topic is the estimation of error bounds on simulated hydrographs produced using complex watershed models. This was the basic objective of the present paper. Specifically, the objective was to test the applicability of first-order uncertainty analysis to a complex watershed model to quantify parameter error propagation and to gain an appreciation of the approximate magnitudes of model output uncertainty caused by different levels of parameter uncertainty. Model output uncertainty due only to parameter uncertainty was analyzed here; the model itself was assumed to be correct.

### PERSPECTIVES ON PROBLEM

A knowledge of the respective predictive accuracies of competing models and the data requirements to achieve these accuracies must be known to choose the model most suitable for a given purpose. Because the many available hydrologic models cover the spectrum from simple to complex—from crude estimates to state-of-the-art accuracy—a decision must be made as to how complex a model is desired; one wishes to use the simplest model that will give hydrologic information with the desired accuracy. One must be aware of the tradeoff that exists between model complexity and accuracy of parameters and input data. As a model becomes more complex, its data and parameter requirements usually

<sup>1</sup>Former Research Asst., Dept. of Civ. Engrg., Univ. of Washington, Seattle, Wash.; now at Envirosphere Co., Bellevue, Wash.

<sup>2</sup>Prof. of Civ. Engrg., Univ. of Washington, Seattle, Wash.

Note.—Discussion open until April 1, 1982. To extend the closing date one month, a written request must be filed with the Manager of Technical and Professional Publications, ASCE. Manuscript was submitted for review for possible publication on April 14, 1980. This paper is part of the Journal of the Hydraulics Division, Proceedings of the American Society of Civil Engineers, ©ASCE, Vol. 107, No. HY11, November, 1981. ISSN 0044-796X/81/0011-1519/\$01.00.

become greater. If the extensive data needed to support a complex model are unavailable, better results can probably be achieved using a simpler model. Clearly, an optimum exists that trades off the greater potential output accuracy from a complex model with the parsimony and greater accuracy of parameters and input data using a simple model.

Errors in the results obtained from watershed models have four basic sources: (1) Errors in input precipitation and evaporation data; (2) errors in streamflow data; (3) errors in parameter values; and (4) inadequate representation by the model. Errors in the input data are caused by various inaccuracies involved in measuring rainfall and evaporation and by the estimation of areal values from point measurements. These errors can be either random or systematic. Streamflow data also suffer from inaccuracies in measurement; thus, flow data for calibration and verification of simulated flows are error-contaminated. The values of model parameters always contain error caused by incomplete or inaccurate information. One cause of poor parameter estimates is calibration with error-laden streamflow data. Another problem is that some parameters, rather than being physically measurable quantities, such as impervious area, are only indices to physical quantities such as upper zone storage capacity, thereby making their estimation difficult. Error due to model unrepresentativeness is a significant source of output uncertainty but is extremely difficult to evaluate. It is a result of the inevitable empiricisms, approximations, and simplifications that make the model an inexact representation of watershed processes. Determining what portion of the nonagreement between simulated and recorded flows that is actually attributable to the model itself and how much is attributable to other error sources is a difficult task and may only be possible for phenomena that can be replicated in the laboratory. Nevertheless, such error is unavoidable and will be present even with perfect data.

#### PREVIOUS WORK

The problem of uncertainty in hydrologic models has not been neglected in the literature. Various aspects of the issue have been examined using a number of approaches and techniques.

The most common measure of error is a goodness-of-fit criterion obtained by comparing simulated and recorded hydrographs. One of the more frequently used measures is the sum of squared differences between simulated and recorded flow values. Typically, this is the objective function to be minimized during calibration. Other objective functions can also be used, depending on the modeling objective (12,14). Another set of measures of the degree of similarity between simulated and recorded hydrographs is the several types of correlation coefficient, which are analogous to linear regression (1,18). Another idea for comparing hydrographs is the approach taken by Amoroch and Espildora (2) using the concept of entropy in the information theory sense. The one thing in common among these approaches to the measurement of uncertainty is that they are all derived from the comparison of simulated and recorded flows. If the historical flow record is representative of a wide range of watershed responses and is of sufficient length to constitute a statistically significant sample, such measures of uncertainty might be extrapolated to estimate uncertainty in subsequent model predictions. If, however, the historical flow record is not representative or lengthy,

simple goodness-of-fit measures of uncertainty may not be adequate to estimate the uncertainty associated with model predictions.

Many empirical studies have been undertaken to attempt to estimate the accuracy of hydrologic model output. Dawdy, et al. (12) have conducted fairly extensive studies of the effects of errors in rainfall and streamflow data on the accuracy of streamflow simulations and parameter estimates. Similar studies can be found in Dawdy (11), Dawdy and O'Donnell (13), and Dawdy and Thompson (14). Salomonson, et al. (23) and Yeh, et al. (24) have conducted parameter perturbation sensitivity analyses using, respectively, the Kentucky version of the Stanford Watershed Model and the Generalized Streamflow Simulation System of the Sacramento office of the National Weather Service. Using the technique of introducing error into assumed error-free data, Ibbitt (17) studied the effects of random errors in precipitation, evaporation, and streamflow data on parameter values. Also using this technique, Parmele (20) examined the effects of error in potential evapotranspiration data on simulated hydrographs. While not giving a broadly applicable set of methods or conclusions, these empirical studies are useful for obtaining an idea of the approximate magnitudes and the more important causes and effects of errors that can occur in hydrologic simulations.

First-order uncertainty analysis (described in more detail later) is a useful tool for approximating error as it propagates through a model. Although it can be used in diverse applications, some examples of its use in water resources include Burges and Lettenmaier (7), Esen and Rathbun (16), Cornell (9), and Coleman and DeCoursey (8). Although this is not an exhaustive list of published works using first-order analysis, these examples have shown that first-order analysis can be a useful and convenient technique for estimating error bounds in water resource phenomena.

Others who have addressed the issue of uncertainties in hydrologic modeling include Mein and Brown (19), Wood (25), and Bras and Rodriguez-Iturbe (6). Mein and Brown studied the issue of parameter sensitivity. While their study was not directly involved with the determination of model output uncertainty, many of their results and conclusions were closely related to the topic. Wood gave an analytical derivation of the effects of uncertainty in the infiltration parameter in Eagleson's (15) kinematic wave flood frequency model. The limitation of the approach, however, is that many deterministic watershed models are more complex than the one Wood used, and it appears likely that his approach would become intractable for even a moderately complex model. Bras and Rodriguez-Iturbe used linear filtering theory with a kinematic wave runoff model to calculate the mean discharge and mean square error of discharge, where rainfall input was not known with certainty. This is one of the few reported studies in which error bounds for entire hydrographs were determined.

## **PRESENT STUDY**

### **Procedures**

**The Model.**—The model chosen for this study was the Stanford Watershed Model (SWM) [Crawford and Linsley (10)] because it is a representative, well-known, and widely used complex model. A simplified version (with evaporation ignored) of the LAND subroutine of the SWM was used. Being the runoff generating mechanism, the LAND subroutine represents the majority of the

watershed processes to be modeled. Even with the simplifications of excluding evaporation and channel routing, the version used is sufficiently complex to test the applicability of first-order analysis and to determine the magnitudes of output uncertainty caused by uncertainty in parameter values. The model used contained 12 parameters and required specification of six initial water storage values. These quantities are listed in Table 1. This simplified version of the SWM is set up as an event model. The maximum precipitation duration is 24 hr, and the simulations are effected for a period of time equal to 1.6 times the number of hours of precipitation or for a period of 5 hr, whichever is longer.

TABLE 1.—Model Parameters and Water Storage Variables

Definition of Terms
(a) Parameters
K1 = raingage scaling factor
A = impervious fraction
UZSN = upper zone storage nominal capacity, in inches
LZSN = lower zone storage nominal capacity, in inches
CB = infiltration index
CC = interflow index
KV = variable groundwater recession parameter
L = overland flow length, in feet
SS = overland flow slope
NN = Manning's $n$ for overland flow
IRC = interflow recession constant
KK24 = daily groundwater recession constant
(b) Water storage variables
UZS = upper zone storage
LZS = lower zone storage
SGW = groundwater storage
GWS = antecedent groundwater inflow index (groundwater slope)
RES = surface detention storage
SRGX = interflow detention storage
Note: 1 in. = 25.4 mm; 1 ft = 0.305 m.

**First-Order Uncertainty Analysis.**—A brief description of first-order uncertainty analysis will be given here; more complete discussions appear in Benjamin and Cornell (4) and Cornell (9). First-order analysis is useful in obtaining approximate means and variances for random variables; the basis of the approximation is a truncated (after the first two terms) Taylor series expansion of the function  $Y = g(x_1, x_2, \dots, x_n)$  such that

$$E[Y] = g(\mu_{x_1}, \mu_{x_2}, \dots, \mu_{x_n}) \dots \dots \dots (1)$$

$$\text{Var}[Y] = \sum_{i=1}^n \sum_{j=1}^n \frac{\partial g}{\partial x_i} \bigg|_{\mu_{x_i}} \frac{\partial g}{\partial x_j} \bigg|_{\mu_{x_j}} \text{Cov}[x_i, x_j] \dots \dots \dots (2)$$

or, if the  $x_i$  are uncorrelated,

$$\text{Var}[Y] = \sum_{i=1}^n \left( \frac{\partial g}{\partial x_i} \bigg|_{\mu_{x_i}} \right)^2 \text{Var}[x_i] \dots \dots \dots (3)$$

in which  $\mu_{x_i}$  = the mean value of parameter  $x_i$ . This is a reasonable approximation if the coefficients of variation (standard deviation/mean) of the  $x_i$  are not large and if the function  $g$  is approximately linear; the relationships are exact if the function is linear. (The degree of nonlinearity that can be accommodated must be determined on a case-by-case basis.)

In many engineering problems, only the means and variances of the parameters are known with any accuracy; the complete distributions are often unknown. Also, in many applications it is not necessary for the purposes of the analysis to carry the complete distributions through the calculations; estimates of the means and variances of the calculated values are sufficient. In such situations, first-order analysis is a relatively simple, easy-to-use method for quantifying uncertainty as it propagates through a set of calculations.

Note that, in a modeling application, the first-order approximation to the mean output simply involves running the model with the mean values of the parameters. This is the standard procedure for the use of hydrologic models. Parameters are estimated through the calibration process, and the model is run using these mean parameter values. Wood (25) has pointed out, however, that in a nonlinear system (as watersheds inevitably are), this procedure gives incorrect values for the mean output, i.e.,  $g(E[x]) \neq E[g(x)]$ . The left side of the inequality represents the standard modeling procedure, whereas the right side is what is really desired. As will be shown later, these two values can be significantly different in situations where watershed response is highly nonlinear. For many applications, though, these two quantities are in close enough agreement to make the first-order approximation satisfactory.

Even for a moderately complex model, it is usually impossible to obtain analytical expressions for the partial derivatives needed for the first-order equations. The derivatives can, however, be approximated conveniently via finite differences, which was the procedure used here.

Means and standard deviations for the model parameters and initial values of the water storages were chosen. The model was initially run using the mean parameter values (Eq. 1) with the test precipitation data to obtain the first-order approximation to the mean watershed response. The model was then rerun repeatedly, incrementing each parameter one at a time by a small amount ( $\Delta x = 0.05 \mu_x$  was used here). After each perturbation the affected parameter was returned to its mean value. The change in output due to a change in parameter value,  $\Delta Q/\Delta x$ , is an approximation of the partial derivative of the model with respect to the parameter. In an attempt to obtain better estimates of the partial derivatives, two perturbations of each parameter were made,  $x + \Delta x$  and  $x - \Delta x$ . The two estimates of each partial derivative thus obtained were then averaged. Partial derivatives were calculated for each hour of the simulation. After the model had been rerun for all uncertain parameters, the calculation in Eq. 3 (the parameters were assumed to be mutually independent) was performed to obtain the variance for each hourly flow, thus giving approximate error bounds on the hydrograph (mean flows) due to uncertainty in the parameters. A similar

calculation was done to obtain the variance for the total runoff volume for the storm.

**Monte Carlo Analysis.**—To check the accuracy and validity of the first-order analysis, Monte Carlo parameter sampling was used with the runoff calculations to determine approximate true means and variances of model output. Because it is often the case that in parameter estimation only bounds can be specified rather than distinct distributions, a uniform distribution was assumed for the Monte Carlo sampling. The procedure involved running the model repeatedly, each run containing a new set of randomly sampled parameters. At the end of the model runs, means and variances of all the simulated hourly flow values and of the total storm runoff volume were calculated. A sample size of 300 was chosen for the majority of the Monte Carlo simulations; this moderate sample size was adequate because only the means and variances, and not the entire probability distributions, of the flow values were required.

As stated earlier, the parameters were assumed to be mutually independent. This is not strictly true for the SWM. By inspection, most of the parameters can be seen to be independent, but Crawford and Linsley (10) state that three of the parameters—UZSN, LZSN, and CB—are interrelated. The assumption of independence was tested in the Monte Carlo analysis by making two simulations for a number of different sets of conditions, one assuming independence among all parameters and one with assumed correlations among UZSN, LZSN, and CB. To test the effects of the worst case, the intercorrelations were assumed to be 1.0. Because only three parameters are intercorrelated, it was found, as expected, that there was little difference in output uncertainty between the simulations that had intercorrelations and those that assumed independence among the parameters. Also because in reality the intercorrelations are less than 1.0, the assumption of independence is acceptable.

The effects of the choice of distribution for the parameters was also tested in the Monte Carlo analysis. Several simulations were made first assuming uniform and then assuming normal distributions. It was found that there was little difference in the means and variances of each hourly flow value obtained using the two distributions but that there was a significant difference in the distribution of these flow values. Not surprisingly, parameters sampled from a uniform distribution produced roughly uniformly distributed output values, and normally distributed parameters produced prominently peaked output distributions. Because either distribution could be argued to be appropriate, because these two distributions gave similar output means and variances, and because only the output means and variances were needed to verify the first-order estimates, the uniform distribution was used throughout the Monte Carlo analysis.

**Test Data Used.**—Nine different storm patterns were used in the simulations (Table 2). Because it makes no difference here whether historical precipitation data are used, the storms were fabricated to provide a range of precipitation durations and intensities. A basic set of parameter values was used for the majority of the analysis (Table 3). These values were chosen using guidelines from Crawford and Linsley (6) and judgment as to what might constitute a "typical" set of values. A few simulations were made using values different from those appearing in Table 3, but they did not vary greatly from the basic values. Three sets of initial watershed conditions (initial values of the water storage variables) were used in the analysis (Table 4). These values were chosen

TABLE 2.—Precipitation Data Used in Simulations, in Inches (Millimeters)

Storm (1)	Hour									
	First (2)	Second (3)	Third (4)	Fourth (5)	Fifth (6)	Sixth (7)	Seventh (8)	Eighth (9)	Ninth (10)	Tenth (11)
A	0.2 (5.1)									
B	1.0 (25.4)									
C	3.0 (76.2)									
D	0.2 (5.1)	0.5 (12.7)	0.3 (7.6)	0.04 (1.0)						
E	0.2 (5.1)	0.2 (5.1)	0.2 (5.1)	0.2 (5.1)	0.2 (5.1)	0.2 (5.1)				
F	0.05 (1.3)	0.4 (10.2)	0.3 (7.6)	0.8 (20.3)	0.6 (15.2)	0.1 (2.5)				
G	0.3 (7.6)	0.9 (22.9)	1.75 (44.5)	0.4 (10.2)	0.97 (24.6)	0.45 (11.4)	0.1 (2.5)	0.5 (12.7)		
H	0.4 (10.2)	0.1 (2.5)	0.02 (0.51)	0.3 (7.6)	0.18 (4.6)	0.7 (17.8)	0.1 (2.5)	0.07 (1.8)	0.05 (1.3)	0.03 (0.76)
I*	0.2 (5.1)	0.2 (5.1)	0.2 (5.1)	0.2 (5.1)	0.2 (5.1)	0 (0)	0 (0)			

\*The sequence shown for storm I was repeated twice to give a 19-hr storm.

TABLE 3.—Basic Set of Parameter Values

K1 (1)	A* (2)	UZSN (3)	LZSN (4)	CB (5)	CC (6)	KV (7)	L (8)	SS (9)	NN (10)	IRC (11)	KK24 (12)
1	0	1.4	14	0.5	2	0.5	200	0.1	0.2	0.65	0.99

\*A = 0 was used initially to attempt to isolate the effects of the natural watershed processes from the complicating factor of impervious area; later, A = 0.1 was used.

TABLE 4.—Initial Values of Water Storage Variables, in Inches (Millimeters)

Initial conditions (1)	Variables					
	UZS (2)	LZS (3)	SGW (4)	GWS (5)	RES (6)	SRGX (7)
Dry	0	7 (177.8)	1.8 (45.7)	0.5 (12.7)	0	0
Medium	0.7 (17.8)	10 (254.0)	2.0 (50.8)	1.0 (25.4)	0.1 (2.5)	0.8 (20.3)
Wet	1.2 (30.5)	16 (406.4)	2.0 (50.8)	1.5 (38.1)	0.3 (7.6)	1.2 (30.5)



taking into account the ratio of storage contents to capacity. This primarily concerns UZS/UZSN and LZS/LZSN because these two ratios are important factors in the model equations. The values of the other storage variables were chosen to be consistent with the values of the above two ratios, considering

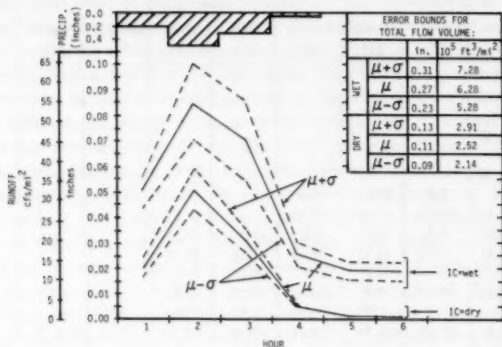


FIG. 1.—Channel Inflow Hydrographs for Storm D, Wet and Dry Initial Conditions, CV of All Parameters = 0.10 (CV of KK24 = 0), Showing 1 Standard Deviation Error Bounds.  $\mu$  = Mean Flow;  $\sigma$  = Standard Deviation of Flow. 1 in. = 25.4 mm; 1 cfs/sq mile =  $1.093 \times 10^{-2} \text{ m}^3/\text{s}/\text{km}^2$

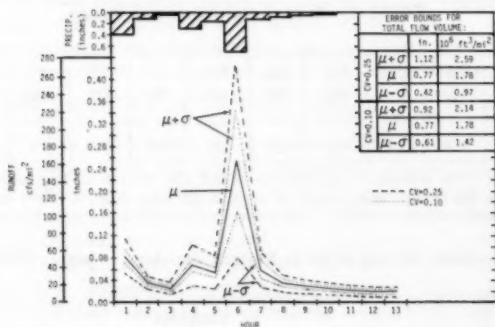


FIG. 2.—Channel Inflow Hydrograph for Storm H, Wet Initial Conditions, CV of All Parameters = 0.10 and 0.25 (CV of KK24 = 0), Showing 1 Standard Deviation Error Bounds.  $\mu$  = Mean Flow;  $\sigma$  = Standard Deviation of Flow. 1 in. = 25.4 mm; 1 cfs/sq mile =  $1.093 \times 10^{-2} \text{ m}^3/\text{s}/\text{km}^2$

also the roles of the variables in the equations. The coefficients of variation (CV's) of the parameters varied from 0.0–0.6 in the simulations. A CV of 0.6 represents a large uncertainty and is probably larger than what might normally be encountered; CV's in the range 0.0–0.25 are more typical. The initial storage



values were assumed to be known with certainty because the immediate goal was to determine the effects of parameter uncertainty. In an event simulation using recorded data, the choice of initial conditions is important to the results of the simulation, but unfortunately is subjective, judgmental, and sometimes difficult to make.

## Results

**Monte Carlo Analysis.**—Generally, the Monte Carlo simulations showed that uncertainty in hourly flows increased with increasing precipitation intensity and duration (with parameter uncertainty held constant) and (obviously) increased with increasing parameter uncertainty (with the same precipitation). Larger uncertainties occurred for wet initial conditions than for dry except for heavy precipitation, when the uncertainty for dry initial conditions became large. The magnitudes of the CV's of hourly flow values varied, in the cases tested, from near zero for light precipitation and low parameter uncertainty to greater than one for heavy precipitation, dry initial conditions, and large uncertainty in sensitive parameters. The maximum CV of hourly flow values in the simulations usually fell in the range 0.2–0.8. A sample of the results from the Monte Carlo simulations is depicted graphically in Figs. 1 and 2. (The mean hydrograph in Fig. 2 is the average of the mean hydrographs for the two uncertainty levels shown; the two mean hydrographs are actually slightly different in magnitude.) These figures show mean hydrographs with one standard deviation error bounds. Although the coefficient of variation is a normalized measure of uncertainty and is useful for making comparisons among flows with different mean levels, it is not the most useful statistic in practical applications. The standard deviation is more valuable in this capacity because it gives the error in terms of actual flow values. It is the standard deviation error bounds, shown in Figs. 1 and 2, that are the primary end product of the uncertainty analyses described in this paper.

Many additional hydrographs and their associated parameter uncertainty corresponding to the combinations shown in Tables 5 and 6 were obtained. Typically, K1 and UZSN, the rainfall weighting factor and upper zone soil moisture capacity, respectively, were found to influence the levels of the mean simulated runoff responses significantly. As the uncertainty level associated with fixed levels of K1 and UZSN was increased, the output uncertainty increased much more noticeably than when uncertainty in other parameters was increased over the same range. While not shown here, simulated hydrograph uncertainty was influenced more by these two parameters than uncertainty in any other parameter or combinations of parameters. L, SS, and NN can, under some conditions, cause substantial output uncertainty, but this is only when overland flow occurs; otherwise, their effects are essentially zero. LZSN, CB, and CC are fairly insensitive parameters and cause significant output certainty only under extreme conditions—heavy precipitation, dry initial conditions, and high parameter uncertainty. Uncertainty in the recessions was small when the recession constants were assumed to be known with certainty, but it was significant in many cases where KV and IRC were uncertain. Uncertainty in the total storm runoff volumes, shown in Figs. 1 and 2, was somewhat smaller than the uncertainty in the peak flow and the maximum CV of hourly flows.

It is instructive to compare the results of this analysis with the results of

TABLE 5.—Comparison of First-

Case (1)	CV of indicated parameters (2)	Dry Initial Conditions			
		Storm B (3)	Storm C (4)	Storm D (5)	Storm H (6)
1	0.1 (K1)		0.84 0.97 G		
2	0.5 (K1)		0.30 0.73 P		
3	0.1 (UZSN)	1.00 1.00 G	0.88 0.87 M		
4	0.3 (UZSN)		0.41 0.56 P		
5	0.1 (LZSN)		1.00 1.00 G		
6	0.5 (LZSN)		0.98 1.11 G		
7	0.4 (CB)		0.99 1.01 G		
8	0.5 (CC)		1.00 1.04 G		
9	0.1 (K1, UZSN)		0.78 0.86 M		
10	0.1 (UZSN, LZSN)				
11	mixed				0.89 0.53 M 0.94 0.75 M
12	mixed				0.95 0.85 G 0.98 0.91 G
13	0.1 (all param- eters)			1.01 0.90 G 1.01 0.90 G	1.00 1.03 G 1.01 1.03 G
14	0.25 (all param- eters)			1.01 0.95 G 1.00 0.95 G	0.95 0.72 M 0.99 0.87 G

Note:  $a \rightarrow$   $\begin{matrix} 0.00 & X & 0.00 \\ 0.00 & & 0.00 \end{matrix}$   $\leftarrow c$   
 $b \rightarrow$   $\begin{matrix} 0.00 & & 0.00 \\ 0.00 & & 0.00 \end{matrix}$   $\leftarrow d$   
 $\uparrow$   $\uparrow$   
 $e$   $f$

$a$  = Ratio of first-order approximation of mean of peak flow to Monte Carlo simulation

$b$  = Ratio of first-order approximation of standard deviation of peak flow to Monte

$c$  = Same as  $a$  but for total storm runoff volume;

$d$  = Same as  $b$  but for total storm runoff volume;

$e, f$  = Descriptive categorization of the goodness of the first-order approximations  
 gories were arbitrarily chosen based on the deviations of ratios  $a$ ,  $b$ ,  $c$ , and  $d$  from  
 For entries with only one set of values, notes  $a$ ,  $b$ , and  $e$  apply.

## Order and Monte Carlo Simulations

Wet Initial Conditions					
Storm B (7)	Storm C (8)	Storm D (9)	Storm E (10)	Storm H (11)	Storm I (12)
0.98 G 0.98 G 0.69 M 0.73 M 0.93 M 0.85 M 0.46 P 0.39	0.98 G 0.98 G 0.89 M 1.14 M 0.98 G 0.98 G 0.88 G 1.04		0.96 G 0.95		1.01 G 0.98
0.90 M 0.84				0.70 M 1.06 M 0.81 M 0.97 M 0.89 G 0.91	0.76 M 0.79 M 0.90 G 0.97 G 0.94 G 0.95
		0.96 G 0.84 0.77 P 0.48	0.96 G 0.87 0.80 P 0.59	0.77 M 1.03	0.84 M 0.94

of mean of peak flow;

Carlo simulation of standard deviation of peak flow;

for peak flow and volume, respectively: G = good; M = medium; P = poor. (Cate-  
unity.)

Bras and Rodriguez-Iturbe (6) mentioned earlier. Because the CV of precipitation input (parameter K1) here was never greater than 0.5, the output uncertainties calculated were generally of a lesser magnitude than those of Bras and Rodriguez-Iturbe, who considered much larger uncertainties in precipitation. The largest uncertainties did occur in the peak, or very near it, and rising limb of the hydrograph, in agreement with Bras and Rodriguez-Iturbe, who used a different model.

**First-Order Uncertainty Analysis.**—A first-order uncertainty analysis was performed a number of times for situations identical to some of the Monte Carlo simulations. The Monte Carlo results were used as the basis for comparison in analyzing the first-order results. A comparison of first-order and corresponding Monte Carlo results appears in Tables 5 and 6; the closer the numerical values in Table 5 are to unity, the better are the first-order approximations to the mean and standard deviation of model output for the given conditions.

Both means and standard deviations tended to be underestimated by first-order analysis. This is not surprising. Because the first-order approximations are truncated Taylor series expansions, one would expect the loss of the higher

TABLE 6.—Explanation of Parameter Values and Uncertainties for Table 5

Case (1)	K1 (2)	A (3)	UZSN (4)	LZSN (5)	CB (6)	CC (7)	KV (8)	L (9)	SS (10)	NN (11)	IRC (12)	KK24 (13)
13	0.2	0.15	0.36	0.29	0.2	0.2	0.4	0.13	0.1	0.05	0.08	0
14	0.3	0.1	0.14	0.14	0.15	0	0	0	0	0	0	0
15	0.1	0.1	0.1	0.1	0.1	0.1	0.1	0.1	0.1	0.1	0.1	0
16	0.25	0.25	0.25	0.25	0.25	0.25	0.25	0.25	0.25	0.25	0.25	0

Note: Cases 1-12: All parameters are known with certainty except the one(s) noted in column 2 of Table 5. Basic parameter values (Table 3) are used, with A = 0.

Cases 13-16: Basic parameter values (Table 3) are used, with A = 0.1. The coefficients of variation used are given above.

order terms to cause an underestimation. In some cases, the mean and standard deviation were underestimated or overestimated in approximately equal proportions so that the CV was estimated to be nearly the same as for the corresponding Monte Carlo simulation.

The applicability of first-order analysis can be determined from Table 5. The limit of parameter uncertainty that still gives good first-order approximations depends heavily on parameter sensitivity. It can be seen that for the two most sensitive parameters, K1 and UZSN, CV's in excess of about 0.25 caused unsatisfactory approximations, especially under the extreme conditions of heavy precipitation (storm C) on a dry watershed (e.g., cases 2 and 4). The model responds in a highly nonlinear fashion under these conditions, making the first-order approximations less valid. Under nonextreme conditions or for CV's of K1 and UZSN less than 0.25, however, the approximation did quite well (e.g., cases 1, 3, and 13). For less sensitive parameters, such as LZSN, CB, and CC, the approximation was fairly robust and was able to handle extreme conditions and high degrees of uncertainty (e.g., cases 5-8). For light precipitation,

such as storm A, the first-order approximations are for all purposes equal to the Monte Carlo values. Had these cases been included in Table 5, all of the ratios would have been 1.00 or close to it.

#### OBSERVATIONS

First-order analysis requires  $2n + 1$  model evaluations in which  $n$  = the number of uncertain parameters, as compared to the much larger number of evaluations (300 in this study) needed for a Monte Carlo analysis. At the risk of some loss of goodness of the approximations, the  $2n + 1$  could be reduced to  $n + 1$  if one were willing to be satisfied with only one estimate of the partial derivatives for each parameter instead of an average of two estimates. Whichever way is used, first-order analysis allows a large reduction in the computational effort required to estimate output uncertainty as opposed to the only other available method at this time, Monte Carlo analysis.

It should be realized that first-order analysis, as used here, is an extension and formalization of traditional perturbation techniques for sensitivity analysis. There are numerous examples in the literature (e.g., Salomonson, et al. (23) and Yeh, et al. (24) discussed earlier) of the sensitivity of parameters being tested by changing their values one at a time by some small amount, rerunning the model, and noting the resultant change in output. First-order analysis goes through a similar procedure systematically and translates the results into standard deviations for output values. It should also be noted that standard model applications, which typically use single estimated parameter values for the simulations, amount to a first-order analysis without the standard deviation calculations.

It has been assumed throughout this analysis that CV's for uncertain parameters could be estimated. Determining CV's, however, may at times be difficult. The estimation is largely subjective, especially for the parameters that are not measures of actual physical characteristics of the watershed. It should be easiest to estimate CV's for A, L, and SS, since topographic maps or aerial photographs used to estimate the mean parameter values can also be used to estimate uncertainty in the chosen mean values, based on the quality of the maps and pictures and on how well the mean values can be judged from amidst the spatial variability. NN is a bit more difficult since it is an index rather than a measurable quantity. Information does exist in the literature on estimating Manning's  $n$  (3) to supplement information from photographs or field trips. Estimates of uncertainty for KV, IRC, and KK24 should not be of great difficulty because these could be determined subjectively considering the quality of the discharge records and the representativeness of the mean parameter values, which are obtained by classical hydrograph analysis. UZSN, LZSN, CB, and CC are not physical quantities but are indices of soil characteristics; their values are determined primarily during calibration. Estimation of uncertainty for these parameters poses a more difficult problem than for the other parameters. The only way to determine uncertainties for these is subjectively to meld together knowledge of the quality of the calibration and knowledge of the watershed. For example, if the calibration results in only a relatively poor replication of historical streamflows, large standard deviations for these parameters would be in order. Also, if it is known that the watershed has a high spatial variability

in soil infiltration and moisture capacity characteristics, or if little is known about the soil characteristics, large parameter standard deviations would again be appropriate. Uncertainty in  $K_1$  can also be difficult to estimate, but problems in estimating area precipitation have received some significant attention (5,6,21, 22). All of the various factors causing uncertain areal precipitation estimates—type of gage, representativeness of its location, its distance from the water-shed, the quality of record, topographic relief, prevailing storm types, wind, number of gages used to estimate areal precipitation—must be combined to give an estimated CV for  $K_1$ . The techniques given in the literature can be used if accurate and systematic estimation of precipitation uncertainty is required; otherwise, subjective judgment could be used to estimate this CV.

Although evaporation was not considered in this analysis, this is not to say it is unimportant. Inclusion of evaporation, whether or not it is assumed to be known with certainty, will change the mean simulated runoff and the values of the water storage variables. The latter change is the more significant in terms of an uncertainty analysis since the level of output uncertainty is highly dependent on the values of the water storage variables. Evaporation will cause the variables to have smaller values (be "drier") than it would otherwise, which can cause a change in the uncertainty of the output with the same precipitation, parameter values, and parameter uncertainties. Of course, inclusion of evaporation also introduces another source of output error that, in some situations, can be significant (20).

It should also be kept in mind that the runoff simulations in this analysis did not include channel routing. It can be expected that the error bounds calculated here would be attenuated somewhat if channel routing were included.

## CONCLUSIONS

By far, the most sensitive parameters, i.e., those having the greatest effect on the mean and standard deviation of simulated hydrographs, of the simplified version of the SWM used herein are  $K_1$  and UZSN. This result can also be expected to hold true for the complete model, although it is conceivable, under some circumstances, that channel flow parameters might be as influential as  $K_1$  and UZSN in estimating hydrographs. The infiltration and interflow parameters—LZSN, CB, and CC—are quite insensitive during the time frame of a single storm event. These parameters are concerned with longer-term runoff volumes; their influences can be expected to be felt in monthly or yearly simulations. A similar argument can be stated for the recession constants—KV, IRC, and KK24. Their effects in event simulations can be considered to be small, but they could be important in longer simulations. The overland flow parameters—L, SS, and NN—are also fairly insensitive, except during very heavy precipitation. For storms or in watersheds where no overland flow occurs, these parameters, of course, have no effect. The impervious fraction  $A$  can be a sensitive parameter if a significant portion of the watershed is impervious, i.e., greater than about 10%. The SWM, however, has only a crude representation of the dynamics of flow from impervious areas. If the watershed to be modeled had significant impervious area, the SWM should probably not be used; a model containing a better representation of urban-area runoff would be desirable.

First-order uncertainty analysis was found to be applicable to a complex model

under certain conditions. For first-order approximations applied to the SWM to be satisfactory, the CV's of the sensitive parameters should be no greater than about 0.25, with a little greater uncertainty tolerable for low intensity storms and a little less for high intensity storms; the upper range of the CV's is, therefore, in the vicinity of 0.2-0.3. The other, less sensitive, parameters can have larger uncertainties, and the first-order approximations will still be satisfactory.

First-order analysis should therefore be applicable in most situations, in which the CV's of the parameters will probably be less than about 0.2. If the parameter uncertainties are large enough to cause first-order analysis to be a poor approximation to output means and standard deviations, the (true) output uncertainty will likely be too large to give acceptable results for the application, and a simpler model should probably be used.

### SUMMARY

Conditions for propagating model parameter errors via a first-order analysis have been examined. The analysis was performed at each time step for which a simulated output (streamflow rate) was estimated. Thus for any storm and initial moisture zone conditions an estimate of the uncertainty in simulated streamflow was available for each time increment. Based upon storm types and initial moisture contents examined here, it is clear that different streamflow uncertainty levels can be expected at different times of the year in any catchment. While the findings given here were developed for the SWM, the method should be applicable to all complex moisture accounting rainfall-runoff models.

### APPENDIX.—REFERENCES

1. Aitken, A. P., "Assessing Systematic Errors in Rainfall-Runoff Models," *Journal of Hydrology*, Vol. 20, No. 2, Oct., 1973, pp. 121-136.
2. Amorocho, J., and Espildora, B., "Entropy in the Assessment of Uncertainty in Hydrologic Systems and Models," *Water Resources Research*, Vol. 9, No. 6, Dec., 1973, pp. 1511-1522.
3. Barnes, H. A., Jr., "Roughness Characteristics of Natural Channels," *USGS Water Supply Paper 1849*, U.S. Geological Survey, Washington, D.C., 1967.
4. Benjamin, J. R., and Cornell, C. A., *Probability, Statistics and Decision for Civil Engineers*, McGraw-Hill Book Co., Inc., New York, N.Y., 1970.
5. Bras, R. L., and Rodriguez-Iturbe, I., "Evaluation of Mean Square Error Involved in Approximating the Areal Average of a Rainfall Event by a Discrete Summation," *Water Resources Research*, Vol. 12, No. 2, Apr., 1976, pp. 181-184.
6. Bras, R. L., and Rodriguez-Iturbe, I., "Rainfall Network Design for Runoff Prediction," *Water Resources Research*, Vol. 12, No. 6, Dec., 1976, pp. 1197-1208.
7. Burges, S. J., and Lettenmaier, D. P., "Probabilistic Methods in Stream Quality Management," *Water Resources Bulletin*, Vol. 11, No. 1, Feb., 1975, pp. 115-130.
8. Coleman, G., and DeCoursey, D. G., "Sensitivity and Model Variance Analysis Applied to Some Evaporation and Evapotranspiration Models," *Water Resources Research*, Vol. 12, No. 5, Oct., 1976, pp. 873-879.
9. Cornell, C. A., "First-Order Analysis of Model and Parameter Uncertainty," *Proceedings, International Symposium on Uncertainties in Hydrologic and Water Resource Systems*, Vol. 3, Tucson, Ariz., Dec., 1972, pp. 1245-1274.
10. Crawford, N. H., and Linsley, R. K., "Digital Simulation in Hydrology: Stanford Watershed Model IV," *Technical Report 39*, Dept. of Civ. Engrg., Stanford Univ., Palo Alto, Calif., 1966.

11. Dawdy, D. R., "Considerations Involved in Evaluating Mathematical Modeling of Urban Hydrologic Systems," *USGS Water Supply Paper 1591-D*, U.S. Geological Survey, Washington, D.C., 1969.
12. Dawdy, D. R., Lichty, R. W., and Bergmann, J. M., "A Rainfall-Runoff Simulation Model for Estimation of Flood Peaks for Small Drainage Basins," *USGS Professional Paper 506-B*, U.S. Geological Survey, Washington, D.C., 1972.
13. Dawdy, D. R., and O'Donnell, T., "Mathematical Models of Catchment Behavior," *Journal of the Hydraulics Division, ASCE*, Vol. 91, No. HY4, Proc. Paper 4410, July, 1965, pp. 123-137.
14. Dawdy, D. R., and Thompson, T. H., "Digital Computer Simulation in Hydrology," *Journal of the American Water Resources Association*, Vol. 59, No. 6, 1967, pp. 685-688.
15. Eagleson, P. S., "Dynamics of Flood Frequency," *Water Resources Research*, Vol. 8, No. 4, Aug., 1972, pp. 878-898.
16. Esen, I. I., and Rathbun, R. E., "A Stochastic Model for Predicting the Probability Distribution of the Dissolved-Oxygen Deficit in Streams," *USGS Professional Paper 913*, U.S. Geological Survey, Washington, D.C., 1976.
17. Ibbitt, R. P., "Effects of Random Data Errors on the Parameter Values for a Conceptual Model," *Water Resources Research*, Vol. 8, No. 1, Feb., 1972, pp. 70-78.
18. McCuen, R. H., and Snyder, W. M., "A Proposed Index for Comparing Hydrographs," *Water Resources Research*, Vol. 11, No. 6, Dec., 1975, pp. 1021-1024.
19. Mein, R. G., and Brown, B. M., "Sensitivity of Optimized Parameters in Watershed Models," *Water Resources Research*, Vol. 14, No. 4, Apr., 1978, pp. 299-303.
20. Parmele, L. H., "Errors in Output of Hydrologic Models Due to Errors in Input Potential Evapotranspiration," *Water Resources Research*, Vol. 8, No. 2, Apr., 1972, pp. 348-359.
21. Rodriguez-Iturbe, I., and Mejia, J. M., "The Design of Rainfall Networks in Time and Space," *Water Resources Research*, Vol. 10, No. 4, Aug., 1974, pp. 713-728.
22. Rodriguez-Iturbe, I., and Mejia, J. M., "On the Transformation of Point Rainfall to Areal Rainfall," *Water Resources Research*, Vol. 10, No. 4, Aug., 1974, pp. 729-735.
23. Salomonson, V. V., et al., "Remote Sensing Requirements as Suggested by Watershed Model Sensitivity Analyses," *Proceedings of the Tenth International Symposium on Remote Sensing of Environment*, Ann Arbor, Mich., Vol. 2, Oct., 1975, pp. 1273-1284.
24. Yeh, W. W-G., Becker, L., and Sohn, R. L., "Information Requirements for Improving Hydropower," *Journal of the Water Resources Planning and Management Division, ASCE*, Vol. 104, No. WR1, Proc. Paper 14165, Nov., 1978, pp. 139-156.
25. Wood, E. F., "An Analysis of the Effects of Parameter Uncertainty in Deterministic Hydrologic Models," *Water Resources Research*, Vol. 12, No. 5, Oct., 1976, pp. 925-932.



## SWMM MODEL AND LEVEL OF DISCRETIZATION

By Nabil A. Zaghoul<sup>1</sup>

### INTRODUCTION

Effective disposition of storm water is essential. Drainage systems have changed from primitive ditches to complex networks of curbs, gutters, and surface and underground conduits. Along with the increasing complexity of these systems has come the need for a more thorough understanding of basic hydrologic processes in order to combine them in a computer model to yield outputs at points of interest in time and space. The wide spread access to large computers and recent instigation of sampling programmes have led to the development of urban runoff models which are normally calibrated and validated by comparisons with field data.

The Storm Water Management Model, SWMM, (1,4,5,7), has been in extensive use to simulate the different elements involved in the phenomenon. The cost of setting up and running a SWMM simulation is determined by the level of discretization utilized for a particular catchment. The number of subcatchments into which an urban area is divided depends on the information available to the user and the objective of the simulation. If flow quantity and quality information describing the conditions in each of the major conduits of a system is of interest, then it is necessary to employ a fine discretization to define the subcatchments tributary to each of the conduits modelled. However, if the objective is merely to simulate the outflow from the entire catchment, it may be desirable to use a coarse discretization, thereby reducing the time and effort required for simulation through the use of a few larger subcatchments and conduits. The problem of catchment discretization was mentioned by different investigators (3,6). The results of these studies show no systematic approach to the method of discretization. The purpose of this study is to investigate the accepted level of discretization used for flow simulation over an urban area and to illustrate the effect of reducing the number of subcatchments on the accuracy of runoff simulation.

---

<sup>1</sup> Asst. Prof., Civ. Engrg. Dept., Univ. of Petroleum and Minerals, Box 396, Dhahran, Saudi Arabia.

Note.—Discussion open until April 1, 1982. To extend the closing date one month, a written request must be filed with the Manager of Technical and Professional Publications, ASCE. Manuscript was submitted for review for possible publication on February 11, 1981. This paper is part of the Journal of the Hydraulics Division, Proceedings of the American Society of Civil Engineers, ©ASCE, Vol. 107, No. HY11, November, 1981. ISSN 0044-796X/81/0011-1535/\$01.00.

## BASIC CONCEPTS AND PROPOSED METHODOLOGY

The SWMM Runoff-Transport Blocks are used to simulate the overland flow and sewer flow over an urban area. The fine discretization of an urban area is achieved by dividing the area into a large number of subcatchment areas, each includes the detailed sewerage system. Whereas, the coarse discretization of the urban area will provide a few larger subcatchments, each containing

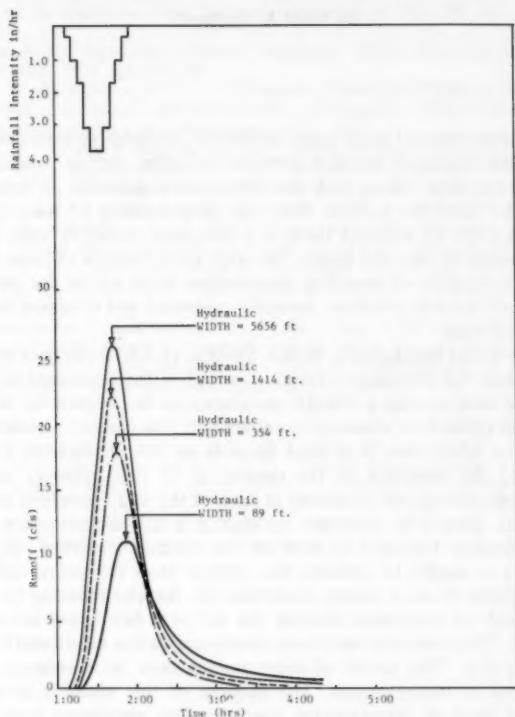


FIG. 1.—Effect of Varying Hydraulic Width on Surface Runoff Hydrograph (1 ft = 0.305 m)

only the major sewerage system. In order to develop a method for coarse discretization without losing the accuracy of the simulation, one should look into the basic concepts utilized in the Runoff and Transport Blocks.

**Runoff Block.**—The overland flow is computed by the Runoff Block. The Runoff Block considers each subcatchment as a plane surface of spatially constant characteristics such as, infiltration rates, detention depth, ground slope, and roughness coefficient. The overland flow hydrograph for the subcatchment is

determined by a series of time steps of average rainfall and outflow values. The excess flow depth (after subtractions of infiltration and depression storage) is assumed constant over the flow plane for a given time step and is used to calculate the rate of overland flow per unit width of the subcatchment. The total runoff from the subcatchment is computed by multiplying the unit overland flow rate by the subcatchment's width. The width of the subcatchment is defined as the dimension across which the overland flow occurs. Obviously the width of the overland flow (hydraulic width) for a particular subcatchment is different than the physical width of the subcatchment. The hydraulic width is a measure of the ease with which surface runoff may discharge from the subcatchment, and is a function of the drainage density and number of inlet manholes. Fig. 1 shows the variation of runoff hydrograph using different values of hydraulic widths for a hypothetical 11.48 acres (4.65 ha) subcatchment subjected to a rainfall hyetograph of 4 in./hr (101.6 mm/hr) for 1-hr duration. The reduced value of the hydraulic width will result in a delayed and attenuated peak hydrograph causing the build up of the surface runoff on the subcatchment plane. Conversely, the increased value of the hydraulic width will allow the rapid drain of water from the subcatchment plane resulting in an advanced larger peak hydrograph. This means that a given group of subcatchments of different characteristics may be grouped into a single catchment with characteristics determined based on the weighted average of the constituent smaller subcatchments and an aggregated hydraulic width based on the sum of the hydraulic widths of the individual subcatchments. The resulting aggregated surface runoff hydrograph will be very similar to the sum of the individual subcatchment hydrographs.

**Transport Block.**—The flow routing through the sewer system is computed by the Transport Block using the equation of continuity and Manning's equation based on the slope of energy line (quasilinear dynamic flow equation). The drainage system is composed of individual sewers. Each has constant characteristics of length, size, roughness, and slope. Using coarse discretization, the problem reduces to providing an equivalent routing effect on the aggregated surface hydrograph to produce an aggregated outflow hydrograph similar to the detailed one. A consideration of the hydraulic theory involved in the flow routing scheme indicates that conduit size, length, slope, and roughness are the factors affecting the routing process. Therefore, by replacing the detailed sewer system with a simplified one made up of weighted (by length) averages of conduits' sizes, slopes and roughness, and an approximate length equal to the length of the major sewers, a similar routed hydrograph may be obtained at the outlet. It may be anticipated that as fewer subcatchments are employed, more small conduits will be neglected with a consequent reduction of conduit storage in the routing computations. Such a reduction will result in higher peak flows and a shorter time to peak of the routed hydrograph. Two methods may be employed to introduce additional storage into the simulation. The length of the equivalent conduit can be increased to add conduit storage or the hydraulic width of the aggregated catchment can be reduced to add surface storage. The coarse discretization procedure may be carried down to a single aggregated catchment with an equivalent transport element. In many cases, it would be possible to use the Runoff Block alone to compute the outlet hydrograph from a single aggregated catchment. In this case a proper calibration of the aggregated hydraulic width is needed to compensate for the loss of conduit storage and routing effects.

### ADOPTED PROCEDURE FOR SIMPLIFIED SIMULATION

Two methods of simplified simulation are proposed here. The first method includes both the Runoff and Transport Blocks. The characteristics of the aggregated catchment is obtained based on the weighted averages of the individual subcatchments characteristics. The hydraulic widths of the different subcatchments are added to get the aggregated hydraulic width. The overland flow is calculated for the aggregated catchment using the Runoff Block. The equivalent transport system is established based on the weighted average of the individual sewer characteristics. The length of the equivalent transport system is approximated to the length of the actual major trunk sewers. The aggregated runoff flow hydrographs are introduced at the upstream ends of the equivalent transport system and routed to the outlet. Proper selection of the length of the equivalent transport system will result in accurate simulation.

The second method of the simplified approach includes only the Runoff Block. In this case the coarse discretization is carried down to a single aggregated catchment. The aggregated catchment characteristics are calculated as mentioned in the first method. In order to compensate for the loss in conduit storage, the aggregated hydraulic width needs to be adjusted to a lesser value than the sum of all subcatchments' hydraulic widths. The adjusted value of the hydraulic width can be calculated from the proposed equation

$$W_{adj} = W_0 \times \left[ \frac{\text{Net rainfall volume} - \% \text{ full of conduit volume}}{\text{Net rainfall volume}} \right] \dots \dots \dots (1)$$

in which  $W_{adj}$  = the adjusted hydraulic width;  $W_0$  = the added hydraulic width from the detailed discretization; Net rainfall volume = rainfall volume - losses; and % full of conduit = assume that sewers are flowing volume 60% full.

### HYPOTHETICAL AND REAL TEST AREAS

The aforementioned simplified procedures are applied on hypothetical and real test areas. The description of the areas and the level of discretization are given in the following two sections:

**Hypothetical Test Area.**—The hypothetical test area is defined to have uniform subcatchment characteristics in order to facilitate the process of aggregation. The total area is 643 acres (260.4 ha). The percentage of imperviousness is taken as 50%. The values of the infiltration rates for the pervious areas and the values of the detention depth for impervious and pervious areas are taken as the default values used by the SWMM user's manual. 25% of the impervious area is assumed to have zero detention storage. Three levels of discretization are employed. Fig. 2 shows the hypothetical area discretized into 37, 5, and 1 subcatchments. The figure also shows the layout and size of the sewer system used for each level of discretization. A 2-hr triangular rainfall hyetograph with peak intensity of 2 in./hr (50.8 mm/hr) is used for the simulation.

**Real Test Areas.**—The real test areas used for this study ranged from a small area 10 acres (4 ha) to a fairly large area 542 acres (219.5 ha) to test the validity of the suggested approach. Detailed information regarding the physical characteristics of the areas and the rainfall data are not given here. The reader should

consult the original work done by the different investigators. A brief description of the areas is given in the following four subsections:

**Chicago 10-acre Tract, USA.**—Information about land use, geometry, and the layout of the drainage system are given in the ASCE manual, No. 37, 1960 (2). The area is 46% impervious and is discretized into 80 subcatchments, 40 gutters, and 4 pipes. Size of subcatchments ranges from 0.04 min–0.48 acres (0.02 ha–1.95 ha). A 181 min design storm is applied to the catchment area.

**Northwood, Baltimore, USA.**—The John Hopkins University has conducted an intensive data gathering program for rainfall-runoff relationships at Northwood, Baltimore. The physical and rainfall data are available from the ASCE Urban Resources Research Publication (6). The Urban area is 47.4 acres (19.2 ha) with 68% imperviousness and average ground slope of 3%. The area is discretized into 12 and 5 subcatchments. The storm of August 1, 1965 is used in the simulation.

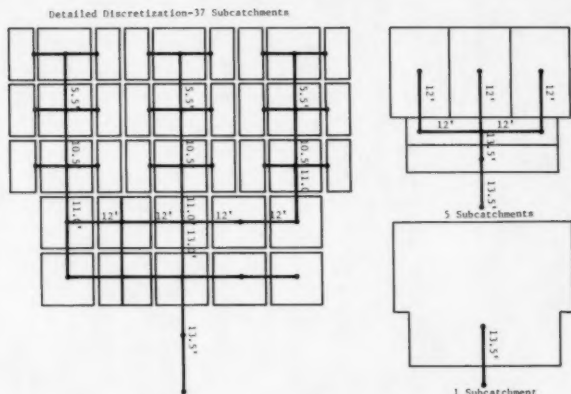


FIG. 2.—Hypothetical Test Area, Different Levels of Discretization (1 ft = 0.305 m)

**Vine Street Main Drain, Australia.**—The Vine street catchment is located on the western side of Melbourne in the city of Sunshine. The total area of the catchment is 173 acres (70 ha) with 36% imperviousness and average ground slope from 0.5%–1%. The physical and rainfall data are given in the research report by Heeps and Mein (3). The area is discretized into 51 and 12 subcatchments. The storm of February 12, 1972 is used in the simulation.

**Bannatyne Sewer District, Canada.**—The Bannatyne sewer district is located in the northwest side of the city of Winnipeg, Canada. The district is relatively flat with average ground slope less than 1%. The total area is 542 acres (219.5 ha) and the imperviousness is 36%. The detailed data is available from Zaghoul (8). The area is discretized into 41 subcatchments. This storm of June 19, 1971 is used in the simulation.

#### APPLICATION OF PROPOSED APPROACH

**Hypothetical Test Area.**—The Runoff and Transport Blocks are used in the

simulation. At both levels of the coarse discretization the total hydraulic width is 79,000 ft (24,095 m), as calculated from the fine discretization. The equivalent Transport elements employed in the simplified simulation are determined from an aggregation of the sewer network used in the detailed system. The results of the simulation using the three level of discretization are shown in Fig. 3. The hydrographs computed by the simplified approach are very similar to those of the detailed simulation. Slight increase in the peak flow is observed with the decrease in the number of subcatchments. The equivalent transport system used in both levels of discretization provide a fairly good approximation of the detailed system in view of the relatively small increase in peak flow.

In order to investigate the effect of eliminating conduit routing, a simplified

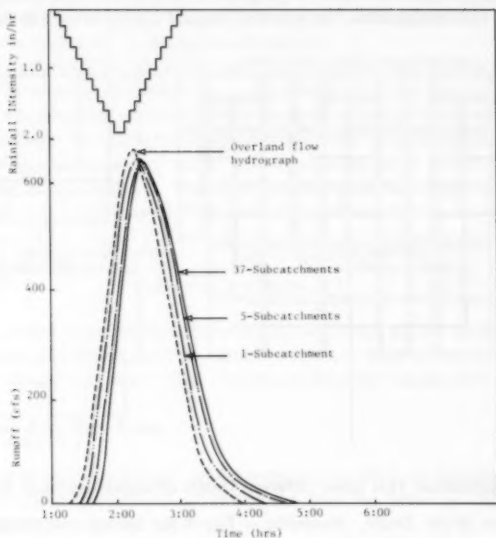


FIG. 3.—Hypothetical Test Area Flow Simulation (1 ft = 0.305 m)

simulation using only the Runoff Block and a single catchment is conducted. The hydraulic width is reduced to induce more surface storage to compensate for the exclusion of all conduit storage. Several simulations were conducted to determine the optimum hydraulic width. The results of the simulations are shown in Fig. 4. The results indicate that, a reduction in the hydraulic width from 79,000 ft (24,095 m)–56,000 ft (17,080 m) is necessary to compensate for the conduit storage. In this case, the total rain is given as 2 in. (50.8 mm) and the net rain can be taken as 1.90 in. (48.3 mm), i.e., 4,433,000 cu ft (124,124 m<sup>3</sup>). The conduits total volume is 2,153,000 cu ft (60,284 m<sup>3</sup>). Considering that the conduits are flowing 60% full, then the percentage full of conduit volume equals 1,300,000 cu ft (36,400 m<sup>3</sup>). Substituting these values in Eq. 1, the adjusted hydraulic width of 56,000 ft (17,080 m) is obtained.

**Chicago 10-Acre Tract.**—In this case, runoff flow simulation is performed to investigate the effect of coarse discretization on a small catchment area in which conduit routing effects are relatively minor. A simplified approach using a single catchment and the Runoff Block is applied. The aggregated hydraulic width is calculated from the 80 subcatchments' widths. The physical characteristics of the single catchment is based on the weighted average of the detailed ones. Fig. 5 shows the hydrographs calculated from the detailed 80 subcatchments and the simplified single subcatchment using Runoff Block. The two simulated hydrographs are almost identical. This result suggests that in small areas, conduit routing is insignificant and a simplified single catchment using Runoff Block is adequate for the flow simulation.

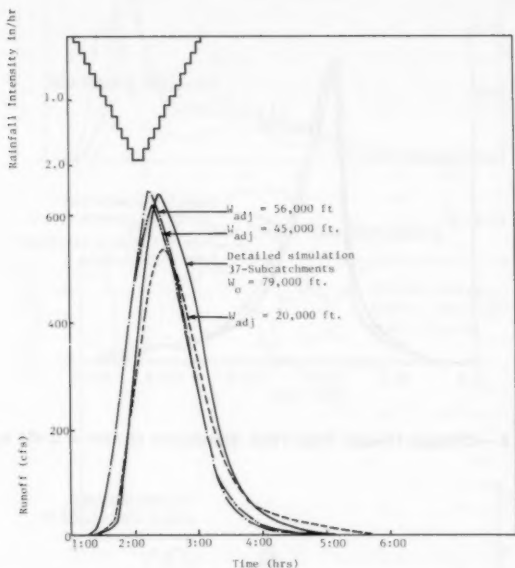


FIG. 4.—Hypothetical Test Area, Effect of Reduced Hydraulic Width, Single Catchment using Runoff-Block (1 ft = 0.305 m)

**Northwood, Baltimore.**—The information available for the detailed 12 subcatchments discretization is considered as the basic data for the proposed 5-subcatchments discretization. The proposed 5-subcatchments' characteristics are calculated based on the weighted averages of the physical characteristics of 12-subcatchments. The proposed 5-subcatchments' hydraulic widths are prepared based on the hydraulic widths of the 12-subcatchments. The equivalent transport system is selected based on the major trunk sewer system available. Fig. 6 shows the simulated hydrographs of the 12, 5 and the proposed 5-subcatchments discretization. The proposed method shows a very good improvement

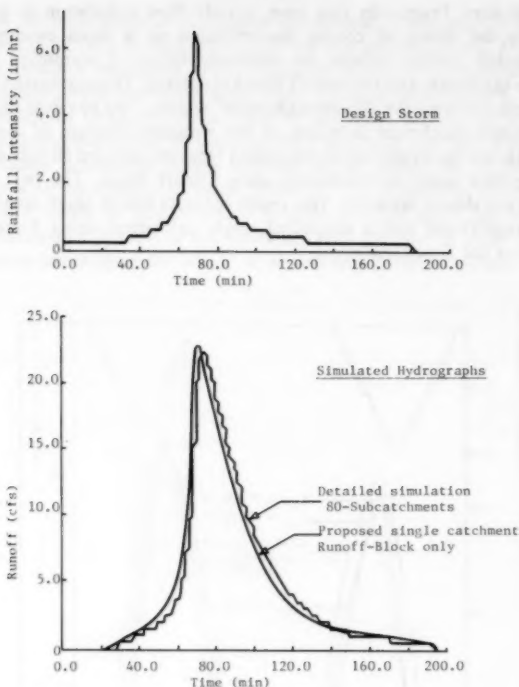


FIG. 5.—Chicago 10-acre Tract Flow Simulation (1 acre = 0.405 ha)

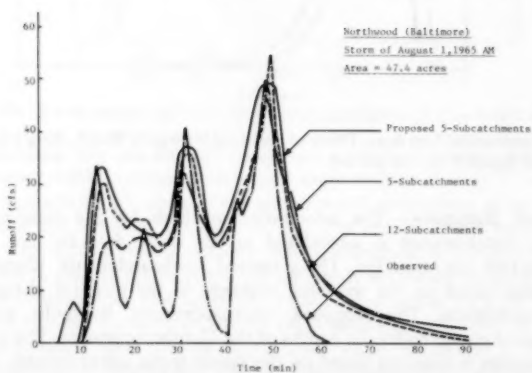


FIG. 6.—Northwood (Baltimore) Flow Simulation (1 acre = 0.405 ha)



of the simulated hydrograph over the 5-subcatchments hydrograph prepared by the original investigator. The proposed 5-subcatchments hydrograph is slightly greater in flow peaks than the 12-subcatchments hydrograph. This result is expected due to loss in conduit storage. The flow peaks of the original 5-subcatchments hydrograph are shown to be consistently less than those of the 12-subcatchments hydrograph.

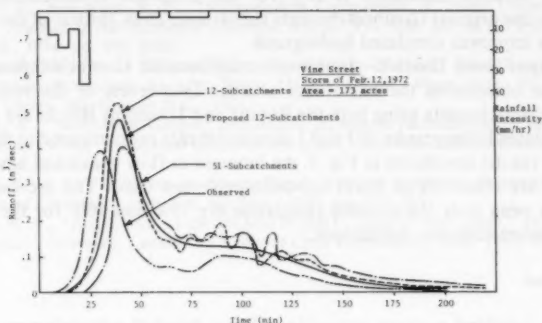


FIG. 7.—Vine Street Flow Simulation

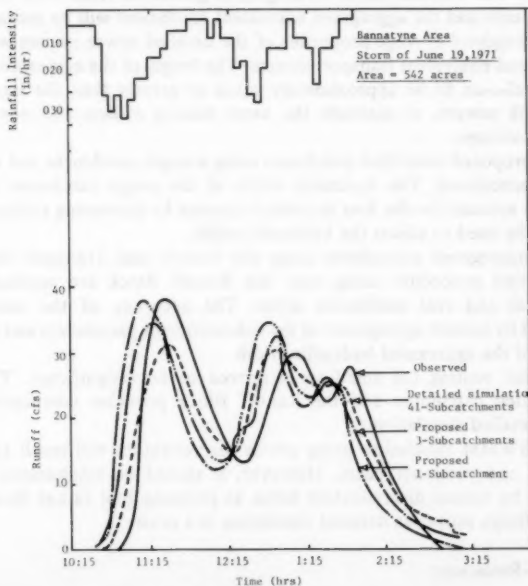


FIG. 8.—Bannatyne Flow Simulation (1 acre = 0.405 ha)

**Vine Street Main Drain.**—The detailed 51-subcatchments discretization is considered the basic data source for the preparation of the proposed 12-subcatchments aggregate discretization using the Runoff and Transport Blocks. Fig. 7 shows the simulated hydrographs of the 51, 12 and the proposed 12-subcatchments discretization. The proposed 12-subcatchments hydrograph shows a lesser flow peak than the original 12-subcatchments simulation. The increase in peak flow over the detailed simulation is 20% for the proposed 12-subcatchments and is 33% for the original 12-subcatchments simulation. Thus, the use of the suggested approach improves simulated hydrograph.

**Bannatyne Sewer District.**—In this case, the detailed 41-subcatchments discretization is considered the basic data source. Two levels of discretizations of 3 and 1 subcatchments using both the Runoff and Transport Blocks are proposed. The simulated hydrographs of 3 and 1 subcatchments are compared to the detailed one. The results are shown in Fig. 8. An increase in flow peaks and advancement in peaks are observed as fewer subcatchments are used. The increases in the first flow peak over the detailed simulation are 10% and 20% for the proposed 3 and 1 subcatchments simulations.

## CONCLUSIONS

1. The weighted average properties of the detailed subcatchments and the summation of the individual hydraulic widths will provide an aggregated equivalent catchment. The surface runoff hydrographs generated from both the detailed subcatchments and the aggregated equivalent catchment will be similar.

2. The weighted average properties of the detailed sewer system will provide an aggregated equivalent transport system. The length of the equivalent transport system is chosen to be approximately equal or greater than the length of the major trunk sewers, to maintain the same routing effects and minimize loss in conduit storage.

3. The proposed simplified simulation using a single catchment and the Runoff Block is introduced. The hydraulic width of the single catchment should be reduced to account for the loss in conduit storage by increasing surface storage. Eq. 1 can be used to adjust the hydraulic width.

4. The aggregated procedures using the Runoff and Transport Blocks and the simplified procedure using only the Runoff Block are applied on both hypothetical and real catchment areas. The accuracy of the simulation is maintained by careful aggregation of the subcatchment parameters and the proper selection of the aggregated hydraulic width.

5. Conduit routing for small areas proved to be insignificant. The use of the simplified catchment and the Runoff Block provides comparable results with the detailed simulation.

6. The SWMM simulation using coarse discretization will result in reducing setting up and computer costs. However, it should be emphasized that flow simulation by coarse discretization helps as planning tool rather than a design one. For design purposes detailed simulation is a must.

## APPENDIX.—REFERENCES

1. Chen, C. W., and Shubinski, R. P., "Computer Simulation of Urban Storm Water

- Runoff," *Journal of the Hydraulic Division*, ASCE, Vol. 97, No. HY2, Proc. Paper 7924, Feb., 1971, pp. 289-301.
2. *Design and Construction of Sanitary and Storm Sewers, Manual No. 37*, 1st ed., by a Joint Committee of the American Society of Civil Engineers and the Water Pollution Control Federation, ASCE, 1960.
  3. Heeps, D. P., and Mein, R. G., "An Independent Evaluation of Three Urban Storm Water Models," *Research Report No. 4*, Monash University, Clayton, Victoria, Australia, 1973.
  4. Heeps, D. P., and Mein, R. G., "Independent Comparison of Three Urban Runoff Models," *Journal of the Hydraulic Division*, ASCE, Vol. 100, No. HY7, Proc. Paper 10685, July, 1974, pp. 995-1009.
  5. Metcalf and Eddy Inc., "Storm Water Management Model," Final Report, U.S. Environmental Protection Agency, Water Quality Office, Water Pollution Control Research Series, Washington D.C., 1971.
  6. Tucker, L. S., "Northwood Gauging Installation, Baltimore-Instrumentation and Data," ASCE Urban Water Resources Research Program, *Technical Memorandum No. 1*, ASCE, Aug., 1968.
  7. Zaghoul, N. A., "Evaluation of Storm Water Routing Models," *Proceedings*, The Institution of Civil Engineers, Vol. 63, Dec., 1977, pp. 925-933.
  8. Zaghoul, N. A., "Application of the SWMM Model to Large Urban Areas," *Proceedings 1980 Annual Conference*, Canadian Society of Civil Engineering, May, 1980, M/6:1-14.



## EFFICIENT COOLING PONDS: DESIGN

By Gerhard H. Jirka,<sup>1</sup> M. ASCE, Carl F. Cerco,<sup>2</sup>  
and Donald R. F. Harleman,<sup>3</sup> M. ASCE

### INTRODUCTION

A framework for classification and predictive modeling of cooling impoundments used for waste heat dissipation has been proposed in several recent publications (6,7,8,9). The design of such cooling impoundments is usually governed by engineering, biological/ecological, and regulatory requirements. These requirements are diverse, often conflicting, and highly site-specific. For this reason it is impossible to propose generally valid design guidelines.

In this paper, emphasis is put on those engineering design considerations which maximize the thermodynamic efficiency of the associated steam-electric power plant. Two performance features are of interest for a continuously operating plant: (1) The steady-state or "average" performance of the cooling impoundment, which relates to its ability to dissipate the artificial heat load while providing the lowest possible average plant intake temperature. This affects the long-term efficiency of the station; and (2) the transient performance, or its "thermal inertia," which relates to the ability of the impoundment to minimize short-term fluctuations in the intake temperature. Such fluctuations can arise because of meteorological variations—diurnal changes and mesoscale weather changes—and because of intermittent plant operation. The plant peak power output at times of maximum electrical demand (summer hot spells) may have to be curtailed, and limits for the turbine back pressure or for safety-related equipment, e.g. nuclear plants, may be exceeded during such temperature extremes.

### HYDRODYNAMIC VARIABLES AFFECTING POND PERFORMANCE

Two cooling impoundments with exactly the same water surface area,  $A_p$ , may exhibit highly disparate performance characteristics. Thus, the utilization of the given surface area for heat dissipation depends on the internal heat

<sup>1</sup>Assoc. Prof., School of Civ. and Environmental Engrg., Cornell Univ., Ithaca, N.Y. 14853.

<sup>2</sup>Asst. Marine Scientist, Virginia Inst. of Marine Sci., Gloucester Point, Va. 23062.

<sup>3</sup>Ford Prof. of Engrg. and Dir., R. M. Parsons Lab. for Water Resources and Hydrodynamics, Massachusetts Inst. of Tech., Cambridge, Mass. 02139.

Note.—Discussion open until April 1, 1982. To extend the closing date one month, a written request must be filed with the Manager of Technical and Professional Publications, ASCE. Manuscript was submitted for review for possible publication on January 30, 1981. This paper is part of the Journal of the Hydraulics Division, Proceedings of the American Society of Civil Engineers, ©ASCE, Vol. 107, No. HY11, November, 1981. ISSN 0044-796X/81/0011-1547/\$01.00.

transport processes within the impoundment. The most important feature of the internal hydrodynamics is related to the vertical thermal structure described by a pond number  $IP$  (7)

$$P = \left( \frac{f_i}{4} \frac{Q_o^2}{\beta \Delta T_o g H^3 W^2} D_v^3 \frac{L}{H} \right)^{1/4} \dots \dots \dots (1)$$

in which  $f_i$  = interfacial friction factor;  $Q_o$  = condenser flow rate;  $\beta$  = coefficient of thermal expansion;  $\Delta T_o$  = condenser temperature difference;  $g$  = gravity;  $H$  = average impoundment depth;  $L$  = length of flowpath through impoundment;  $W = A_p/L$  = average width; and  $D_v$  = vertical entrance dilution at inflow.

Well stratified deep impoundments,  $P \leq 0.3$ , exhibit a distinct thin surface layer with longitudinal temperature variation and a deep subsurface zone in which the temperature varies with depth and is horizontally uniform. The surface layer thickness  $h_s$  is related to the pond number,  $h_s = P H$  (7). The surface area of deep impoundments tends to be well-utilized for heat transfer because of the action of density currents which distribute the heat effectively even into seemingly isolated regions (sidearms). Thus, good steady-state performance is guaranteed. Furthermore, the deep subsurface zone insulates the intake flow from the surface layer and therefore provides excellent thermal inertia. Field and laboratory data supporting these conclusions have been given (6,9,10).

The temperature distribution in shallow impoundments,  $P \geq 0.3$ , which have been further classified into partially-mixed,  $0.3 \leq P \leq 1$ , and vertically fully-mixed,  $P \geq 1$ , types, is dominated by throughflow currents rather than density currents. Shallow impoundments tend to possess either internal flow circulations caused by inflow jetting and by flow separations due to boundary changes, or longitudinal dispersion caused by regular boundary shear effects. Consequently, their surface area utilization for heat transfer is much poorer. In the extreme, some short-circuiting can result. Also, because of the absence of a well-established vertical structure, shallow ponds have limited thermal inertia.

Indeed, a deep stratified impoundment with a low densimetric Froude number discharge (which minimizes  $D_v$ ) and a submerged skimmer wall intake can be regarded as the ideal design (Ryan and Harleman, 10). Many impoundments which are formed by damming a river valley, thereby forming an artificial reservoir, fall into this category and have been conveniently labeled as "cooling lakes" (6). On the other hand, there are many examples of perched or off-stream "cooling ponds" which are formed by diking in or excavating some available land area and supplying make-up water from an external source. Application of the pond number criterion to these off-stream ponds shows that it is often not feasible to attain the well-stratified deep impoundment condition.

Consider these typical pond conditions:  $A_p = 1,000$  acres (404 ha);  $L/W = 3$  (open elongated plan shape);  $Q_o = 1,800$  cfs (51 m<sup>3</sup>/s);  $\Delta T_o = 20^\circ F$  (11 $^\circ C$ ), i.e. roughly corresponding to a 1,200 MW nuclear plant with a thermal loading of 2.4 MW waste heat per acre;  $D_v = 1.5$  (well designed discharge channel);  $\beta = 0.00018/^\circ F$ ; and  $f_i = 0.01$ . The required depth for a stratified pond,  $P = 0.3$ , is computed from Eq. 1 as  $H = 12.3$  ft (3.8 m). In view of diking or excavation costs, or both, this required depth is large and most of the artificial cooling ponds which have been analyzed are more shallow (9). Furthermore, if the pond conditions are close to the shallow range ( $P \approx 0.3$ ),

it then becomes necessary to have a sufficient separation between discharge and intake locations to prevent undesirable, sometimes wind-induced, short-circuiting. Unless a long discharge or intake channel is built to the other end of the pond, this separation is most readily achieved by inserting interior baffles to control the flow path. Yet, any baffle increases the  $L/W$  ratio which, in turn, would require an even larger depth,  $H$ , to maintain full stratification, as can be seen from the definition of  $P$ .

Hence, for practical purposes, many existing and future cooling ponds must be expected to operate in the shallow water range. In fact, the range  $0.3 < P < 1$  is typical for the off-stream designs summarized in (9). Their average performance can be understood by considering the parameters of simple steady-state models for shallow ponds (8). Two objectives emerge: First, the prevention of internal recirculations, both at the discharge and at flow direction changes, and secondly, the minimization of longitudinal dispersion to approach plug flow conditions. The latter objective is met by minimizing the dispersion parameter,  $E_L^* = E_L / UL$ , in which  $E_L$  = longitudinal dispersion coefficient; and  $U = Q_o / HW$  = mean flow velocity. Using a typical relationship between longitudinal dispersion and internal turbulent characteristics of the channel shear flow such as Fischer's (3) equation  $E_L \approx 0.3 u_* b^2 / \kappa^2 H$  in which  $u_* = \sqrt{f/8}$ ;  $U$  = shear velocity;  $f$  = bottom friction coefficient;  $b$  = characteristic transverse width ( $\approx W/2$ ); and  $\kappa = 0.4$  = von Karman's constant. We find, after appropriate substitution

$$E_L^* \sim \frac{W}{L} \frac{W}{H} \dots \dots \dots (2)$$

Since the depth,  $H$ , is governed by the aforementioned reasons, Eq. 2 indicates that a high  $L/W$  ratio, i.e. a baffled pond, is desirable from the point of view of minimizing longitudinal dispersion effects. The benefit of this requirement, however, is questionable, since it would further increase the pond number and diminish any advantages which arise from the influence of density current and from the thermal inertia of an at least partially stratified pond. Also, high baffle density causes, in practice, many flow reversals and local recirculation zones, reduces the available surface area and is expensive.

The laboratory research described that follows was aimed at a resolution of the effect of baffle density on dispersion suppression and at the evaluation of two novel design concepts: (1) A radial discharge structure to minimize discharge induced recirculation zones; and (2) a deep intake reservoir in front of the skimmer wall intake to provide some thermal inertia to a shallow pond.

#### LABORATORY SIMULATIONS ON SHALLOW COOLING PONDS

**Equipment and Procedure.**—Laboratory simulations were carried out in an insulated 17.7 ft (5.4 m)  $\times$  35.7 ft (10.9 m)  $\times$  1.0 ft (0.3 m) modeling basin in the R. M. Parsons Laboratory at MIT. The basic rectangular plan shape ( $L/W \approx 2$ ) of the pond could be changed through the insertion of internal baffles. The discharge flow was introduced in either of two ways: Either, a rectangular box of 18 in. (458 mm) length and 11 in. (279 mm) maximum width simulating a standard discharge canal, or a radial discharge structure of 24 in. (609 mm) radius, inscribing a 90° arc, subdivided by vanes into six sectors. In both schemes, gravel and horsehair filters were used to insure uniform initial

flow distributions. The outflow (intake) structure was a rectangular box with a submerged skimmer wall opening of 18 in. (458 mm) width and 0.5 in. (127 mm) height. The structures could be placed anywhere in the model pond.

A vertically traversing platform supported 60 thermistor probes which were automatically read and recorded at fixed time intervals. Additional thermistor probes recorded discharge and outflow temperatures and the equilibrium temperature within a separate shallow insulated tank. Relevant laboratory "meteorological" variables were monitored.

In several simulation runs, insight into the behavior of experimental pond configurations was gained through the instantaneous injection of 50 cm<sup>3</sup> of fluorescent Rhodamine WT dye (10 ppt concentration) into the heated influent. The highly visible red dye provided visual studies of the flow pattern and stratification of the pond, as well as a unit impulse response (UIR) curve for each configuration. The curves were obtained by periodically sampling intake water outflow for analysis in a Turner Model III Fluorometer calibrated to detect concentrations in the range of 0–500 parts per billion. In addition to instantaneous injections, an apparatus was also available to provide continuous dye injections for further visual analysis of throughflow patterns.

All simulations were performed in a "once-through" mode, i.e. a specified discharge temperature  $T_o$  was maintained, rather than a specified temperature differential  $\Delta T_o$  across the pond as in actual "closed-cycle" operation. The experiments were started from a uniform equilibrium temperature,  $T_E$ , condition at which time the discharge temperature was raised to the desired value  $T_o$ . The time to steady-state, ascertained from repeated temperature readings at the intake, was between 8 hr and 24 hr, depending on run conditions. Several complete temperature recordings and dye experiments were performed at steady-state. Continuous monitoring was performed during transient experiments. More complete experimental descriptions are available (2,9).

**Diagnostic Modeling.**—The simulations were intended as a diagnostic tool to examine different design configurations in an efficient and inexpensive manner and in a controlled environment. In order to claim validity for the resulting design guidelines for field cooling ponds, the laboratory simulation must meet two basic requirements: (1) It must be free of low Reynolds number effects in order to characterize the turbulent field conditions; and (2) it must operate under the thermal structure, measured by  $P$ , that is typical for field ponds.

**Avoidance of Low Reynolds Number Effects.**—The theoretical conditions for the maintenance of a fully turbulent free surface shear flow condition is  $R_o \geq 2,300$ , in which  $R_o$  is defined in pipe analogy as

$$R_o = \frac{4 V H}{\nu} \quad \dots \dots \dots (3)$$

in which  $V$  = average velocity of flow path; and  $\nu$  = kinematic viscosity. The typical  $R_o$  numbers in the experimental investigation varied between 500 and 1,000 and thus would indicate significant laminarity effects. In a pond receiving heated discharges or containing a three-dimensional flow field, or both, however, there are a number of sources of turbulence not reflected in the Reynolds number. Jet entrainment and velocity nonuniformities created by flow constrictions and counterflows result in velocities much higher than the cross-sectional



average, and turbulent mixing occurs as heated, buoyant surface water cools and mixes with subsurface water. These conditions may allow the criterion

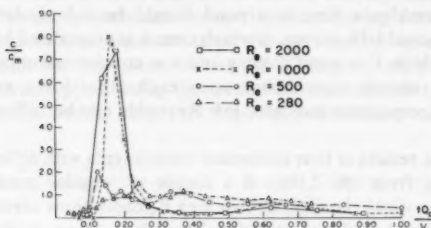


FIG. 1.—Dye UIR Curves for Isothermal Discharges in a Rectangular Pond ( $L/W = 3/2$ ) as a Function of Reynolds Numbers

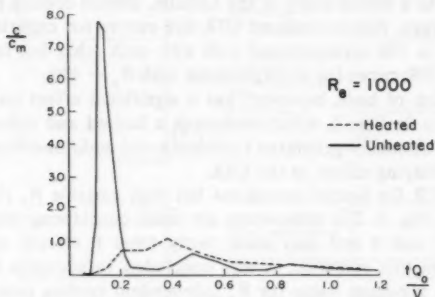


FIG. 2.—Effect of Heated Discharge on Dye UIR Curve

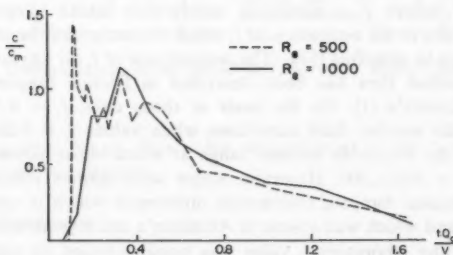


FIG. 3.—Dye UIR Curves for Heated Discharge for Two Reynolds Number Conditions

of Eq. 3 to be relaxed while still providing sufficient turbulence in the model. A series of experiments was conducted to ascertain these effects based on observations of dye UIR functions.

In the absence of heat, and for sufficiently high Reynolds numbers, the distribution of relative velocities in the current and the relative size of the main flow and eddy zones should be independent of  $R_o$ . As a result, the nondimensional residence time in a pond should be independent of the flow rate. Non-dimensional UIR curves, in which time,  $t$ , is normalized by the residence time  $V/Q_o$ , in which  $V$  = pond volume and  $c$  = concentration by its uniformly mixed value  $c_m$ , should superimpose upon each other for a variety of flow rates. Lack of superposition indicates low Reynolds number effects are present in the flow field.

Fig. 1 shows the results of four isothermal experiments with different discharge flows ( $R_o$  ranging from 280–2,000) in a simple rectangular pond arrangement using 1/3 of the available basin. The two high  $R_o$  cases show identical behavior, as would be expected in the above-critical turbulent range. A sharp initial dye peak results from a short-circuiting eddy which formed in the pond. The low  $R_o$  cases show a smoothed out UIR and are definitely affected by laminarity. These results compare reasonably with the data of Tatinclaux, Jain, and Sayre (11) who found, in a model study of the LaSalle, Illinois cooling pond involving unheated discharges, that normalized UIR dye curves for experiments with  $R_o = 1,000$  and  $R_o = 730$  superimposed well with each other but failed to match the normalized UIR curve for an experiment with  $R_o = 420$ .

The introduction of heat, however, has a significant effect on the turbulent UIR, as is shown in Fig. 2, which compares a heated and unheated case for  $R_o = 1,000$ . The thermally-generated turbulence and additional buoyancy driven motion have a delaying effect on the UIR.

Finally, the UIR for heated conditions but with variable  $R_o$  (500 and 1,000) are compared in Fig. 3. The differences are small considering the scale change between Figs. 1 and 3 and may arise partly from P effects rather than  $R_o$  effects. Based on this evidence, it was concluded to accept a lower limit of  $R_o \sim 500$  as the minimum value for  $R_o$  independent cooling pond experiments with buoyancy induced turbulent effects.

**Equivalent Thermal Structure.**—The pond number,  $P$ , of a laboratory simulation can be estimated by using all relevant model variables in Eq. 1 together with  $\Delta T_o = T_o - T_i$  where  $T_i$  = measured steady-state intake temperature. The major difficulty lies in the estimation of  $f_i$  which characterizes the shear induced energy dissipation in stratified flow. The dependence of  $f_i$  on Reynolds numbers with stably stratified flow has been described in friction diagrams, such as Abraham and Eysink's (1). On the basis of those data,  $f_i = 0.01$  is typical for high Reynolds number field conditions while values  $f_i = 0.06$ –0.1 appear appropriate for the Reynolds number range at which most experiments were performed— $R_o = 500$ –1,000. However, major uncertainties remain regarding the role of additional buoyant convection turbulence which is caused by the surface cooling and which was absent in Abraham's and Eysink's data base.

Calibration of the laboratory  $f_i$  value was possible based on comparison of laboratory experiments with field data from the Powerton, Illinois cooling pond as a typical partially mixed pond,  $P \approx 0.5$  (6). A baffled S-shaped pond with the same schematic geometry as Powerton was simulated in the laboratory (Fig. 4). Note, that pond number equivalence for prototype and model,  $P_r = 1$ , together with the usual geometric and densimetric Froude number dynamic similarity requirements, yields a distortion ratio  $\Delta = h_r/l_r = f_r$  in which  $l_r$  = horizontal

length ratio (given by model size);  $h_r$  = vertical length ratio; and  $f_r$  = interfacial friction factor ratio. Thus, the laboratory model was run in an iterative fashion choosing different distortions  $\Delta$ , between 5 and 10, and adjusting the discharge temperature  $T_o$  so as to maintain similar buoyant driving forces,  $(\Delta\beta T_o)_r = 1$ . The resulting vertical temperature structure was observed in each experiment and compared with the field observations (3). Ultimately, an inclined isotherm structure in a vertical plane along the mean flow path similar to the prototype was observed in the model at  $\Delta = 7.5$  giving a laboratory value  $f_r \approx 0.075$ ,

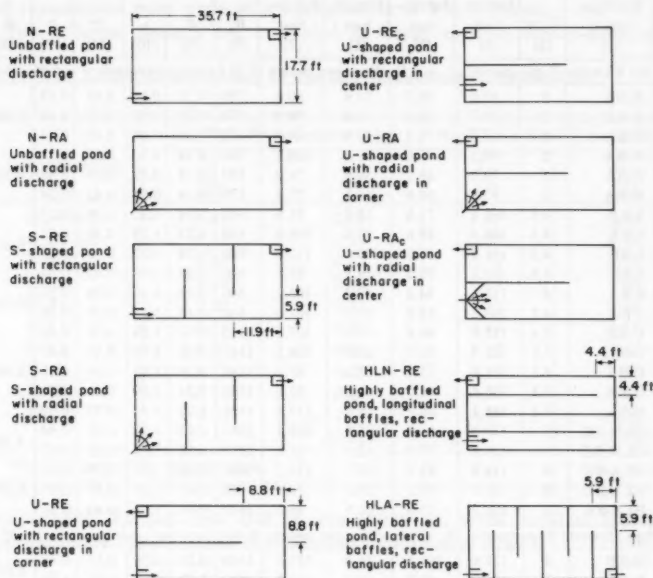


FIG. 4.—Pond Configurations Investigated in Laboratory Study, Depth = 0.25 ft (1 ft = 0.305 m)

i.e. in the expected range. This value was adopted in the computation of  $P$  for the laboratory simulations.

#### STEADY-STATE SIMULATIONS

About 50 steady-state experiments were performed for different combinations of five pond configurations—The unbaffled pond, N, the S-shaped pond, S, the U-shaped pond, U, the highly baffled pond with longitudinal baffles, HLN, and the highly baffled pond with lateral baffles, HLA—of two discharge configurations, standard rectangular RE and radial RA, and of two flow rates, which gave two ranges of cooling capacity,  $r$ , for

TABLE 1.—Parameters and Results of Laboratory Simulations

Run (1)	Configu- ration (2)	L/W (3)	$T_o$ , in degrees Fahren- heit (4)	$T_r$ , in degrees Fahren- heit (5)	$T_E$ , in degrees Fahren- heit (6)	$K$ , in British thermal units per square feet- day- degrees Fahren- heit (7)	$R_a$ (8)	P (9)	r (10)	$T_i^*$ (11)	D (12)	$\bar{D}$ (13)
(a) Low Flowrate Experiments: $Q_o = 4.5$ gallons per minute (0.28 Liters per second), $r = 0.89-1.38$												
5	N-RE	2	87.0	68.7	53.9	80.6	570	0.21	0.97	0.45	0.53	0.60
6	N-RE	2	99.7	76.6	58.8	89.9	570	0.20	1.08	0.43	0.66	
7	N-RE	2	94.8	74.3	57.9	84.4	570	0.21	1.01	0.44	0.60	
8	N-RA	2	99.5	75.0	59.7	100.1	570	0.14	1.20	0.38	0.54	0.39
9	N-RA	2	79.7	66.1	54.8	74.0	570	0.14	0.89	0.45	0.38	
10	N-RA	2	87.9	69.6	56.5	77.4	570	0.14	0.93	0.42	0.24	
2	S-RE	4.5	101.8	71.0	53.3	91.6	840	0.24	1.10	0.36	0.27	0.47
22	S-RE	4.5	108.4	85.6	73.0	108.0	840	0.23	1.29	0.36	0.51	
40	S-RE	4.5	116.8	87.0	70.4	110.0	840	0.24	1.32	0.36	0.55	
60	S-RE	4.5	103.8	78.2	59.1	85.8	840	0.23	1.03	0.43	0.53	0.53
58	S-RA	4.5	110.1	84.2	69.3	104.2	840	0.18	1.25	0.36	0.51	
62	S-RA	4.5	109.6	82.8	66.5	102.6	840	0.18	1.23	0.38	0.55	
48	U-RE	8.2	113.9	86.8	72.2	107.8	1140	0.31	1.29	0.35	0.48	0.48
51	U-RE <sub>C</sub>	8.2	112.9	83.0	66.9	108.2	1140	0.32	1.30	0.35	0.49	
64	U-RA	8.2	101.8	75.4	58.6	86.3	1140	0.23	1.03	0.39	0.31	
67	U-RA <sub>C</sub>	8.2	100.8	79.0	63.8	93.8	1140	0.24	1.09	0.41	0.54	0.36
68	U-RA <sub>C</sub>	8.2	125.1	86.3	65.8	117.4	1140	0.22	1.41	0.35	0.59	
55	HLN-RE	33	110.3	81.8	66.5	105.8	2280	0.52	1.27	0.35	0.44	
69	HLN-RE	33	106.1	77.9	62.6	95.1	2280	0.52	1.14	0.35	0.27	0.31
17	HLA-RE	18	114.8	82.7	69.1	115.2	1690	0.40	1.38	0.30	0.31	
19	HLA-RE	18	93.5	76.1	65.7	89.5	1690	0.47	1.07	0.37	0.27	
71	HLA-RE	18	102.2	77.0	60.5	86.2	1690	0.44	1.03	0.40	0.34	
(b) High Flowrate Experiments: $Q_o = 9.0$ gallons per minute (0.56 Liters per second) $r = 0.62-0.95$												
44	N-RE	2	127.9	103.1	76.0	157.8	1140	0.27	0.94	0.52	0.98	1.02
78	N-RE	2	106.0	90.2	64.5	110.2	1140	0.27	0.66	0.62	1.06	
46	N-RA	2	110.2	91.6	69.6	120.6	1140	0.19	0.72	0.54	0.59	
79	N-RA	2	107.1	88.6	63.4	110.2	1140	0.21	0.66	0.58	0.67	0.63
24	S-RE	4.5	109.5	93.2	75.1	117.0	1680	0.36	0.70	0.53	0.40	
41	S-RE	4.5	119.7	96.1	72.7	137.8	1680	0.37	0.83	0.50	0.55	
42	S-RE	4.5	131.7	101.9	76.2	158.2	1680	0.35	0.95	0.46	0.60	0.51
61	S-RE	4.5	110.3	90.8	67.4	115.3	1680	0.38	0.69	0.54	0.51	
14	S-RA	4.5	105.3	87.7	67.9	117.0	1680	0.29	0.70	0.53	0.40	
59	S-RA	4.5	109.8	91.5	70.3	119.2	1680	0.29	0.71	0.54	0.52	0.45
63	S-RA	4.5	111.2	90.6	68.0	120.2	1680	0.29	0.72	0.52	0.43	
49	U-RE	8.2	113.6	94.7	72.5	123.0	2280	0.48	0.74	0.54	0.62	
50	U-RE <sub>C</sub>	8.2	112.3	91.7	67.5	119.2	2280	0.55	0.71	0.54	0.55	0.44
65	U-RA	8.2	106.8	87.1	62.9	107.2	2280	0.35	0.64	0.55	0.37	
66	U-RA <sub>C</sub>	8.2	101.0	82.2	57.0	97.7	2280	0.35	0.57	0.57	0.22	
54	HLN-RE	33	102.7	86.9	66.6	108.2	4560	0.85	0.65	0.56	0.49	0.49
16	HLA-RE	18	99.8	84.4	61.6	104.2	3380	0.69	0.62	0.60	0.72	
18	HLA-RE	18	117.5	96.7	77.0	138.6	3380	0.75	0.84	0.49	0.50	
72	HLA-RE	18	105.4	87.9	64.1	106.2	3380	0.66	0.64	0.58	0.57	0.60

Note: °C = (°F - 32) 5/9.

$$r = \frac{KA_p}{\rho c_p Q_o} \dots \dots \dots (4)$$

in which  $K$  = steady-state heat exchange coefficient; and  $\rho c_p$  = specific heat per unit volume. The fundamental role of the parameter  $r$  in determining the steady-state or average heat transfer characteristics of cooling ponds has been summarized (8). The low flow rate yielded the range  $r = 0.89$ –1.38 and the high flowrate  $r = 0.62$ –0.95. Fig. 4 gives a summary of the design combinations while Table 1 gives all relevant data with runs grouped into similar ranges. All experiments were made with a pond depth of 3 in. (76 mm).

The different designs are evaluated in terms of their steady-state intake

TABLE 2.—Summary of Dye UIR for Laboratory Simulations

Configuration (1)	Low Flow Rate Experiments		High Flow Rate Experiments	
	$\hat{t}_a$ (2)	$\hat{t}_m$ (3)	$\hat{t}_a$ (4)	$\hat{t}_m$ (5)
HLN-RE	0.44	0.65	0.61	0.85
HLA-RE	0.33	0.57	0.37	0.74
U-RA <sub>c</sub>	0.22	0.41	0.33	0.52
U-RA	0.24	0.44	0.37	0.48
U-RE <sub>c</sub>	0.20	0.42	0.30	0.52
U-RE	0.18	0.48	0.15	0.63
S-RA	0.20	0.26	0.22	0.44
S-RE	0.13	0.22	0.15	0.37
N-RA	0.17	0.21	0.24	0.31
N-RE	0.07	0.07 (0.21) <sup>a</sup>	0.07	0.08 (0.25) <sup>a</sup>

<sup>a</sup>Time of arrival for second peak.

temperature,  $T_i$ , and their UIR to dye injections. Since constant laboratory "meteorology" prevailed, it is convenient to normalize  $T_i$  as

$$T_i^* = \frac{T_i - T_E}{T_o - T_E} \dots \dots \dots (5)$$

in which  $T_E$  = equilibrium temperature; and  $T_o$  = discharge temperature. Low values of  $T_i^*$  would appear to be indicative of better pond performance. However,  $T_i^*$  alone is not a reliable measure, due to its sharp dependence on the cooling capacity,  $r$ , as is evident from steady-state analytical models (8). Thus, when comparing ponds with different  $r$  and different geometry, it would be possible to attribute changes in  $T_i^*$  to either effect. An alternative measure which can be shown (2,9) to be only weakly dependent on  $r$  has been adopted, namely, the deficiency  $D$ , for

$$D = \frac{T_i^* - T_p^*}{T_m^* - T_p^*} \dots \dots \dots (6)$$

in which  $T_p^* = e^{-r}$ ; and  $T_m^* = 1/1 + r$  are the normalized intake temperature values for the plug flow pond and the completely mixed pond, respectively

(8). The deficiency indicates how closely a pond approaches ideal plug-flow performance. Lower values of  $D$  indicate better pond performance with the limiting value,  $D = 0$ . A value  $D = 1.0$  indicates performance equivalent to a completely mixed pond, which is usually considered the worst case except for ponds with strong recirculation patterns which may exhibit deficiencies even greater than unity (8). An error analysis (2) based on the experimental accuracy of all variables contributing to  $D$  showed a standard deviation of  $\pm 25\%$  for any run. To reduce this uncertainty, most runs were repeated and the average  $\bar{D}$  value is included in Table 1 for each group of similar experiments.

The UIR curves, together with visual studies of the dyed flow field, provided information on short-circuiting and residence time for each configuration. Quantitative analysis of the dye curves was made using two parameters: (1)  $\hat{t}_a = t_a Q_o / V$ , the time to the first arrival of the dye patch at the intake; and (2)  $\hat{t}_m = t_m Q_o / V$ , the time for the peak concentration of dye to arrive at the intake (Table 2). Ponds with longer times to first arrival and times to peak may be considered to exhibit less short circuiting and longer effective residence times.

**Effect of Baffle Configuration.**—The difference in surface isotherm and flow patterns between an unbaffled, an S-shaped, and a highly baffled pond, all with rectangular discharges and low flow rates, is shown in Fig. 5. Clearly, baffles constrain the size of recirculating eddies. Eddies are still observed in the highly baffled pond, however, and their cumulative effect, due to the many corners, may still be significant.

Examination of Table 1 shows that for the low flow case, deficiency is inversely correlated with the density of the baffles. With the exception of the unbaffled, radial configuration, increasing the number of baffles decreases the deficiency. For the high flow case, however, the relationship is different. There is a tendency for moderately baffled ponds, that is, the S-shaped and U-shaped ponds, to be less deficient than either the highly baffled or unbaffled ponds.

Two hypotheses may be formulated to explain the anomalies between the low and high flow results. As shown by their UIR curves, the highly baffled ponds exhibit longer effective residence times than their less densely baffled counterparts. Intuitively, better performance for the ponds with longer residence times is expected as verified by the results for the low flow rates. For the high flow runs, however, increased dispersion in the narrow channels and mixing at the bends in the flow path may cause the deficiency of the highly baffled configurations to rise relative to the more moderately baffled S and U-shaped ponds. A second hypothesis is that some remaining low Reynolds number effects are responsible for the discrepancy between the low and high flow results.

In summary, although the highly baffled pond design was less deficient in some cases, the incremental costs of constructing dense prototype baffle configuration and the associated loss of water surface area probably render this design unwarranted. Thus, the U-shaped or S-shaped ponds with a moderate length/width ratio of order 5–10 appear to represent the most desirable baffle configuration.

**Effect of Radial Discharge Design.**—All rectangular discharges had the desirable condition of a small discharge densimetric Froude number so that their mixing should be minimal. However, the rectangular design always produced significant recirculating eddies. The use of a radial discharge, also with low exit Froude

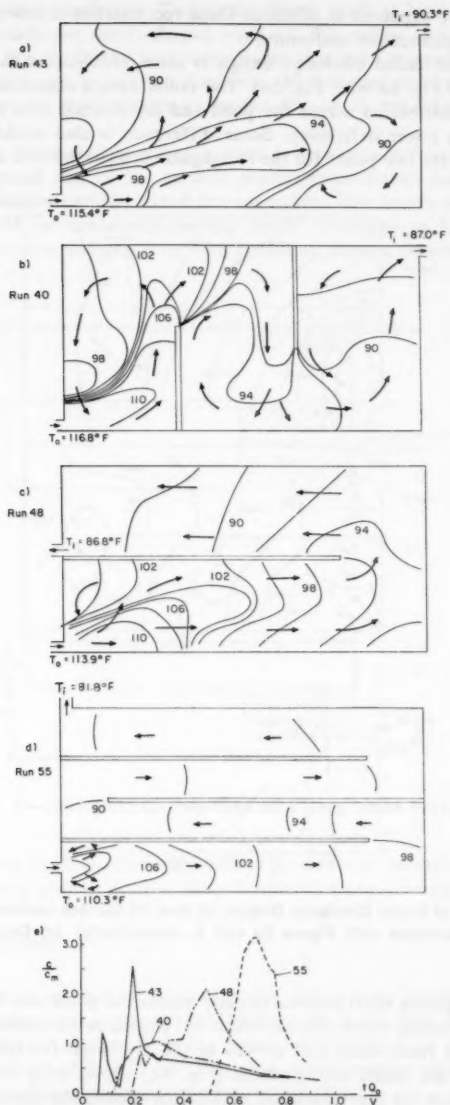


FIG. 5.—Effect of Pond Baffles (a) to (d) Surface Isotherm and Velocity Distributions for Increasing  $L/W$  Ratios, (e) Corresponding UIR Curves

number, can be expected to minimize these recirculation zones as it distributes the discharge momentum uniformly.

The effect of radial discharge design is most pronounced in the unbaffled case (compare Fig. 6a with Fig. 5a). The radial design causes a more uniform temperature distribution across the pond and the thermal data (Table 1) show conclusively a lower deficiency. Some difference is also evident in the UIR curves: There are two peaks for the rectangular design, the first occurring when

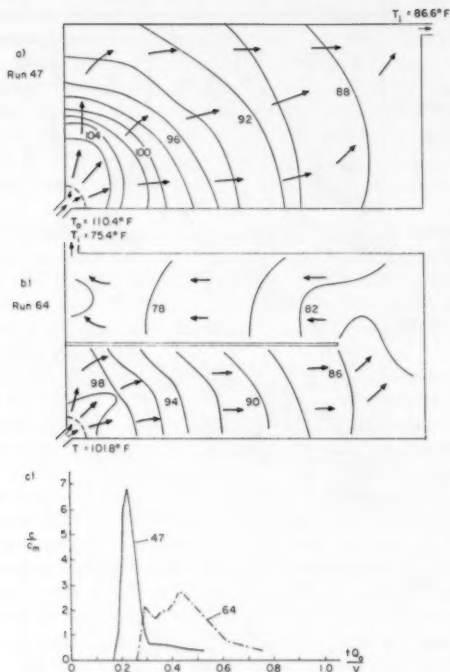


FIG. 6.—Effect of Radial Discharge Design, (a) and (b) Surface Isotherm and Velocity Distribution (Compare with Figure 5a and b, respectively). (c) Corresponding UIR Curves

the discharge plume short-circuits directly across the pond into the intake, and the second occurring when effluent which has passed to the recirculating regions of the pond is reentrained and arrives at the discharge for the second time. The UIR for the radial configuration (Fig. 6c) shows only one peak which arrives later than the short-circuited peak of the rectangular discharge.

The incremental effect of the radial discharge is, of course, much less for the baffled designs, by virtue of the physical reduction of the discharge eddy due to the lateral constraint. Thus, in view of the experimental error on  $D$ ,



the results are less conclusive. Two comparisons, each at high and low flow rates, can be made for the U-shaped pond—U-RE versus U-RA and U-RE<sub>c</sub> versus U-RA<sub>c</sub> (Fig. 4). Of the four comparisons (Table 1), three show the radial design as superior, one as inferior. Similarly, the S-shaped pond showed poorer performance for the radial design at the low flow rate, but better at the high flowrate.

In summary, the radial discharge is seen to influence deficiency chiefly in the unbaffled pond and its use in such ponds seems highly desirable if they operate in the shallow partially mixed thermal regime. The use of a radial discharge is also advisable for moderately baffled ponds (U-shaped or S-shaped) as it reduces the entrance eddying zone with beneficial effects on pond deficiency.

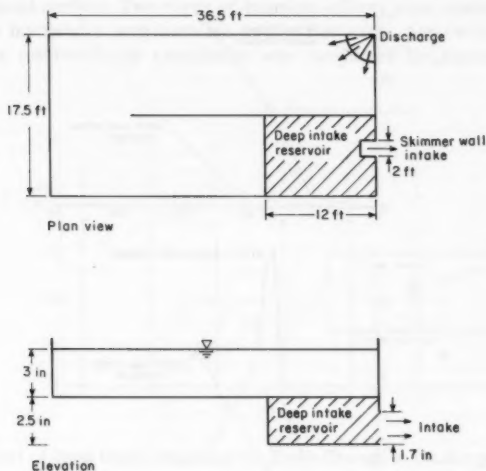


FIG. 7.—Laboratory Cooling Pond with Deep Intake Reservoir

The use of radial discharges in highly baffled ponds seems superfluous, however, since the baffling density alone is likely to constrain any discharge eddies.

#### TRANSIENT SIMULATIONS

A disadvantage of shallow cooling ponds lay in their restricted ability to minimize transient intake temperature fluctuations. In the field, typical summer diurnal temperature changes over the entire water column of a shallow pond can be of the order of  $2-4^{\circ}\text{F}$  ( $1^{\circ}-2^{\circ}\text{C}$ ) and corresponding intake temperature fluctuations have been observed at power plants (9).

Several experiments were performed to test the hypothesis that the addition to a shallow pond of a small deep reservoir in front of the submerged skimmer wall intake would provide sufficient added thermal inertia to reduce, or even

eliminate, the diurnal intake temperature variability. For a field pond, some stratification will then be generated during the warmest hours of the day in the deep portion of the pond, allowing the power plant to selectively withdraw cool water from the deep reservoir. As the cool water supply in the lower layer of the deep reservoir is exhausted and replaced by warmer surface water, enhanced surface cooling during the evening hours will cause vertical overturn in the deep reservoir. The combined action of stratification and overturn on a daily cycle should have a damping effect on cooling pond behavior, minimizing fluctuations in the intake temperature.

The experiments concentrated on the U-shaped pond with radial discharge (U-RA, Fig. 4) which has been observed to have desirable steady-state charac-

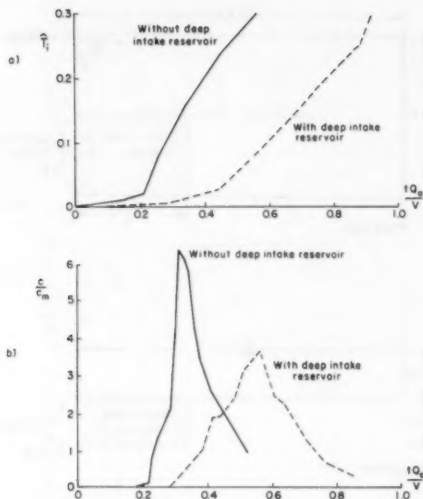


FIG. 8.—Effect of Deep Intake Reservoir for Step Increase in Discharge Temperature, (a) Normalized Intake Temperature, (b) UIR Curves

teristics. The pond was alternatively studied as: (1) uniformly shallow (as in all steady-state simulations); and (2) with a deep intake reservoir "excavated" in front of the submerged skimmer wall intake. The shallow pond with the deep intake reservoir is shown in Fig. 7. The volume  $V_d$  of the deep "excavation" was computed from the design relationship

$$V_d = Q_o \frac{T}{2} \dots \dots \dots (7)$$

in which  $Q_o$  = plant flow rate; and  $T$  = period of fluctuation (one day under prototype conditions). With an approximate time ratio  $t_r = 1/48$  between laboratory and prototype conditions and a high flow rate case, Eq. 7 yielded

a deep reservoir volume of 18 ft<sup>3</sup> (0.5 m<sup>3</sup>), or a 13% increase of the total pond volume. The submerged intake height was chosen as 1.7 in. (43 mm), with a 24 in. (610 mm) width, based on Harleman and Elder's (4) design condition, an expected stratification of 3° F (1.7° C) and a layer depth equal to  $H = 3$  in. (76 mm) in front of the skimmer wall. During periods of weaker stratification, the skimmer wall will continue to operate as partially selective as shown by Jirka's analysis (5).

**Simulation Results.**—It proved experimentally impossible to produce transient meteorological conditions in the laboratory. Instead, transient effects were created by providing a variable discharge temperature  $T_o(t)$ . Because of the dispersive effect in the flow through the pond, this type of transient effect is not as significant as the meteorologically-induced variation which acts uniformly over the entire pond surface. Two types of transient effects were simulated:

The first involved a step increase in  $T_o$ . For each case (with and without deep intake reservoir) the experiment was conducted by running the model

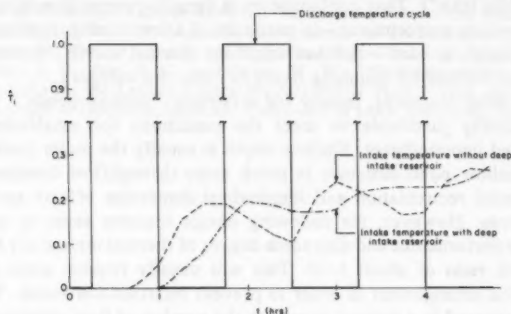


FIG. 9.—Effect of Deep Intake Reservoir for Cyclic Change in Discharge Temperature

to steady-state at a discharge temperature,  $T_{o1}$ , and then suddenly raising the discharge temperature by 50° F (10° C) to a constant value  $T_{o2}$  ( $= T_{o1} + 50^\circ$  F). The resulting normalized intake temperatures  $\hat{T}_i = (T_i - T_{o1}) / (T_{o2} - T_{o1})$  are shown in Fig. 8a as a function of normalized time, i.e. the time normalization takes account of the increased volumes. A considerably delayed response in intake temperature is observed in the case with the deep intake reservoir. During the rising phase in  $\hat{T}_i$  a stratification of 10° F (5.6° C) was observed in the vicinity of the intake, producing good skimmer wall selectivity. A dye injection which followed the discharge temperature increase indicated a similarly delayed response through utilization of the stratification in the deep intake reservoir (Fig. 8b).

The second simulation involved a cyclic change in  $T_o$ . The simulation of model diurnal changes (0.5 hr periodicity) was abandoned due to the strength of the dispersive effects which, in combination with pond residence time, smoothed out intake temperature fluctuations even for the shallow case. A 1.5 hr periodicity (3 model days) was instead used. The simulations were initiated

by running the model to steady state at discharge temperature,  $T_{o1}$ . Next, a cyclical switch of approximately 17° F (8.3° C) to a higher discharge temperature,  $T_{o2}$ , was maintained, as shown in a normalized manner in Fig. 9. The intake temperature  $T_i$  shows a transient response consisting of a steady increase due to the increased heat load and superimposed cyclical variations. The magnitude of the variations is considerably stronger for the uniformly deep pond. The amplitude of the deviation between the two cases is about 1° F (0.6° C) in actual temperature values. This result proves the capability of a shallow pond with a deep intake reservoir to damp out intake temperature fluctuations.

## CONCLUSIONS

The following design conclusions for cooling impoundments are appropriate in view of the laboratory study reported herein and field and laboratory data reported earlier (6,9,10):

The most desirable impoundment configuration is the deep well stratified case ("cooling lake"). That configuration is density-current-dominated, ensures good steady-state performance—in particular if a low mixing, preferably radial, discharge design is used—and has excellent thermal inertia. Several existing cooling lakes formed by damming rivers fall into this category.

In many other instances, mostly for offstream "cooling ponds," it may not be economically justifiable to meet the conditions for establishment of a well-stratified impoundment. Shallow depth is usually the major limitation. The resulting shallow pond structure is much more throughflow dominated, tends toward internal recirculation and longitudinal dispersion effects and has poor thermal inertia. However, the following design features seem to insure good steady-state performance and also some degree of thermal inertia: (1) A moderate length/width ratio of about 5–10. This will usually require some amount of internal baffle arrangement in order to prevent recirculation zones. The baffles should be arranged in a manner to reduce the number of flow direction changes. Given a common rectangular shape of available land, a U-shaped pond is frequently most attractive and a good tradeoff against the increased costs of a more dense baffle arrangement; (2) a radial discharge structure which minimizes the recirculation caused by the entering discharge momentum; and (3) a deep intake reservoir with a residence time of at least one half day to insure damping of diurnal fluctuations.

## ACKNOWLEDGMENTS

The study reported herein was conducted at the R. M. Parsons Laboratory at M.I.T. and was sponsored by Commonwealth Edison Company, Chicago, Illinois, and NUS Corporation, Rockville, Maryland.

## APPENDIX.—REFERENCES

1. Abraham, G., and Eysink, W. D., "Magnitude of Interfacial Shear in Exchange Flow," *Journal of Hydraulic Research*, Vol. 9, 1971, pp. 125–151.
2. Cerco, C. F., "Experimental and Analytical Study of the Design of Shallow Cooling Ponds," thesis presented to the Massachusetts Institute of Technology, at Cambridge,

- Mass., in 1977, in fulfillment of the requirements for the degree of Master of Science.
3. Fischer, J. B., "The Mechanics of Dispersion in Natural Streams," *Journal of the Hydraulics Division*, ASCE, Vol. 93, No. HY6, 1967.
  4. Harleman, D. R. F., and Elder, R. E., "Withdrawal from Two-Layer Stratified Flows," *Journal of the Hydraulics Division*, ASCE, Vol. 91, No. HY4, 1965.
  5. Jirka, G. H., "Supercritical Withdrawal from Two-Layered Fluid Systems. Part 1: Two-Dimensional Skimmer Wall," *Journal of Hydraulic Research*, Vol. 17, 1979, pp. 43-51.
  6. Jirka, G. H., and Harleman, D. R. F., "Cooling Impoundments: Classification and Analysis," *Journal of the Energy Division*, ASCE, Vol. 105, No. EY2, 1979.
  7. Jirka, G. H., and Watanabe, M., "Thermal Structure of Cooling Ponds," *Journal of the Hydraulics Division*, ASCE, Vol. 106, No. HY5, 1980.
  8. Jirka, G. H., and Watanabe, M., "Steady-State Estimation of Cooling Pond Performance," *Journal of the Hydraulics Division*, ASCE, Vol. 106, No. HY6, 1980.
  9. Jirka, G. H., Watanabe, J., Octavio, K. H., Cerco, C. F., and Harleman, D. R. F., "Mathematical Predictive Models for Cooling Lakes and Ponds. Part A: Model Development and Design Considerations," *Technical Report No. 238*, Massachusetts Institute of Technology, R. M. Parsons Laboratory for Water Resources and Hydrodynamics, Cambridge, Mass, 1978.
  10. Ryan, P. J., and Harleman, D. R. F., "Prediction of the Annual Cycle of Temperature Changes in a Stratified Lake or Reservoir: Mathematical Model and User's Manual," *Technical Report No. 137*, Massachusetts Institute of Technology, R. M. Parsons Laboratory for Water Resources and Hydrodynamics, Cambridge, Mass., 1971.
  11. Tatinclaux, J. E., Jain, S. C., and Sayre, W. W., "Hydraulic Model Study of the Cooling Lake for the LaSalle County Nuclear Power Plant," *Tech. Report No. 152*, Iowa Institute of Hydraulic Research, University of Iowa, Iowa City, Iowa.



## DISCUSSION

Note.—This paper is part of the Journal of the Hydraulics Division, Proceedings of the American Society of Civil Engineers, ©ASCE, Vol. 107, No. HY11, November, 1981. ISSN 0044-796X/81/0011-1567/\$01.00.

## DISCUSSIONS

Discussions may be submitted on any Proceedings paper or technical note published in any *Journal* or on any paper presented at any Specialty Conference or other meeting, the *Proceedings* of which have been published by ASCE. Discussion of a paper/technical note is open to anyone who has significant comments or questions regarding the content of the paper/technical note. Discussions are accepted for a period of 4 months following the date of publication of a paper/technical note and they should be sent to the Manager of Technical and Professional Publications, ASCE, 345 East 47th Street, New York, N.Y. 10017. The discussion period may be extended by a written request from a discussor.

The original and three copies of the Discussion should be submitted on 8-1/2-in. (220-mm) by 11-in. (280-mm) white bond paper, typed double-spaced with wide margins. The length of a Discussion is restricted to two *Journal* pages (about four typewritten double-spaced pages of manuscript including figures and tables); the editors will delete matter extraneous to the subject under discussion. If a Discussion is over two pages long it will be returned for shortening. All Discussions will be reviewed by the editors and the Division's or Council's Publications Committees. In some cases, Discussions will be returned to discussors for rewriting, or they may be encouraged to submit a paper or technical note rather than a Discussion.

Standards for Discussions are the same as those for Proceedings Papers. A Discussion is subject to rejection if it contains matter readily found elsewhere, advocates special interests, is carelessly prepared, controverts established fact, is purely speculative, introduces personalities, or is foreign to the purposes of the Society. All Discussions should be written in the third person, and the discussor should use the term "the writer" when referring to himself. The author of the original paper/technical note is referred to as "the author."

Discussions have a specific format. The title of the original paper/technical note appears at the top of the first page with a superscript that corresponds to a footnote indicating the month, year, author(s), and number of the original paper/technical note. The discussor's full name should be indicated below the title (see Discussions herein as an example) together with his ASCE membership grade (if applicable).

The discussor's title, company affiliation, and business address should appear on the first page of the manuscript, along with the *Proceedings* paper number of the original paper/technical note, the date and name of the *Journal* in which it appeared, and the original author's name.

Note that the discussor's identification footnote should follow consecutively from the original paper/technical note. If the paper/technical note under discussion contained footnote numbers 1 and 2, the first Discussion would begin with footnote 3, and subsequent Discussions would continue in sequence.

Figures supplied by the discussor should be designated by letters, starting with A. This also applies separately to tables and references. In referring to a figure, table, or reference that appeared in the original paper/technical note use the same number used in the original.

It is suggested that potential discussors request a copy of the *ASCE Authors' Guide to the Publications of ASCE* for more detailed information on preparation and submission of manuscripts.



# AGGRADATION IN STREAMS DUE TO OVERLOADING<sup>a</sup>

Closure by Jagdish P. Soni,<sup>6</sup> Ramchandra J. Garde,<sup>7</sup> M. ASCE  
and Kittur G. Ranga Raju<sup>8</sup>

The writers thank Jain and Gill for their comments. Both of them refer to the fact that  $Z_0$  is assumed to be independent of time in solving Eq. 6, whereas, eventually,  $Z_0$  is found to be a function of time. Recently the writers have also obtained (16) a solution considering the variation of  $Z_0$  with time, which is identical with Eq. 32. But the experimental data do not agree with Eq. 32 either, thereby still necessitating modification of  $K$  or a "Forced Fit." To that extent, despite the lack of mathematical rigor, the method proposed in the paper should be considered satisfactory, particularly because of its simplicity.

## APPENDIX.—REFERENCE

16. Garde, R. J., Ranga Raju, K. G., and Metha, P. J., "Bed Level Variation in Aggrading Alluvial Streams," *Proceedings of the International Association for Hydraulics Research*, 19th Congress, New Delhi, India.

**Errata.**—The following corrections should be made to the original paper:

Page 121, Eq. 15 should read:

$$\frac{1}{96} \left( \frac{1}{\sqrt{kt}} \right)^3 \text{ " instead of " } \left( \frac{1}{96} \frac{1}{\sqrt{kt}} \right)^3 \text{ "}$$

Page 126, line 4: Should read " $x/2\sqrt{K_0 t}$ " instead of " $x/(2\sqrt{Kt})$ "

Page 127, Fig. 10: Should read " $h \times 10^2 \text{ m}$ " instead of " $h \times 10^2 \text{ m/s}$ "

<sup>a</sup>January, 1980, by Jagdish P. Soni, Ramchandra J. Garde, and Kittur G. Ranga Raju (Proc. Paper 15147).

<sup>6</sup>Assoc. Prof., Dept. of Civ. Engrg., Punjab Agricultural Univ., Ludhiana, India.

<sup>7</sup>Prof., Dept. of Civ. Engrg., Univ. of Roorkee, Roorkee, India.

<sup>8</sup>Prof. of Civ. Engrg., Univ. of Roorkee, Roorkee, India.

## FINITE ELEMENT METHOD FOR DIRECT RUNOFF FLOW<sup>a</sup>

Closure by Mutsuto Kawahara<sup>4</sup> and Teruyuki Yokoyama<sup>5</sup>

The writers would like to thank Raymond J. Dever for his interest in the paper. The main purpose of this work is to present a method of solving the rainfall runoff flow problem. Namely, the paper states that the finite element method has proved to be a useful tool for the analysis of the direct runoff flow. Also, the adaptability of the method is limited to solving mainly the surface runoff flow.

The insufficient points of the methodology are: rainfall losses are not included, the river and the watershed are not separated, and the effect of numerical damping which arises from the numerical integration scheme is included.

Dever pointed out that the method does not include rainfall losses. The finite element method presented in the paper can be adaptable when the basic equations include the effects of rainfall losses. In Eq. 2, rainfall losses are included in the last term. This term is related to the infiltration and other surface effects. The term can be expressed by the empirical functions. This term has no significant inefficiency on the numerical method itself. In the case of practical application in which the equation of continuity includes a loss term, the finite element method presented in the paper can be used effectively, without any modification of the scheme. In the practical computation, it is recommended that the river flow be computed by separating from the flow on the watershed. The numerical integration scheme can be modified to avoid the artificial numerical damping effect.

---

<sup>a</sup>April, 1980, by Mutsuto Kawahara and Teruyuki Yokoyama (Proc. Paper 15341).

<sup>4</sup>Assoc. Prof. of Civ. Engrg., Dept. of Civ. Engrg., Chuo Univ., Kasuga, Bunkyo-ku, Tokyo, Japan.

<sup>5</sup>Grad. Student, Dept. of Civ. Engrg., Chuo Univ., Kasuga, Bunkyo-ku, Tokyo, Japan.

## CALIBRATION OF BED-LOAD SAMPLERS<sup>a</sup>

Closure by Peter Engel<sup>4</sup> and Y. Lam Lau<sup>5</sup>

In his discussion, Stevens presents a variety of statements and questions which, although quite typical of the persistent problems of bed-load measurement, are not all directly pertinent to the paper. The writers are fully aware of the fact that "voluminous" amounts of data have been gathered, not only on the Mississippi River but on other rivers throughout the world as well. However, this knowledge does not contribute anything to the problem of sampler calibration. On the contrary, it raises further questions regarding the quality of these data considering the present state of sampler calibrations.

The discussor expresses criticism of the use of laboratory flumes to study sediment transport problems. Unfortunately he seems to have confused the difficulties experienced with the use of moveable bed-scale models with the simple practice of conducting two-dimensional experiments to study basic sediment transport processes. We are all aware of the difficulty with mobile bed scale models, the variability existing in nature, and that the degree of uniformity which one can achieve in the laboratory is seldom realized in natural rivers. However, this is no excuse for not studying the problem of sediment transport in the laboratory where the effect of each variable can be isolated.

Stevens raises some specific questions on the definition of bed load, size of sampler openings, position of sampler on the bed, and calculation of bed load. Surely, these are questions the discussor has found some answers to during his many years of conducting sediment measurements on the Mississippi River. However, one question the writers consider directly pertinent to the efficiency of basket samplers is that pertaining to the local effects of the sampler on the bed when bed movement is impending. At this critical stage,  $U_* \approx U_{*,cr}$  in which  $U_{*,cr}$  = critical shear velocity. When the sampler is placed on the bed, there may be some locations around its entrance where for a brief time  $U_* > U_{*,cr}$ . However, one would expect that conditions will reach a new equilibrium quickly, although some sediment may enter the sampler. Nevertheless,  $U_*$  will be quite small and therefore  $W_s$  in which  $W_s$  = submerged weight of sample will be small. As a result,  $t_*$  would have to be large in order to satisfy the condition  $t_* U_* / L_s > 25$ ; therefore, the computed sediment transport at the sampler location computed as  $100 W_s / Et_*$  will have to be small. The result would be a negligible error in the overall bed-load computation for the entire river cross section.

Stevens refers to "up-to-date methods" as an alternative to the use of model

<sup>a</sup>October, 1980, by Peter Engel and Y. Lam Lau (Proc. Paper 15725).

<sup>4</sup>Research Engr., Environmental Hydr. Section, Hydr. Research Div., National Water Research Inst., Burlington, Ontario, Canada.

<sup>5</sup>Head, Environmental Hydr. Section, Hydr. Research Div., National Water Research Inst., Burlington, Ontario, Canada.

data but does not give an example of what he considers up to date. The writers consider such generalizations to be quite misleading and unproductive. The writers are aware of all methods currently in use and at the development stage have themselves (2) contributed toward the development of new methods to determine bed-load transport rate. Unless the discussor is advocating that we abandon the collection and calculation of bed-load transport or can suggest some better methods, one has to accept that bed-load samplers will have to be used for some time to come. Therefore, some effort has to be made to relate the catch to the actual transport rate. Towards this end, tests on model samplers in large flumes can provide valuable information on the variables affecting the sampler catch.

**Errata.**—The following correction should be made to the original paper:

Page 1684, paragraph 1, line 7: Should read " $t_* U_* / L_s < 25$ " instead of " $t_* U_* / L_s > 25$ "

---

## ADAPTATION OF ILLUDAS FOR CONTINUOUS SIMULATION<sup>a</sup>

### Errata

The following corrections should be made to the original paper:

Page 1797, immediately following Eq. 1: Should read "in which  $Q_n$  = runoff at the end of time period  $n$ ;  $i_j$  = effective rainfall rate during time interval  $j$ ; and  $A_n - j + 1$  = additional area on time-area curve contributing to runoff during time period  $n - j + 1$ " instead of "in which  $Q_n$  = runoff at the end of time period  $n$ ;  $i_j$  = effective rainfall rate during interval  $j$ ; and  $A_n - j + 1$  = area contributing to runoff at time period  $n - j + 1$ "

---

<sup>a</sup>November, 1980, by Harry G. Wenzel, Jr. and Michael L. Voorhees (Proc. Paper 15840).

## EROSION BY CIRCULAR WALL JETS IN CROSS FLOW<sup>a</sup>

### Errata

The following corrections should be made to the original paper:

Eq. 4, Should read " $\frac{\epsilon}{\epsilon_m} = e^{-0.693(\eta/b)^2}$ ," instead of " $-0.693\left(\frac{7^2}{b}\right); \frac{\epsilon}{\epsilon_m} = e$ "

## SAND BED INSTABILITY DUE TO BED LOAD MOTION<sup>b</sup>

Discussion by A. J. Sutherland,<sup>3</sup> B. C. Phillips,<sup>4</sup> A. M. ASCE  
and R. G. Bell<sup>5</sup>

The authors have presented results from an interesting series of experiments in which water flowed from a fixed bed to an alluvial bed at constant discharge. Fig. 5 shows bed-load transport rates for different values of the distance downstream from the fixed to alluvial transition,  $x$ . Unfortunately, insufficient detail concerning the experimental method was given, and, thus, the results are difficult to interpret.

The experiments could have been conducted in one of two ways. First, before the start of the experiment, there could have been equilibrium bed load transport at rate  $q_{BO}$  everywhere along the bed. This would be maintained by adding sediment at the appropriate rate at the upstream end. At the start of the experiment, the sediment supply would be removed and the initial condition at  $t = 0$  would be  $1 - q_B(x)/q_{BO} = 0$ . Local transport rates,  $q_B(x)$ , at points close to the transition would start to decrease with time while those at points further downstream would remain unchanged. As time progressed, the region over which transport rates were reduced would lengthen and finally extend the full length,  $L$ , of the working section. The transport rate everywhere would eventually drop to zero as a result of bed degradation and the onset of threshold conditions. Results from such an experiment are presented in Fig. 14(a), which has the same

<sup>a</sup> November, 1980, by Nallamuthu Rajaratnam (Proc. Paper 15842).

<sup>b</sup> December, 1980, by Hijoji Nakagawa and Tetsuro Tsujimoto (Proc. Paper 15936).

<sup>3</sup> Reader in Civ. Engrg., Univ. of Canterbury, Canterbury, New Zealand.

<sup>4</sup> Postgraduate student, Univ. of Canterbury, Canterbury, New Zealand.

<sup>5</sup> Scientist, M.W.D. Science Centre, Hamilton, New Zealand.

coordinates as Fig. 5, but a linear scale has been used on the ordinate so the origin, and, thus, the equilibrium transport conditions at  $t = 0$  can be included. Full details of these experiments are given by Bell (26) who used 2.1 mm gravel in a flume 0.31 m wide with a 10 m long working section on a slope of 0.002.

Alternatively, the experiments may have been done by imposing the selected discharge onto the bed as rapidly as possible so that the initial condition becomes  $q_B(x) = 0$  everywhere. In this case, local transport rates,  $q_B(x)$ , would increase with time over the whole working section initially. At downstream sections, the equilibrium rate may be reached and maintained for a time until bed degradation

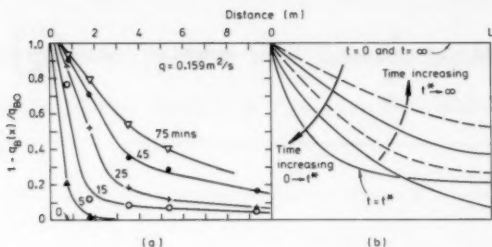


FIG. 14.—Bed-Load Transport Rates Downstream of Transition from Fixed to Alluvial Bed: (a)  $q_B(x) = q_{BO}$  at  $t = 0$ . (from Ref. 26); Expected Trends for  $q_B(x) = 0$  at  $t = 0$

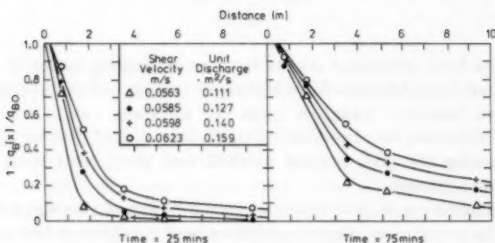


FIG. 15.—Bed-Load Transport Rates Downstream from a Transition from Fixed to Alluvial Bed (from Ref. 26)

reduces the transport rate, which will eventually reach zero everywhere. The equilibrium rate reached is of course less than  $q_{BO}$  since the bed must have degraded in the time taken to reach the equilibrium rate. Diagrammatically, the process can be represented as in Fig. 14(b). It is difficult to visualize this process in detail so the shapes of lines in Fig. 15 are speculative, but the trends are given with confidence.

Whichever way the experiments were done,  $q_B(x)$  is certainly a function of both  $x$  and  $t$ . The following questions can now be posed:

1. Which method of doing the experiments was followed?

2. Were all the data in Fig. 5 recorded at the same time so that they can be compared directly?

3. At what times were the measurements taken?

If one orders the Runs according to shear velocity and then examines the relative position of the curves in Fig. 5, then results from the Runs, which the authors numbered 7 and 3, are clearly out of sequence, particularly the latter which has the highest shear velocity. This may be explained if the data from these runs was taken at times different from those of the other runs. The authors' comments on this point would be welcome.

The influence of shear velocity on Bell's (a) results may be seen in Fig. 15 for both 25 and 75 min after the start of experiment.

#### APPENDIX.—REFERENCE

26. Bell, R. G., "Nonequilibrium Bed-load Transport by Steady and Non-Steady Flows," Research Report 80-23, Department of Civil Engineering, University of Canterbury, Christchurch, New Zealand, Nov., 1980, p. 237.

## RE-EXAMINATION OF NIKURADSE ROUGHNESS DATA<sup>a</sup>

Discussion by R. Fuentes<sup>2</sup> and S. Carrasquel<sup>2</sup>

The writers wish to congratulate the author on his contribution to a subject of wide interest. The purpose of this discussion is to add some comments concerning Eqs. 1, 2, and 3, proposed by the author for the overall friction factor,  $f$ . By convenience, the writers introduce the following notations.

$$\Delta = \frac{1}{\sqrt{f}} - 2 \log \frac{D}{2ks}; \dots \dots \dots (11)$$

$$Re^* = \frac{R^*}{\frac{D}{ks}} \dots \dots \dots (12)$$

The author describes the evolution of the  $\Delta - Re^*$  curve by means of three different equations for the smooth, transition, and rough turbulent zones, respectively. The use of three separate equations not only could be tedious for calculations, but could also suggest that the phenomenon involved is not continuous.

<sup>a</sup>January, 1981, by William R. Brownlie (Proc. Paper 15957).

<sup>2</sup>Research Officers, National Hydr. Lab., Apartado 2035, Caracas, Venezuela.

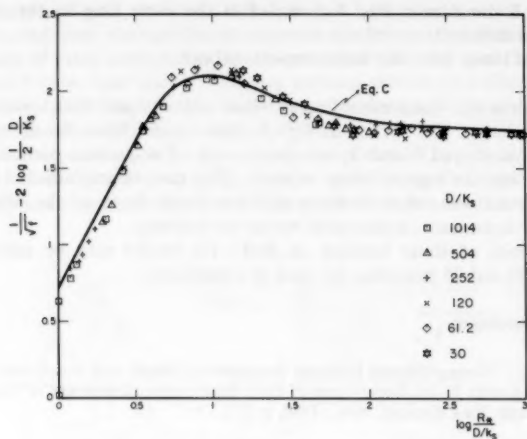


FIG. 3.—Proposed Equation with Nikuradse Selected Data

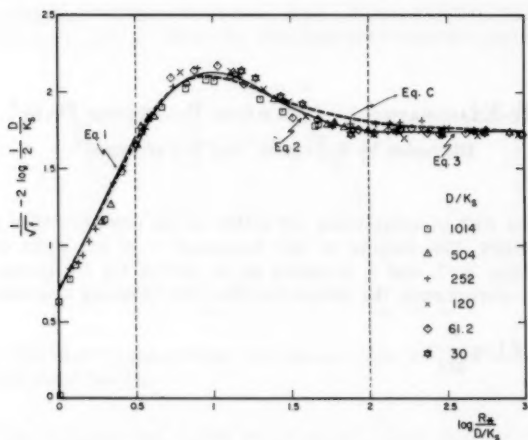


FIG. 4.—Comparison between Author Equations and Proposed Equation, Showing Nikuradse Selected Data

The writers recently have developed and published (5) a single equation that can be used to describe all three zones in the  $\Delta - Re^*$  graph. The logarithmic velocity law is currently written as

$$\frac{v}{V^*} = \frac{1}{k} \ln \frac{y}{y'} \dots \dots \dots (13)$$



in which  $v$  = mean local velocity;  $V^*$  = shear velocity;  $k$  = Von Kármán's constant;  $y$  = distance to the boundary; and  $y'$  = reference thickness.

The writers have proposed (5) the following equation for  $y'$ :

$$\frac{y'}{ks} = \frac{a_s}{Re^*} + a_r \exp\left(-\frac{\alpha}{Re^*}\right) \dots \dots \dots (14)$$

In the above equation,  $a_s$  and  $a_r$  = constant values corresponding to the smooth ( $Re^* \rightarrow 0$ ) and rough turbulent ( $Re^* \rightarrow \infty$ ) zones; and  $\alpha$  = a shape parameter of the  $y'/ks - Re^*$  curve. As an example,  $\alpha = 0$  for the Colebrook and White's data. As a test trial, the writers have determined the values of  $a_s$  and  $a_r$  from the integrated version of Eq. 13 for the smooth and rough turbulent zones (6). The value of  $\alpha$  was obtained using least squares for the experimental points in Fig. 3. The adopted values are  $a_s = 0.0965$ ;  $a_r = 0.0293$ ; and  $\alpha = 11$ . With these values and from the integrated version of Eq. 13, the following single equation for  $\Delta$  is obtained:

$$\Delta = \frac{1}{\sqrt{f}} - 2 \log \frac{D}{ks} = -2 \log \left[ \frac{0.444}{Re^*} + 0.135 \exp\left(-\frac{11}{Re^*}\right) \right] \dots \dots (15)$$

Eq. 15 is shown in Fig. 3, with the Nikuradse experimental points selected by the author. It is clear that Eq. 15 gives a fairly good prediction of the experimental mean curve. Also, for purposes of comparison, in Fig. 4 the author's and writers' equations are shown together with the experimental points. The "jump" exhibited by the relationships proposed by the author at  $\log Re^* = 0.5$  (see circled area in Fig. 4) is not clear to the writers. Nevertheless, this "jump" is not shown in Fig. 1.

#### APPENDIX.—REFERENCES

5. Fuentes, R. and Carrasquel, S., "An Empirical Equation for Transition Zones," (in Spanish), presented at the June 30-July 4, 1980, 9th Latin American International Association for Hydraulic Research Congress, held at Mérida, Venezuela.
6. Schlichting, H., "Boundary Layer Theory," 6th ed., McGraw-Hill Book Co., Inc., New York, N.Y., 1968.

## MODELING TRANSVERSE MIXING IN NATURAL STREAMS<sup>a</sup>

Discussion by Forrest M. Holly, Jr.,<sup>3</sup> M. ASCE

Although one-dimensional mixing in natural streams has received considerable attention in recent years, two-dimensional mixing appears to have been neglected.

<sup>a</sup>February, 1981, by Y. Lam Lau and B. G. Krishnappan (Proc. Paper 16048).

<sup>3</sup>Engr., Applied Mathematics Service, Sogreah, Grenoble, France.

Therefore, it is encouraging to see the authors' interesting work, for which they are to be congratulated.

Based on their model simulations of a transverse mixing experiment in Grand River, the authors concluded that "... variations of the dispersion coefficient in the downstream direction have a bigger influence on the accuracy of the simulations than the possible variations across the stream."

The writer reached essentially the same conclusion in a similar study of transverse mixing in a triangular laboratory flume (16). In particular, he tested the following transverse diffusivity functions suggested by Holly (15):

$$e_z = \alpha_1 U_* H \quad (18)$$

$$e_z = \alpha_2 \frac{U_*}{U_a} u h \quad (19)$$

$$e_z = \alpha_3 u_* h \quad (20)$$

$$e_z = \alpha_4 U_a h \quad (21)$$

in which  $\alpha_1, \alpha_2, \alpha_3, \alpha_4$  = dimensionless constant coefficients;  $U_*$  ( $x$ ) = mean shear velocity;  $u_*$  ( $x, z$ ) = local shear velocity;  $H$  ( $x$ ) = mean depth;  $h$  ( $x, z$ ) = local depth;  $U_a$  ( $x$ ) = mean velocity; and  $u$  ( $x, z$ ) = local velocity.

Holley's experiments in nearly rectangular cross sections with lateral groins suggested that Eqs. 19-21, allowing  $e_z(x, z)$  to vary laterally as well as longitudinally, were more appropriate than the simple longitudinal variation of Eq. 18,  $e_z(x)$ . However, the writer's experiments, in which strong lateral depth and roughness variations were introduced, were best reproduced by numerical model simulations using Eq. 18. Since the stream-tube model employed systematically used local values of  $h(x, z)$  in the transverse diffusion term (analogous to the righthand side of Eq. 6), the apparent applicability of Eq. 18 corresponds to the authors' conclusion that the first expression for  $D_z$  (p. 216) is the most appropriate one.

Both the authors' and the writer's conclusions are based on particular experiments. Nonetheless, the writer has been able to successfully reproduce steady and unsteady mixing experiments in other natural rivers using the cross-sectional average value of  $e_z(x)$ , Eq. 18, in a stream tube model (steady water flow, unsteady tracer injection, as in Ref. 14).

Concerning the applicability of stream tube models to transverse mixing in rivers with bends, it should not be forgotten that transformation of the transport equation into a curvilinear system is only one part of the problem. The use of the cumulative discharge,  $q$ , instead of  $z$  as the transverse independent variable takes into account the effect of the *depth-averaged* transverse velocity  $\bar{w}(x, y)$ . But in assuming that transverse mixing can be represented as a simple gradient diffusion process, the additional transverse mixing due to differential advection in the transverse direction, i.e. to the difference between local values of  $w(x, y, z)$  and the depth-average  $\bar{w}(x, z)$  ( $y$  = the vertical coordinate), is not rigorously taken into account. If this additional mixing cannot be assimilated into  $e_z$  through model calibration, then the stream-tube approach loses its utility. Unfortunately, at the present time, a modelling method capable of taking into account this secondary circulation in a satisfactory manner does not appear to be available.

## APPENDIX.—REFERENCES

14. Cunge, J. A., Holly, F., and Verwey, A., *Practical Aspects of Computational River Hydraulics*, Pitman Publishing Company, London, England, 1980.
15. Holley, E. R., "Transverse Mixing in Rivers," Report No. S 132, Delft Hydraulics Laboratory, Delft, The Netherlands, 1971.
16. Holly, F. M. Jr., "Two Dimensional Mass Dispersion in Rivers," Hydrology Paper No. 78, Colorado State University, Ft. Collins, Colo., Sept., 1975.

Discussion by Nobuhiro Yotsukura,<sup>4</sup> M. ASCE

It is gratifying to see another verification of the stream-tube equation for two-dimensional transport in a natural river flow. As far as the writer knows, the authors' study is the most thorough and detailed of available tests including the writer's own. Moreover, the authors' successful simulation of the contraction-expansion of geometric width of a tracer plume observed in the Grand River provides additional solid evidence that the stream-tube approach is useful in correctly defining the mixing zone downstream of a waste disposal site in natural rivers (17). The authors are commended for this thorough and complete modeling study.

The authors present six different simulations in Figs. 4(a) and 4(b), which correspond to various assumed forms of  $D_z$ , the factor of diffusion. Because this factor is a new and unfamiliar parameter to the discipline, the authors' comparison of these simulations with data is useful and informative in presenting an overall picture of response sensitivity of the stream-tube equation. Such information is going to be important in future predictive applications. On the other hand, one realizes that the quantities,  $u$ ,  $h$ , and  $m_x$ , contained in  $D_z$ , are measurable ones while  $e_z$  is a defined parameter that is neither measurable nor accurately predictable. With the currently limited knowledge about  $e_z$ , the only means of determining correct values of  $e_z$  for a model equation appears to be seeking the best fit simulation with data by trial and error. From this standpoint, the writer would like to focus his comments on the simulation by scheme 1 in Fig. 4(a) and that by the analytical solution in Fig. 4(b).

In assessing the three simulations presented in Fig. 4(a), it must be recalled that Eqs. 6 and 7 are an exact transformation of Eq. 4 by means of Eq. 3. Thus, there is little question that quantities,  $u$ ,  $h$ , and  $m_x$  in  $D_z$ , should be locally measured values in any test of the validity of Eqs. 6 and 7. On the other hand,  $e_z$  represents the effect of transverse mixing including dispersion and diffusion. Just as in the well-known analysis of longitudinal dispersion (3), transverse mixing requires a certain time or distance to pass through an initial advection-dominated period before it behaves like a diffusion process. Therefore,  $e_z$  cannot possibly be a local quantity, and, moreover, is probably correlated with averaged values of  $h$  and  $U$ , within a certain time or space. Accordingly, the writer believes that scheme 1 alone, among the three simulations in Fig. 4(a), provides a rigorous test of Eqs. 6 and 7. Also, following the same argument, the writer agrees with the authors' observation that some conclusions on transverse

<sup>4</sup>Research Hydro., U.S. Geological Survey, National Center-430, Reston, Va. 22092.

variation of  $D_z$  as presented in 1972 by Yotsukura and Cobb were only approximate because of limited numerical tests.

When the authors' scheme 1 simulation is examined with the view of obtaining the best fit simulation, it is clear that the result at section 2 is not the best fit because the simulated curve crosses over the data curve at midpoint. In other words, the best fit  $e_z$  value at section 2 should be larger. It is also noted that the authors define  $\bar{e}_z$  as the cross-section-averaged value. However, this definition appears to come from restrictions of the numerical scheme employed. In essence, what the authors obtained as  $\bar{e}_z$  is actually an averaged value over the particular region that is covered by the tracer plume.

As for the three simulations in Fig. 4(b), one may assume that these represent solutions to some approximate form of Eqs. 6 and 7. In particular, the simulation by analytical solution is based on an approximate form of Eqs. 6 and 7, namely

$$\frac{\partial c}{\partial x} = D_z \frac{\partial^2 c}{\partial q_c^2} \quad \dots \dots \dots (22)$$

in which  $D_z$  is assumed to be independent of  $q_c$ . There is no question that the analytical solution, Eq. 16, mathematically assumes that  $D_z$  is constant. However, this does not necessarily mean that  $D_z$  must be physically constant everywhere in the whole reach of the study, as the authors appear to interpret in the simulation. The writer takes another interpretation, that  $D_z$  represents an averaged value over the distance from the solute release site to the particular cross section of interest. In order to test the validity of Eqs. 22 and 16, the writer would compute the product,  $uh^2m_z$ , averaged over the width and also the distance to the cross section from measured data, and then, determine the best fit simulation by trial and error to obtain a reach-averaged value of  $e_z$ . Naturally, the calculation will have to be carried out independently for each cross section in the study reach. The  $e_z$  values thus obtained could vary considerably from section to section at short distances from the tracer release site but would tend toward a constant value as the distance becomes larger, because of the reach-averaging effect.

From the above interpretation of Eqs. 22 and 16, it is seen that the authors' simulations by analytical solution at Sections 2 and 3 do not achieve the best fit, because the simulated curves again cross over the data curves at midpoints. The writer feels that these simulations at sections 2 and 3 are not indicative of the limitation of Eqs. 22 and 16. On the other hand, the authors' simulations at sections 5 and 6 appear to indicate the limitations or approximate nature of Eqs. 22 and 16 because at these downstream sections the authors' values for  $uh^2m_z$  would be close to the reach-averaged ones, and these simulations appear to be the best fit to the data. The writer would like to repeat that the above comments have been made from the strict sense of testing the validity of Eqs. 6, 7, and 22.

Finally, the writer would like to summarize his latest views on the stream-tube equations as their development and testing are nearly complete. The writer still believes that the most basic reason for formulating Eqs. 6, 7, and 22 is the repeated empirical observation that the transverse mass transfer in an open channel flow tends to be a diffusive process, often pure, with respect to the cumulative discharge, namely, the two-dimensional stream function, rather than

with respect to the transverse distance. Other features, such as the use of natural coordinates and the elimination of the transverse advection term, though mathematically attractive and practically convenient, are secondary to this empirical fact. A similar stream-tube approach under the name of Von Mises coordinates has been independently developed and used for solving flow and transport problems in boundary layers of axisymmetric flow by a group from the Imperial College (18).

#### APPENDIX.—REFERENCES

17. Sayre, W. W., and Caro-Cordero, R., "Shore-Attached Thermal Plumes in Rivers," *Modeling of Rivers*, H. W. Shen, ed. John Wiley and Sons, Inc., New York, N.Y. 1979.
18. Spalding, D. B., "GENMIX: A General Computer Program for Two-Dimensional Parabolic Phenomena," *The Science and Applications of Heat and Mass Transfer* Vol. 1, Pergamon Press, Inc., New York, N.Y., 1977.

---

### UNCERTAINTIES RESULTING FROM CHANGES IN RIVER FORM<sup>a</sup>

Discussion by Victor M. Ponce,<sup>2</sup> M. ASCE

There are three mechanisms responsible for flood-wave attenuation in stream channels: infiltration, valley storage, and dynamic effects. In the absence of infiltration, the usual attenuating mechanism is valley storage, i.e., the reservoir-like action leading to flood plain inundation and an associated increase in cross-sectional flow area. Barring infiltration and valley storage, as in the case of idealized prismatic channels of rectangular crosssection, the only attenuating mechanism left is the dynamic effect. According to this mechanism, steeper waves will attenuate faster, while slow-rising waves will attenuate at a much reduced rate and often will attenuate hardly at all. The latter waves are those which the author has referred to as "uniformly progressive." The author has attributed the lack of diffusion of these waves to the small variation in resistance along the channel. In the writers's opinion, this is a misconception. Uniformly progressive waves, often referred to as kinematic waves, owe their lack of diffusion to the predominance of resistance and gravity forces over inertia forces (21). It is not immediately discernible how the variation in resistance along the channel can be used to explain the presence or absence of attenuation.

#### APPENDIX.—REFERENCE

21. Ponce, V. M., and Simons, D. B., "Shallow Wave Propagation in Open Channel Flow," *Journal of the Hydraulics Division, ASCE*, Vol. 103, No. HY12, Proc. Paper 13392, Dec., 1977, pp. 1461-1476.

---

<sup>a</sup>May, 1981, by Durl E. Burkham (Proc. Paper 16245).

<sup>2</sup>Assoc. Prof. of Civ. Engrg., San Diego State Univ., San Diego, Calif.

## TECHNICAL PAPERS

Original papers should be submitted in triplicate to the Manager of Technical and Professional Publications, ASCE, 345 East 47th Street, New York, N.Y. 10017. Authors must indicate the Technical Division or Council, Technical Committee, Subcommittee, and Task Committee (if any) to which the paper should be referred. Those who are planning to submit material will expedite the review and publication procedures by complying with the following basic requirements:

1. Titles must have a length not exceeding 50 characters and spaces.
2. The manuscript (an original ribbon copy and two duplicate copies) should be double-spaced on one side of 8-1/2-in. (220-mm) by 11-in. (280-mm) paper. Three copies of all figures and tables must be included.
3. Generally, the maximum length of a paper is 10,000 word-equivalents. As an *approximation*, each full manuscript page of text, tables or figures is the equivalent of 300 words. If a particular subject cannot be adequately presented within the 10,000-word limit, the paper should be accompanied by a rationale for the overlength. This will permit rapid review and approval by the Division or Council Publications and Executive Committees and the Society's Committee on Publications. Valuable contributions to the Society's publications are not intended to be discouraged by this procedure.
4. The author's full name, Society membership grade, and a footnote stating present employment must appear on the first page of the paper. Authors need not be Society members.
5. All mathematics must be typewritten and special symbols must be identified properly. The letter symbols used should be defined where they first appear, in figures, tables, or text, and arranged alphabetically in an appendix at the end of the paper titled Appendix.—Notation.
6. Standard definitions and symbols should be used. Reference should be made to the lists published by the American National Standards Institute and to the *Authors' Guide to the Publications of ASCE*.
7. Figures should be drawn in black ink, at a size that, with a 50% reduction, would have a published width in the *Journals* of from 3 in. (76 mm) to 4-1/2 in. (110 mm). The lettering must be legible at the reduced size. Photographs should be submitted as glossy prints. Explanations and descriptions must be placed in text rather than within the figure.
8. Tables should be typed (an original ribbon copy and two duplicates) on one side of 8-1/2-in. (220-mm) by 11-in. (280-mm) paper. An explanation of each table must appear in the text.
9. References cited in text should be arranged in alphabetical order in an appendix at the end of the paper, or preceding the Appendix.—Notation, as an Appendix.—References.
10. A list of key words and an information retrieval abstract of 175 words should be provided with each paper.
11. A summary of approximately 40 words must accompany the paper.
12. A set of conclusions must end the paper.
13. Dual units, i.e., U.S. Customary followed by SI (International System) units in parentheses, should be used throughout the paper.
14. A practical applications section should be included also, if appropriate.

